X-ray Spectroscopy of Cool Core Galaxy Clusters

Haonan Liu

Supervisor: Prof. A. C. Fabian
Dr. C. Pinto

Institute of Astronomy
University of Cambridge

This dissertation is submitted for the degree of
Doctor of Philosophy

Clare College September 2021

Declaration

I hereby declare that except where specific reference is made to the work of others, the contents of this dissertation are original and have not been submitted in whole or in part for consideration for any other degree or qualification in this, or any other university. This dissertation is my own work and contains nothing which is the outcome of work done in collaboration with others, except as specified in the text and Acknowledgements. This dissertation contains fewer than 60,000 words including appendices, bibliography, footnotes, tables and equations.

The chapters of this thesis based on published work are as follows:

- **Chapter 3** H. Liu, C. Pinto, A.C. Fabian, H.R. Russell and J.S. Sanders, "Searching for cool and cooling X-ray emitting gas in 45 galaxy clusters and groups", Monthly Notices of the Royal Astronomical Society, Vol. 485, Issue 2, p. 1757-1774, May 2019.

- **Chapter 4** H. Liu, A.C. Fabian and C. Pinto, "The inner gas mass-temperature profile in the core of nearby galaxy clusters", Monthly Notices of the Royal Astronomical Society, Vol. 497, Issue 1, p. 1256-1262, September 2020.

- **Chapter 5** H. Liu, A.C. Fabian, C. Pinto, H.R. Russell, J.S. Sanders and B.R. McNamara, "Searching for cool and cooling X-ray emitting gas in 45 galaxy clusters and groups", Monthly Notices of the Royal Astronomical Society, Vol. 505, Issue 2, p. 1589-1599, August 2021.

Haonan Liu
September 2021

Abstract

X-ray Studies of Radiative Cooling Flow in Cool Core Clusters of Galaxies

Haonan Liu

In this thesis, I present the results of my PhD research on the cooling flow problem in galaxy clusters. The centre of relaxed galaxy clusters has a short radiative cooling time suggesting the presence of a massive cooling flow. However, early studies using high resolution X-ray spectroscopy indicated much lower levels of cooling rate. AGN feedback is thought to be the most likely energy source to balance radiative cooling, though the energy transport and dissipation mechanisms are still under debate. In this work, I study whether AGN feedback can actually balance radiative cooling in a large number of galaxy clusters using high resolution X-ray spectroscopy.

The first chapter contains the necessary background of the cooling flow problem and AGN feedback. This is followed by a chapter describing data reduction of XMM-*Newton* observations. In the third chapter, I present a study of 45 nearby cool core galaxy clusters and groups, where I measure the radiative cooling rate in the softest X-ray band. Then I select a small sub sample of bright clusters to understand the mass temperature profile of the gas in Chapter 4. In Chapter 5, I present a deep study of recent XMM-*Newton* observations of two luminous clusters at intermediate redshift. Finally, I extend my research on 40 more clusters within a much larger range of distances corresponding to redshift up to 0.6.

To all kind people in my life . . .

Acknowledgements

First and foremost, I would like to express my deepest and most sincere gratitude to both of my supervisors, Professor Andrew Fabian and Dr. Ciro Pinto. Remote supervision has been challenging in the last one and half years of my PhD. Without their continuous guidance and support, the work in this thesis would not have been possible. I would like to thank the co-authors of my published work and the anonymous referees who made incredibly helpful comments.

Many thanks to Peter Kosec and Junjie Mao for their instant responses to all my queries on spectral analysis. I have enjoyed my PhD working alongside everyone else from the X-ray group: George, Dom, James, Sergei, Chris, Jiachen, Naoki, Annabelle and all the others. I have been extremely lucky to have the opportunity to meet Lord Martin Rees who motivated me to do my PhD in astronomy. I am very excited that we had conversations on the train between London and Cambridge, twice. I cannot forget the friendship with my course mates from my masters, in particular, Joseph Breuer-Well and Tak Chuanraksasat who shared the Part III exam experience with me. Many thanks also go out to my great office mates Chris Desira and Danial Rothchild and the others.

Next, I would like to express my gratitude to Roderick Johnstone and the rest of the IoA helpdesk. You work very hard so that I could just relax and enjoy the computing resources of the institute. I would like to thank Paul Hewett, Vasily Belokurov, who was also the supervisor of my master project, Debbie Peterson, Judith Moss and the rest of the administrative staff for their kindness and help.

All of you have made my experience in Cambridge incredible. I would not be standing here without you. I wish you all best of luck.

Finally, I must thank my family and friends for their unconditional trust. I am very grateful that my parents are willing to financially support me for eight years studying in the UK. Special thanks to my grandma who raised me and I wish I could tell you in person that I did it. I would like to thank Costa, Angelos, Ethan, Stacy and Melissa, and all other friends in my life. I wish you all happiness every day and our friendship can last forever.

Table of contents

List of figures

List of tables

Chapter 1

Introduction

1.1 Clusters of Galaxies

Clusters of galaxies are the largest gravitationally bound structures in the Universe and typically consist of tens to hundreds of galaxies. These virialised systems form and evolve by mergers and accretion of gas and dark matter. They have a total mass ranging from $10^{14}\,\mathrm{M}_\odot$ up to a few $10^{15}\,\mathrm{M}_\odot$ [153]. The largest mass fraction in galaxy clusters is in dark matter of 84 per cent [150], which forms a deep potential well and only interacts gravitationally. About 13 per cent of mass is in the form of gas, where most gas mass lies in the intracluster medium (ICM). Only 3 per cent of mass is in the stars in galaxies.

Galaxy clusters evolve on timescales of at least a few Gyr and are sufficiently isolated from each others. From simulations, the primordial gas is likely contributing about 75 per cent of the gas in the ICM. The remaining gas comes from the constituent galaxies, either through ram pressure stripping or supernovae [108]. This has also enriched the metallicity of the ICM to about 30 per cent of the Solar values [116, 110].

Most gas in the ICM falls into the dark matter gravitational well [77] which releases a huge amount of energy to heat the gas. The centre of clusters naturally has the highest density [49], where the central galaxy is the most massive and normally the most luminous and known as the brightest cluster galaxy (BCG). Catastrophic collapse is prevented on the scale of clusters as hydrostatic equilibrium is reached locally. Galaxy clusters form in a hierarchical sense, where smaller systems such as star clusters and galaxies are formed first. These subsystems merge and accrete on each other controlled by gravity as they evolve. As clusters become increasingly stable gravitationally, non-gravitational processes start to modify the thermodynamic properties of the gas.

1.2 The Intracluster Medium

The gas of the ICM is almost fully ionised, such that electrons are completely stripped off from the mass dominating hydrogen and helium content. Heavy elements such as O, Ne and Mg, are able to retain the electrons in the K shell. Heavier elements such as Fe are ionised up to the L shell electrons. The interaction of particles due to infall of the ICM causes the cluster centre to be highly luminous in X-rays. A significant fraction of energy of the emission originates from bremsstrahlung emission from the highly ionised plasma which produces a continuum spectrum. The line emission of partially ionised heavy elements also contributes to the observed X-ray spectra. The physics of these radiation processes is described in detail in section 1.3.1. The same processes also apply to less massive structures, such as ellipitcal galaxies and groups of galaxies, while the temperature of the bulk of the gas depends on the mass of the system. Examples of cool core clusters are shown in 1.1. The X-ray emission fills the space between central BCG and its satellite galaxies. The emission of the ICM is typically in the energy band between 0.1 and 10 keV. As galaxy clusters extend over a Mpc, they can be resolved by telescope to study the thermodynamic properties in detail such as the radial temperature and density profiles. It is also possible to focus on the central BCG on a physical scale of 10 to 100 kpc. The gas temperature in the core of many clusters is typically found in the energy band between 0.1 and 4 keV, which drops by a factor of 3 from the temperature of the outskirts [100, 152, 197, 37].

Before we proceed to the physics of the radiation processes, it is important to make necessary assumptions in the environment of the ICM (for a review, see [150]). One of the most basic assumptions is that plasma in the ICM is in collisional ionisation equilibrium where the collisional ionisation rate balances the rate of recombination. The X-ray emission can then be described by the coronal approximation [48], which has three important conditions. The first condition is that the plasma is optically thin. This means the gas has a low enough density that photons does not interact with either the electron or the ions, and photo-ionisation and photo-excitation processes are negligible in this case. Such a condition is not always met in special situations where the density is highest and resonant scattering can then occur for some strong emission lines with high oscillator strength. The second condition is that the electrons in atoms and ions can be treated as if they are in the ground state. This requires the electron and radiation densities are low enough that radiative decays are more frequent than excitations. Finally, the electrons and the ions both have a Maxwellian distribution at the same temperature. Such a condition holds in the core of clusters, where the dynamical timescales are much longer than the timescale for the energy exchange between the electrons and ions. These three conditions are well met in collisional equilibrium.

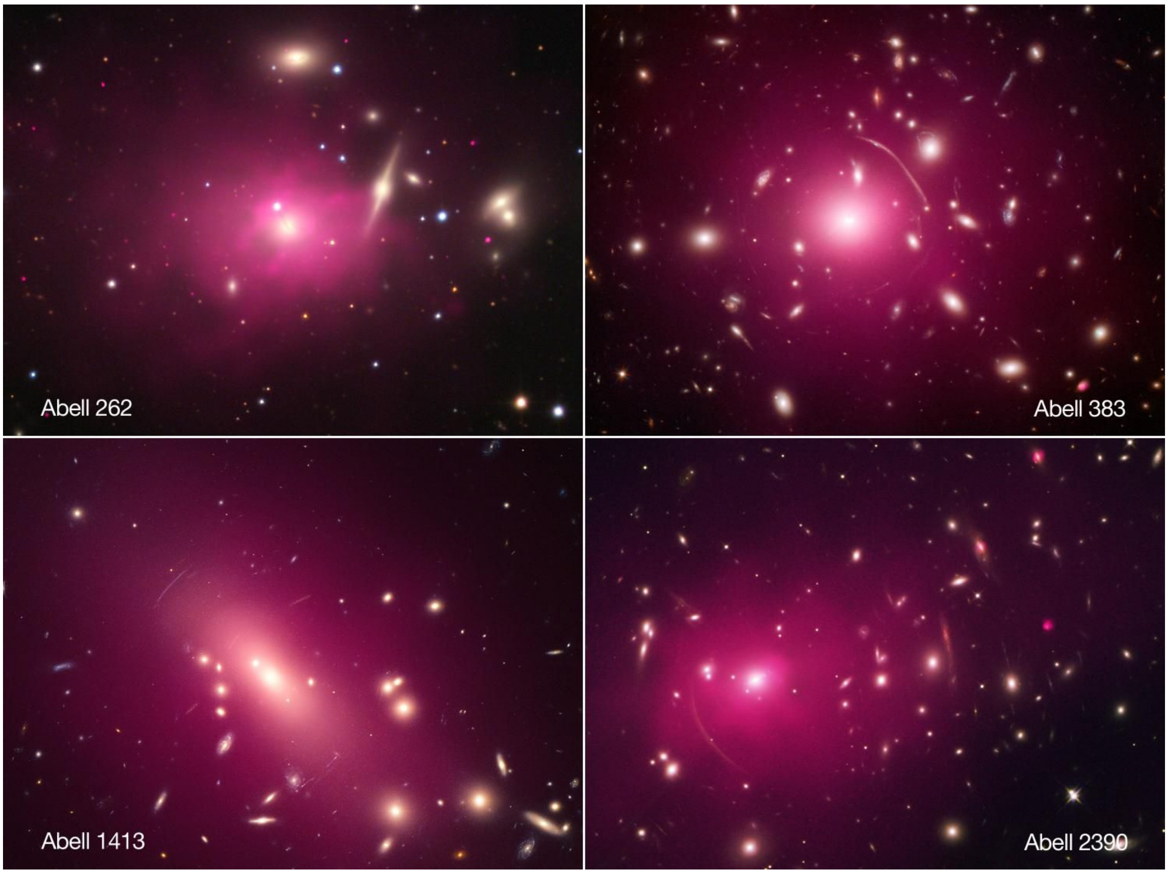

Fig. 1.1 Chandra X-ray (red) and DSS optical (yellow) composite image of four cool core galaxy clusters. The extended intracluster medium is seen occupying the empty space between its satellite galaxies shown in the optical image [11]. (Credit: X-ray: NASA/CXC/CfA/W. Optical: Mt. Lemmon SkyCenter, U. Arizona. Images taken from http://www.chandra.harvard.edu/)

1.3 Radiation Processes

In this section, we describe the physics of important X-ray emission processes (for a full review of thermal processes, see [102]).

1.3.1 Collisional ionisation

Collisional ionisation occurs when a free electron comes close to and interacts with an atom or ion. The free electron transfers part of its kinetic energy E to one of the bound electrons with a binding energy I which escapes from the nucleus. In this case, it is necessary to have $E > I$. The formula of Lotz [115] gives the cross section to the correct order of magnitude

$$\sigma = \frac{a n_{\mathrm{s}} ln(E/I)}{EI} \tag{1.1}$$

where a is the normalisation and n_{s} is the number of electrons in the same shell. This equation shows that low energy electrons have a higher ionising power. For a Maxwellian distribution of plasma, the cross section of the process approaches zero for both the high temperature and low temperature gas.

1.3.2 Bremsstrahlung

In the ICM of galaxy clusters, the most important source of continuum emission is the bremsstrahlung process. This is caused by the deceleration of a free electron in the electric field of ions in the plasma. The emissivity $\varepsilon_{\mathrm{ff}}$ in photons per second per volume per energy can be written as

$$\varepsilon_{\mathrm{ff}} = \frac{2\sqrt{2}\alpha\sigma_{\mathrm{T}} c n_{\mathrm{e}} n_{\mathrm{i}} Z_{\mathrm{eff}}^{2}}{\sqrt{3\pi}E} \left(\frac{m_{\mathrm{e}}c^{2}}{kT}\right)^{\frac{1}{2}} g_{\mathrm{ff}} e^{-E/kT} \tag{1.2}$$

where α is the fine structure constant, σ_{T} is the Thomson cross section, n_{e} and n_{i} are the electron and ion densities, and E is the energy of the emitted photon and c is the speed of light in vacuum. The Gaunt factor g_{ff} is a dimensionless normalisation of order unity. The effective charge of the ion Z_{eff} is defined as

$$Z_{\mathrm{eff}} = \left(\frac{n_{\mathrm{r}}^{2} I_{\mathrm{r}}}{E_{\mathrm{H}}}\right)^{\frac{1}{2}} \tag{1.3}$$

where I_{r} is the ionisation potential of the ion after a recombination, n_{r} is the corresponding principal quantum number and E_{H} is the ionisation energy of hydrogen (13.6 eV). By integrating over all energies and summing over all ions in the electric field, the bremsstrahlung process produces a total power of

$$W_{\mathrm{tot}} = \frac{4.856 \times 10^{-37} \mathrm{Wm}^3}{\sqrt{T_{\mathrm{keV}}}} \int_0^{\infty} Z_{\mathrm{eff}}^2 G_{\mathrm{ff}} e^{-E/kT} dE_{\mathrm{keV}} \tag{1.4}$$

where G_{ff} is the averaged Gaunt factor over all ions and T_{keV} and E_{keV} are expressed in unit of keV. This shows the energy emitted by the bremsstrahlung process depends on the square of gas density. As the gas density increases steeply with a decrease in radius, the continuum emission gives a sharp peak in the surface brightness in the core which would lead to the cooling flow problem in the absence of heating (described in detail in section 1.4).

1.3.3 Line emission

The integrated line emission can dominate the total power over a broad energy band where the gas temperature is below 1 keV. As electrons in ions are considered in the ground state under the assumption of collisional ionisation equilibrium, the line emission process requires the electrons to be excited first. The most important excitation process for plasma in the ICM is collisional excitation, where a bound electron is brought to an excited state by the collision of a free electron with an ion. Bound electrons can also be excited by photo-excitation, inner shell ionisation and capturing a free electron.

The excited electron can then decay back into the ground state or other lower energy states. This can be achieved by spontaneous transition, where the total line power depends on the number density of ions in the same excited state. In a realistic situation, the excited electron can decay into any allowed state before returning to the ground state, which means the observed spectrum is significantly more complicated.

In galaxy clusters, one of the most important emission lines is the He-like 1s–2p triplet. A famous example is the resonant line of Fe XXV in the Fe K (n=1) complex at 6.7 keV. The Fe xxv forbidden line occurs at a lower energy and emits a similar power. The intercombination line is located between the resonance line and the forbidden line and has much lower power. In the core of relaxed clusters, the typical gas temperature is between 1 and 4 keV. In this energy band, the Fe L (n=2) complex is the most prominent near 1 keV. It includes the Fe xvii resonant line at 15 Å (0.82 keV) and the Fe xvii forbidden line at 17.1 Å (0.72 keV). The O vii triplet represents a gas component at a very cold temperature of 0.2 keV. It can be detected in cooler elliptical galaxies [178, 155].

1.3.4 Resonant scattering

The final physical process in this section is resonant scattering, which is only important in a smaller number of cool core clusters. Resonant scattering occurs when a photon with energy equal to a resonant line is absorbed by an ion, and then re-emitted into a different direction. The energy of the photon is preserved in the process. For strong resonant lines, the oscillator strength or the frequency between absorption and emission is high due to the large spontaneous transition probability. On the other hand, the oscillator strength is much lower for the forbidden lines. This means that scattering occurs more frequently for the resonant lines, which can be underpredicted in the core spectra of some clusters. The cooling rate is typically also underpredicted in these clusters.

1.4 Cooling Flow Problem

1.4.1 Cool core clusters

What is a cool core cluster?

Gravitational collapse of the ICM prevents galaxy clusters to be uniform in density and temperature. The ICM is heated by the gravitational potential energy of the gas as it falls into the potential well. If the evolution of clusters only involves gravitational processes, they would be self-similar and dominated by dark matter. This means that the thermodynamic properties of clusters are similar and can be scaled by mass. It is possible to define a characteristic radius where the average density within that radius is a multiple times the critical density of the universe at the redshift of the cluster. A multiple of 200 is typically used. The total mass enclosed can then be applied in scaling. If the ICM is virialised within such a radius, the total energy of clusters is proportional to the average temperature.

However, non-gravitational processes become important as galaxy clusters evolve. Within the virial radius, the ICM achieves hydrostatic equilibrium where the internal gas pressure balances out the inward gravitational contraction. As the ICM is an optically thin plasma, the Coulomb collision between ions and electrons emits photons in X-rays via bremsstrahlung (see section 1.3.2 for details). The density and temperature dependence of the bremsstrahlung process suggests that galaxy clusters are cooling faster in the core and hence the core will have a lower temperature over time (see section 1.4.2). These relaxed systems are known as cool core clusters and have a peak in their surface brightness profile (see Fig. 1.2). Non cool core clusters are observed as well, which have a flattened surface brightness. These are likely due to recent merger activities. Other non-gravitational processes such as Active galactic nuclei (AGN) feedback or supernovae can also affect galaxy evolution. They can both heat the gas and prevent catastrophic cooling (see section 1.5) and enrich the ICM.

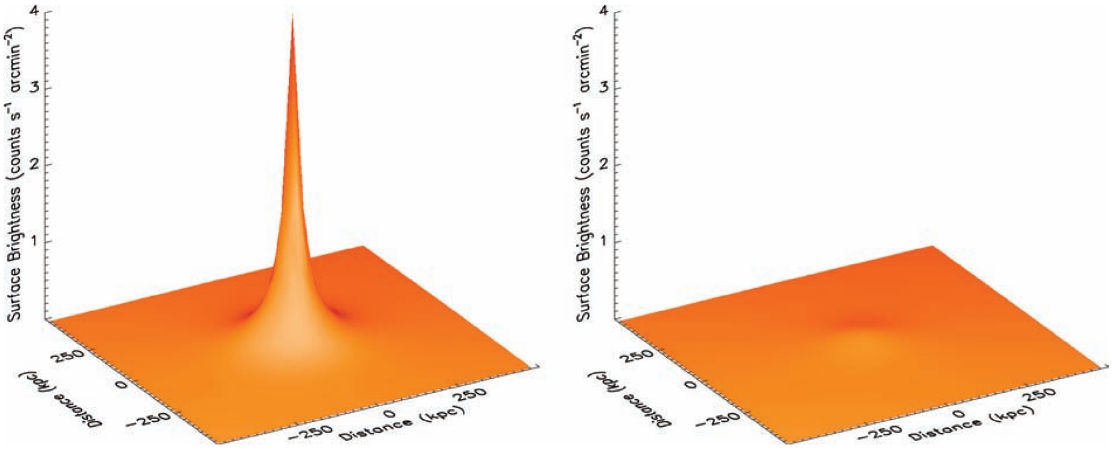

Fig. 1.2 The three-dimensional surface brightness maps for the cool core cluster Abell 2029 (left) and non cool core cluster Abell 2319 with a radio halo (right). This image is taken from [133].

Classification of cool core

One way to classify cool core clusters is by defining a concentration parameter C_{SB} [187] of surface brightness SB

$$C_{\mathrm{SB}} = \frac{SB(40\mathrm{kpc})}{SB(400\mathrm{kpc})}. \tag{1.5}$$

This classification conveniently avoids temperature measurements which requires X-ray spectroscopy. Clusters have a $C_{\mathrm{SB}} > 0.155$ are defined to have a strong cool core, while non cool core clusters have a lower C_{SB} less than 0.075. It is somewhat difficult to trace cool core clusters through redshift as detection of distant galaxy clusters is likely subject to a selection effect. For low redshift clusters ($z < 0.2$), about 44 per cent of clusters are found to satisfy the condition to have a strong cool core [90]. Clusters at intermediate redshift ($0.2 < z < 0.5$) are found to have a lower fraction of cool core of 26 per cent using South Pole Telescope (SPT) [188]. This agrees with 25 per cent detection of X-ray cavities at $0.3 < z < 0.7$ by Chandra X-ray observatory, which also indicates the presence of a cool core [85]. Very few cool core clusters have been observed at higher redshift but are likely above 7 per cent [188].

Cool core clusters usually have additional unique characteristics allowing classification in other wavelengths. In the optical band, the line emission of ionising gas is observed in most cool cores, either in extended nebula or star formation. When the core is relaxed, the gas can also cool into the molecular phase, which is observed in far-IR. Merger or AGN activities are more frequent at higher redshift and potentially prevent the formation of cool cores. However, observations and simulations show that cool cores can survive from merging events. Furthermore, it is possible for cool cores to coexist with powerful quasars (e.g. H1821+643 [165, 207]). Nevertheless, most cool core clusters known do not have a quasar and jets from the AGN are observed in radio. A larger sample must be studied to understand the evolution of cool cores, which will be possible with future data release of eROSITA.

Thermodynamic properties

With high resolution X-ray spectroscopy, it is possible to study radial profiles of thermodynamic properties using concentric annuli under the assumption of spherical symmetry (e.g. [36, 26, 147]). Deprojection routine (e.g. [177]) can be applied to account for the projection effect due to the hot ICM in front of the cool core in our line of sight. The temperature can then be determined from the shape of the continuum spectrum, which originates from the mass dominating hydrogen and helium in the ICM. Observations of clusters show that the core temperature drops by a factor of three from the outskirts (see Fig. 1.3, [51]). Little evidence is seen for gas below 1-2 keV in these profiles. In this thesis, we will search for the presence of gas cooler than 1 keV with line emission. A combination of emission measure EM and spectroscopic information can be used to calculate the gas density (see Fig. 1.4, [36]). The radius is rescaled so that clusters of different sizes can be compared. The inner density ($< 0.1R_{500}$) has a much larger scatter than the density at outer radii, which suggests non-gravitational processes are important in the core.

Three powerful properties can be calculated from gas temperature and density. Entropy is only susceptible to energy gains and losses of a system, which reflects the thermodynamic history of the ICM more accurately than temperature alone. High entropy gas rises buoyantly and expands until the surface of constant entropy matches the surface of equal gravitational potential. It can therefore determine the structure of the ICM. It is conventional to calculate the pseudo entropy directly from temperature and pressure instead of the formal definition

$$K = \frac{kT}{n^{2/3}}. \tag{1.6}$$

Observations in a sample of 66 clusters show that the deprojected entropy profiles always drop with lower radius [147], which suggests the ICM is cooling faster in the core.

Alternatively, the cooling time represents the timescale, of which the gas completely loses its energy by cooling. It can be calculated by the enthalpy and the energy lost rate per volume, which gives

$$t_{\mathrm{cool}} = \frac{5}{2} \frac{nkT}{n^2 \Lambda(T,Z)}, \tag{1.7}$$

where $\Lambda(T,Z)$ is the radiative cooling function that depends on both temperature and metallicity. From observations, the cooling time drops much lower than 1 Gyr within 10 kpc for many clusters (e.g. [147], see Fig. 1.3 and 1.5). This suggests the gas within the radius will cooling rapidly without a balancing heat source, leading to a strong radiatively cooling flow (see section 1.4.2).

Finally, the condition for hydrostatic equilibrium is pressure balance within gravitational potential. The gas pressure dominates and is simply the product of density and temperature

$$P = nkT. \tag{1.8}$$

Gas pressure is much less affected by the thermodynamic history and shows self-similarity at out radii. This supports the idea that the Sunyaev-Zeldovich (SZ) effect signal can be used in the calculation of cluster mass [195]. Non-thermal pressure such as magnetic pressure is sometimes important locally maintaining the integrity of gas filament in plasma.

Chemical enrichment

It is important to consider the metal abundance in galaxy clusters, as the production of the observed X-ray spectrum seen requires a self-consistent physical model (see section 1.4.3) and the full knowledge of atomic physics. Galaxy clusters can be considered as closed systems, and simulations show that the baryonic fraction does not change significantly. The metal enrichment is therefore dominated by processes within the clusters, retaining all information of the metal production history. This is contrary to the evolution of galaxies, where much gas can be lost via outflows.

Most of the heavy elements are produced by massive stars in galaxies. They are subsequently ejected into the ICM via a number of possible processes. Potential mechanisms include merger of protogalactic fragments, ram pressure on galaxies as it falls into the ICM, and galactic outflows driven by either AGN or supernovae, which are likely important on different scales and evolutionary stages.

Supernovae are only responsible for the presence of lower velocity winds. These winds with high metal concentrations rise the core metallicity to up to 2 to 3 times the solar value, which is significantly higher than the outskirts. Some clusters are found to have a drop in abundance in the inner core, where the peak of abundance lies closer to the centre of clusters

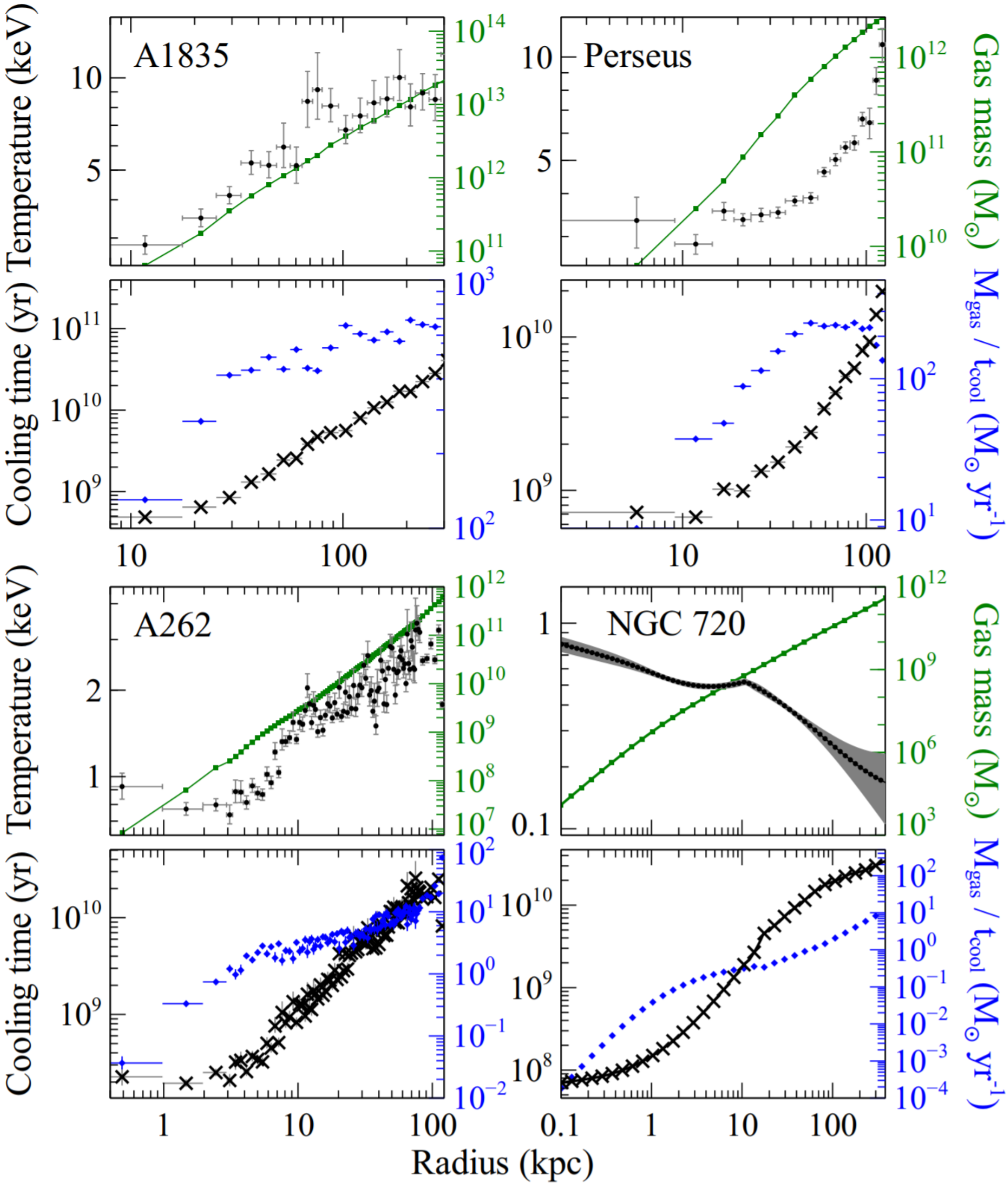

Fig. 1.3 Radial profiles of three cool core clusters and the elliptical galaxy NGC720. For each object, the top panel shows the gas temperature in black and the total enclosed gas mass in green. In the bottom panel, the radiative cooling time is seen in black cross, and the predicted cooling rate in the absence of heating is seen in blue. This figure is taken from [51].

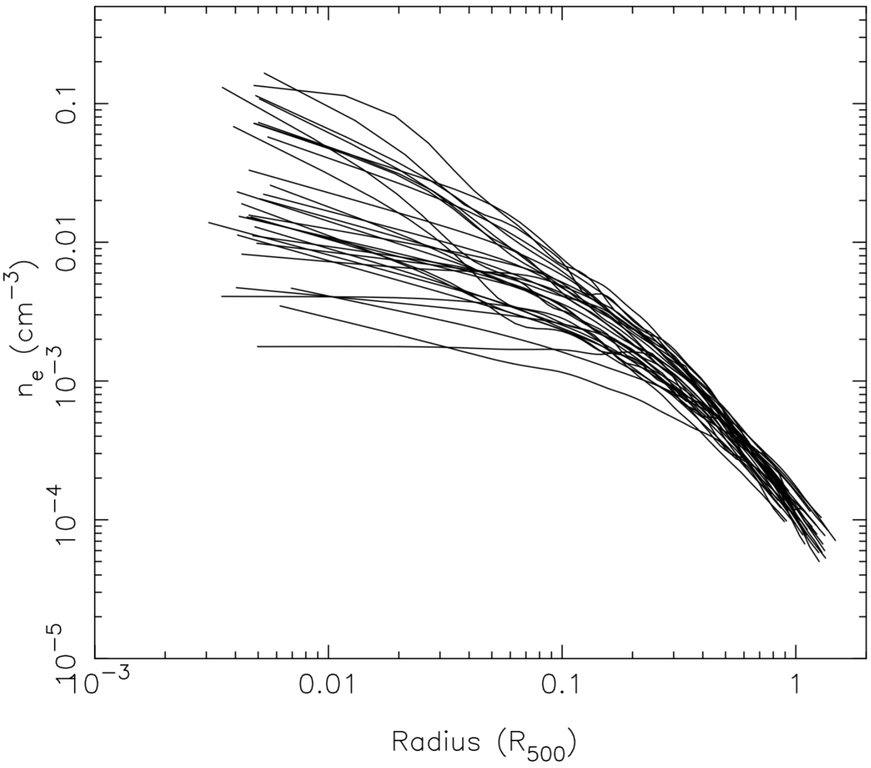

Fig. 1.4 The radial density profile of 31 nearby clusters observed with XMM-*Newton*. The radius is rescaled to R_{500}. This figure is taken from [36].

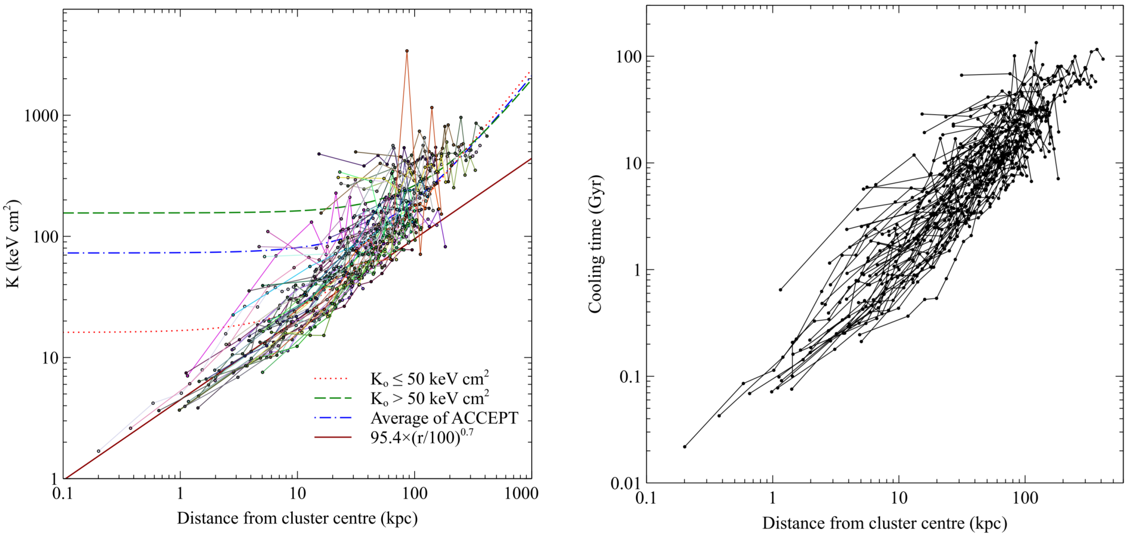

Fig. 1.5 Left: entropy profiles of 66 clusters. The green dashed line, the red dotted line and the blue dashed dotted line represent the average best-fitting entropy profiles for different K_0 values in [26]. The brown line represents the best fit power-law model. Right: radiative cooling time for the same 66 clusters. This figure is taken from [147].

than X-ray cavities. Enrichment by AGN outflows is likely the most probable mechanism on large scales. With a velocity over 500 kms^{-1}, it can lift the metal rich gas up from the centre and distribute to larger radii. The radial metallicity profile then flattens in the outskirts. Both simulations and observations confirm that the overall metallicity of the ICM reaches ~ 0.3 times the solar value in most clusters.

1.4.2 The cooling flow problem

From the mass profile and the cooling time, we obtain the quantity

$$\dot{M}_{\rm cool} = \frac{M(< R_0)}{t_{\rm cool}(< R_0)}, \tag{1.9}$$

where R_0 is normally chosen where the cooling time is 7.7 Gyr [51]. This is a classical way to calculate (or predict) the cooling rate in the absence of heating. The classical cooling rate is predicted to be over 100 $\mathrm{M_\odot\,yr^{-1}}$ in a typical (moderately massive) galaxy cluster (see Fig. 1.3). Such a high cooling rate will exhibit strong spectral features due to line emission of low temperature gas. However, no evidence of extreme cooling is seen in most clusters with high resolution spectroscopy. The standard isobaric cooling flow model (see section 1.4.3) does not provide a sufficient spectral fit to the RGS spectra and overpredicts line emission below 20 Å(0.031 keV; see Fig. 1.6). This is known as the cooling flow problem [150].

The second issue is whether the gas continues to cool below 1 keV which we call the residual cooling problem. If the gas stops cooling at that temperature, hundreds of $\mathrm{M_\odot\,yr^{-1}}$ of gas will accumulate at this temperature. On the other hand, the same amount of gas mass should be observed in the cooled form (such as molecular or optical line-emitting gas) if cooling continues. The BCG of cool core clusters often have an excess of blue light as an indication of star formation. However, the inferred star formation rate is normally less than 10 per cent of the predicted cooling rate. We will discuss a possible route for the fate of the cooling gas in section 1.4.4. In this thesis, we investigate the cooling and residual cooling problems in a large sample of galaxy clusters.

1.4.3 Physical model of radiative cooling flow

In this subsection, I briefly introduce the standard physical model of radiative cooling flows and some key equations which control the mechanism.

The single phase model of radiative cooling flows starts with the assumption of a system in spherical geometry and in a steady-state. It further assumes that radiative cooling dominates the flow. At a radius tens of kpc from the centre, the radiative cooling time exceeds the

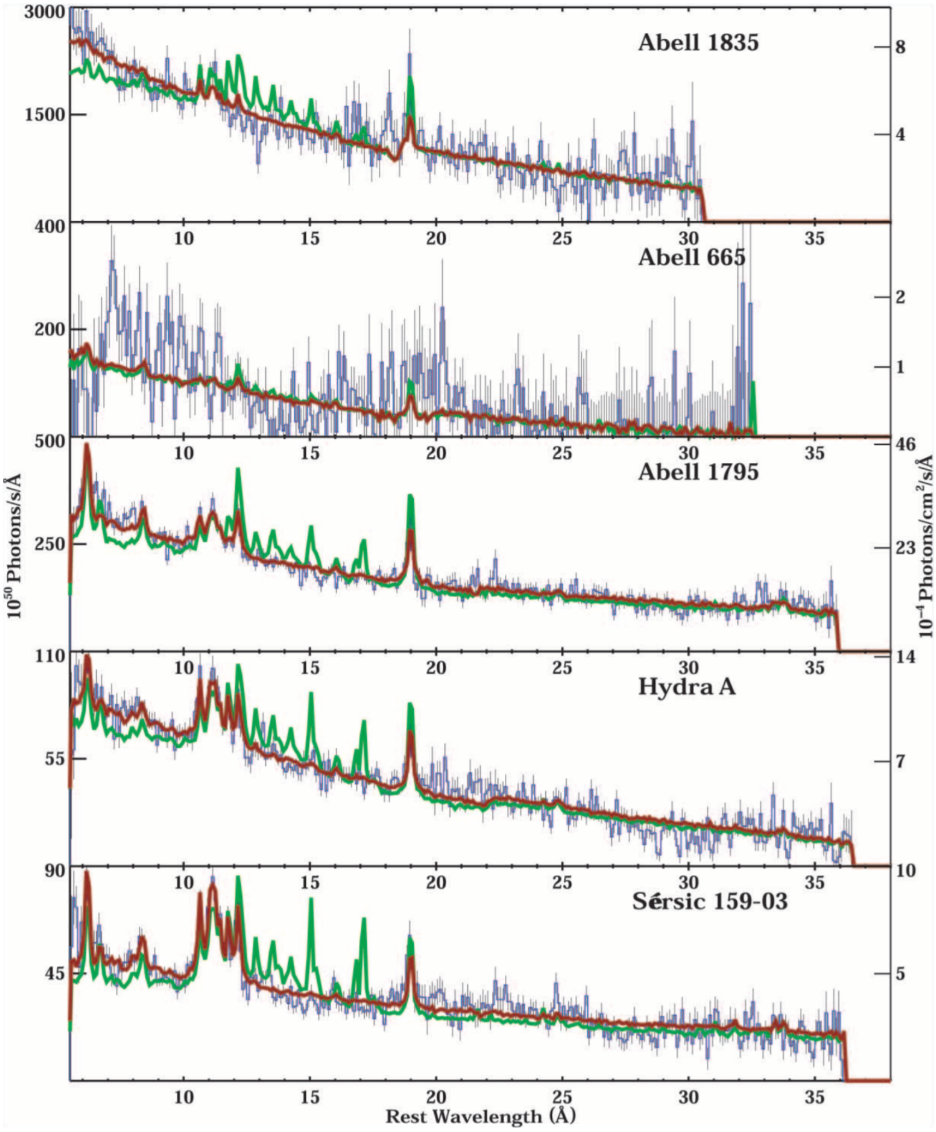

Fig. 1.6 The RGS spectra (blue) of cool core clusters fitted by the standard isobaric cooling flow model (green). The empirical best fit model is in red. This figure is taken from [151].

gravitational dynamical timescale. This means that cooling leads to a subsonic inflow of gas. The density inside rises to maintain pressure determined by the weight of the overlaying gas. Although the ICM is a fully ionised plasma, the classical model neglects the effect of magnetic fields and hence the induction equation. These assumptions simplify the magnetohydrodynamic (MHD) equations. From the mass conservation equation, we obtain

$$\dot{M} = 4\pi r^2 v = \text{constant}. \tag{1.10}$$

The Navier-Stoker equation becomes

$$\rho \frac{d\Phi}{dr} = \frac{d(\rho T)}{dr}. \tag{1.11}$$

The first law of thermodynamics gives

$$\rho v \frac{d}{dr}(\frac{5}{2}T - \Phi) = -n_{\mathrm{e}} n_{\mathrm{H}} \Lambda(T, Z). \tag{1.12}$$

Finally the gravitational potential is

$$\frac{1}{r^2}\frac{d}{dr}(r^2 \frac{d\Phi}{dr}) = 4\pi \mathrm{G}(\rho + \rho_{\mathrm{DM}}), \tag{1.13}$$

where all the symbols have their usual meaning. Such a simple model above does not describe cooling on small scale. Small parcels of cooling gas perturbs the inner core as it flows inward, which lead to thermal instability [66]. The issue of thermal instability likely involves conduction and magnetic field, which is beyond the scope of this thesis.

The single phase model can be reexamined to study the cooling flow as a function of temperature. If the time derivatives is included as opposed to the steady-state, the first law of thermodynamics can be written as

$$\rho(\frac{5}{2}\frac{dT}{dt} - \frac{1}{\rho}\frac{dp}{dt})dV = -n_{\mathrm{e}} n_{\mathrm{H}} \Lambda(T, Z). \tag{1.14}$$

The RHS of the equations is equivalent to a differential X-ray luminosity, dL_{X} and the mass cooling rate can be defined as

$$\dot{M} = -\rho \frac{dV}{dt}. \tag{1.15}$$

As gravitational field is smooth due to dark matter, pressure is roughly constant on small scales. If $\frac{dp}{dT}$ is small, we obtain the equation for the isobaric cooling flow model

$$\frac{dL_{\mathrm{X}}}{dT} = \frac{5}{2}\frac{\dot{M}k}{\mu m_{\mathrm{p}}}, \tag{1.16}$$

where μ is the mean particle mass. If we assume that the ICM is fully ionised containing $\sim$ 75 per cent hydrogen, $\sim$ 24 per cent helium and $\sim$ 1 per cent heavier elements, the mean particle mass is ~ 0.62. If the density is constant, we further obtain the equation for the isochoric cooling

$$\frac{dL_{\mathrm{X}}}{dT} = \frac{3}{2}\frac{\dot{M}k}{\mu m_{\mathrm{p}}}. \tag{1.17}$$

The difference between the last 2 equations is whether PdV work is done on the gas or not.

1.4.4 Connection between soft X-ray emission and cooler gas

As mentioned in section 1.4.2, early observations show little evidence that the core of galaxy clusters cools below 1 keV. Surprisingly, the luminosity expected from the missing cooling flow is similar to the luminosity of the optical/UV line emission. From spatially resolved images, the soft X-ray emitting region is often found to spatially coincide with the Hα nebula, which often has a filamentary structure (e.g. [58, 57, 35, 34, 59, 62]). This is illustrated in the Centaurus cluster in Fig. 1.7. A similar filamentary structure is seen in both the Hα nebula and the soft X-ray emitting gas. These suggest that the energy of the 'missing' X-ray component is likely the energy source responsible for the emission at longer wavelengths [57]. Additionally, the X-ray emitting gas needs to cool faster than radiative processes below 1-2 keV in the same picture.

A possible non-radiative mechanism of powering the optical/UV nebula is the mixing of the two gas phases. As the two gas phases are in contact, the hot X-ray emitting gas interpenetrates the cold gas filaments through the process of reconnection diffusion [109, 60]. This process requires a magnetic field to maintain the integrity of the filaments but does not prevent hot gas from entering [54]. The excitation of cold gas is then mediated by reconnection while the magnetic energy is maintained. This process is limited to the hot gas flow near the interface, where the material is transported by turbulence in the filaments. An alternative way of heating the cold filaments is via the penetration of cosmic rays [65]. However, this requires a high energy density in cosmic rays.

The next problem is the mass of the cooling gas. If the soft X-ray gas indeed powers the optical nebula losing all of its energy, the remaining gas mass probably has a temperature of the order of 50 K, similar to that of the molecular gas. Observations show that galaxy clusters contain massive molecular gas clouds up to a few $10^{10} M_{\odot}$ [46, 47, 171, 145, 168]. In the example of the Centaurus cluster in the bottom panel of Fig. 1.7, molecular gas traced by CO(1-0) resides within the brightest region of the Hα nebula. The molecular gas clouds are therefore a possible sink for the cooled X-ray gas mass.

1.5 AGN Feedback

1.5.1 Active galactic nuclei

A supermassive black hole (SMBH) resides in the centre of most galaxy clusters. As the ICM cools and falls into the BCG, some of the gas forms a disc and accretes on the SMBH. A fraction of the gravitational energy of the gas is then released in the form of powerful radiation. The central (i.e. nuclear) region around the BCG is known as active galactic nuclei (AGN), as oppose to non-accreting inactive galaxies. The most luminous AGN are also called quasars, where the overall radiation from the galaxies is dominated by the nuclear region. The intense flux of energetic photons and particles can clear the interstellar gas from the galactic bulge. If the cold gas on the accretion disc is not replenished, the fuel for further accretion depletes as more material accretes on SMBH. This will eventually terminate the AGN, and the ICM continues to cool with more fuel arrives. This is the basic principle of AGN feedback.

There are at least two major modes of feedback categorised by the amount of energy output from the SMBH. The first is the radiative mode in the extreme case of quasars, where SMBH is accreting close to the Eddington limit. In this case, radiation pressure exceeds the gravitational force on charged dust grains formed by binding normal dust grains to partially ionised gas. As dust grains have about 1000 times larger cross section than electron scattering [61], the effective Eddington limit can be reached in both the AGN and its host galaxy. Radiation on dust is likely responsible for the tight relation between the masses of the SMBH and the velocity dispersion. High velocity winds of up to thousands of kms^{-1} can be driven by radiation and magnetic processes on ionised disc material (e.g. [81]). These winds can typically be observed in UV as transitions in the UV band can provide sufficient amplification of gas opacity.

The second mode is the kinetic mode which operates mostly on nearby clusters. In this mode, accretion on SMBH generates powerful jets, which inflates the surrounding gas

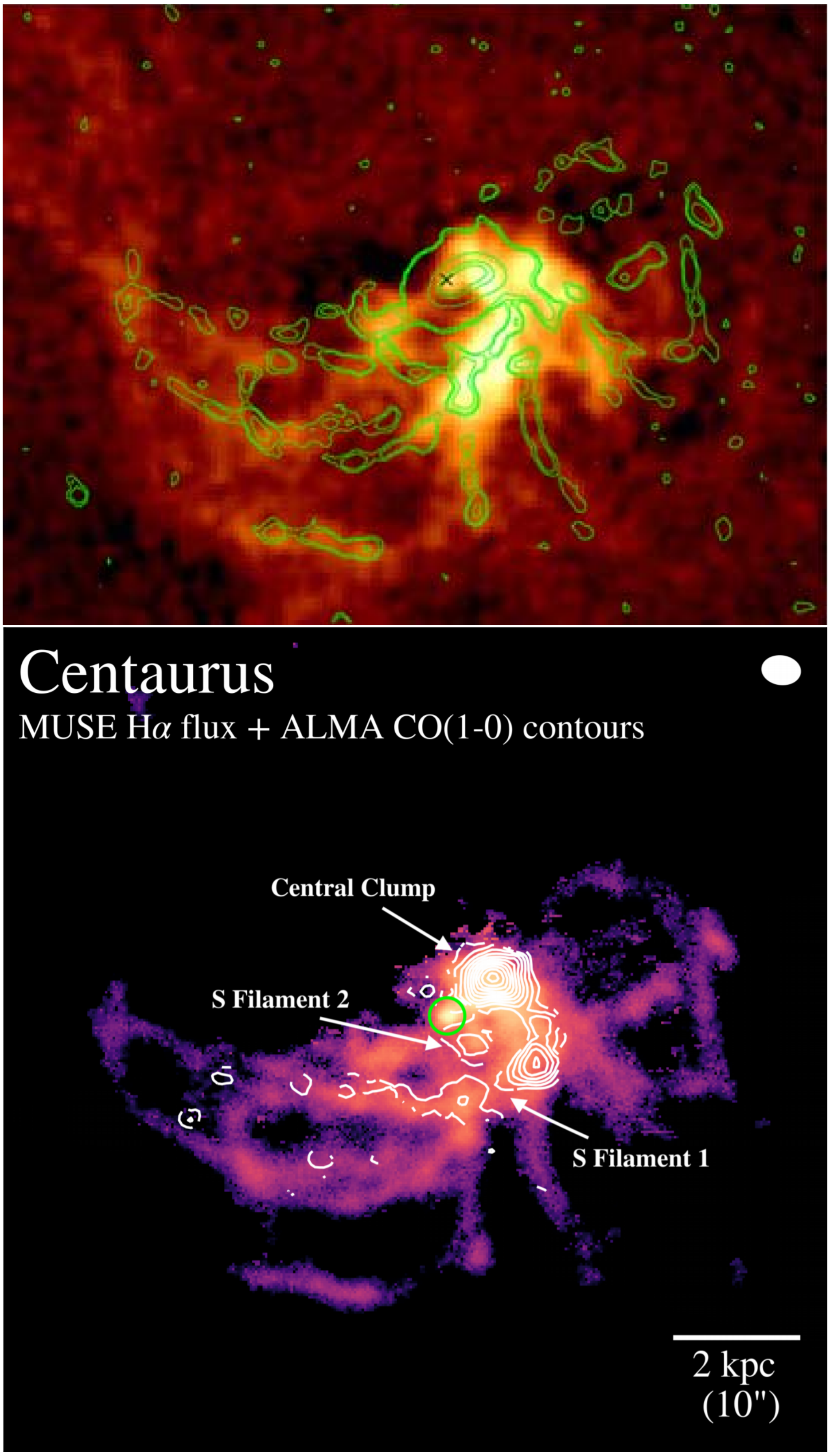

Fig. 1.7 Top: The Hα contours of the Centaurus cluster (at relative levels of 0.6, 1.5 and 4.5) superposed on the soft X-ray emission (0.3-1 keV). This image is taken from [34]. Bottom: The contours from CO(1-0) integrated intensity map superposed on the Hα flux map. This image is taken from [145].

and creates X-ray cavities (or bubbles). This occurs on both sides of the nucleus. The cavities have a lower density than the surrounding gas and hence are buoyant in the ICM. Weak shocks occur at the front of bubbles as it expands and creates high pressure regions. Observations with Chandra have shown cavities, shock fronts, and cool filaments near the central radio sources in almost all cool core clusters (e.g. [59, 175, 90, 87]).

One of the most important consequences of AGN feedback is the ability to suppress cooling in the ICM. In the Kinetic mode of AGN feedback, the total heating available can be estimated from the mechanical power of the X-ray cavities as they inflate [162, 86]. This can be gauged by the product of the volume of X-ray cavities and the pressure of the surrounding gas to the correct order of magnitude. A common thermodynamic quantity used here is the enthalpy, which is the total internal energy of the gas plus pV work. If the cavities are inflated by relativistic jets, the enthalpy then equals $4pV$. This approximation of cavity power is roughly consistent with MHD simulations. A comparison between the cavity power and the cooling luminosity is seen in Fig. 1.8. This shows that heating from AGN feedback is energetically feasible to offset cooling in most clusters.

While AGN feedback dominates heating in the inner core ($\sim$ 10 kpc), other phenomena such as minor mergers and gas sloshing might be important on larger scales (e.g. [210]). Minor mergers can induce sharp cold fronts where the temperature and density change significantly. Heating is possible as the denser front moves in the less dense ICM. X-ray Chandra and radio observations both found concave features in surface brightness in some clusters. This is seen in Perseus, Centaurus and A1795 [59, 209, 186, 208]. This cannot be explained by AGN feedback as heating propagates outward to produce a convex curvature. Walker et al. [210] studied the X-ray surface brightness fluctuations using the gas sloshing simulation of [226, 227] and found that the level of fluctuations is consistent with being driven by sloshing alone on 60 kpc scale. This implies that turbulence generated by AGN feedback is insufficient to balance cooling at even larger radii.

1.5.2 Energy transport

Although the study of X-ray cavities confirms that AGN feedback has enough energy to offset cooling, this simple picture of the heating-cooling loop does not include an explanation for energy dissipation in directions away from the radio jets. So the next big question is, how does heating distribute efficiently and rapidly throughout the ICM? In this section, we briefly introduce possible energy transport mechanisms.

One promising mechanism is a powerful sound wave [55, 63]. Sound waves can be generated by the expansion of the central pressure peaks as bubble inflates. The heat energy in this mechanism is travelling at the speed of sound. In the example of the Perseus cluster,

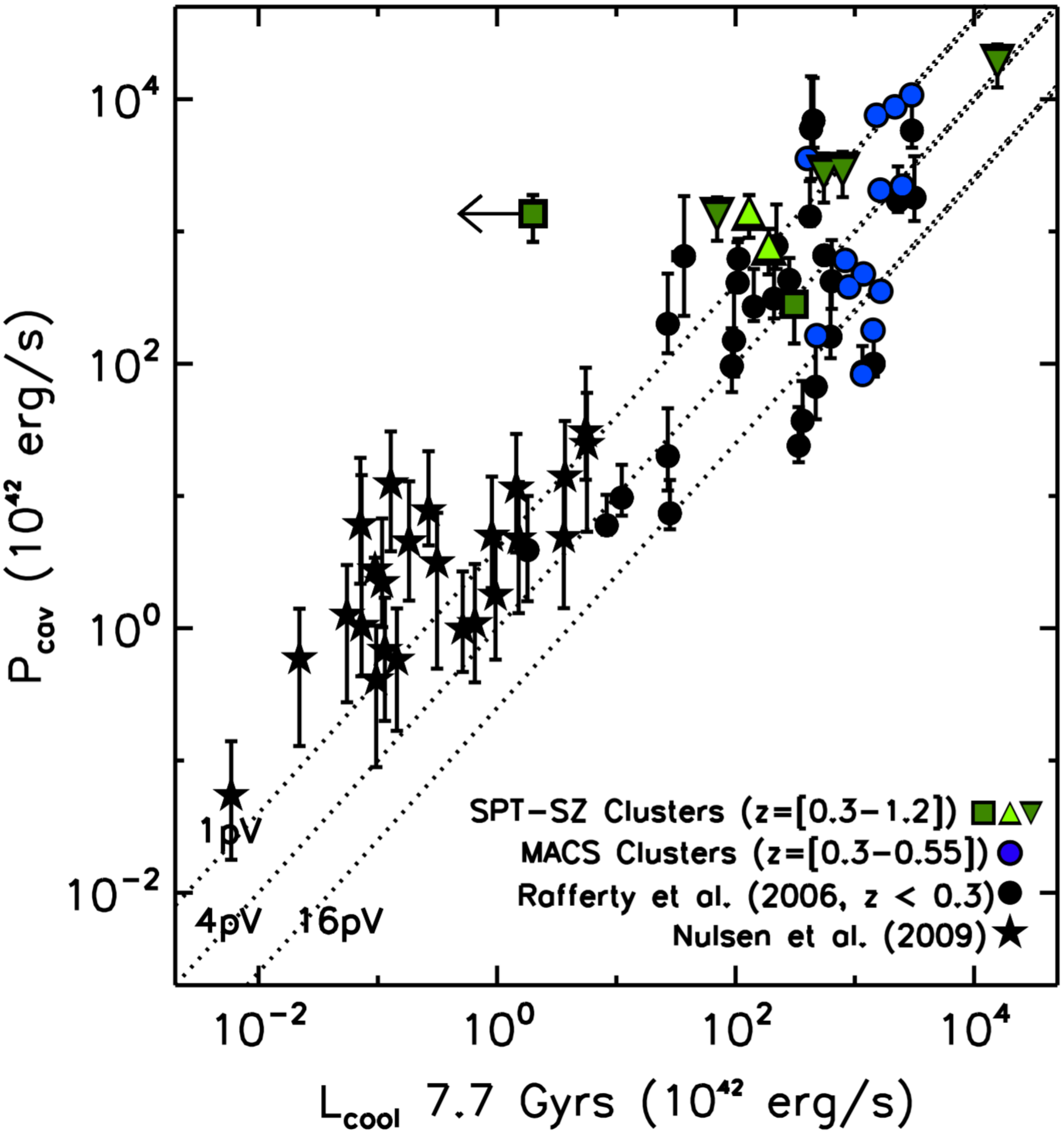

Fig. 1.8 Comparison between the mechanical power being injected by the AGN in the BCG and the bolometric X-ray luminosity within the radius where the radiative cooling time equals 7.7 Gyr. Nearby ($z < 0.3$) clusters are shown in black stars and circles. The more distance MACS sample is in blue. The SPT-SZ sample of clusters with redshift up to 1.2 is seen in green. Dotted line of $4pV$ represents total enthalpy of the X-ray cavity. This figure is taken from [86].

energy needs to be transported at least 700 kms^{-1} in order to reach the outer part of the cluster. The local sound speed there is $\sim$ 1000 kms^{-1}. The energy flux in the sound waves is also comparable to expected cooling rates. Recent simulations show that sound waves are likely to be a major contributor to gas velocities in the ICM [164]. This leaves the question of energy dissipation. Fabian et al. [55] discussed the dissipation of sound energy by viscosity and thermal conduction. Viscous dissipation can provide continuous and gentle distributed heat. On the other hand, thermal conduction can be significantly more important if the dissipation wavelength is large compared to the wavelength of sound waves. A complete self-consistent model of sound waves in conjunction with a suitable energy dissipation process is still under development.

The turbulent motion of gas offers a second way to heat the ICM. The turbulence in the ICM is likely caused by mergers or sloshing or AGN activities such as the interaction between the expansion of lobes and previous cavities. The Hitomi observation of the Perseus cluster finds a turbulent velocity of $164 \pm 10\mathrm{kms}^{-1}$ [84]. It represents an energy density of only 4 per cent of the thermal energy density. This rejects the possibility that the heating from AGN is transported by turbulence alone. Nevertheless, turbulent motion can probably operate with other processes such as sound waves.

Gas heating is also possible by weak shocks [139]. A single weak shock carries a small amount of energy, whereas the total energy of repeated weak shocks is likely comparable to the cooling rate. Multiple shocks have been observed in nearby systems, M87 and NGC5813, where the time interval between the shocks is less than the cooling time [140, 68]. As the shock strength decreases with radius, it is likely only effective on small scales.

Gravity waves (g modes) are another proposed mechanism. AGN activities can launch gravity waves into the ICM, which subsequently decays into turbulence. Simulation from [164] shows that this process is inefficient at transferring energy, with only 1 per cent of AGN heat is retained in turbulence. Further, gravity waves propagate very subsonically with a radial velocity of 20-30 kms^{-1} [63]. This is an order of magnitude lower than the turbulent velocity seen in clusters. Gravity wave is likely unimportant in heating in AGN feedback.

1.6 X-ray Observatories

The Earth's atmosphere absorbs X-rays and other energetic radiation. For X-ray astronomers, it requires space observatories in order to observe the distant universe. In this section, I will introduce the X-ray observatories which collected the data I used in my PhD.

1.6.1 XMM-*Newton*

The X-ray Multi-Mirror Mission (XMM-*Newton*) [94] was launched on 10th December 1999, which means it has successfully operated for nearly 22 years. XMM-*Newton* is built by the European Space Agency (ESA) which aims to provide a high effective area in the 0.3-10 keV band. The observatory has three X-ray telescopes, a smaller optical/UV instrument and two star trackers onboard. Two X-ray telescopes have mirrors which have the Reflection Grating Spectrometers (RGS) [41] and the European Photon Imaging Camera (EPIC) with Metal Oxide Semi-conductor (MOS) CCD (Charge-Coupled Device) arrays [200]. The remaining telescope is equipped with pn CCDs [194].

All the X-ray telescopes onboard XMM-*Newton* use 58 Wolter type-I mirrors. These mirrors are nested in a coaxial and cofocal configuration where a very shallow grazing angle of 30 arcmin or less is utilized. This allows hard (high energy) X-ray radiation to be reflected and provides reflectivity across a wide energy band. X-ray photons are either absorbed or transmitted if they enter the mirror perpendicularly. The telescopes have a focal length of 7.5 m with a field of view (FOV) of 30 arcmin. The spatial resolution is 6 arcsec (FWHM). Other technical details of individual X-ray telescopes are described in the following sub sections. These instruments onboard XMM-*Newton* have a high photon collecting area only exceeded by *NICER* which has poor spatial resolution. The additional Optical Monitor (OM) is pointing at the central 17 arc minute square region of the X-ray FOV. It provides coverage between 170 nm and 650 nm, which gives the possibility of multiwavelength research. However, this thesis does not include data from the OM telescope.

Successful XMM-Newton observations have a proprietary period of 1 year and become publicly accessible afterwards on the XMM-Newton Science Archive (XSA). Since galaxy clusters evolve on very long timescales, new observations can be stacked with the archival data to achieve a higher signal-to-noise ratio.

REFLECTION GRATING SPECTROMETER

Each of the two RGS detectors contains an array of 182 identical reflection gratings placed in the converging beam at the exit from the X-ray telescope. The RGS Focal Cameras (RFC) consist of linear arrays of 9 back-illuminated CCD chips. Back-illuminated CCDs have a quantum efficiency (QE) up to 95 per cent, whereas front-illuminated CCDs only have 50-60 per cent QE. The gratings and the RFC are located on a toroidal surface. The schematic layout of the RGS detectors is shown in Fig. 1.9.

X-ray photons collected by the RGS detectors disperse along the CCD array based on the photon energy. The dispersion direction is therefore the same as the wavelength direction.

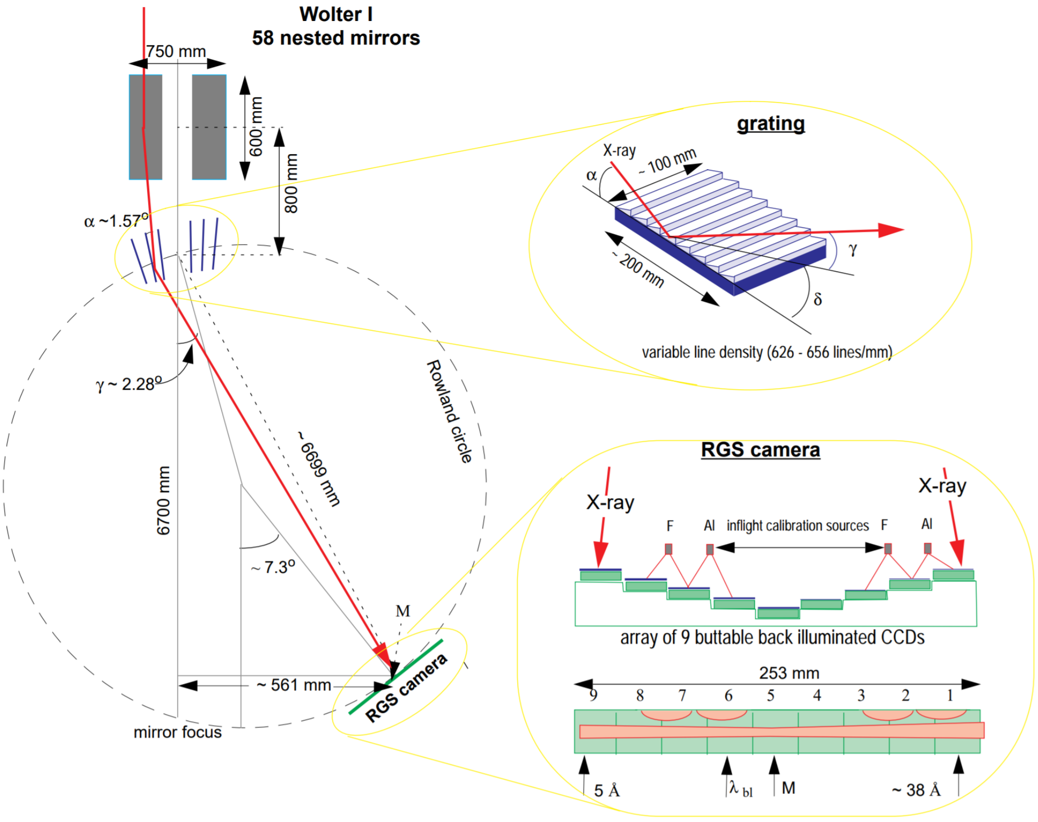

Fig. 1.9 Schematic layout of the RGS taken from [19].

The distribution of photons is governed by the RGS dispersion law along the dispersion direction

$$m\lambda = d(cos\beta - cos\alpha) \tag{1.18}$$

where m is the spectral order of the diffraction, λ is the wavelength of incident photons, d is the groove spacing of the grating, β is the angle between the outgoing ray and the grating plane and α is the angle between the incoming ray and the grating plane.

Incident photons from a point source also disperse in the direction perpendicular to wavelength known as the cross-dispersion direction. The distribution is then described by the Point Spread Function (PSF). One of the advantages of XMM-*Newton* is that the on-axis PSF is narrow and nearly independent of energy over a wide energy band (0.3-6 keV). Off-axis PSF depends on the distance of the source to the centre of the FOV. The FOV in the cross-dispersion direction is 5 arcmin. For extended sources such as galaxy clusters, the spatial position is projected along the cross-dispersion direction. This suggests the roll angle of the spacecraft is crucially important to the slitless RGS detectors as any off-axis photons parallel to the dispersion direction will be assigned to an incorrect wavelength. This is known as the spatial line broadening, which can be partially corrected during analysis using the spatial surface brightness profile from the other telescopes onboard XMM-*Newton*. The level of broadening can be estimated by a simplified RGS dispersion law (see XMM-Newton Users Handbook)

$$\Delta\lambda = 0.138\,\Delta\theta/m \tag{1.19}$$

where $\Delta\theta$ is the angular offset distance of incident photons. This equation can also be interpreted as the spectral resolution for extended sources. The PSF in the cross-dispersion direction can then be exploited to select particular rectangular regions in galaxy clusters.

Another key characteristic is the effective area, which represents the ability of the mirrors to collect radiation at different photon energies. The RGS has a high effective area between 0.3 and 2.5 keV (5 to 38 Å) in the first spectral order and has a resolving power ($E/\Delta E$) of 150 to 800 such that the spectral resolution is roughly constant (a full width half maximum of $\sim$0.06 Å or 0.005 keV). This surpasses most current instruments operated by other X-ray missions over a range of energy in the soft band. A comparison of the effective area between the RGS, grating instruments onboard Chandra and SXS onboard Hitomi and XRISM is shown in Fig. 1.10. Two gaps in the RGS effective area are caused by inoperative CCD chips of the RGS detectors. CCD 7 (high energy) is disabled in RGS 1 and CCD 4 (low energy) is disabled in RGS 2. These correspond to the gap in their spectra between 10.6-13.8 Å

(0.89-1.16 keV) and 20.0-24.1 Å (0.51-0.62 keV), respectively. Apparent oscillations with small amplitude of the effective area are due to data selections by regions that are defined as polygons across the surface of binned two dimensional data. Inter-chip gaps also contribute to lower areas but they do not coincide in wavelength between RGS 1 and 2 due to the configuration of the detectors. The second spectral order has doubled the resolving power, but the effective area is much poorer than the first spectral order and has a limited wavelength band (5 to 20 Å or 0.62 to 2.5 keV).

Although the other instruments onboard XMM-*Newton* have a much higher effective area, RGS detectors have at least 10 times better spectral resolution. The energy band of the RGS matches the temperature of the inner cool core of galaxy clusters, which makes the spectrometers most suitable for tracing cooler gas components in these extended sources.

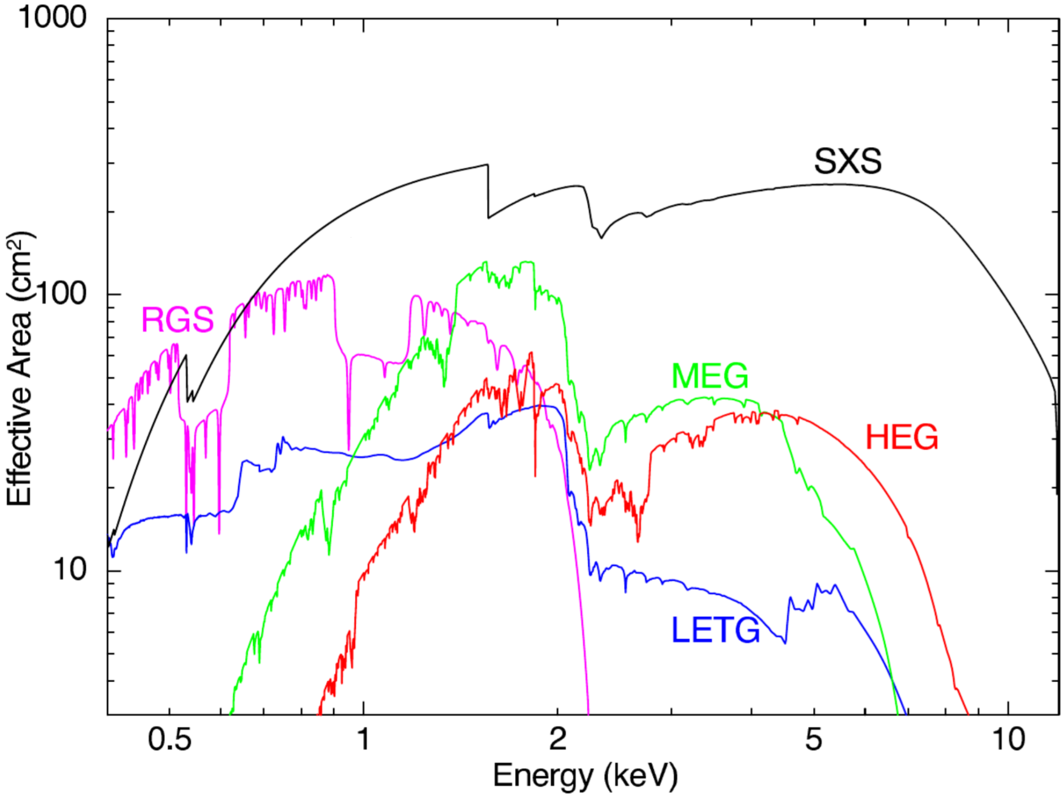

Fig. 1.10 Comparison of effective area between the RGS detectors and other high-spectral resolution X-ray observatories. The combined first order effective area of RGS is seen in magenta. Three grating instruments onboard the Chandra X-ray observatory is seen blue (LETG), green (MEG) and red (HEG) respectively. SXS (black) was the high-resolution instrument onboard the Hitomi X-ray observatory and an identical instrument will be placed onboard the X-ray Imaging and Spectroscopy Mission (XRISM) to be launched in 2023. This figure is taken from [196].

European Photon Imaging Camera

Each of the MOS cameras consists of 7 front-illuminated CCD chips. They are installed behind the X-ray telescopes that are equipped with the RGS, and aligned with the RGS detectors. The CCD chips receive 44 per cent of the incident photons, while the remaining 56 per cent is collected by the RGS. The 12 CCDs of the pn camera are back-illuminated.

While the RGS offers the best spectral resolution, the EPIC instruments have better spatial resolution and a larger FOV which makes them suitable for imaging. Each MOS CCD chip has a FOV of 10.9×10.9 arcmin, where the pn chip is rectangular with a FOV of 13.6×4.4 arcmin. The geometry of the CCD chips enables the telescopes to have a total FOV of 30 arcmin. These broadband (0.3-10 keV) instruments have a much larger effective area than the RGS. The largest effective area of the pn camera peaks over 1000 cm^2 between the 0.7 to 2.5 keV energy band and is between 600-1000 cm^2 below 8 keV. These energy bands include the important Fe K complex. The MOS cameras have a lower combined effective area of less than 800 cm^2 above 2 keV and are much less sensitive below 1 keV due to the front-illuminated CCDs.

The EPIC instruments have a comparable moderate spectral resolving power between 20-50 over a broad X-ray band ranging from 0.2 to 12 keV. The angular resolution is 6 arcsec (FWHM) for both instruments, which makes the XMM-*Newton* the second best X-ray imaging telescope after the Chandra X-ray observatory. Since ACIS QE is contaminated by the deposition of dust over time, the EPIC instruments are currently the most suitable for new observations on galaxy clusters, unless the primary goal is to resolve the inner few arcsec of the cool core.

All instruments onboard XMM-*Newton* have different operating modes dedicating to different source types. While the RGS detectors almost operate exclusively on the so-called Spectroscopy mode using all CCDs, EPIC instruments have more flexible options. The full frame mode employs all pixels of all CCDs to cover the full FOV. The pn camera can also use longer image collection time in its extended full frame mode, which can cause pile-up if bright sources are in the FOV. Photon pile-up occurs when more than one photon arrives at the same pixel before it is read out. These low energy photons will be therefore registered as a single photon of higher energy and hence distort the spectral response. Galaxy clusters are typically observed in these modes. The second mode only includes a partial window that uses part of the CCD chips. The Large Window mode supports observations of bright point sources with a count rate between 0.5 and 1.7 $\mathrm{cts\,s^{-1}}$ in MOS and up to 3 $\mathrm{cts\,s^{-1}}$ in pn. The Small Window mode further allows count rates up to 4.5 and 25 $\mathrm{cts\,s^{-1}}$ in MOS and pn respectively. For extremely bright sources such as nearby X-ray binaries, observations can be made for up to 100 $\mathrm{cts\,s^{-1}}$ in MOS and up to 800 in pn in the Timing mode. It is possible to observe events with a count rate up to 60000 $\mathrm{cts\,s^{-1}}$ in the Burst mode of the pn camera. However, the highest time resolution only has a very low duty cycle of 3 per cent. In general, time resolution improves with the allowed maximum count rate.

1.6.2 Chandra X-ray Observatory

The Chandra X-ray observatory [211] offers an alternative opportunity to observe extended objects, which was launched a few months earlier than XMM-*Newton*. The observatory provides high spatial resolution imaging better than 0.5 arcsec as well as spectroscopy.

The X-ray photons of the source of interest are focused onto one of the imaging instruments, ACIS and High Resolution Camera (HRC), at any given time. The ACIS consists of two arrays of CCDs (see Fig. 1.11). Four CCDS are arranged in a 2×2 array to form ACIS-I and six more in ACIS-S are in the 1×6 linear configuration. Each chip has a field of view of 8.3 arcmin. Observations are often made by the back-illuminated CCD chip S3 as it has better energy resolution at low energies without using a grating. The energy resolution of S3 at aimpoint is 95 eV at 1.49 keV and 150 eV at 5.9 keV comparable to the EPIC cameras. Nevertheless, the spatial resolution of ACIS is around 1 arcsec, which is 6 times better than EPIC. S1 is also back-illuminated, while the remaining 10 ACIS chips are front-illuminated. ACIS-I and S2-S3 are used for wide field imaging. The HRC can also be used for imaging with the largest FOV of 30×30 arcmin and the best spatial resolution of 0.5 arsec in HRC-I. The time resolution is also the highest in HRC-I. However, the resolving power of the HRC is relatively low ($\sim$1). Both imaging instruments have a broad energy band (0.08-10 keV in ACIS and 0.06-10 keV in HRC). Unfortunately, the QE of the ACIS chips is affected by the contamination due to the deposition of material, and has dropped significantly at low energies than when the Chandra X-ray observatory was launched. It is therefore unsuitable for new observations of the sub 1 keV gas in cool core galaxy clusters.

ACIS can also be used in conjunction with the High Energy Transmission Grating (HETG) for high resolution spectroscopy. There are two grating spectrometers onboard the Chandra X-ray observatory, the HETG and the Low Energy Transmission Grating (LETG). The design of Chandra gratings is unsuitable for extended sources as the photon dispersion is much more severe than RGS. Moreover Chandra gratings have substantially lower effective area than RGS in the soft band, especially near the crucial O VIII and Fe XVII transitions. The resolving power of the HETG is between 65 and 1000 over the 0.4-10 keV energy band when studying extended sources, and is even higher for single point sources. The LETG studies the lowest energy in the X-ray band. It has the highest spectral resolving power over 1000 at 0.07-0.15 keV, and a lower resolving power of 20 times the wavelength at higher energies. The LETG is often used to study point sources and other soft sources such as stellar coronae with HRC-S.

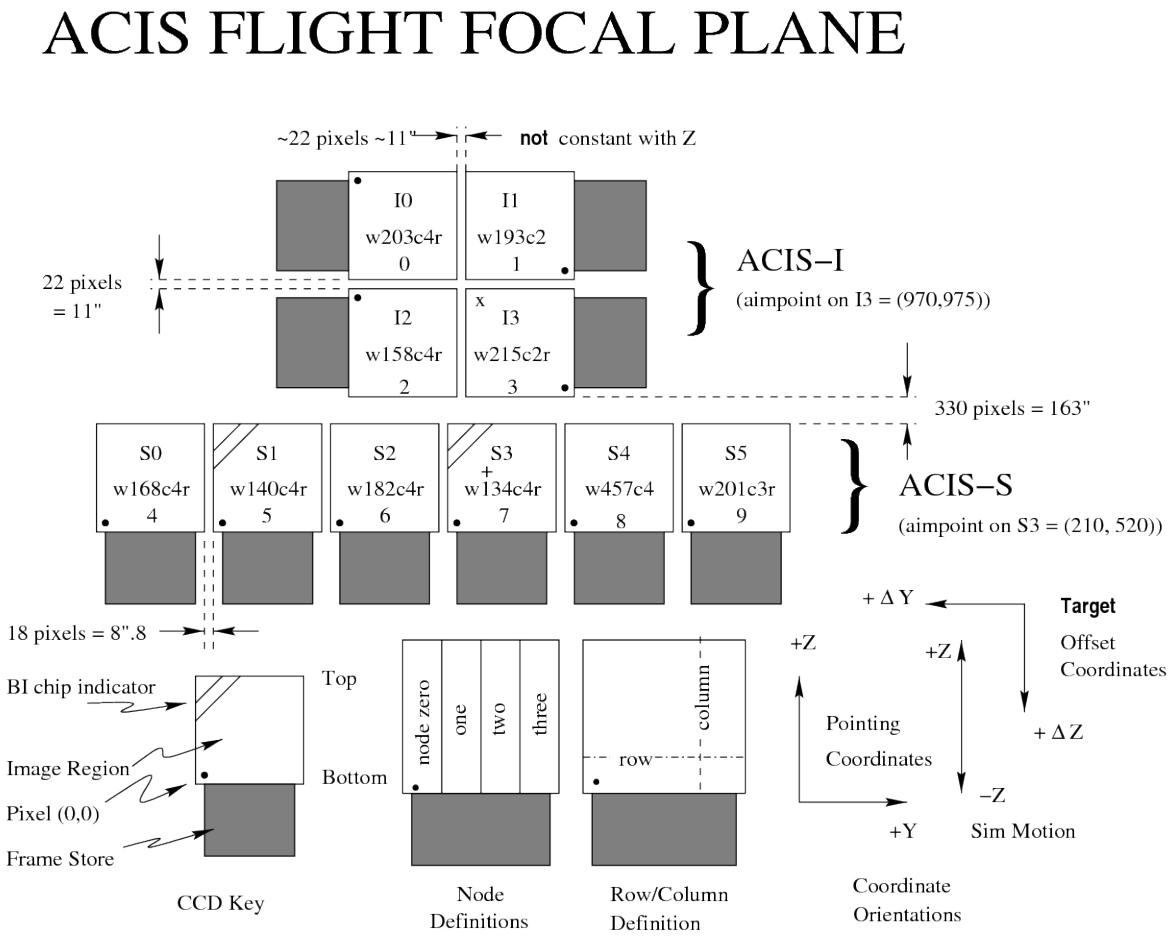

Fig. 1.11 The CCD configuration of the Advanced CCD Imaging Spectrometer onboard Chandra X-ray observatory. This figure is taken from https://cxc.cfa.harvard.edu/R.

1.7 X-ray spectroscopy in galaxy clusters

The spectroscopic picture of galaxy cluster is relatively simple. The mass dominating atmosphere can be well approximated by one to several gas components in collisional ionisation equilibrium (cie) at different temperatures. Each cie component produces its own continuum and emission lines, where the spectral shape depends on the temperature and abundance. The X-ray band (0.3-10 keV) of the XMM-*Newton* instruments contains the energy levels for transitions from different ionisation levels of the most abundant elements.

In the cool core of galaxy clusters, some of the most prominent emission lines include the Fe XVII resonant (15.01 Å or 0.82 keV) and forbidden (17.06 Å or 0.72 keV) lines, the O VIII Lyα (18.97 Å or 0.65 keV) and Lyβ (16.00 Å or 0.77 keV) and Fe XVIII lines at 14.20 Å (0.87 keV) and 16.08 Å (0.77 keV). Other transitions of the Fe L complex are also in clusters between 7 and 14 Å (0.88-1.76 keV). In the most inner region of the core, the O VII triplet has been revealed in some clusters, groups and elliptical galaxies [178, 155]. This is the indication of the presence of cold ($\sim$ 0.2 keV) X-ray emitting gas. In this thesis, our definitions of 'cold', 'cooling' and 'hot' are relative between different X-ray emitting gas phases unless otherwise stated. Line emission due to other heavier elements is generally weaker, for example Si XIII-XIV, Mg XI-XII, Ne IX-X and N VI-VII transitions.

In real clusters, emission lines are intrinsically broadened by the Maxwellian distribution of gas. Turbulent gas motion on larger scales can also lead to line broadening. Broadening effects on small scale are unimportant in the spectra of galaxy clusters. Some clusters host very powerful AGNs, which have a significant contribution to the observed flux, for example, the Perseus and Virgo clusters. The strongest emission of AGN originates from a hot corona of electrons, which gives a power law spectrum with a typical slope between 1.5 and 2.5. This is caused by the inverse Compton scattering of disc photons due to the energetic electrons in the corona.

The intrinsic spectra of clusters are also affected by Galactic absorption from the interstellar medium. The total column density is typically low (a few 10^{20} to 10^{21} cm^{-2}) for clusters in our sample. Absorption intrinsic to the clusters is generally ignored. In Chapter 5 and 6, we will try to investigate the effect of intrinsic absorption due to cold gas with similar conditions as our own Galaxy.

Spectral models can generally be categorised as linear (additive) or multiplicative. Examples of additive models includes cie and cooling flow (cf) from the ICM and power law from AGN. These are independent of each other and represent emission from different sources. Line broadening and absorption are multiplicative processes, which means they change the shape of the spectrum according to specific laws and equations.

In this thesis, I use the SPEX fitting package [101] to study the spectra of clusters. Alternatively, the XSPEC fitting package can provide the same analysis. It is convenient to define the emission measure of gas as

$$EM = n_{\mathrm{e}} n_{\mathrm{H}} V. \tag{1.20}$$

This is because the emission is proportional to the product of electron and ion densities and the volume. By integrating over all volume, the equation for isobaric cooling flow can then be rewritten as

$$\frac{dEM(T)}{dT} = \frac{5}{2} \frac{\dot{M}k}{\mu m_{\mathrm{p}}} \frac{1}{\Lambda}. \tag{1.21}$$

1.8 This thesis

In this thesis, I present my studies of cool core clusters of low to medium redshifts ($0.01 < z < 0.6$) with high resolution X-ray spectroscopy using RGS onboard XMM-Newton. The first goal of my PhD project was to study the remaining problem of radiative cooling by placing constraints on the cooling rate. It is then possible to compare with the prediction of cooling rate in the absence of heating. Due to the remarkable spatial coincidence of the optical/UV line emitting gas with the soft X-ray emitting region found in many nearby clusters, the second goal was to understand whether the further cooling of the X-ray gas supports the emission of the optical/UV nebula. The third goal was to confirm that heating from AGN cannot propagate in clusters by turbulence alone which has been ruled out by Hitomi studying the Perseus cluster. Since only Perseus has been observed by Hitomi, we need to verify the result in a large sample of clusters using current instruments such as the RGS.

In the first research chapter (Chapter 3), I begin with the Chemical Enrichment RGS Sample (CHEERS), which composes of 44 nearby galaxy clusters and groups and elliptical galaxies with a value of a $\sim 5\sigma$ detection for the O VIII 1s-2p line at 19 Å (0.65 keV) in rest wavelength [158, 39]. The peak of emissivity of the O VIII line suggests the presence of gas below 2 keV. For galaxy clusters, this indicates that the ICM has a multi-temperature structure. It is therefore ideal to measure the rate of radiative cooling in this sample.

In Chapter 4, I examine the spectra of a sub-sample of clusters selected from the CHEERS sample from a different perspective. For the innermost 10 kpc of the core, which includes most of the optical/UV emission and the molecular gas, I investigate the mass at different temperatures. This allows direct comparison between the hot X-ray emitting phase and the cooler gas components.

In Chapter 5, I present the analysis of deep observations of two X-ray luminous cool core clusters, RXCJ1504.1-0248 and Abell 1664. They are observed with high star formation activities and predicted to have a strong cooling flow in the absence of heating. In Chapter 6, I perform the cooling flow analysis for an additional 40 clusters in redshift ranging from 0.01 to 0.6. Such a sample includes most cool core clusters observed by XMM-*Newton* RGS with an Hα emission.

In the final chapter, I conclude the main outcomes of this thesis and discuss possible future projects on cool core clusters. Furthermore, I will describe the research potential in this field with upcoming X-ray missions such as XRISM and Athena.

Chapter 2

Data reduction

In this chapter, I briefly introduce the general data reduction procedure used in this thesis. Then I discuss overbinning of spectra for galaxy clusters and appropriate fitting statistics.

2.1 XMM-*Newton* Data Reduction

Public XMM-*Newton* data can be downloaded directly from the XSA archive. The XMM-*Newton* data are available in two formats, Observation Data Files (ODF) and Pipeline Processing System (PPS) products. In this thesis, we produce PPS products directly from ODF files to avoid substantial changes in the software and/or instrument calibrations. The general data reduction procedure is conducted by a standard pipeline software known as the Science Analysis System (SAS). It allows the extraction of customised science products. The data reduction method is different for each instrument. We describe the reduction procedure for the RGS and EPIC in the following sections.

2.1.1 Background

The knowledge of background for each observation is of great importance. It determines the quality of observed spectra and must be fitted to retrieve any spectral information.

The instrumental background of the RGS detectors has several distinct time dependent components. The most significant, unpredictable background originates from the solar activity, which can completely ruin the observation during that period. When particle background is detected by the instrument, the count rate of the RGS light curve can increase more than a hundred times. The RGS light curve is typically create using events from CCD 9 (highest energy) which has a minimum source emission and is the most affected by flaring. It is therefore possible to only select time intervals when the RGS count rate is below a certain threshold. From the standard guideline, this threshold is usually taken to be 0.15 or 0.25 $\mathrm{cts\,s^{-1}}$. While most observations in this thesis are not significantly affected by solar activities, the total clean time is much shorter than the exposure for some objects. The in-flight particle background from other ionised particles is generally stable. Low energy electrons and soft protons entering the telescope also contribute to the background. The count rate of the latter varies by a factor of 20 for similar length observations and likely dominates the background during the quiet (no particle background) period. As the spectral shape of the background correlates with its intensity, it can be modelled by a linear combination of templates of different intensities from CCD 9. The model background is particularly important for extended sources such as galaxy clusters. This can provide a better signal-to-noise ratio allowing detection of weak features. Other background contributions from fluorescence lines in the detector and calibration sources are less important.

The EPIC background is relatively simpler and can be divided into two major categories, a cosmic X-ray background and an instrumental background. The astrophysical background from thermal emission varies over the sky at low energies ($<$1 keV), and hard X-ray background dominates over internal background below 5 keV. The internal background is important above 5 keV, which is caused by the interaction between high energy particles and detectors. These backgrounds are typically temporally independent. Solar activities also affect the EPIC instruments and vary significantly over time.

2.1.2 RGS

The standard RGS data reduction pipeline is called RGSPROC. It generates background-subtracted spectra and response matrices for a given sky coordinate. Observations used in this thesis are processed twice by RGSPROC. While the first run provides standard science products, RGSPROC can be executed again from a later processing stage to produce customised data files.

In the first processing stage, RGSPROC sub-tasks gather essential observation (event) information and add table columns to raw data. Source independent calibrations are conducted at this stage and default options for the sub-tasks are generally sufficient. The customisation starts with the correction of event coordinates for aspect drift. This is particularly important for multiple observations of the same target and off-axis sources in order to produce the most rigorous spectra. After the first run of RGSPROC, an RGS light curve is created to identify the good time intervals (GTI), where the count rate drops below a threshold of 0.15 $\mathrm{cts\,s^{-1}}$ as an indication of weak solar activities. Only data from the GTIs are processed afterwards. The source region of the RGS is usually a rectangle along the dispersion direction. An example of the RGS extraction region is shown in Fig 2.1. The width of the rectangle is slightly wavelength-dependent in the cross-dispersion direction. For extended objects, the fraction of the PSF in the cross-dispersion direction provides a limited spatial resolution. Once the cross-dispersion PSF is chosen, it is common to make the PI (selected pulse height) versus wavelength and cross dispersion angle versus wavelength plots to show the distribution of photons (see Fig. 2.2). We use this property in chapter 4 to select a fixed 20 kpc width region in nearby clusters. For most clusters in this thesis, we choose to include 90 per cent of the cross-dispersion PSF as the source region, which corresponds to $\sim$0.9 arcmin. The background regions for extended objects consist of two rectangles at the edges of RGS in the cross-dispersion direction. We normally choose background regions away from the source to avoid contamination. It is possible to produce both an observed background and a template background.

Finally, RGSPROC generates the source and background spectra from the selected regions as well as response matrices for each exposure. The source spectra and the corresponding response matrices are order-specific and in the OGIP format. The first order spectra have a broad wavelength band as well as high effective area and are used in most cases. As we use the SPEX fitting package, the final spectra must be converted to SPEX usable format using the TRAFO tool.

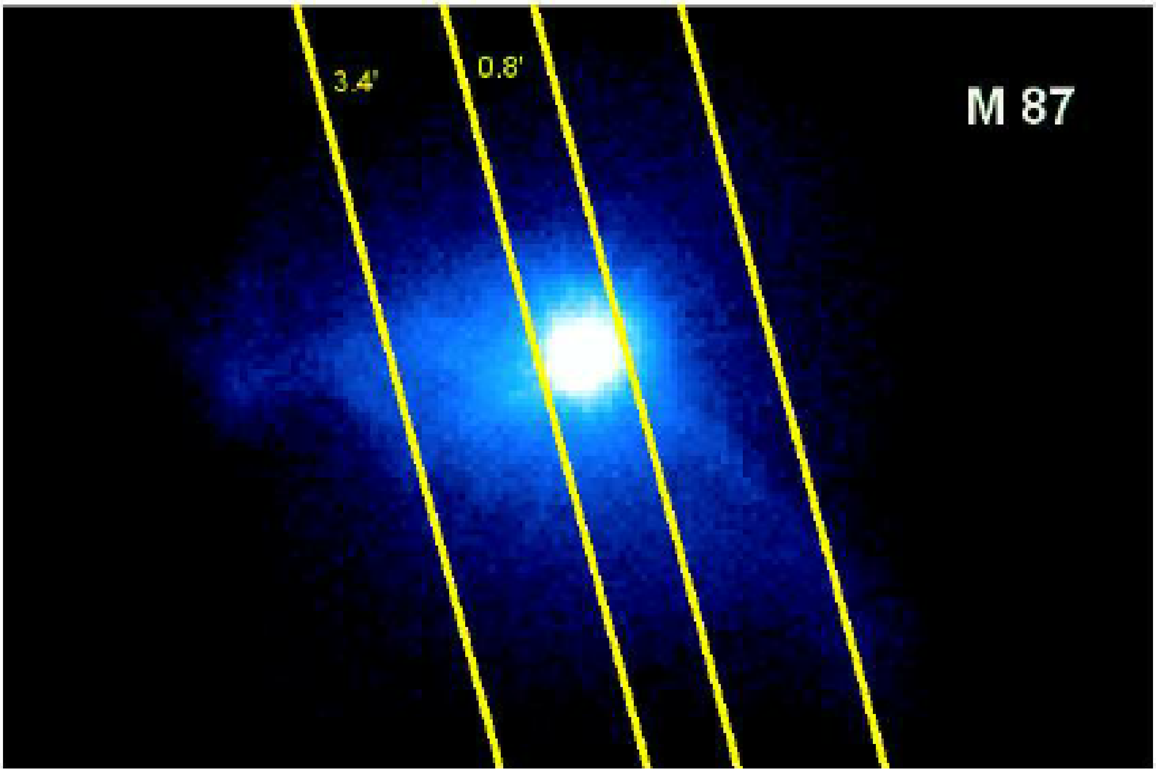

Fig. 2.1 RGS extraction region on MOS 1 stacked image of M87. 0.8 arcmin region here is equivalent to 90 per cent cross dispersion PSF. This figure is taken from [158].

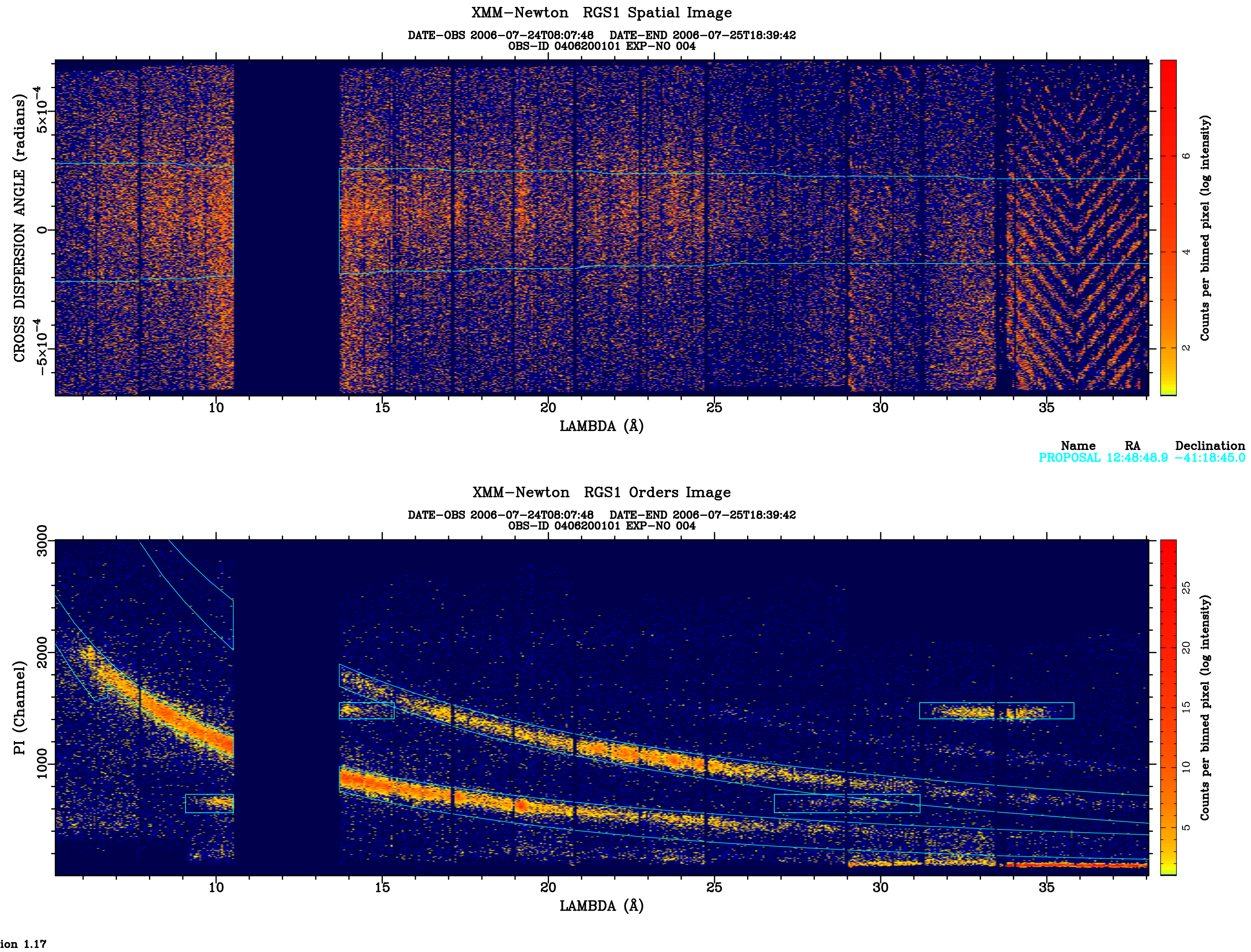

Fig. 2.2 Top: RGS1 cross dispersion photon distribution versus wavelength of the Centaurus cluster. 94.5 per cent cross dispersion PSF is included. Bottom: The RGS1 PI versus wavelength also known as the 'banana plot'. The photons of the lower banana-shaped clump are first order.

2.1.3 Stacking multiple observations

The spectra of most galaxy clusters are time invariant due to the long evolutionary timescale of the ICM except a few with a strong variable AGN. This suggests that stacking multiple short observations is an option to maximise the sign-to-noise ratio. It is also possible to stack spectra from both the RGS 1 and RGS 2 detectors. There are several potential problems for stacked spectra. First, all observations have a slightly different pointing. This can be avoided by specifying the coordinate of the primary source either found in an external catalogue or measured by the EPIC instruments. As the RGS are dispersive instruments, the roll angle of the spacecraft can generate spurious features in the spectra if the clusters have asymmetrical surface brightness profiles, but the effect is typically negligible. Finally, the RGS 1 and RGS 2 detectors have a slightly different alignment and so the stacked spectra will be artificially broadened. This is important for Gaussian line search studies but is acceptable for analysis in this thesis as it is dominated by spatial broadening. Stacking is possible by using the RGSCOMBINE routine.

2.1.4 EPIC

Different EPIC instruments have their separate processing routines. Similar to the RGS, EPIC-pn data are processed by EPPROC and EPIC-MOS data are processed by EMPROC. The SAS task *evselect* then extracts EPIC light curves using the energy band above 10 keV, which identifies the time intervals affected by particle background. The standard flaring thresholds are 0.25 $\mathrm{cts\,s^{-1}}$ for MOS and 0.5 $\mathrm{cts\,s^{-1}}$ for pn. It is possible to produce clean images in specific energy bands, where only events of PATTERN<=4 are accepted for pn and events of PATTERN<=12 are accepted for MOS. The task *vprof* generates cumulated surface brightness profiles from MOS images in the 0.5-1.8 keV band. The selection region corresponds to the source size in the RGS dispersion direction. These profiles are used to correct for the RGS spatial line broadening in SPEX. EPIC spectra have a much lower spectral resolution than the RGS and are not used in this thesis. An example of pn image of RXCJ1504.1-0248 is shown in Fig. 2.3.

2.2 Oversampling and Goodness-of-fit

The raw RGS spectra are heavily oversampled with a resolution of 0.01 Å, while the instruments have a spectral resolution of 0.06 Å (FWHM). This can be avoided by overbinning the spectra to ensure that at least half of the spectral resolution is achieved. The level of overbinning needs to satisfy two criteria. First, the overbinned spectra must conserve as

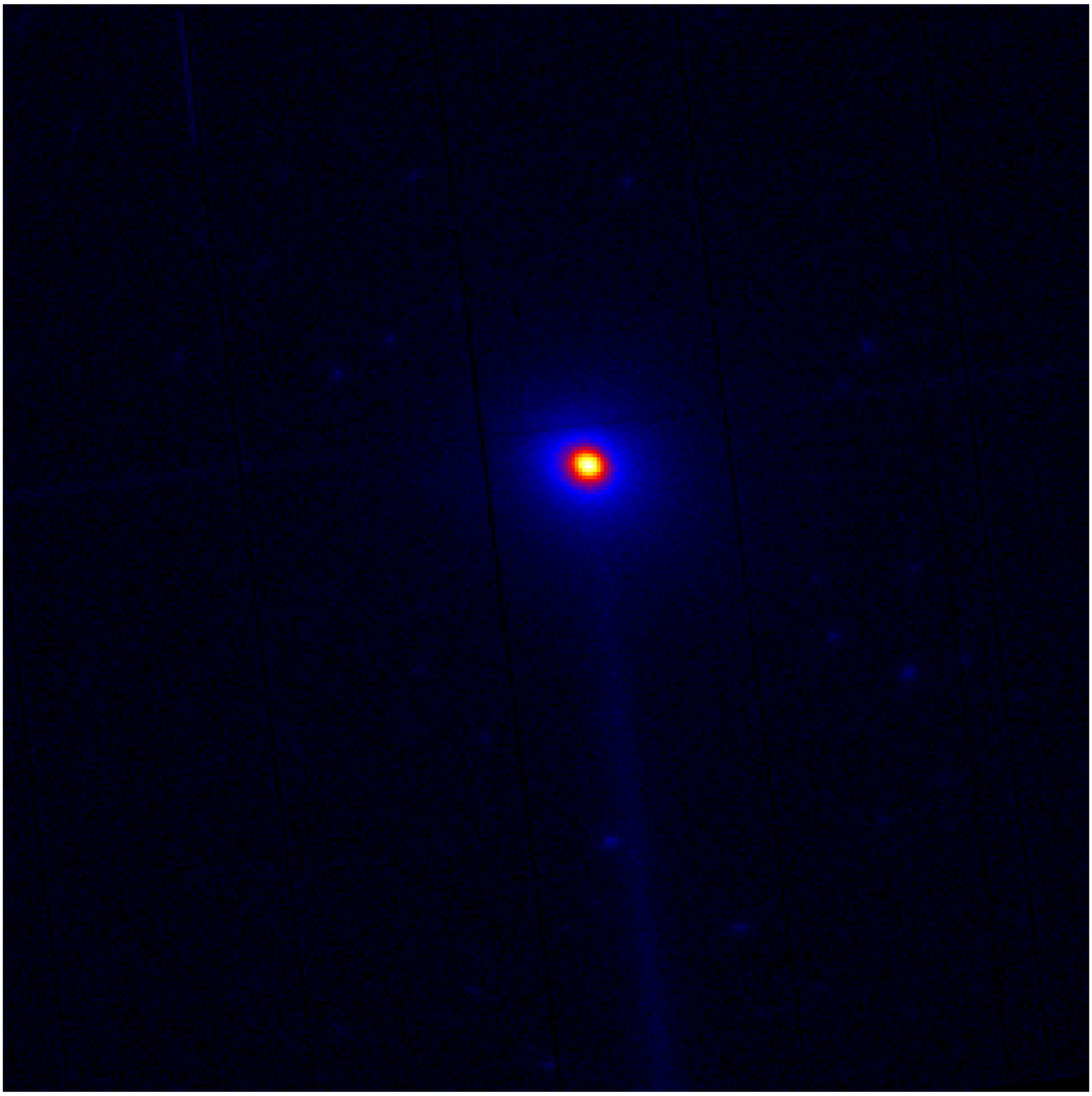

Fig. 2.3 Smoothed PN image of RXCJ1504.1-0248 in the 0.7-1.2 keV band (20 arcmin × 20 arcmin).

Table 2.1 ΔC-stat as a function of confidence level and degree of freedom

Confidence level	degree of freedom					
	1	2	3	4	5	6
68.3%	1.00	2.30	3.53	4.72	5.89	7.04
90%	2.71	4.61	6.25	7.78	9.24	10.6
95.4%	4.00	6.17	8.02	9.70	11.3	12.8
99%	6.63	9.21	11.3	13.3	15.1	16.8
99.99%	15.1	18.4	21.1	23.5	25.7	27.8

much spectral information as possible. This is particularly important for nearby bright clusters which have high counts in the spectra. Sufficient spectral information allows accurate measurements of temperature and metallicity of the ICM. The second condition is that the overbinned spectra need to have higher counts per energy (wavelength) bin for easier spectral fitting. In practice, it is reasonable to overbin the raw spectra by a factor of 3 to 6.

The majority of counts in the spectra of galaxy clusters are found between 7 and 28 Å (0.44-1.76 keV). For a typical cluster that has a total count of 5000-50000 in the stacked spectrum, for example A133 and A1991, the average counts per bin is roughly 10-100. This satisfies the condition for Poisson distribution in Cash statistics [24]. χ^2 is not generally used when analysing X-ray spectra, because it can lead to biased results [136, 132, 91]. It is shown that C-stat is a good approximation to χ^2 in the low count regime for more than 10-30 counts, and is also valid even for the high count limit. The latest SPEX fitting package uses a modified C-stat from the original form [99]

$$C = 2\sum_{i=1}^{n} s_i - N_i + N_i ln(N_i/s_i), \tag{2.1}$$

where s_i is the expected number of counts of the model and N_i is the observed spectra in the bin i. This modified C-stat (and C-stat thereafter) can be used as a goodness-of-fit measure similar to χ^2. The relation between the confidence level and degree of freedom (DoF) is shown in Table 2.1. Observations of clusters with fewer than 1000 counts are not studied in this thesis unless otherwise stated.

Chapter 3

Searching for cool and cooling X-ray emitting gas in 45 galaxy clusters and groups

Abstract

We present a spectral analysis of cool and cooling gas in 45 cool-core clusters and groups of galaxies obtained from Reflection Grating Spectrometer (RGS) XMM-*Newton* observations. The high-resolution spectra show Fe XVII emission in many clusters, which implies the existence of cooling flows. The cooling rates are measured between the bulk Intracluster Medium (ICM) temperature and 0.01 keV and are typically weak, operating at less than a few tens of $M_{\odot}yr^{-1}$ in clusters, and less than 1 $M_{\odot}yr^{-1}$ in groups of galaxies. They are 10-30 per cent of the classical cooling rates in the absence of heating, which suggests that AGN feedback has a high level of efficiency. If cooling flows terminate at 0.7 keV in clusters, the associated cooling rates are higher, and have a typical value of a few to a few tens of $M_{\odot}yr^{-1}$. Since the soft X-ray emitting region, where the temperature $kT < 1$ keV, is spatially associated with Hα nebulosity, we examine the relation between the cooling rates above 0.7 keV and the Hα nebulae. We find that the cooling of gas at 0.7 keV can power the total UV-optical emission, and the cooling rates are 5 to 50 times higher than the observed star formation rates for low luminosity objects. In 3 high luminosity clusters, the cooling rates above 0.7 keV are not sufficient and an inflow at a higher temperature is required. Further residual cooling below 0.7 keV indicates very low complete cooling rates in most clusters.

3.1 Introduction

The centre of gravitational systems is one of the key aspects in understanding structure formation. In a hierarchical formation scheme, more massive structures form through merging of smaller components in overdense regions. This self-similar behaviour implies that the dominance of dark matter potential wells in galaxy clusters leads to an inflow of baryons which will deposit the gravitational energy in the core. In hydrostatic equilibrium, such a system will have a high gas temperature and pressure, while preventing overdensity in the central region. However, it is realised that the evolution of galaxy clusters involves processes other than gravitational collapse, such as cooling and feedback (e.g. [103, 223, 206]). Most evidently, a large fraction of galaxy clusters have been found to host cool cores where the temperature drops towards the centre (e.g. [193, 10, 26, 90]). The central radiative cooling time drops below a few 10^8 yr (e.g. [50, 52, 14, 59, 129, 147]), and the entropy K also decreases inwards by a power law [25, 26, 147]. These suggest that a radiative cooling flow forms in the central region [50], where the energy loss can be observed directly in X-rays by thermal bremsstrahlung. In the cooling flow model, cool gas is compressed by the weight of overlaying gas, and a subsonic inflow of hot gas from outer region is required to sustain pressure. In the absence of heating, cooling rates are predicted to be 100s to more than 1000 $\mathrm{M}_{\odot}\,\mathrm{yr}^{-1}$ in rich clusters [216, 149, 3, 90, 119]. This suggests that we expect not only low temperature components in X-rays but also a large amount of cold molecular gas if it is not consumed in star formation.

On the contrary, observations have shown that the star formation rate is only a small fraction of the predicted cooling rate [138, 96, 141, 161, 119], and the molecular gas detected by CO line emission [46, 171] is at least 20 times lower. Meanwhile, far less cooling gas is observed below 1-2 keV in rich clusters (e.g. [100, 152, 197, 37]). Peterson et al. [151] demonstrated that the standard cooling flow model overpredicts the emission lines from the lowest temperatures in X-rays. The analysis of the Centaurus cluster showed that the cooling rate below 0.8 keV is much lower than the cooling rates measured at hotter temperatures [181]; a similar result was obtained for M87 by [213]. Therefore, cooling must be suppressed by heating mechanisms. AGN feedback is the most likely mechanism, which is energetically strong enough to prevent cooling and yet not overheat the core (for reviews in AGN feedback, see [127, 128, 51]). The energy transport mechanism is still uncertain, which should distribute heat spatially within a few tens of kpc. Some possible processes are sound waves and gravity waves (see e.g. [55, 63]). Other mechanisms such as dissipation through turbulence and conduction are found to be insufficient to operate the heating process by themselves [205, 158, 154, 7].

On the other hand, we can still detect mild cooling flows at around 0.4-0.8 keV from the Fe XVII line emission seen in some objects (e.g. [181]). This suggests that AGN feedback cannot perfectly quench radiative cooling. Further cooling in X-rays is usually not detected from the O VII emission peaking at around 0.1-0.2 keV, though there is evidence of detecting weak O VII emission in less massive clusters and groups of galaxies [178, 156, 155]. This raises the question about whether cooling flows can cool further [52]. From spatially-resolved *Chandra* spectra, soft X-ray emitting regions at these temperatures spatially coincide with cooler ultraviolet/optical line-emitting filaments in massive clusters (e.g. [58, 57, 34]). These filaments are highly luminous and most of them have luminosities comparable to their soft X-ray emission. This suggests that the cool X-ray emitting gas is likely mixing with cold atomic and molecular line-emitting material. The thermal energy of the hotter X-ray emitting gas is then rapidly radiated at longer wavelengths, e.g. in UV and optical bands [52].

In this work, we primarily focus on measuring the cooling rates of galaxy clusters, and deduce the efficiency of AGN feedback on suppressing cooling. It is also interesting to compare the measured cooling rates to the energy required to power the observed luminosities at longer wavelengths in filaments. We then search for residual cooling rates below 0.7 keV which determine whether the gas can continue to cool radiatively in X-rays. Finally, the cooling rates are then linked to star formation rates, and we wish to know how they contribute to the massive molecular gas reservoir seen.

Throughout this work, we assume the following cosmological parameters: $H_0 = 73\,\mathrm{km}^{-1}\mathrm{Mpc}^{-1}$, $\Omega_\mathrm{M} = 0.27$, $\Omega_\Lambda = 0.73$. The results from literature are corrected using the same cosmology. This chapter is organised as follows. Section 3.2 provides the observations used in our sample and the data reduction procedure. The spectral analysis is presented in section 3.3, and we discuss the significance of our result in section 3.4. Finally, we present our conclusions in section 3.5.

3.2 Data reduction

In this chapter, we present our analysis of the soft X-ray spectra of 45 nearby cool-core galaxy clusters and groups, including the CHEmical Enrichment RGS Sample (CHEERS) sample and the more distant cluster A1835 [158, 39]. The CHEERS project includes clusters, groups and elliptical galaxies with the O VIII line detected at 5 σ in the Reflection Grating Spectrometer (RGS) spectra [158], and provides a moderately large sample of objects with deep exposure times. Some of the original aims of the CHEERS project were to accurately measure the abundances of key elements, e.g, O and Fe [39] and constrain the level of turbulence [158]. These suggest that the sample is also suitable for measuring the cooling structure of clusters below 1-2 keV, since the relevant O and Fe ionisation stages in the soft X-ray band are strong and usually peak at different temperatures. Furthermore, the CHEERS sample is relatively complete, which contains all suitable targets with different size and bulk temperature within a low redshift of $z \leq 0.1$.

The observations were made by the XMM-*Newton* observatory, and are listed in Table 3.1 and 3.2. The source redshift and Galactic column density are listed in Table 3.3 and 3.4. We use data from both the RGS and EPIC MOS detectors. The sources typically have high counts (> 5000) in the RGS spectra.

We follow the data reduction procedure described in section 2.1 with the XMM-*Newton* Science Analysis System (SAS) v 13.5.0. We use the task *rgsproc* while setting the *xpsfincl* mask to include 90 per cent of the cross-dispersion PSF, which is equivalent to a narrow ~0.9 arcmin region containing the central core. All RGS observations are stacked using the task *rgscombine* to produce average spectra with high statistics, which are then converted into SPEX usable format.

RGS spectra are broadened due to spatial (angular) extent of sources in the dispersion direction by $\Delta\lambda = 0.138\Delta\theta/m$ Å, where $\Delta\lambda$ is the wavelength shift, $\Delta\theta$ is the angular offset from the central source in arcmin and m is the spectral order. Spatial broadening is expected to be more important for nearby sources due to the redshift dependence of the angular extent. To correct for broadening effects, the surface brightness profile of all sources are extracted from their MOS 1 image in the 0.5-1.8 keV energy band with the task *vprof*, where the products are used as the input of the spatial broadening (*lpro*) model in SPEX. We perform spectral analysis with SPEX version 3.04.00 with its default proto-Solar abundances of [114]. In this work, we use C-statistics (C-stat), and adopt $1\,\sigma$ uncertainties (ΔC-stat = 1) for measurements and $2\,\sigma$ uncertainties (ΔC-stat = 2.71) for upper limits, unless otherwise stated.

3.3 Spectral analysis

In our analysis, we only include the $7-28$ Å (0.44-1.76 keV) band, since background usually dominates above 28 Å. The spectra are binned by a factor of 5 with the bin size in wavelength of 0.05 Å, which ensures that more than half of the RGS spectral resolution is achieved and the data are not heavily overbinned. The typical core temperature of our sample is between 0.5 and 4 keV fitted with a simple one-temperature model (see Table 3.3 and 3.4). In the chosen energy band, we expect emission lines from O, Ne, Mg and Fe with different emissivities. For these elements, we set their abundances free relative to hydrogen, except Mg is coupled to Ne to reduce degeneracy in our models which does not significantly change our results. The abundance of N cannot be measured precisely, because the background noise is comparable to the N VII emission at rest frame 24.779 Å (0.50 keV). We choose to couple the abundances of N and all the other elements to Fe. The abundance is found to be sub-solar ($Z < Z_{\odot}$) in most objects, though it is possible for the abundance of Fe to be slightly above solar in a few objects such as the Centaurus cluster.

To search for cool and cooling gas, we model the spectra with collisional ionisation equilibrium (*cie*) and cooling flow (*cf*) components. The *cie* component describes an isothermal ICM with a free temperature T and emission measure $EM = n_{\mathrm{e}}\, n_{\mathrm{H}}\, V$. The X-ray luminosities of *cie* components are calculated in the 0.01-10 keV band. The *cf* component measures the cooling rate of an isobaric cooling flow from a maximum temperature T_{max}

Table 3.1 XMM-*Newton*/RGS observations of galaxy clusters

Source	Observation ID	Total clean duration (ks)[1]
2A0335+096	0109870101/0201 0147800201	120.5
A85	0723802101/22011	195.8
A133	0144310101 0723801301/2001	168.1
A262	0109980101/0601 0504780101/0201	172.6
Perseus 90% PSF (A426)	0085110101/0201 0305780101	162.8
Perseus 99% PSF		
A496	0135120201/0801 0506260301/0401	141.2
A1795	0097820101	37.8
A1835	0098010101 0147330201 0551830101/0201	294.7
A1991	0145020101	41.6
A2029	0111270201 0551780201/0301/0401/0501	155.0
A2052	0109920101 0401520301/0501/0601/080 0401520901/1101/1201/1301/1601/1701	104.3
A2199	0008030201/0301/0601 0723801101/1201	129.7
A2597	0108460201 0147330101 0723801601/1701	163.9
A2626	0083150201 0148310101	56.4
A3112	0105660101 0603050101/0201	173.2
Centaurus (A3526)	0046340101 0406200101	152.8
A3581	0205990101 0504780301/0401	123.8
A4038	0204460101 0723800801	82.7
A4059	0109950101/0201 0723800901/1001	208.2
AS1101	0147800101 0123900101	131.2
AWM7	0135950301 0605540101	158.7
EXO0422-086	0300210401	41.1
Fornax (NGC1399)	0012830101 0400620101	123.9
Hydra A	0109980301 0504260101	110.4
Virgo (M87)	0114120101 0200920101	129.0
MKW3s	0109930101 0723801501	145.6
MKW4	0093060101 0723800601/0701	110.3

We extract both the 90 and 99 per cent cross-dispersion PSF spectra for the Perseus cluster. For A1795, we extracted the 97 per cent cross-dispersion PSF spectrum. M87 is considered as a galaxy cluster in this work. [1] The total clean exposure of stacked spectra after removing particle background.

Table 3.2 XMM-*Newton*/RGS observations of galaxy groups and elliptical galaxies

Source	Observation ID	Total clean duration (ks)
HCG62	0112270701 0504780501 0504780601	164.6
NGC5044	0037950101 0584680101	127.1
NGC5813	0302460101 0554680201/0301/0401	146.8
NGC5846	0021540101/0501 0723800101/0201	162.8
M49	0200130101	81.4
M86	0108260201	63.5
M89	0141570101	29.1
NGC507	0723800301	94.5
NGC533	0109860101	34.7
NGC1316	0302780101 0502070201	165.9
NGC1404	0304940101	29.2
NGC1550	0152150101 0723800401/0501	173.4
NGC3411	0146510301	27.1
NGC4261	0056340101 0502120101	134.9
NGC4325	0108860101	21.5
NGC4374	0673310101	91.5
NGC4636	0111190101/0201/0501/0701	102.5
NGC4649	0021540201 0502160101	129.8

Table 3.3 Redshift, Galactic column density and core temperature of galaxy clusters

Source	Redshift[1]	$N_{\mathrm{H,tot}}(N_{\mathrm{HI}})$ [2]	kT_{1cie} (keV)[3]
2A0335+096	0.0363 (151)	30.7 (17.6)	1.49±0.02
A85	0.0551 (236)	3.10 (2.78)	3.10±0.12
A133	0.0566 (243)	1.67 (1.59)	2.20±0.06
A262	0.0174 (72.5)	7.15 (5.67)	1.32±0.01
Perseus 90% PSF (A426)	0.0179 (74.6)	20.7 (13.6)	1.98±0.03
Perseus 99% PSF			1.86±0.02
A496	0.0329 (139)	6.12 (3.81)	2.11±0.05
A1795	0.0625 (269)	1.24 (1.19)	3.09±0.15
A1835	0.2532 (1230)	2.24 (2.04)	3.89±0.27
A1991	0.0587 (252)	2.72 (2.46)	1.55±0.05
A2029	0.0773 (336)	3.70 (3.25)	3.45±0.13
A2052	0.0355 (150)	3.03 (2.71)	1.74±0.04
A2199	0.0302 (126)	0.909 (0.888)	2.57±0.09
A2597	0.0852 (373)	2.75 (2.48)	2.48±0.14
A2626	0.0553 (236)	4.59 (3.82)	3.07±0.46
A3112	0.0753 (327)	1.38 (1.33)	2.60±0.08
Centaurus (A3526)	0.0114 (47.2)	12.2 (8.56)	1.33±0.00
A3581	0.023 (96.2)	5.32 (4.36)	1.33±0.02
A4038	0.0282 (118)	1.62 (1.53)	2.31±0.12
A4059	0.0487 (208)	1.26 (1.21)	2.47±0.11
AS1101	0.0580 (249)	1.17 (1.14)	1.95±0.04
AWM7	0.0172 (71.8)	11.9 (8.69)	1.72±0.04
EXO0422-086	0.0397 (168)	12.4 (7.86)	2.31±0.18
Fornax (NGC1399)	0.0046 (19.0)	1.56 (1.5)	0.98±0.00
Hydra A	0.0549 (235)	5.53 (4.68)	2.44±0.16
Virgo (M87)	0.0043 (16.7)	2.11 (1.94)	1.32±0.00
MKW3s	0.0442 (188)	3.00 (2.68)	2.29±0.08
MKW4	0.02 (83.4)	1.88 (1.75)	1.44±0.02

The redshifts are taken from the NED database (https://ned.ipac.caltech.edu/). [1] The luminosity distances in Mpc shown in brackets are either calculated using [222] (for $z > 0.006$) or taken directly from the NED database (for $z < 0.006$). [2] Total ($N_{\mathrm{H,tot}}$) and atomic (N_{HI}) hydrogen column densities in $10^{20}\,\mathrm{cm}^{-2}$ (see http://www.swift.ac.uk/analysis/nhtot/; [104, 217]). [3] The core temperature measured by fitting the spectra with a simple 1-temperature model.

Table 3.4 Redshift, Galactic column density and core temperature of galaxy groups and elliptical galaxies

Source	Redshift	$N_{\mathrm{H,tot}}(N_{\mathrm{HI}})$	kT_{1cie} (keV)
HCG62	0.0147 (61.2)	3.81 (3.31)	0.84±0.01
NGC5044	0.0093 (38.4)	6.24 (4.87)	0.87±0.00
NGC5813	0.0065 (26.9)	5.19 (4.37)	0.68±0.00
NGC5846	0.0057 (23.6)	5.12 (4.29)	0.70±0.00
M49	0.0033 (16.0)	1.63 (1.53)	0.89±0.01
M86	-0.0008 (16.4)	2.98 (2.67)	0.79±0.01
M89	0.0011 (16.5)	2.96 (2.62)	0.60±0.02
NGC507	0.0165 (68.5)	6.38 (5.25)	1.07±0.01
NGC533	0.0328 (138)	3.38 (3.08)	0.89±0.01
NGC1316	0.0059 (24.2)	2.56 (2.4)	0.68±0.01
NGC1404	0.0065 (26.8)	1.57 (1.51)	0.66±0.01
NGC1550	0.0129 (51.4)	16.2 (10.2)	1.15±0.01
NGC3411	0.0153 (63.5)	4.55 (3.87)	0.91±0.01
NGC4261	0.0074 (30.5)	1.86 (1.75)	0.73±0.01
NGC4325	0.0257 (108)	2.54 (2.32)	0.89±0.01
NGC4374	0.0034 (17.0)	3.38 (2.99)	0.68±0.01
NGC4636	0.0031 (16.3)	2.07 (1.9)	0.67±0.01
NGC4649	0.0037 (16.9)	2.23 (2.04)	0.84±0.01

down to a minimum temperature $T_{\rm min}$ [134]. The cooling rate $\dot{M}$ can be derived from the differential emission measure (see section 1.4.3).

Both the *cie* and *cf* components are modified by redshift (*red*), Galactic absorption (*hot*) and then convolved by spatial broadening (*lpro*). In the *hot* component, we assume a very cold temperature of T=0.5 eV with solar abundances [157], and allow hydrogen column density free to vary between $N_{\rm HI}$ and $N_{\rm H,tot}$ (see Table 3.3 and 3.4; [104, 217]). The hydrogen column densities are crucial in determining the quality of spectral fits and the magnitude of cooling rates (e.g. 2A0335+096). Although the intrinsic hydrogen column density of the source can usually be ignored, it can potentially be problematic for clusters with powerful AGN (e.g. the Perseus cluster; [29]), since the emission of the central AGN is processed by the ICM before leaving the clusters. These components assume a Maxwellian electron distribution, and calculate the effect of thermal line broadening. Although turbulence is intrinsic to ICM, it also broadens emission lines usually at a few 100 $\rm km\,s^{-1}$ (e.g. [183, 180, 158]). For the CHEERS sample, the FWHM of total line widths is at least a few 1000 km/s in the RGS spectra dominated by spatial broadening [158, 155, 7]. Therefore we ignore turbulent velocity in our sample and fit the scaling parameter s in the *lpro* component, which can account for any residual broadening. It is possible for our analysis to have minor statistical effects on line widths from stacking multiple observations, though net fluxes are not affected. We include an additional power law (*pow*) component for clusters with a bright variable AGN (the Perseus and Virgo clusters; see section 3.3.4). The *pow* component is not convolved with the spatial profile as the central AGN is a point source. Finally, we assume that any diffuse emission features due to the cosmic X-ray background are smeared out into a broad continuum-like component.

3.3.1 Isothermal collisional ionisation equilibrium

We start with a single collisional ionisation equilibrium component (1 *cie*), and the best fit temperatures are shown in Table 3.3 and 3.4. These temperatures are consistently lower than the cluster values listed by [28, 190], since the 90 per cent PSF spectra exclude most of the very hot (>4 keV) ICM emission. We demonstrate an example spectral fit of the Centaurus cluster in Fig. 3.1, where we also show the residuals of both the 1 *cie* and 2 *cie* models. It is seen that the Fe XVII/XVIII lines between 14 and 17 Å (0.72-0.88 keV) are underestimated in the 1 *cie* model, which gives a poor C-stat/DoF of 1952/407. The spectral fit is improved significantly by the 2 *cie* model, or by adding an additional *cf* component (see [181] for more detailed analysis on the Centaurus cluster). We attempt to trace any cooler component in our sample first by an additional *cie* component at a lower temperature (2 *cie* model; see section 3.3.2). We then replace this cooler *cie* component with a *cf* component cooling from the hotter *cie* temperature down to 0.01 keV (1 *cie* + 1 *cf* model; section 3.3.3). Finally, we use a two-stage cooling flow model (1 *cie* + 2 *cf* model; section 3.3.3).

3.3.2 Multi-temperature model

The two-temperature (2 *cie*) model includes the possibility of a cooler gas component. To reduce degeneracy of our model, we assume both *cie* components have the same abundances, and are convolved by the same *lpro* component except the Centaurus cluster where the spectral fit is improved by an additional *lpro* component [155]. This is because the Centaurus cluster has a much smaller extent of cooling gas [181, 186]. The 2 *cie* model provides acceptable spectral fits for most clusters which is consistent with [39]. In Fig. 3.1, the example of the Centaurus cluster demonstrates that the cooler *cie* component has a temperature that gives emission from the Fe-L complex and O VII/VIII lines, which dominate the total line emissivity below 1 keV (e.g. see Fig. 2 of [184]). The emissivity of each ionisation stage peaks at different temperatures, and the best indicators for low temperature gas are O VII lines at around 0.2 keV and Fe XVII lines which have the strongest emissivity below 0.8 keV in the Fe-L complex. However, O VII is usually only found in elliptical galaxies but not massive clusters (except e.g. the Centaurus and Perseus clusters; [178, 155]). Since the spatial extent of O VII is generally small (e.g. only in the innermost 5 kpc in the Centaurus cluster; [62]), it is difficult to measure such lines in our broader 90 per cent PSF spectra. The temperature of the cooler component cannot be constrained from O VIII emission alone, because it has a much wider temperature range. Hence, we are mainly interested in detecting cooling gas which emits Fe XVII lines peaking at 0.5 keV.

We apply the 2 *cie* model to clusters and two bright groups, and the key parameters are listed in Table 3.5. There are four objects with a cooler temperature below 0.4 keV, and such a low temperature raises the concern on resonant scattering, which can have a significant impact on measuring the gas temperature through certain emission lines. Since turbulent velocity is generally low in our sample [158], the ICM can be optically thick to radiation at resonant lines. As a result, photons at the resonant wavelengths are absorbed and re-emitted in random directions, and the resonant lines are suppressed in the core and enhanced from the outer region. However, the forbidden line has a much smaller oscillator strength and so is unaffected. Consequently, we expect to see a low Fe XVII resonant-to-forbidden ratio in the 90 per cent PSF spectra. We also calculate theoretical emissivities of both the Fe XVII and the O VII lines in Fig. 3.2. The resonant-to-forbidden ratio decreases monotonically below around 1 keV with decreasing temperature, and reaches 0.5 at 0.18 keV where the O VII peaks. In Pinto et al. [155], it is shown that the Fe XVII resonant-to-forbidden ratio is usually 0.7 or lower. Hence, such a low resonance-to-forbidden ratio can be achieved by either a cool

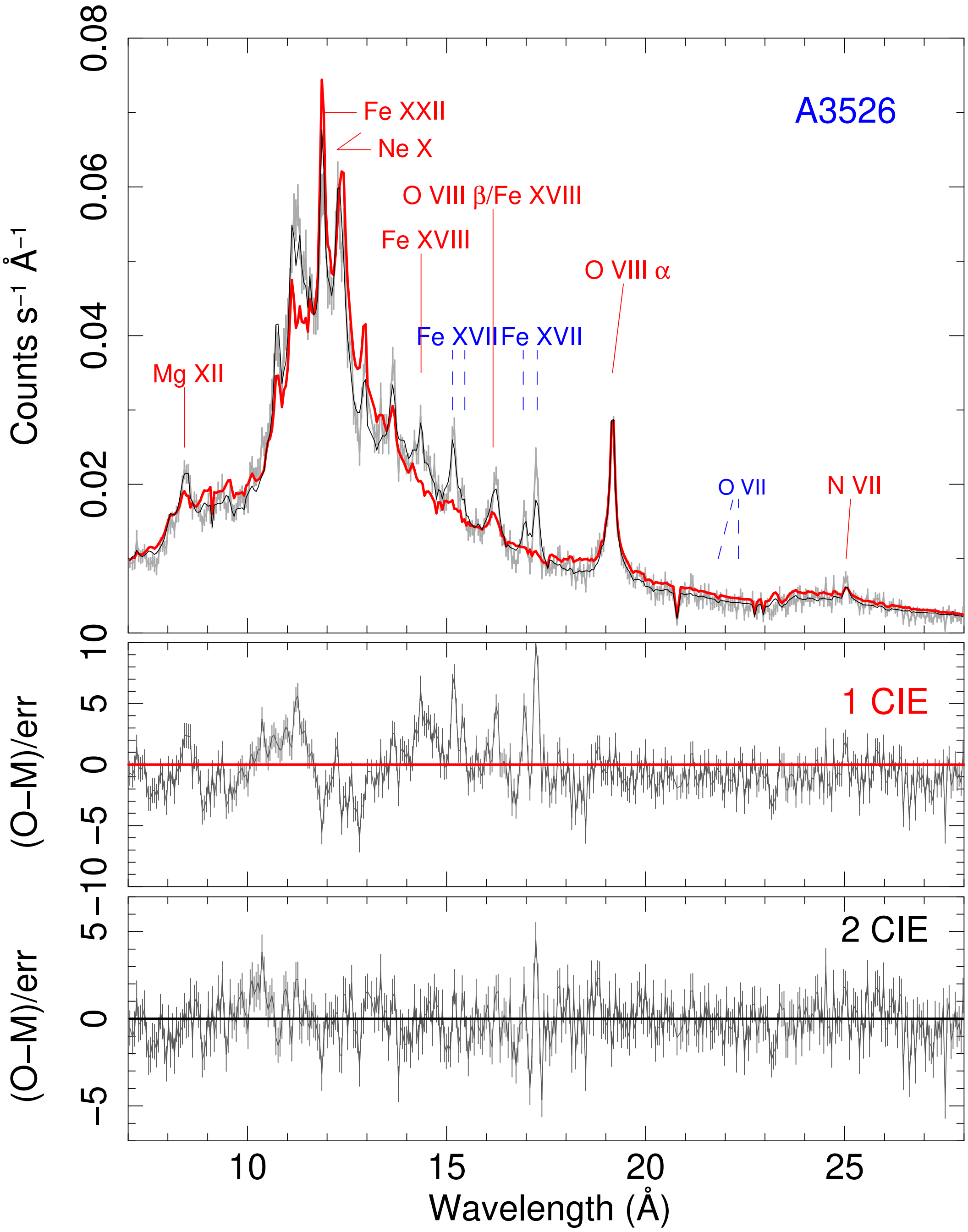

Fig. 3.1 Top: The 90 per cent PSF RGS spectrum of the Centaurus cluster (grey) with the best-fit isothermal collisional equilibrium model (red) and the 2 temperature model (black). Important emission lines are labelled at the observed wavelengths. Dash lines indicate line emission due to cooling gas below 0.8 keV (Fe XVII) and cooled gas below 0.2 keV (O VII). We show the residuals of both models in the middle (1 *cie*) and in the bottom (2 *cie*) panels. Notice that the 2 *cie* model significantly improves the fit to the Fe XVII, Fe XVIII and Fe XXII emission lines.

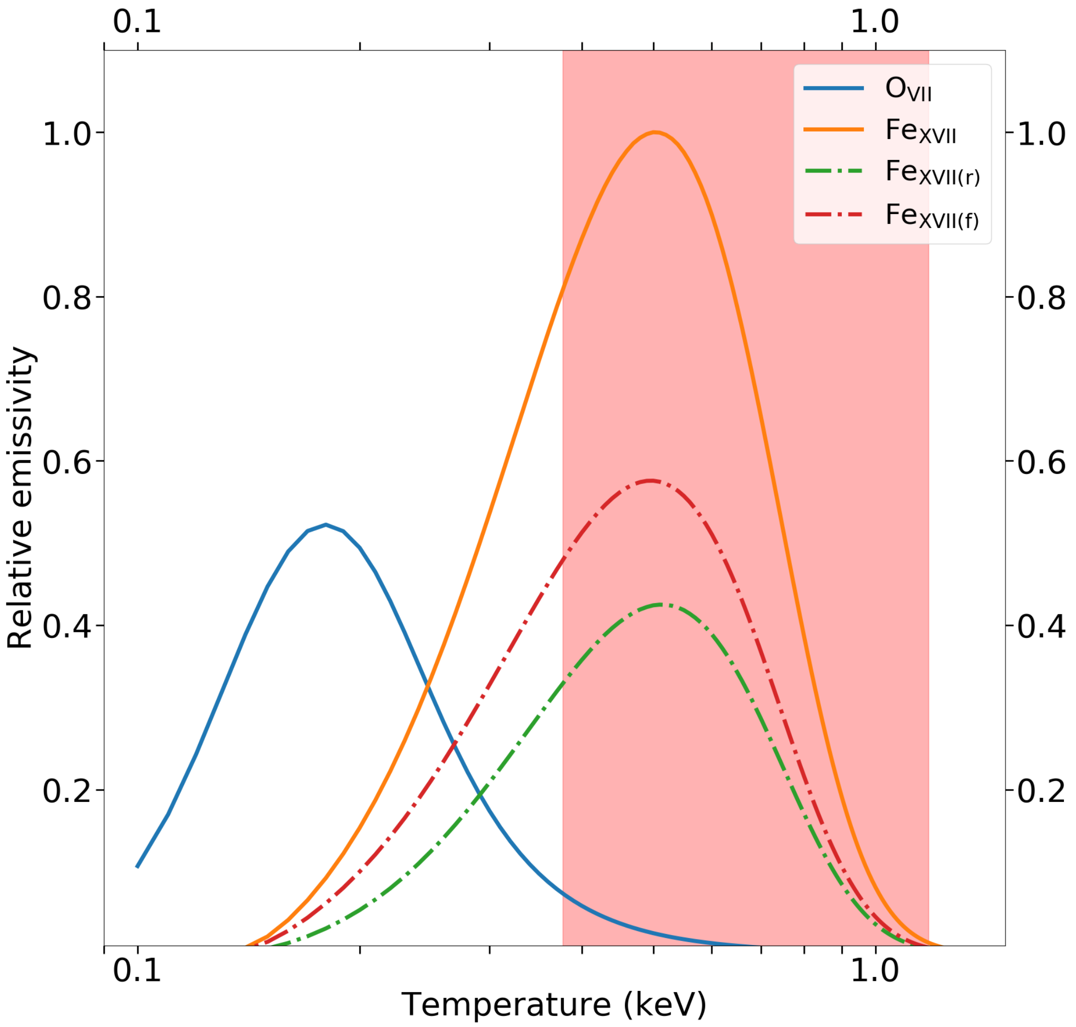

Fig. 3.2 The emissivity of O vii and Fe xvii lines are shown relative to gas temperature. For Fe xvii we include the emissivities of both the resonance and forbidden lines and their sum. The emissivities are normalized such that the peak of the total Fe xvii emissivity is unity. The red shaded region encloses a temperature range 3 times the standard deviation from the average cooler temperature in the 2 *cie* model. This average temperature excludes four objects with their cooler temperature below 0.4 keV.

(<0.2 keV) component or a cooling (∼0.7 keV) component with resonant scattering or a combination of these situations. Since no O VII lines are observed in most clusters [155], it suggests the cool temperature (<0.2 keV) in some objects are likely spurious driven by resonant scattering. It is also possible that background subtraction is affecting the spectra.

Excluding the four objects with a cooler temperature below 0.4 keV, the average temperature of the cooler component is determined to be 0.78±0.13 keV. We do not expect the intrinsic temperature of the cooler component to distribute much beyond 3 times the standard deviation from the average, or equivalently below a minimum temperature of 0.39 keV. The distribution of the cooler *cie* temperature is seen in Fig. 3.3. For EXO0422-086, there is a large uncertainty in the cooler temperature due to limited statistics and the luminosity of the same component only gives an upper limit. Therefore it does not violate our simple expectation of a minimum cooler temperature of 0.39 keV. The best fit models of A1795, AS1101 and MKW3s all give $T_{\mathrm{C,2\,cie}}$ at around 0.22 keV. These temperatures are inconsistent with our expectation, and the luminosities also give upper limits. We conclude that these measurements are affected by resonant scattering. For clusters marked by $*$, no Hα filament is detect in A2029 [93], hence we strongly suspect it has no cooler *cie* component. Both A2626 and Hydra A have limited statistics and the 1 *cie* model can fit their spectra well [39]. Although there is a large uncertainty in $T_{\mathrm{H,2\,cie}}$ in Fornax, the 2 *cie* model improves the spectral fit significantly.

The X-ray luminosity of the cooler component is usually $10^{42}-10^{43}\,\mathrm{erg\,s^{-1}}$. Luminosity can be converted into a mass flow rate,

$$\dot{M} = \frac{2}{3} \times \frac{L\mu m_{\mathrm{p}}}{kT}. \tag{3.1}$$

We ignore the PdV work done on the cooling gas, and find the 'cooling rate' is less than 25 $\mathrm{M_{\odot}yr^{-1}}$ in most objects. This allows us to estimate the volume occupied by the cooler component, the associated gas mass and the cooling time if we know the associated electron density. Cavagnolo et al. [26] provided spatially resolved analysis of clusters, where they measured the temperatures and electron densities of gas at hot phase. We extrapolate/interpolate these profiles, and evaluate the temperature T_{e} and density n_{e} at a fiducial radius of 5 kpc from the centre. This approximation gives an estimated 5 per cent uncertainties in both quantities. By assuming the hotter gas is at pressure equilibrium with the cooler *cie* component, we can estimate the electron density n_{C} associated with the cooler gas by $n_{\mathrm{e}}T_{\mathrm{e}} = n_{\mathrm{C}}T_{\mathrm{C,2\,cie}}$. The volume of the component can then be easily evaluated by emission measure in SPEX, which is the product of the electron and hydrogen densities and the volume. If the cool gas is spherical and has an approximately constant density, we can calculate the filling radius

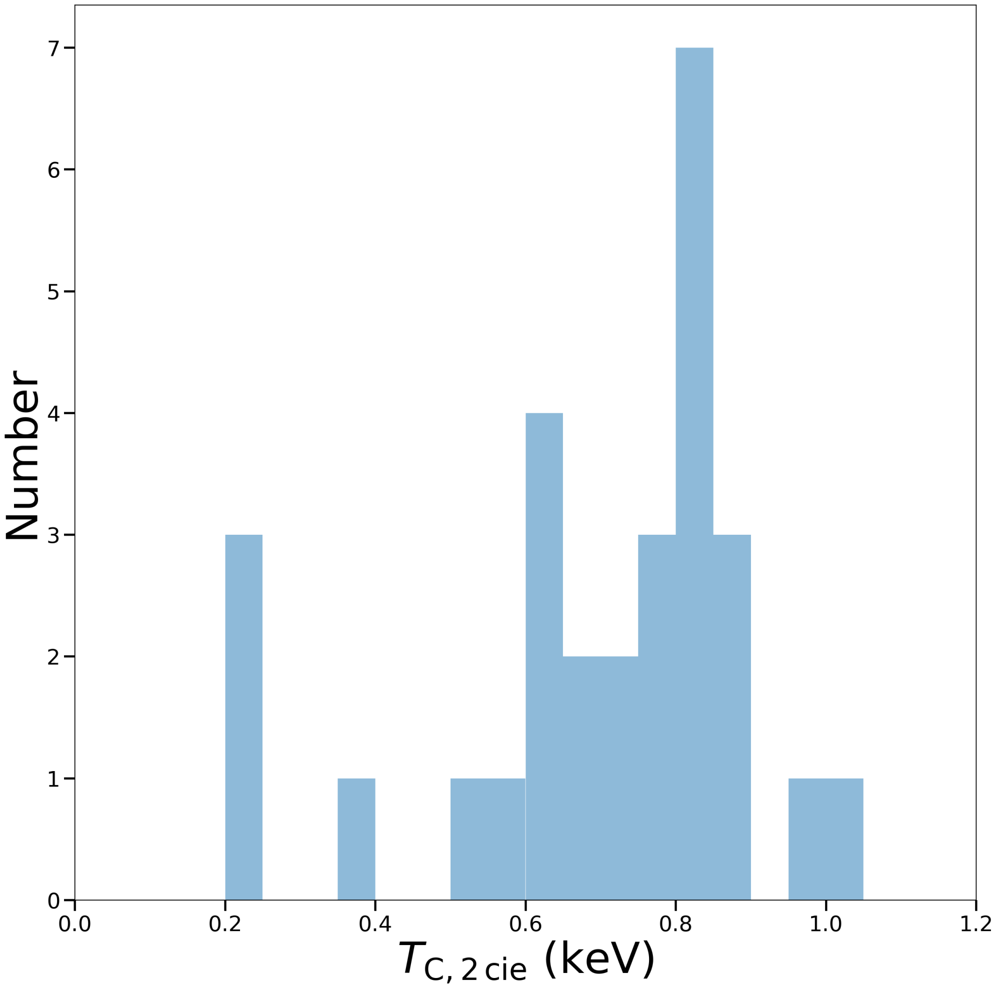

Fig. 3.3 The distribution of the cooler temperature in the 2 *cie* model in rich clusters with a bin size of 0.05 keV.

$R_{\mathrm{C,2cie}}$ and the mass of the cooler gas by $M_{\mathrm{C,2cie}} = 1.14 \times n_{\mathrm{C}} m_{\mathrm{H}} V$, where we assume the hydrogen fraction is 75 per cent and V is the volume. In most objects, we find the filling radius less than 5 kpc and the volume filling ratio of 10-20 per cent. It implies that if the cool gas were distributing throughout the 5 kpc core, the gas has to form either narrow filaments or several separated gas clouds. There are a few objects with the volume filling ratio larger than 100 per cent, which suggests a larger fiducial radius. Since electron densities decrease with larger radii, it is uncertain whether the filling ratio can drop below unity. It is likely that the cooler component in these objects are very extended. On the other hand, we deduce that the mass of the cooler gas is of the order of $10^8 - 10^9 M_{\odot}$. For A262 and 2A0335+096, we find this mass consistent with the molecular mass within a factor of 2 [46, 168]. However, the molecular mass is not consistent with $M_{\mathrm{C,2cie}}$ for other objects. Finally, we define the cooling time of the cooler *cie* component to be $t_{\mathrm{cool,2cie}} = 2.31 \times 3kT_{\mathrm{C,2cie}}/2n_{\mathrm{C}}\Lambda$, where we get the factor 2.31 by assuming the total hydrogen and ion density is $0.92 n_{\mathrm{C}}$, and the proton density is 0.83 n_{C} [119]. This is larger but proportional to $M_{\mathrm{C,2cie}}/\dot{M}_{\mathrm{C,2cie}}$ using our assumptions.

We do not use the same 2 *cie* model on most groups of galaxies, where some objects can be well described by an isothermal ICM (e.g. NGC3411). From the improvement of reduced C-stat, we find that a few more groups can be fitted by the 2 *cie* model, which is mostly consistent with [39]. Since these objects typically have 1 *cie* temperatures less than 1 keV, it is difficult to resolve the temperature of the additional component. Additionally, the cooler *cie* may suppress the original component and force it to have an unexpectedly high temperature in some objects.

We simulate a spectrum of a cooling flow model from 2 down to 0.01 keV, which is then fitted by a *cie* component. This *cie* temperature is found to be 0.86 keV, in agreement with the average temperature of the cooler component. Sanders et al. [182] performed a Markov Chain Monte Carlo analysis on a simulated cooling flow with three variable temperature components and one component at a fixed temperature. The distribution also showed that there is a component at 0.6-0.8 keV. Sanders et al. [182] suggested that this particular temperature range is due to gas temperatures which are easily differentiated spectrally. These simulations suggest that the cooler *cie* component can instead be a cooling flow in clusters. We attempt to trace such a cooling flow with two different models in section 3.3.3.

Table 3.5 Key parameters of the 2 *cie* model in clusters and two bright groups.

Source	$T_{\mathrm{H,2\,cie}}$	$T_{\mathrm{C,2\,cie}}$	$L_{\mathrm{C,2\,cie}}$	$\dot{M}_{\mathrm{C,2\,cie}}$	$R_{\mathrm{C,2\,cie}}$	$M_{\mathrm{C,2\,cie}}$	$t_{\mathrm{cool,2\,cie}}$
2A0335+096	1.71 ± 0.04	0.79 ± 0.03	650 ± 60	54 ± 5	5.3 ± 0.3	2.8 ± 0.6	43 ± 6
A85	3.14 ± 0.12	0.82 ± 0.14	<126	<10.2	<2.15	<0.331	>26.9
A133	2.37 ± 0.10	0.86 ± 0.06	160 ± 40	12 ± 3	4.2 ± 0.5	0.8 ± 0.4	60 ± 20
A262	1.52 ± 0.03	0.79 ± 0.03	49 ± 6	4.1 ± 0.5	4.8 ± 0.4	0.7 ± 0.2	130 ± 20
Perseus 90% PSF	2.25 ± 0.05	0.57 ± 0.03	190 ± 10	22 ± 2	2.2 ± 0.1	0.50 ± 0.1	18 ± 2
Perseus 99% PSF	2.07 ± 0.03	0.62 ± 0.02	600 ± 20	64 ± 3	3.3 ± 0.2	1.6 ± 0.3	20 ± 2
A496	2.21 ± 0.07	0.83 ± 0.06	84 ± 10	6.7 ± 0.8	2.7 ± 0.2	0.40 ± 0.1	47 ± 8
A1795	3.22 ± 0.18	0.18 ± 0.03	800 ± 300	300 ± 100	1.8 ± 0.4	0.6 ± 0.4	2 ± 1
A1835	4.14 ± 0.18	0.73 ± 0.07	1600 ± 500	150 ± 40	2.8 ± 0.4	1.9 ± 0.9	11 ± 5
A1991	1.78 ± 0.11	0.83 ± 0.07	270 ± 80	21 ± 6	5.8 ± 0.9	2.0 ± 0.9	80 ± 30
A2029 *	3.46 ± 0.16	$0.64\pm^{0.86}_{0.63}$	<575	<59.6	<2.19	<0.908	>12.6
A2052	1.98 ± 0.07	0.89 ± 0.04	180 ± 40	13 ± 3	6.0 ± 0.6	1.8 ± 0.6	110 ± 30
A2199	2.66 ± 0.10	0.74 ± 0.06	60 ± 10	5 ± 1	2.3 ± 0.3	0.25 ± 0.10	40 ± 10
A2597	2.61 ± 0.10	0.83 ± 0.09	300 ± 100	22 ± 9	3.4 ± 0.7	1.0 ± 0.7	40 ± 20
A2626 *	$3.28\pm^{0.58}_{0.43}$	$1.02\pm^{0.48}_{0.33}$	<83.8	<5.47	<8.55	<5.16	>111
A3112	2.64 ± 0.09	0.65 ± 0.08	100 ± 40	10 ± 4	2.0 ± 0.4	0.26 ± 0.16	20 ± 10
Centaurus	1.64 ± 0.02	0.82 ± 0.01	77 ± 2	6.2 ± 0.2	3.2 ± 0.2	0.38 ± 0.06	50 ± 3
A3581	1.38 ± 0.02	0.62 ± 0.07	37 ± 7	3.9 ± 0.7	3.4 ± 0.4	0.4 ± 0.1	80 ± 20
A4038	2.40 ± 0.14	0.54 ± 0.10	25 ± 7	3.1 ± 0.8	2.4 ± 0.4	0.2 ± 0.1	50 ± 20
A4059	2.55 ± 0.12	0.84 ± 0.09	60 ± 20	4 ± 2	3.5 ± 0.7	0.4 ± 0.3	80 ± 50
AS1101	1.96 ± 0.05	0.23 ± 0.15	<129	<36.6	<1.61	<0.244	>5.51
AWM7	1.98 ± 0.10	0.68 ± 0.04	28 ± 4	2.8 ± 0.4	2.7 ± 0.2	0.23 ± 0.06	70 ± 10
EXO0422-086	2.30 ± 0.16	$0.37\pm^{0.27}_{0.14}$	<59.4	<10.6	<1.61	<0.106	>8.25
Fornax	$2.70\pm^{0.77}_{0.63}$	0.95 ± 0.01	13 ± 2	0.9 ± 0.1	/	/	/
Hydra A *	2.44 ± 0.09	$0.62\pm^{0.88}_{0.61}$	<79.8	<8.46	<2.09	<0.297	>29.0
Virgo	1.42 ± 0.01	0.80 ± 0.02	13 ± 1	1.1 ± 0.1	2.2 ± 0.2	0.11 ± 0.02	80 ± 10
MKW3s	2.35 ± 0.09	0.21 ± 0.05	120 ± 60	40 ± 20	1.7 ± 0.5	0.2 ± 0.2	5 ± 4
MKW4	1.67 ± 0.16	1.11 ± 0.10	60 ± 20	3 ± 1	5.2 ± 0.9	0.7 ± 0.4	170 ± 90
HCG62	1.22 ± 0.10	0.78 ± 0.02	74 ± 8	6.3 ± 0.6	9.1 ± 0.6	2.1 ± 0.5	270 ± 40
NGC5044	$1.27\pm^{0.29}_{0.16}$	0.86 ± 0.01	164 ± 10	12.7 ± 0.8	10.8 ± 0.6	4.2 ± 0.8	270 ± 30

We define the condition $\frac{x}{\sigma_x} > 2$ for a value x (except temperature) to be a measurement, otherwise it is considered as an upper limit. This rule does not apply to the last three column due to rounding. The best fit temperatures of the 2 *cie* model measured in keV. The luminosities of the cooler *cie* component $L_{\mathrm{C,2\,cie}}$ are calculated in the 0.01-10 keV energy band in $10^{40}\,\mathrm{erg\,s^{-1}}$, and are converted into mass flow rates $\dot{M}_{\mathrm{C,2\,cie}}$ in $\mathrm{M_{\odot}\,yr^{-1}}$ using equation 3.1 [52]. Assuming the cool gas at $T_{\mathrm{C,2\,cie}}$ is at pressure equilibrium with the hotter gas, it can fill a sphere with effective radius of $R_{\mathrm{C,2\,cie}}$ in kpc. Such a sphere with constant density contains the mass of the cool gas $M_{\mathrm{C,2\,cie}}$ in $10^9\,\mathrm{M_{\odot}}$. The cooling time of the cool gas is also included in Myr. Clusters and two bright groups are included in this table, and those marked by $*$ usually have high uncertainties in $T_{\mathrm{H,2\,cie}}$ or $T_{\mathrm{C,2\,cie}}$ and $L_{\mathrm{C,2\,cie}}$ gives upper limits.

3.3.3 Cooling flow models

One-stage cooling flow model

The one-stage cooling flow model includes 1 *cie* and 1 *cf* components which have the same abundances. We assume that the maximum temperature of the cooling flow is the same as the *cie* temperature, and the minimum temperature is fixed at 0.01 keV.

We find a low level of cooling rate in most clusters, typically less than $10\,\mathrm{M_{\odot}yr^{-1}}$ (see Table 3.6). For clusters with *cie* temperature higher than 1.6 keV, the measured cooling rates are compared with the 'simple' cooling rates $\dot{M}_{\mathrm{simple}}(<r) = M_{\mathrm{gas}}(r)/t_{\mathrm{cool}}(r)$, where $M_{\mathrm{gas}}(r)$ is the total gas mass enclosed within a radius r. The radius is determined where the radiative cooling time $t_{\mathrm{cool}}(r)$ is 3 Gyr. We use the electron density and the cooling time profiles in [26], where we model the electron density by a power law with the function of form $n_e = Ar^b$. We assume the clusters are spherically symmetric and integrate the electron densities between 0.1 kpc and the radius where the cooling time is 3 Gyr. This calculation will give approximately 20 per cent systematic uncertainty from the actual density profile and the asymmetry of clusters. As an example, if we use the density profiles of the eastern and western halves of the Centaurus cluster [186], the 'simple' cooling rate is slightly lower at $9.5\,\mathrm{M_{\odot}yr^{-1}}$, as opposed to $11.7\,\mathrm{M_{\odot}yr^{-1}}$ from the symmetric density profile. These 'simple' cooling rates are consistent with the clusters values calculated by [119]. We repeat the same calculation for the classical cooling rates, which have the radiative cooling time of 7.7 Gyr. In this work, we denote the 'simple' and classical cooling rates as $\dot{M}_{\mathrm{simple,3Gyr}}$ and $\dot{M}_{\mathrm{simple,7.7Gyr}}$ respectively [1]. In general, we find that $\dot{M}_{\mathrm{simple,3Gyr}} < \dot{M}_{\mathrm{simple,7.7Gyr}}$.

Since the 'simple' and classical cooling rates can serve as a proxy for predicted cooling rates in the absence of heating, we can infer the efficiency of heating due to feedback between the measured-to-predicted ratio and unity. The distribution is shown in the top panels of Fig. 3.4. The great majority of clusters have a measured-to-predicted ratio less than 0.4 if we use $\dot{M}_{\mathrm{simple,3Gyr}}$, which is equivalent to a minimum heating efficiency of 60 per cent. 19 out of 22 clusters have a measured-to-predicted ratio less than 0.2. In the $\dot{M}_{\mathrm{simple,7.7Gyr}}$ case, the measured cooling rates are less than 30 per cent of $\dot{M}_{\mathrm{simple,7.7Gyr}}$ for all clusters, and less than 10 per cent in 18 out of 22 clusters, which is consistent with [90]. We further notice that clusters with upper limits in the measured cooling rates are suppressed more effectively than those with measurements.

For groups, very weak cooling flows are sometimes detected, typically less than $1\,\mathrm{M_{\odot}yr^{-1}}$, and many objects only have upper limits in the measured cooling rates (see Table 3.7). The

---

[1] Note that the classical cooling rate differs from that determined if a cooling *flow* has been established. If the gas flows inward, gravitational energy is released and must be accounted for [53].

level of cooling rates is similar to the values reported by [18], usually consistent within 1 σ uncertainty. The minimum temperature of 0.01 keV is important for groups since their *cie* temperature is typically less than 1 keV. If we use a higher value, it is likely to overpredict the cooling rates when the range between the maximum and minimum temperatures is very narrow. Note that it is possible that some objects which can be well fitted by the 1 *cie* model may also be fitted by a single cooling flow model (see e.g. [156]).

Two-stage cooling flow model

For clusters, it is also possible that the cooling flow terminates at a temperature higher than 0.01 keV, because no O VII is seen in most objects [155]. We choose a terminal temperature (i.e. the minimum temperature of the *cf* component) of 0.7 keV, and use an additional *cf* component to measure the residual cooling rate between 0.7 and 0.01 keV (two-stage model). This terminal temperature is the average cooler temperature of all objects in the 2 *cie* model, which is higher than the average terminal temperature of 0.6 keV if we set the terminal temperature free in the one-stage model. For 5 clusters, we show the measured cooling rates with different terminal temperatures T_{terminal} (Fig. 3.5a), and hence the initial temperatures T_{initial} for the residual cooling rates (Fig. 3.5b). It is seen that the cooling rates of the hotter cooling flow component gradually decrease with lower terminal temperatures, and do not change our conclusions. The trend is slightly more complicated for the residual cooling rates, where more upper limits are detected. They do not always decrease as the cooling rates of the hotter cooling flow, because fitting the component in a narrower temperature range may boost the measured values. Additionally, we simulate the spectrum of a cooling flow of $100\,\mathrm{M_{\odot}yr^{-1}}$ between 0.01 and 5 keV using the response matrix of A133, which is then fitted by two cooling flow components with the terminal temperature of the hotter cooling flow component changing between 0.5 and 0.9 keV, and find that both $\dot{M}_{\mathrm{H,\,1cie+2cf}}$ and $\dot{M}_{\mathrm{C,\,1cie+2cf}}$ are consistent with $100\,\mathrm{M_{\odot}yr^{-1}}$ within 1 σ uncertainty. Therefore, we only present our measured cooling rates with a terminal temperature of 0.7 keV in Table 3.6.

Comparing the cooling flow models

Comparing the two cooling flow models, we find that the cooling rates of the hotter *cf* component of the two-stage model are generally higher than the one-stage cooling rates. This is because the hotter *cf* component of the two-stage model need to contribute to Fe XVII emission between a narrow temperature range (0.7-0.9 keV) where its emissivity dominates, and the one-stage model can contribute to Fe XVII emission between 0.01-0.9 keV. Since the two-stage cooling flow model is fitting one more parameter than the one-stage model, we

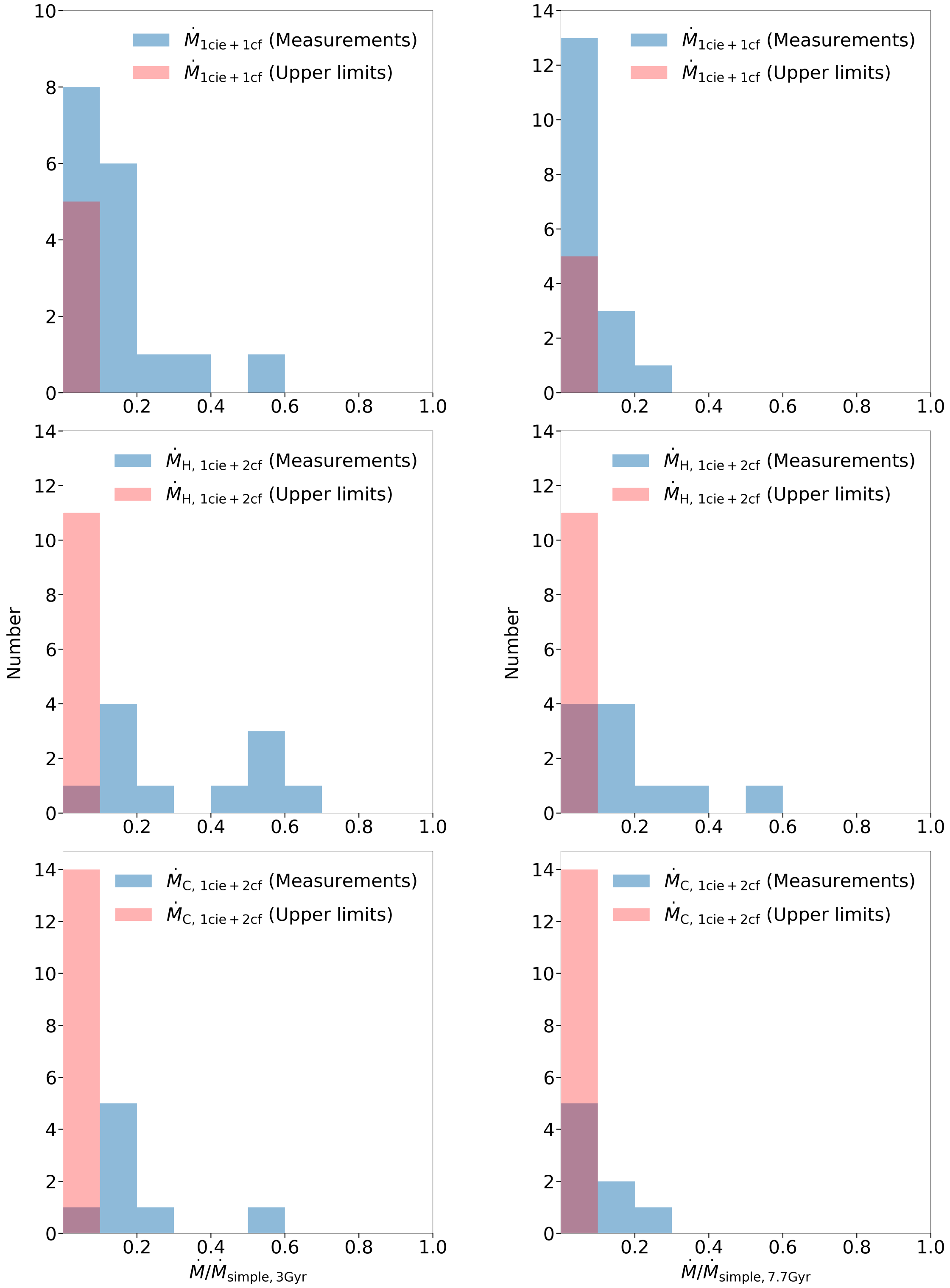

Fig. 3.4 Left: The histograms of the ratio of measured cooling rates to $\dot{M}_{\rm simple,3Gyr}$ for clusters with $T_{\rm Max,\,1cie+2cf} > 1.6$ keV, where $\dot{M}_{\rm simple,3Gyr}$ are deduced from the gas parameters tabulated by [26]. Top: cooling rates of the one-stage model. Middle: cooling rates between $T_{\rm Max,\,1cie+2cf}$ and 0.7 keV in the two-stage model. Bottom: the residual cooling rates below 0.7 keV. Right: the measured cooling rates compared to $\dot{M}_{\rm simple,7.7Gyr}$.

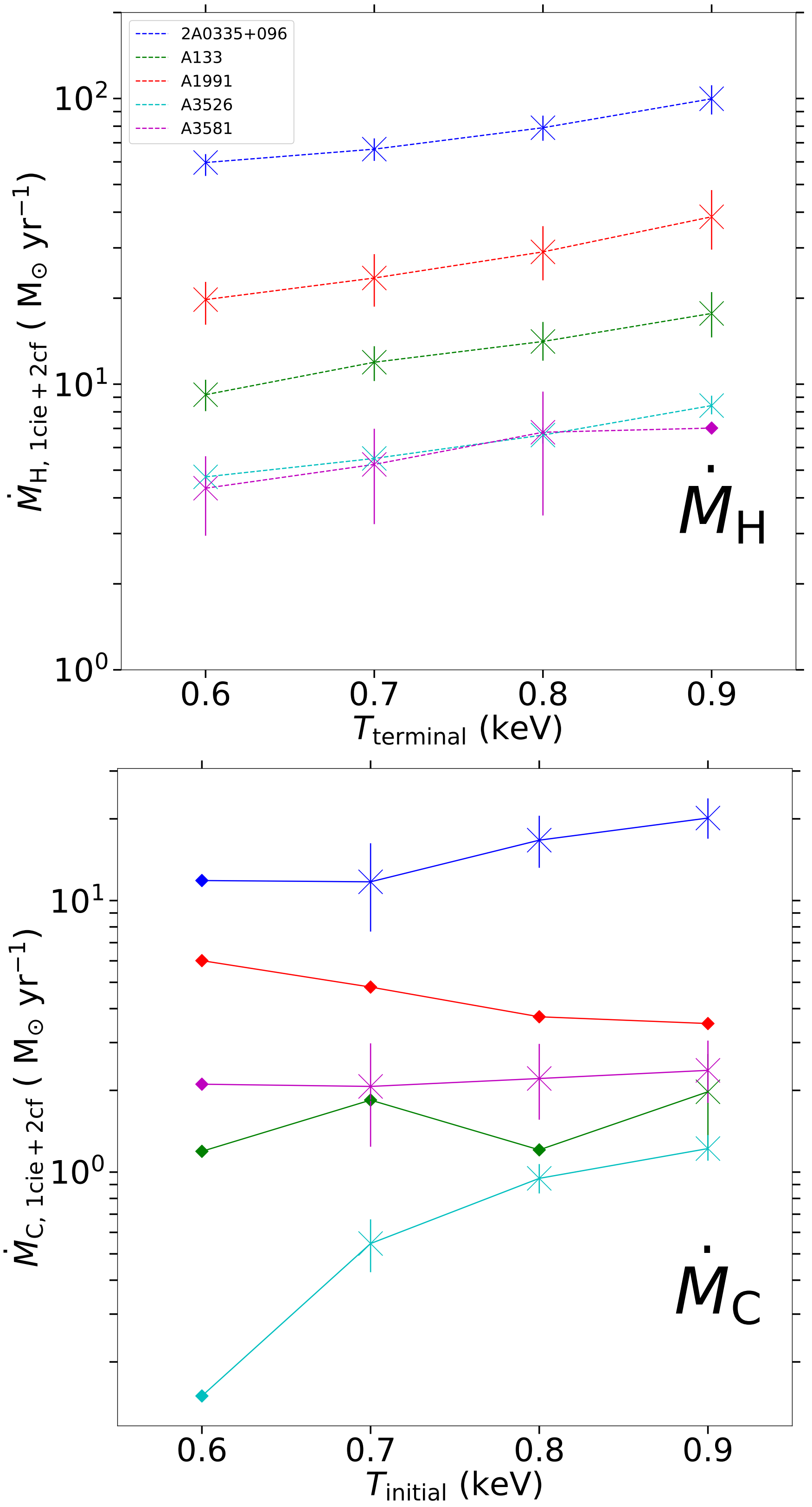

Fig. 3.5 Top: (a) The measured cooling rates between the *cie* temperature and different terminal temperatures in the two-stage cooling flow model. The diamond shape represents 2 σ upper limit. Bottom: (b) The residual cooling rates between different initial temperatures and 0.01 keV in the two-stage cooling flow model. The initial temperatures match the terminal temperatures of the hotter cooling flow component.

Table 3.6 Key parameters of the one-stage and two-stage cooling flow models in clusters and groups.

Source	$\dot{M}_{\rm simple,3Gyr}$	$\dot{M}_{\rm simple,7.7Gyr}$	$\dot{M}_{\rm 1cie+1cf}$	$\dot{M}_{\rm H,\,1cie+2cf}$	$\dot{M}_{\rm C,\,1cie+2cf}$
2A0335+096	112	185	36±3	66±6	12±4
A85	81.7	142	1.3±0.7	<4.15	<2.82
A133	47.7	62.5	4.3±0.5	12±2	<1.84
A262	3.38	11.4	2.4±0.2	5.3±0.5	0.9±0.3
Perseus 90% PSF	306	303	18±6	<5.33	31±2
Perseus 99% PSF	306	303	56±15	21±7	82±4
A496	47.6	66.9	3.2±0.5	8±2	<1.92
A1795	140	224	<14.9	<19.5	<21.9
A1835	1010	1080	80±30	<114.8	<97.3
A1991	37.6	45.1	10±2	24±5	<4.80
A2029	204	369	<14.8	<30.5	<24.3
A2052	28.9	53.6	5.7±0.6	16±1	<1.32
A2199	31.8	107	3.2±0.6	5±2	2±1
A2597	279	611	11±4	30±10	<12.3
A2626	15.4	24.8	0.9±0.7	3±2	<2.18
A3112	75.2	118	6±2	<8.02	9±3
Centaurus	11.7	26.2	3.3±0.1	5.5±0.3	0.6±0.1
A3581	18.8	20.3	3.0±0.4	5±2	2.1±0.9
A4038	16.7	40.1	2.0±0.5	<2.39	3.1±0.9
A4059	10.8	36.5	2.0±0.5	4±2	<1.51
AS1101	156	227	<3.80	<5.90	<5.09
AWM7	3.79	27.7	2.1±0.3	2.0±0.7	2.2±0.6
EXO0422-086	26.6	38.6	<1.53	<4.28	<2.61
Fornax	/	/	0.04±0.01	0.85±0.05	<0.01
Hydra A	86.4	109	<5.25	<1.93	<10.8
Virgo	11.1	37.4	0.62±0.03	2.33±0.09	<0.07
MKW3s	24.9	48.2	3±1	<2.10	5±2
MKW4	4.55	7.24	0.11±0.06	0.9±0.2	<0.06
HCG62	3.66	4.46	1.5±0.2	/	/
NGC5044	13.5	34.6	<0.10	/	/
NGC5813	3.34	4.8	<0.08	/	/
NGC5846	2.22	4.3	0.43±0.06	/	/

$\dot{M}_{\rm simple,3Gyr}$ and $\dot{M}_{\rm simple,7.7Gyr}$ are the 'simple' and classical cooling rates in the absence of heating, which are deduced from [26]. The measured cooling rates (column 4-6) assume isobaric cooling flows, where $\dot{M}_{1cie+1cf}$ is measured from the *cie* temperature $T_{\rm Max,\,1cie+1cf}$ down to 0.01 keV in the one-stage model (see Table 3.7), $\dot{M}_{\rm H,\,1cie+2cf}$ is the cooling rate of the hotter cooling flow component from $T_{\rm Max,\,1cie+2cf}$ down to 0.7 keV and $\dot{M}_{\rm C,\,1cie+2cf}$ is measured between 0.7 and 0.01 keV both in the two-stage model. All of the mass rates are measured in $\rm M_{\odot}yr^{-1}$.

Table 3.7 Key parameters continued.

Source	$T_{\mathrm{Max,\,1cie+1cf}}$	$T_{\mathrm{Max,\,1cie+2cf}}$	Source	$T_{\mathrm{Max,\,1cie+1cf}}$	$T_{\mathrm{Max,\,1cie+2cf}}$
2A0335+096	1.66±0.03	1.81±0.05	Centaurus	1.52±0.01	1.82±0.05
A85	3.14±0.13	3.18±0.15	A3581	1.40±0.02	1.43±0.03
A133	2.36±0.10	2.54±0.14	A4038	2.46±0.16	2.42±0.15
A262	1.48±0.01	1.60±0.04	A4059	2.57±0.12	2.64±0.14
Perseus 90% PSF	2.36±0.06	2.21±0.04	AS1101	1.96±0.05	1.96±0.04
Perseus 99% PSF	2.14±0.02	2.05±0.02	AWM7	2.02±0.12	2.02±0.13
A496	2.20±0.05	2.27±0.08	EXO0422-086	2.32±0.19	2.30±0.17
A1795	3.10±0.16	3.12±0.15	Fornax	0.99±0.01	1.56±0.04
A1835	$4.34\pm^{0.22}_{0.32}$	$4.36\pm^{0.25}_{0.33}$	Hydra A	2.44±0.08	2.43±0.09
A1991	1.71±0.08	1.88±0.14	Virgo	1.37±0.01	1.43±0.01
A2029	3.47±0.14	3.46±0.13	MKW3s	2.34±0.08	2.33±0.08
A2052	1.87±0.05	2.07±0.07	MKW4	1.46±0.01	1.53±0.03
A2199	2.73±0.11	2.76±0.11	HCG62	0.90±0.01	/
A2597	2.62±0.11	2.67±0.11	NGC5044	0.87±0.01	/
A2626	$3.22\pm^{0.54}_{0.37}$	$3.38\pm^{0.62}_{0.47}$	NGC5813	0.68±0.01	/
A3112	2.66±0.09	2.64±0.09	NGC5846	0.75±0.01	/

The temperatures of the *cie* component (the maximum temperature of the cooling flow) in both the one-stage and two-stage models.

Table 3.8 One-stage model for galaxies.

Source	$\dot{M}_{\mathrm{1cie+1cf}}$	$T_{\mathrm{Max,\,1cie+1cf}}$	Source	$\dot{M}_{\mathrm{1cie+1cf}}$	$T_{\mathrm{Max,\,1cie+1cf}}$
M49	0.07±0.02	0.92±0.01	NGC1550	0.5±0.1	1.17±0.01
M86	0.20±0.08	0.84±0.02	NGC3411	<0.32	0.91±0.01
M89	0.3±2	0.64±0.02	NGC4261	<0.10	0.73±0.01
NGC507	0.69±0.06	1.17±0.01	NGC4325	<2.67	0.90±0.02
NGC533	<2.64	0.90±0.04	NGC4374	0.2±0.1	0.71±0.04
NGC1316	0.26±0.04	1.34±0.03	NGC4636	1.1±0.2	0.72±0.01
NGC1404	0.6±0.3	0.69±0.03	NGC4649	<0.01	0.84±0.01

Only the one-stage cooling flow model is used for galaxies.

are also interested in whether the two-stage model is statistically better and the difference in spectral fit.

We find that the two-stage model has a lower C-stat than the one-stage model (ΔC-stat$\geq$ 10 for 1 degree of freedom) in 9 out of 22 clusters. However, there are a few special clusters where we prefer the one-stage model, such as Perseus and MKW3s, because the residual cooling rate is higher than the cooling rate above 0.7 keV. For AWM7, we find that there is no difference between the two cooling flow models, both in terms of C-stat and cooling rates. Therefore, we conclude that the one-stage cooling flow is sufficient for AWM7 [2].

To demonstrate the difference in the spectral fit, we show the spectrum and cooling flow models of A133 in Fig. 3.6. The two-stage model improves the spectral fit to the Fe XVII forbidden line at 17.1 Å (0.72 keV), which is related to the cooling gas. Furthermore, the models differ between 12.5 and 14.5 Å (0.85-0.96 keV), which has emission from different ionisation stages of Fe which peak at hotter temperatures, e.g. Fe XX. However, neither of the cooling flow models is significantly better at these wavelengths. We also show the contribution from different components in the two-stage model in Fig. 3.7. It is seen that the contribution from the two cooling flow components are comparable at important lines, e.g. Fe XVII, O VIII and O VII. In conclusion, we have statistical and spectral evidence that the two-stage cooling flow model is better in at least 9 out of 22 clusters.

3.3.4 Special clusters

Perseus and Virgo

It is well known that both the X-ray bright Perseus and Virgo clusters have a bright variable AGN at the centre, and it is well described by a *pow* component. The X-ray emission of the AGN can vary by an order of magnitude in only a few years, and hence we need to fix the parameters of the *pow* component at the time of our observation. Churazov et al. [29] found that the AGN emission in Perseus can be well fitted by an absorbed ($N_{\mathrm{H}} = 10^{21}\,\mathrm{cm}^{-2}$) *pow* component with a photon index of 1.65, where such a column density is comparable to N_{HI} from our own galaxy. The luminosity of the nucleus (OBSID = 0085110101) is constrained to be of the order of $10^{43}\,\mathrm{erg\,s^{-1}}$ in the 0.5-8 keV band with 20 per cent systematic uncertainties. In this work, we choose the emission measure such that the *pow* component only produces $10^{43}\,\mathrm{erg\,s^{-1}}$ in the same energy band. We fit both the 90 and 99 per cent PSF (0.9 arcmin and 4 arcmin) spectra in this work, and the variable AGN gives an additional 5 and 15 $\mathrm{M_{\odot}yr^{-1}}$

---

[2] AWM7 is unusual: Chandra data [179] shows a small ($\sim$ 10 kpc) bright core with a low cooling time in a hotter diffuse medium.

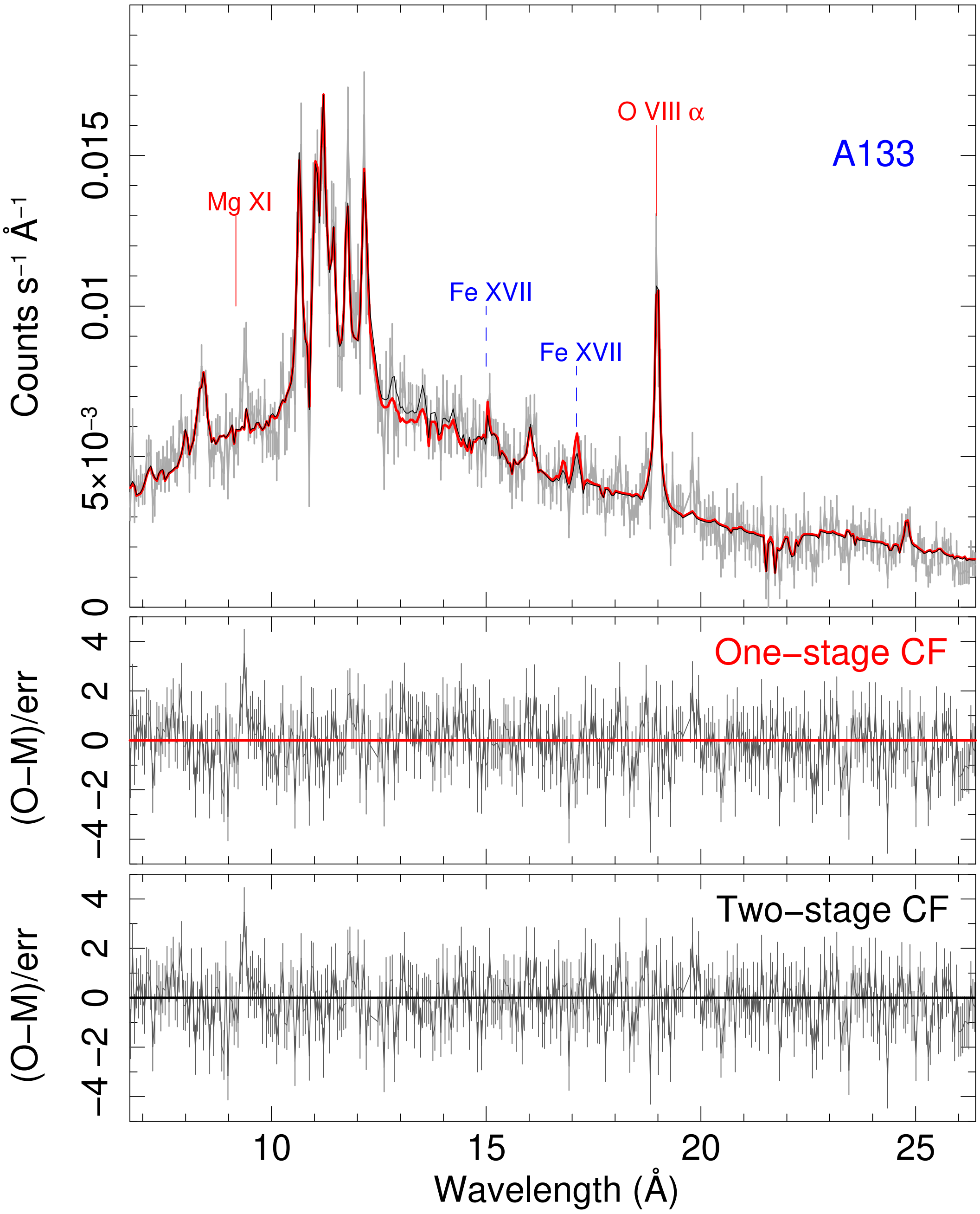

Fig. 3.6 The spectrum (grey) and best fit cooling flow models of A133 in rest wavelength. The spectrum has a peak at around 9.4 Å (1.31 keV), which is an artefact and cannot be fitted.

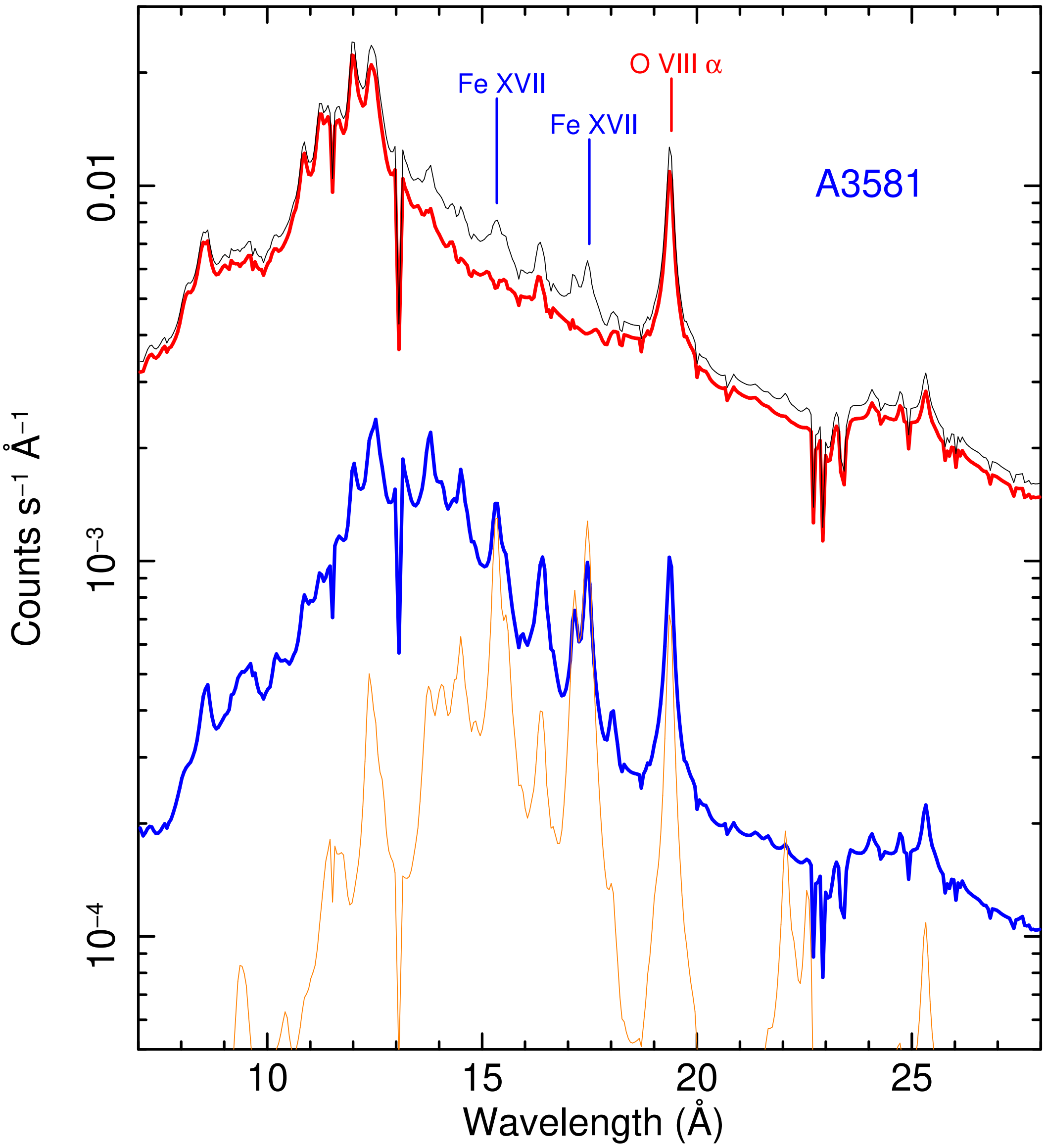

Fig. 3.7 The best fit two-stage cooling flow model of A3581. The top black thin line is the total emission, the thick red line is the contribution from the *cie* component, the thick blue line is the hotter cooling flow component and the thin orange line at the bottom is the residual cooling flow.

statistical uncertainty respectively in the one-stage cooling flow model. The actual cooling structure of Perseus is likely to be more complicated than our models because of the existence of the O VII emission [155], which is beyond the scope of this work.

The initial study on Virgo suggests that it is inadequate to use only the stacked spectrum, and hence we perform simultaneous spectral fitting on the non-stacked spectra. The difference in spectra between the two observations is purely due to the variation of the *pow* component since the ICM emission is constant. We choose the photon index of the first observation to be 2.4 with a flux of $3.76 \times 10^{-12}\,\mathrm{erg\,cm^{-2}\,s^{-1}}$ in 0.3-8 keV (Observation date: *Chandra*= 30 July 2000, XMM-*Newton*= 19 June 2000; see [44]). For the second observation, we use the same photon index and set the emission measure free. The *pow* component of the second observation yields a flux of $5.19 \times 10^{-11}\,\mathrm{erg\,cm^{-2}\,s^{-1}}$, which is 13.8 times brighter than the previous observation, and comparable to the ICM luminosity. The scale of the variability of the AGN flux is similar to the observation of Suzaku in 2006 and Chandra in 2017 [92].

Centaurus

In addition to the multi-temperature and cooling flow models, we apply a 5 *cf* model to both the 90 and 99 per cent PSF spectra of the Centaurus cluster, which has been used by [181]. The temperatures of the *cf* components are 3.2-2.4, 2.4-1.6, 1.6-0.8, 0.8-0.4, 0.4-0.0808 keV. The components below 0.8 keV are convolved by the same *lpro* component, and we use a second *lpro* component for the hotter *cf* components (3.2 to 0.8 keV) to improve the spectral fit. From the spatial analysis by [181], the components below 0.8 keV are located in the innermost core, which supports this critical temperature. The best fit values are shown in Table 3.9.

We compare these cooling rates of the 90 per cent PSF spectrum with the two-stage model in section 3.3.3. The residual cooling rate $\dot{M}_{\mathrm{C,\,1cie+2cf}}$ is lower than Comp 4 (0.8-0.4 keV), and Comp 5 only gives an upper limit. They suggest that the cluster cools below 0.7 keV, and stops cooling potentially at around 0.2 keV, where O VII emission was found by [155]. However, it is difficult to constrain the exact terminal temperature, since the O VII lines are very weak comparinged to the continuum.

For the 99 per cent PSF spectrum, we find our results different from those reported by [181]. Our model does not fit the hottest *cf* component (3.2-2.4 keV), which has unexpectedly low upper limits. Further investigation suggests that this can be strongly influenced by different free abundances and the calibration below 8.5 Å (1.45 keV) is very poor. Nevertheless, we can still confirm that the Centaurus cluster can be resolved with more than two components (see Table 3.9 for *cf* models).

Table 3.9 The best fit parameters of the 5 *cf* model for the Centaurus cluster.

	$\dot{M}$ (90% PSF)	$\dot{M}$ (99% PSF)	$\dot{M}$ from [181]
Comp 1	< 6.41	< 15.9	46.4±2.7
Comp 2	21.2±2.43	60.0±4.56	32.1±2.8
Comp 3	4.69±0.23	7.06±0.30	6.30±0.37
Comp 4	0.99±0.08	1.37±0.13	2.13±0.48
Comp 5	< 0.13	< 0.16	< 2.25

The temperature grids are 3.2-2.4, 2.4-1.6, 1.6-0.8, 0.8-0.4, 0.4-0.0808 keV (from Comp 1 to Comp 5). The cooling rates are in $\mathrm{M_{\odot} yr^{-1}}$. The second and third columns are our measured values. The fourth column has been revised using the update XSPEC package, where the upper limit in Comp 5 is 1 σ only.

Unfortunately, 5-component models cannot be repeated for other objects. Since the thermal structures of clusters are intrinsically different, it is very difficult to define a universal temperature grid. The limited statistics in many objects also forbid us from resolving them further. Hence, we have limited a maximum of 2 *cf* components for the remaining clusters.

3.4 Discussion

3.4.1 The missing soft X-ray emission and Hα filaments

Our spectral fits indicate that little cooled gas is seen in the X-ray band below 0.4 keV (Table 3.5), and the upper limits obtained on $\dot{M}_{\mathrm{C,\,1cie+2cf}}$ show little evidence for cooling gas either. Gas may be cooling down due to X-ray emission above ~ 0.7 keV but if it does then it does not continue cooling in that way below that energy. Such behaviour is peculiar because the radiative cooling time shortens rapidly as the gas temperature drops.

The situation was modelled by [57] in terms of 'missing' soft X-ray luminosity, L_{miss}. This is the luminosity difference between gas cooling at a rate $\dot{M}$ down to a terminal temperature and gas cooling at the same rate to zero. It was noted that L_{miss} is similar to the luminosity of the optical-UV emission-line nebulosity L_{neb} around the Brightest Cluster Galaxies (BCGs) of the cool core clusters studied, suggesting that L_{neb} was powered by the remaining thermal energy of the cooling gas at T_{min}. The hypothesis is supported by the spatial-coincidence of the nebulae and the soft X-ray emission (e.g. Perseus: [57, 59];

Centaurus: [34, 62]; A1795: [58, 35]). In order to capture the full emission from the nebula, we increase the observed Hα luminosity by a factor of 15 [3] [65].

The idea agrees with the heating and excitation of the cold gas being due to fast particles [65]. Fabian et al. [60] suggested that the fast particles are the result of interpenetration of the hot and cold gas. In this case, $L_{\rm miss} = \frac{3}{2}\dot{M}_{\rm H,\,1cie+2cf}\frac{kT}{\mu m_{\rm p}}$ should equal $L_{\rm neb} = 15L_{\rm H\alpha}$. We can rewrite the above as $\dot{M}_{\rm H,\,1cie+2cf} = \dot{M}_{\rm neb}$, where

$$\dot{M}_{\rm neb} = 0.99\times(\frac{L_{\rm H\alpha}}{10^{40}\,{\rm erg\,s^{-1}}})(\frac{kT}{1keV})^{-1}{\rm M_\odot\,yr^{-1}}, \tag{3.2}$$

which is the mass inflow rate into the nebula of particles at energy 0.7 keV. The Hα luminosity and $\dot{M}_{\rm neb}$ of clusters are listed in Table 3.10. We plot $\dot{M}_{\rm H,\,1cie+2cf}$ against $\dot{M}_{\rm neb}$ in Fig. 3.8 [4]. Most of the objects lying to the lower left in the plot and $\dot{M}_{\rm H,\,1cie+2cf} > \dot{M}_{\rm neb}$, whereas the opposite is true for the 3 objects up and to the right of the plot.

The situation is more complex than assumed above and we now examine a cluster from the right hand side (Perseus) and the left hand side (Centaurus) in more detail. The Perseus cluster has an extensive Hα nebula [32, 54], and its Hα luminosity is significantly higher than most other objects in our sample. Fabian et al. [57] used the $4'$ region image of the Perseus cluster and found the filaments are UV/optically bright, where the soft X-ray emission is an energetically minor component. Therefore, we use a broader 3.4 arcmin spectrum for Perseus (red circle) here to measure the cooling rate. The two-stage cooling model is affected by resonance scattering, and the residual cooling rate below 0.7 keV is stronger than the cooling rate above. This is problematic because we expect residual cooling to be replenished by the cooling flow above 0.7 keV. Instead, we use the cooling rate $55.5\pm15.3{\rm M_\odot\,yr^{-1}}$ in the one-stage cooling model, which is 30 per cent lower than the cooling rate of a one-stage model that cools down to 0.7 keV. To better match this cooling rate to $\dot{M}_{\rm neb}$ we need to use gas at a higher temperature, $\sim T_{\rm Max,\,1cie+1cf}$, rather than 0.7 keV. This would not show up in our analysis here and remains a possible, but unconfirmed solution for powering of the filaments. A detailed study with Chandra of the X-ray spectra of the nebula filaments in the Perseus cluster by [209] reveals components at both ~ 2 keV and 0.7 keV. Several other clusters (M87, Centaurus and A1795) also show the need for the 0.7 keV component. If the Perseus nebula is powered by particles from the surrounding hot gas then an inflow from the surrounding gas at a rate of $\sim 100{\rm M_\odot yr^{-1}}$ is required.

For the Centaurus cluster (the blue point in Fig. 3.8), to power the nebula requires an inflow of $\sim 2{\rm M_\odot yr^{-1}}$, which is significantly less than our RGS measured value of

---

[3] The actual ratio of $L_{\rm neb}$ to $L_{\rm H\alpha}$ should be between 10 to 20.

[4] We caution against drawing any correlations from this and the next two plots since both axes involve the square of the distance.

$\dot{M}_{\mathrm{H,\,1cie+2cf}} = 5.2 \pm 0.2 \mathrm{M_{\odot}yr^{-1}}$. However, we note that Chandra images of the soft X-ray emission in the cluster reveal emission which is much more extended than the bright filamentary nebula [186]. If we refine the estimate of $\dot{M}_{\mathrm{H,\,1cie+2cf}}$ to an area coincident with the main filaments using Chandra spectra, then we find that $\dot{M}_{\mathrm{H,\,1cie+2cf}}$ drops by a factor of 3 and there is agreement with the particle heating model. Inspection of other clusters with $\dot{M}_{\mathrm{neb}} < 10\mathrm{M_{\odot}yr^{-1}}$ shows that they also have soft emission more extended than the nebula. Note that [80] find weak optical [NII] line emission outside the filamentary nebula in the Centaurus cluster that, if common in other clusters, implies that the nebula emission is yet more extended than assumed above. The nature of the extended 0.7 keV gas component in the Centaurus cluster and other clusters on the left hand side of Fig. 3.8 is unclear. The low value of $\dot{M}_{\mathrm{H,\,1cie+2cf}}$ shows that it is not rapidly radiatively cooling.

For completeness we now also consider the effect of different metallicity, in the light of the inner abundance gradient seen in the Centaurus [146, 107] and other clusters [148]. This takes the form of a pronounced drop in Fe and other abundances within the innermost 10 kpc. In Centaurus the Fe abundance is about twice the Solar value at 15–20 kpc and drops to below 0.4 Solar within 5 kpc. Panagoulia et al. [146] hypothesise that this is due to most metals in stellar mass-loss being in the form of grains which remain trapped in cold clouds. They are then transported out of the cluster centre by the bubbling feedback process and dumped at 10-20 kpc where they mix into the ICM. This means that the region where the ICM temperature is lowest and where a cooling flow might otherwise be expected has a low metallicity. A cooling flow would then produce only weak lines and any detection or limit would rely more on the continuum shape. As examples we have fitted the RGS spectra of the Centaurus cluster and A3581 with the two-stage cooling flow model setting $Z = 0.05 Z_{\odot}$ for the second stage (cooling from 0.7 to 0.01 keV). The rates for that stage are 15 and $24\,\mathrm{M_{\odot}\,yr^{-1}}$, respectively. We are not claiming that these are solutions for any continuous cooling flow as we have no reason to suspect that the abundance could drop as the temperature passed below 0.7 keV. But the possibility remains that some cooling may occur within the coolest central gas, which may be in the process of being dragged out from the centre [146].

It is possible that intrinsic absorption could reduce the level of cooling of the lowest temperature components. The molecular nebula is a potential source of such obscuring gas. We have not included intrinsic absorption in this work and refer the reader to Fig. 18 in [181] for the effect it has on the data from the Centaurus cluster. Results for other clusters in our sample will be relatively similar.

In summary, the current spectra neither support nor rule out the idea that the Hα/CO filaments are powered by interpenetration by the surrounding gas. It remains possible that if it does occur, then it can be from gas at around 0.7 keV in most of the clusters studied but requires hotter gas at $T_{\rm Max,\,1cie+2cf}$ for the most luminous objects.

3.4.2 Star formation rates

Another aspect we can investigate is whether there is a link between cooling rates and the observed star formation rates. Assuming soft X-ray cooling flows lose their energy to the filaments and the cooled gas is consumed directly in star formation, their difference gives us hints on the rate of change in molecular mass. We compare these parameters in Fig. 3.9. Most clusters and groups have a star formation rate lower than 5 $\rm M_{\odot}yr^{-1}$, which is 5 to more than 50 times lower than the measured cooling rate. Only for the more massive clusters Perseus and A1835 with strong star formation activity, the cooling rate close matches the star formation rate and the formation efficiency is around 80 per cent. This efficiency is higher than the minimum star formation efficiency predicted by [119] using the 'simple' cooling rates. We find a weak trend of increasing in star formation efficiency with the cooling rate in agreement with [119]. Since Hα filaments are not necessarily aligned with star formation regions (e.g. the Perseus cluster, [21, 22]), the connection between cooling flows and star formation can be very complicated in massive clusters. The measured cooling rates and upper limits are above the line of unity, and therefore the cooling flows give a net increase in their molecular mass, which accumulates at a level of a few or a few tens of $\rm M_{\odot}yr^{-1}$. Assuming the mass of clusters is of the order of $10^9 - 10^{10}\rm M_{\odot}$ (e.g., $4 \times 10^{10}\rm M_{\odot}$ in the Perseus cluster, [172]; $9 \times 10^8\rm M_{\odot}$ in A262, [46]), a constant mass accumulation rate means that the age of molecular gas is at around a few 10^8yr to 10^9yr, which is comparable to the age of clusters. Therefore, it is possible that no significant molecular gas content was present at sufficiently early epoch.

3.5 Conclusion

In this chapter, we analysed the RGS spectra of the core of 45 clusters and groups of galaxies, and searched for cool and cooling gas. The continuum of the spectra are modelled by a collisional ionisation equilibrium (*cie*) component, which has a typical bulk temperature of 1-4 keV. Since Fe XVII emission is observed, there is either a cooling flow or a cooler gas component. If cooling flows were taking place in these objects, we can measure the cooling rates with both the one-stage and two-stage cooling flow models. Alternatively, we search for cooler gas with the 2 *cie* model. The results are as follows.

Table 3.10 Hα luminosity and star formation rate in clusters and groups.

Source	$L_{\mathrm{H}\alpha}$	$\dot{M}_{\mathrm{neb}}$	$\dot{M}_{\mathrm{SFR}}$	Reference
2A0335+096	7.86	11.3	$0.4\pm^{0.2}_{0.1}$	[a,b]
A85	1.52	2.15	$0.1\pm^{2.5}_{0.1}$	[b]
A133	1.14	1.61	$0.2\pm^{1.4}_{0.2}$	[b]
A262	0.94	1.33	0.21 ± 0.03	[c]
Perseus 90% PSF	224	317	$70\pm^{60}_{30}$	[d]
Perseus 99% PSF	224	317	$70\pm^{60}_{30}$	[d]
A496	2.95	4.17	0.18 ± 0.01	[b]
A1795	5.85	8.27	$3\pm^{13}_{3}$	[c]
A1835	441	624	$110\pm^{60}_{40}$	[e]
A1991	3.80	5.37	$0.7\pm^{2.8}_{0.5}$	[b]
A2029	<4.8	<6.79	$0.8\pm^{0.10}_{0.09}$	[f]
A2052	1.69	2.39	$0.4\pm^{1.0}_{0.3}$	[b]
A2199	1.32	1.87	$1\pm^{9}_{1}$	[c]
A2597	79.1	112	$4\pm^{5}_{2}$	[f]
A2626	0.46	0.651	$0.2\pm^{0.7}_{0.2}$	[c]
A3112	6.75	9.55	$0.8\pm^{1.8}_{0.6}$	[b]
Centaurus	1.71	2.42	$0.15\pm^{0.5}_{0.04}$	[g]
A3581	2.28	3.23	$0.6\pm^{1.7}_{0.4}$	[b]
A4038	/	/	/	
A4059	3.90	5.52	$0.3\pm^{1.0}_{0.2}$	[b]
AS1101	8.23	11.6	$0.9\pm^{1.5}_{0.6}$	[f]
AWM7	/	/	$0.3\pm^{0.3}_{0.1}$	
EXO0422-086	/	/	/	
Fornax	/	/	/	
Hydra A	0.272	0.385	$4\pm^{7}_{2}$	[b]
Virgo	0.46	0.651	$0.1\pm^{1.8}_{0.1}$	[d]
MKW3s	1.33	1.88	$0.3\pm^{0.4}_{0.2}$	[d]
MKW4	/	/	/	
HCG62	0.0827	0.117	$0.06\pm^{1.05}_{0.06}$	[b]
NGC5044	0.513	0.726	$0.20\pm^{0.06}_{0.05}$	[b]
NGC5813	0.0414	0.0586	$0.04\pm^{0.01}_{0.01}$	[b]
NGC5846	0.0722	0.10	$0.09\pm^{0.06}_{0.04}$	[b]

$L_{\mathrm{H}\alpha}$ is expressed in $10^{40}\,\mathrm{erg\,s^{-1}}$ and converted into $\dot{M}_{\mathrm{neb}}$ using equation 3.2. The references for $L_{\mathrm{H}\alpha}$ are [a] Donahue et al. [43], [b] Hamer et al. [79], [c] Crawford et al. [33], [d] Heckman et al. [83], [e] Wilman et al. [220], [f] Jaffe et al. [93], [g] Crawford et al. [34]. We use the star formation rates from [119]. All of the mass rates are expressed in $\mathrm{M_{\odot}yr^{-1}}$.

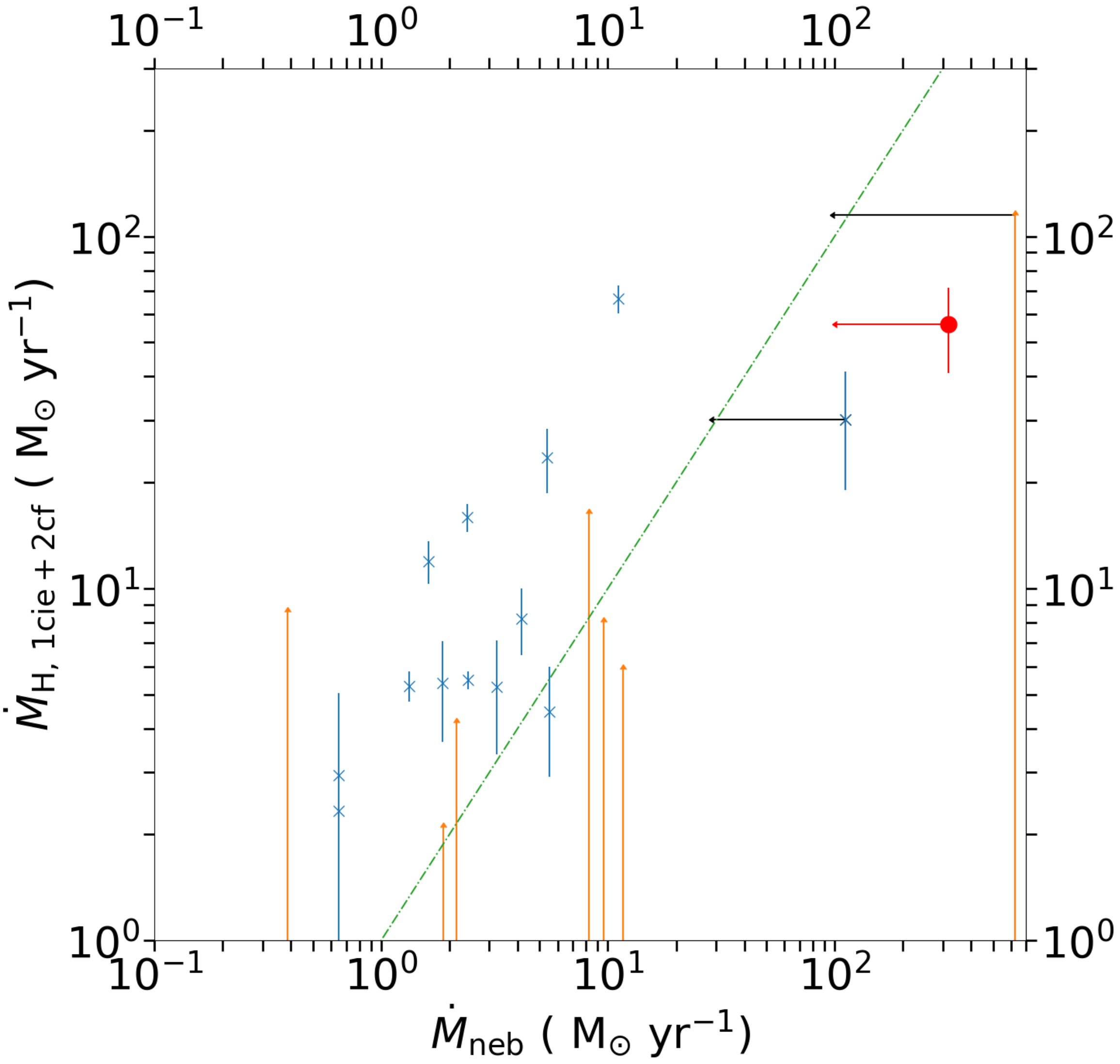

Fig. 3.8 The cooling rates $\dot{M}_{\mathrm{H,\,1cie+2cf}}$ in the two-stage model (between $T_{\mathrm{Max,\,1cie+2cf}}$ and 0.7 keV) against thermal energy required to sustain emission at longer wavelengths in filaments. The horizontal arrows give the extreme values of $\dot{M}_{\mathrm{neb}}$ when using $T_{\mathrm{Max,\,1cie+2cf}}$ instead of 0.7 keV in equation 3.2. For the Perseus cluster, the cooling rate is measured from the 99 per cent PSF spectrum in the one-stage model (red circle).

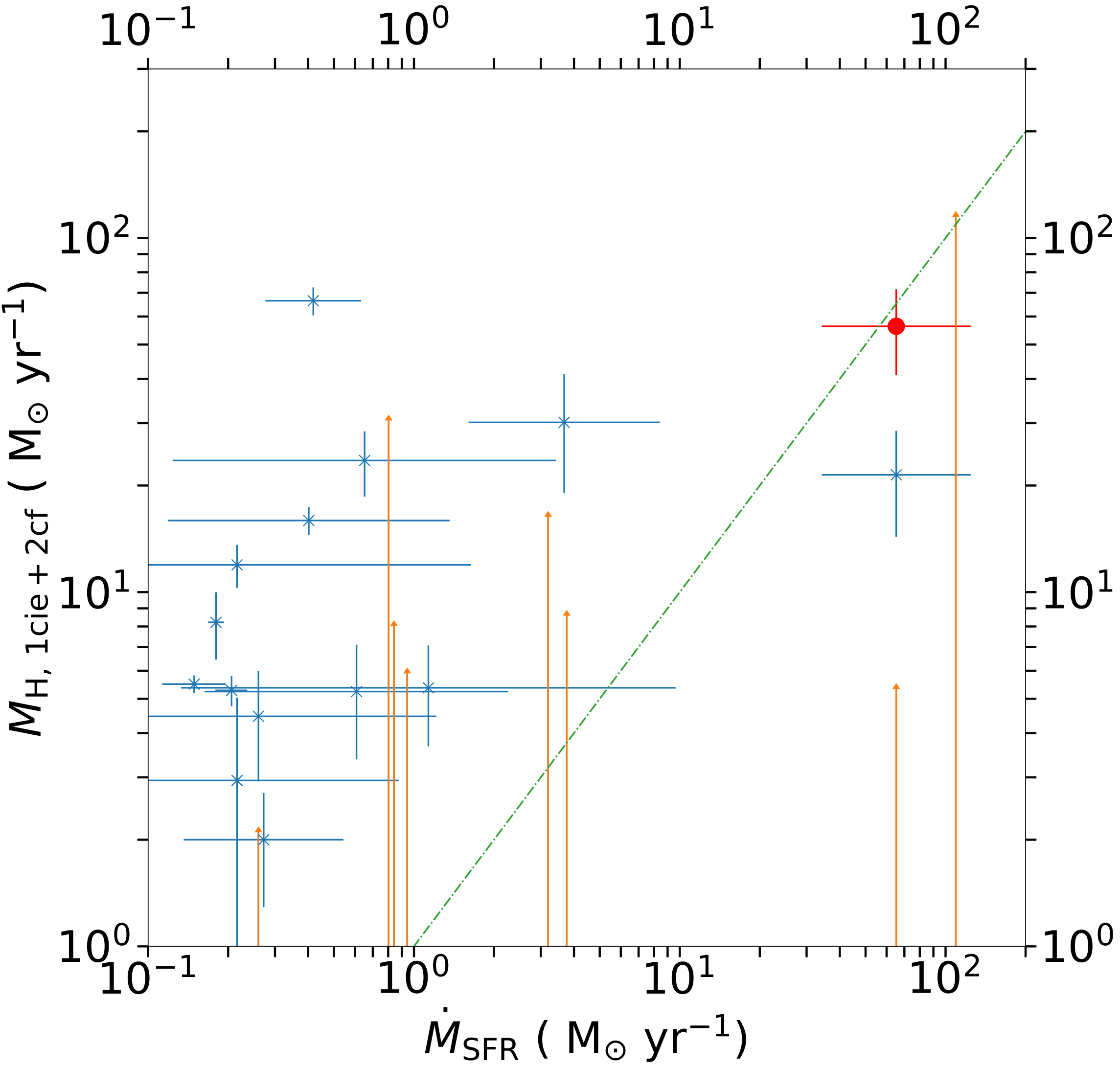

Fig. 3.9 X-ray cooling rates against observed star formation rates ([119] references therein). The red circles are the Perseus cluster with 99 per cent PSF spectrum. The cooling rate equals the star formation rate at the green dash-dot line.

- In the one-stage cooling flow model, all but one (AWM7) have $\dot{M}/\dot{M}_{\rm simple,3Gyr}$ less than 0.4 and 19 out of 22 clusters have the ratio less than 0.2.

- In the two-stage cooling flow model, we measured the cooling rates between the bulk temperature and 0.7 keV. We find that all clusters but one (A262) have cooling rates less than 70 per cent of $\dot{M}_{\rm simple,3Gyr}$, and 17 out of 22 clusters have cooling rates less than 30 per cent of $\dot{M}_{\rm simple,3Gyr}$.

- The residual cooling rates below 0.7 keV are less than 30 per cent of $\dot{M}_{\rm simple,3Gyr}$ in all clusters except AWM7, and only 10 per cent in 15/22 clusters. Therefore we find no strong evidence that clusters are rapidly radiatively cooling below 0.7 keV. which suggest that cooling flows appear to stop cooling at around 0.7 keV.

- The 2 *cie* model gives the cooler temperature between 0.5-0.9 keV in most clusters with the mean temperature of 0.78 ± 0.13 keV for those higher than 0.4 keV.

- In 9 out of 22 clusters, we have statistical evidence that the two-stage model provides a better spectral fit than the one-stage model (ΔC-stat$\geq$ 10 for 1 degree of freedom). For most clusters, we cannot determine whether the 2 *cie* model or the cooling flow models provide a significantly better spectral fit.

Since the soft X-ray emission is spatially associated with Hα nebulosity, we investigated the relation between the cooling rates above 0.7 keV and the total optical-UV luminosity. We find that if the gas continues to cool below 0.7 keV, the missing X-ray luminosity is more than sufficient to power the total optical-UV luminosity for low luminosity objects. For the 3 high luminosity objects, an inflow at a higher temperature is required if the X-ray cooling gas were powering the nebulae. Finally, we find the cooling rates between the bulk ICM temperature and 0.7 keV are 5 to 50 times higher than the observed star formation rates, which suggests that it is possible that the mass of the molecular gas reservoir is gradually increasing in most objects.

Chapter 4

The inner gas mass-temperature profile in the core of nearby galaxy clusters

Abstract

We present a mass-temperature profile of gas within the central 10 kpc of a small sample of cool core clusters. The mass of the hottest gas phases, at 1.5 and 0.7 keV, is determined from X-ray spectra from the XMM Reflection Grating Spectrometers. The masses of the partially ionised atomic and the molecular phases are obtained from published Hα and CO measurements. We find that the mass of gas at 0.7 keV in a cluster is remarkably similar to that of the molecular gas. Assuming pressure equilibrium between the phases, this means that they occupy volumes differing by 10^5. The molecular gas is located within the Hα nebula which is often filamentary and coincides radially and in position angle with the soft X-ray emitting gas.

4.1 Introduction

In Chapter 3, we have shown that the cool core of relaxed galaxy clusters has a temperature component of around 0.7 keV using a two-temperature model [113], while the hot ICM temperature is usually between 1.5 and 4 keV. In the most central region, O VII line emission has been revealed by [178, 156, 155], characterising cold gas with $kT < 0.2$ keV. The existence of gas at all X-ray temperatures suggests the inexact balance between the cooling and AGN heating. Some cooling is presumably necessary, if the central supermassive black hole is powered by gas accretion and a sustaining accretion-feedback loop. This would suggest that the multi-phasedness of gas (i.e. the mass-temperature profile) is an important step in completing the understanding of the feedback process.

A complete mass-temperature profile should contain at least four phases: the mass and volume dominating hot ionised gas, a soft X-ray emitting phase, an intermediate phase where the gas is partially ionised and the cold molecular gas. The bulk of the hot X-ray emitting ICM extends to over a few hundreds of kpc. In order to probe any 'soft' X-ray gas below the bulk temperature, we search for the strongest emission lines that peaks at low temperatures such as Fe XVII and O VII lines. These lines require the high spectral resolution of RGS, which has a limited spatial resolution in the cross dispersion direction. This means it is possible to resolve the core in nearby ($z < 0.1$) clusters.

Most cool core clusters are found to have an Hα emission nebula. The filamentary structure of the nebula spatially coincides with the soft X-ray components (e.g.[58, 57, 35, 34, 59, 62]). In the far UV, the O VI line emission indicates the presence of $10^{5.5} - 10^{6}$ K gas, just below the minimum temperatures in X-rays. It has been observed in just a few clusters, e.g. the Perseus cluster [18], A1795 [18, 122] and the Phoenix cluster [120, 121]. At the lowest temperatures, massive $10^{8} - 10^{10}\,\mathrm{M}_{\odot}$ reservoirs of cold ($\sim$ 50 K) molecular gas have been observed through CO lines in many clusters [46, 171, 173, 168, 145]. For most moderately cooling clusters with a cooling rate between a few to $\sim 10\,\mathrm{M}_{\odot}\,\mathrm{yr}^{-1}$, the bulk of the molecular gas is located within a few kpc of the centre. The molecular gas exists in a filamentary structure which is likely to form *in situ* from X-ray cooling (e.g. [130, 168]). Molecular hydrogen is also found at a higher temperature of $\sim$ 2000 K [219]. It is observed from molecular hydrogen lines at around 2 μm (e.g. [42, 218, 82]). However, it has significantly less mass than the cold molecular gas [218, 97].

Here, we select 9 nearby cool core clusters from the CHEERS Sample (see Chapter 3 [158, 39]), all of which have deep (>100 ks) RGS spectra. The source information is listed in Table 4.1. Optical line-emitting and molecular gas phases are observed in all 9 clusters, and are more precisely confined within a 10 kpc radius region than the full conventional cool core (e.g. 0.9 arcmin in Chapter 3).

We summarise the previous spatial analyses of the inner core of these 9 clusters. **2A0335+096** The optical image shows a 20 kpc bar feature [43], which is surrounded by the soft X-ray emitting gas below 1 keV [185]. The morphology of the molecular filament matches well to the peak of the optical emission [204]. **A262** The molecular gas is in the form of a compact disk around the nucleus [168, 145]. It spatially coincides with the optical image and the soft X-ray gas at ~0.5 keV [182]. All these components are surrounded by the soft X-ray gas at ~0.9 keV. **A496** The filaments in the Hα nebula do not extend beyond the presence of the X-ray cold front at 15 kpc [124]. **A2052** Two Hα emitting regions are separated by the X-ray cavity [125, 13]. The southern nebula covers the X-ray brightest cluster centre and two filaments extend along the soft X-ray emitting region. The northern Hα emitting region is located 8-15 kpc from the centre. This morphology is the same as the soft X-ray emitting gas at ~0.8 keV gas. **A3526** The core of the Centaurus cluster has a soft X-ray plume structure about 10 kpc across [186]. The same structure has also been observed in the optical and radio band (e.g. [192, 34, 198, 62]). The molecular gas is in clumps and filaments within the Hα nebula [145]. **A3581** The thin Hα filaments extend $\sim$ 13 kpc (30 arcsec) from the centre on both sides and surround the molecular gas which is less than 5 kpc across [145]. They align with the X-ray emitting gas below 1 keV [23]. **AS1101** Also known as Sérsic 159-03, the cluster has a $\sim$ 40 kpc long Hα filament which extends along the far UV emission [214, 126]. Most molecular gas is in small clumps of a few kpc within the Hα filaments [145]. **Perseus** The Hα nebula in the Perseus cluster is very extended [32, 54, 71], and coincides with the distributed molecular gas [172, 173]. These also correspond with the 0.5-1 keV gas [177]. It is found that the X-ray cooling flow down to 0.25 keV can produce the same flux as the Hα in filaments. Walker et al. [209] also found that the X-ray gas surrounding the Hα filaments can be modelled by a charge exchange component in addition to the standard thermal component. This provides a potential pathway for the energy transport between the hot ICM and the Hα filaments. **Virgo** Two major filaments of Hα and 0.7-0.9 keV X-ray emitting gas are found in the Virgo cluster, both of which are less than 2 kpc long [213, 212]. The molecular filament is very small (0.6 kpc) and less massive than any other clusters in our sample [189, 145].

This chapter contains 4 sections. The observation and data reduction is described in section 4.2. The spectral analysis and discussion are shown in section 4.3. Section 4.4 concludes this chapter.

4.2 Data

The XMM-Newton data were downloaded from the XSA archive. We followed the RGS data reduction procedure described in section 2.1.2 with the *XMM-Newton* Science Analysis System v 16.1.0. The background is subtracted using template background files based on count rates in CCD 9. To spatially resolve extended sources in RGS, we draw a long slit in the dispersion direction. The width of the slit is tuned by varying the fraction of PSF included in the cross dispersion direction. For a core radius of 10 kpc, the slit width must be 20 kpc, containing the inner cool core as well as hot ambient ICM. Table 4.1 lists the angular width for such a slit and the corresponding cross dispersion PSF in our sample. For the most distant cluster AS1101, the 20 kpc slit translates to an angular width of 0.305 arcmin, which is still safe to be resolved by RGS. The spectra from different observations are stacked through task *rgscombine*, where the products were converted to SPEX usable format via task *trafo*. These clusters have at least 10000 counts in the 10 kpc stacked RGS spectrum.

Spatial line broadening dominates over the intrinsic velocity for nearby ($z < 0.1$) objects [158] following the RGS dispersion law (see section section 1.6.1). Surface brightness profiles are extracted from the MOS 1 images with the same slit size as the RGS spectra. These profiles are used spatial broadening (*lpro*) model in the SPEX fitting package.

We use SPEX version 3.05.00 for spectral analysis with its default proto-Solar abundances of [114]. The first order spectra are only fitting in the 7-28 Å (0.44-1.76 keV) wavelength band, while the data is binned by a factor of 3. This gives around 700 energy bins, which guarantees > 15 counts per bin on average. We therefore adopt C-statistics in spectral fitting. All the measurements include 1σ ($\Delta C = 1$) uncertainty, unless otherwise stated. The upper limits are quoted at 2σ ($\Delta C = 2.71$) level.

We further set O, Ne and Fe as free parameters, and couple Mg to Ne and other metals to Fe. The spectra are modelled by collisional ionisation equilibrium components (*cie*), using multiple combinations of *cie* in SPEX which calculates X-ray emission from a collisionally-ionised plasma at a given temperature T and emission meausure $EM = n_{\mathrm{e}} n_{\mathrm{H}} V$. Each *cie* component is modified by redshift, galactic absorption with a cold temperature of 0.5 eV and solar abundances [157]. It is then convolved with the line broadening (*lpro*) component in SPEX. These settings are the same as Chapter 3 except metallicity [113].

Table 4.1 Targets, observations and known properties.

Name	Redshift [a]	Observations	Total clean time (ks) [b]	$N_{H,tot}$ [c]	$\theta = 20\,\mathrm{kpc}/D_A$ (arcmin) [d]	xPSF [e]
2A0335+096	0.0363	0109870101/0201 0147800201	137	30.7	0.475	74
A262	0.0174	0109980101/0601 0504780101/0201	113	7.15	0.968	90.5
A496	0.0329	0135120201/0801 0506260301/0401	132	6.12	0.522	77.5
A2052	0.0355	0109920101 0401520301/0501/0601/0801 0401520901/1101/1201/1301/1601/1701	123	3.03	0.485	74.5
A3526	0.0114	0046340101 0406200101	159	12.2	1.47	94.5
A3581	0.023	0205990101 0504780301/0401	147	5.32	0.737	86.5
AS1101	0.0580	0147800101 0123900101	100	1.17	0.305	56
Perseus	0.0179	0085110101/0201 0305780101	181	20.7	0.942	90
Virgo	0.0043	0114120101 0200920101	190	2.11	4.06	99

(a) The redshifts are taken from the NED database (https://ned.ipac.caltech.edu/). (b) RGS net exposure time. (c) Total hydrogen column densities in $10^{20}\,\mathrm{cm}^{-2}$ (see http://www.swift.ac.uk/analysis/nhtot/; [104, 217]). (d) The angular width of a fixed 20 kpc RGS slit region at the redshift of the source. (e) The percentage of the PSF included in the cross dispersion direction in RGS which corresponds to the angular size in (d).

4.3 Results and discussion

4.3.1 Mass measurement of X-ray components

It was recently shown that clusters in our sample can be modelled by a two-component model with free temperatures (see e.g. [39, 113]). The Fe XVII lines are observable in these clusters, which indicate the temperature of the cooler component is at around 0.7 keV. On the other hand, using RGS spectroscopy means that a fraction of hot and massive gas is projected along the 20 kpc slit, which can have a higher temperature than the two-component model. To effectively introduce a third temperature component that accounts for the hotter gas while reducing degeneracy in the emission measure, we fix the temperature of three components at 3, 1.5 and 0.7 keV. The temperature of these components is separated by at least 0.8 keV and hence they represent distinct gas phases. The O VII signature is weak in our sample. We find a further component at 0.2 keV usually gives an upper limit. Resonant scattering of Fe XVII lines also leads to degeneracy in the emission measure of the 0.2 and 0.7 keV components as found in some clusters in the CHEERS sample [158, 113]. Therefore we only use the three-component model in this work.

To estimate the gas masses, we assume that the inner core is in hydrostatic equilibrium, and that the different gas phases are in pressure equilibrium with each other at any chosen radii. We interpolate the radial mean density and temperature profiles from the ACCEPT catalogue [26] to calculate the pressure at 10 kpc, within which most of the gas at 1.5 and 0.7 keV lies. The ACCEPT catalogue contains projected temperature profiles. Panagoulia et al. [147] and Lakhchaura et al. [106] have shown that projected temperatures are higher which causes higher core entropy within $\sim$ 10 kpc. This has a similar effect on pressure. Hogan et al. [88] showed that, in A496, the deprojected temperature at 10 kpc is $\sim$ 10 per cent lower than the projected temperature while the density is consistent with that reported in the ACCEPT catalogue. They further showed that the shape of the radial density profile is similar to four other cool core clusters, where the density varies as $1/r^{0.6}$ and the deprojected temperature as $r^{0.3}$. This means that, if the radial dependence of temperature and density holds in general in the rest of our sample, the pressure $n_e T$ typically rises by a factor of 1.6 to 2.2 at 2 kpc from the value at 10 kpc and is even higher at the innermost 1 kpc. Exact scaling of radial profiles is often not possible due to the complexity of the inner structure of the core. Different gas phases are neither spherically symmetric nor completely volume-filling. For simplicity, we estimate the gas mass using the pressure at 10 kpc in this work. For a given temperature, the mass of the X-ray emitting component is proportional to the ratio of its emission measure to the pressure. The net effect is that our masses may be overestimated by a factor of up to 2.

The mass-temperature profile is seen in Fig. 4.1 (and detailed in Table 4.2). The RGS slit only selects a fraction of the 3 keV gas, so the mass of the 3 keV component is only a lower limit. We see that, for the most relevant components at 1.5 and 0.7 keV, the gas mass decreases by at least an order of magnitude towards lower temperatures. In 6 out of 9 clusters, the ratio of the mass of these two components is between 20 and 60, with two more with a ratio of 10. This pattern is likely intrinsically regulated, whereas the reason for the connection is unclear. The comparison between the gas mass and corresponding emission measure for either the 1.5 or 0.7 keV component also shows that the mass scatter is smaller than that of the emission measure.

The 1.5 and 0.7 keV components do not always have the same spatial extent. From Chandra analysis, the 0.7 keV gas exhibits spatial coincidence with the 1.5 keV component in the Centaurus cluster [181, 186]. However, the 0.7 keV gas occupies a significantly smaller region in A3581 [95], Virgo [213] and Perseus [59], that region mainly lies within the extent of the next hotter component. Although the angle-averaged temperature profile of the hot gas drops steadily inward within a cool core, the gas is formed of non-spherical phases that occupy complex shapes. Some of these shapes may be due to the AGN bubbling process. The 0.7 and 1.5 keV components are not volume-filling in a radial sense.

Li et al. [111] has attempted to measure the spectrum of turbulence in the hot gas of several cool core clusters by using Hα velocity measurements of cold gas. This assumes that the cold gas is a tracer in the hot gas. Our results here, however, show that the *total* mass of the cold gas and the hot gas below 1 keV, (typical of the hot gas around the Hα filaments) are comparable. This must surely be taken into consideration in calculations of turbulence and may contribute to the steepness of the velocity function at small radii.

Table 4.2 Mass of different temperature components

Name	M_{500}	$M_{\rm mol}$	$M_{{\rm H}\alpha}$	$M_{\rm X,0.7\,keV}$	$M_{\rm X,1.5\,keV}$	$M_{\rm X,3.0\,keV}$	Reference
2A0335+096	3.45×10^{14}	$1.2\pm0.2\times10^{9}$	8.71×10^{7}	$1.8\pm0.2\times10^{9}$	$9.1\pm0.1\times10^{10}$	$>1.5\times10^{9}$	[1,2,5]
A262	1.19×10^{14}	$3.62\pm0.02\times10^{8}$	4.71×10^{6}	$7.8\pm0.8\times10^{8}$	$1.7\pm0.3\times10^{10}$	$>3.2\times10^{10}$	[1,3,6]
A496	2.91×10^{14}	$4.0\pm0.9\times10^{8}$	4.04×10^{6}	$1.8\pm0.4\times10^{8}$	$9\pm2\times10^{9}$	$>6.4\times10^{10}$	[3,7]
A2052	2.49×10^{14}	$2.8\pm0.4\times10^{8}$	4.49×10^{6}	$3\pm1\times10^{8}$	$6.6\pm0.6\times10^{10}$	$>1.7\times10^{10}$	[1,7]
A3526	1.62×10^{14}	1.04×10^{8}	3.26×10^{6}	$4.0\pm0.2\times10^{8}$	$1.9\pm0.1\times10^{10}$	$>6.3\times10^{9}$	[2,8]
A3581	1.08×10^{14}	5.55×10^{8}	9.46×10^{6}	$6.2\pm0.5\times10^{8}$	$3.6\pm0.1\times10^{10}$	$>4.5\times10^{8}$	[2,7]
AS1101	2.83×10^{14}	1.06×10^{9}	1.12×10^{7}	$4\pm1\times10^{8}$	$<1.4\times10^{10}$	$>1.6\times10^{11}$	[2,9]
Perseus	6.15×10^{14}	1.06×10^{10}	1.64×10^{8}	$1.30\pm0.05\times10^{9}$	$1.8\pm0.1\times10^{10}$	$>1.2\times10^{11}$	[4,10]
Virgo	N/A	5.06×10^{5}	2.31×10^{5}	$1.26\pm0.03\times10^{8}$	$1.26\pm0.01\times10^{10}$	$>8.2\times10^{6}$	[2,10]

The masses are in $M_\odot$. M_{500} are taken from the MCXC catalog [153]. The molecular masses are taken from [1] Russell et al. [168] [2] Olivares et al. [145] [3] Salomé and Combes [171] [4] Salomé et al. [173]. The references for Hα emission are [5] Donahue et al. [43] [6] Crawford et al. [33] [7] Hamer et al. [79] [8] Crawford et al. [34] [9] Jaffe et al. [93] [10] Heckman et al. [83].

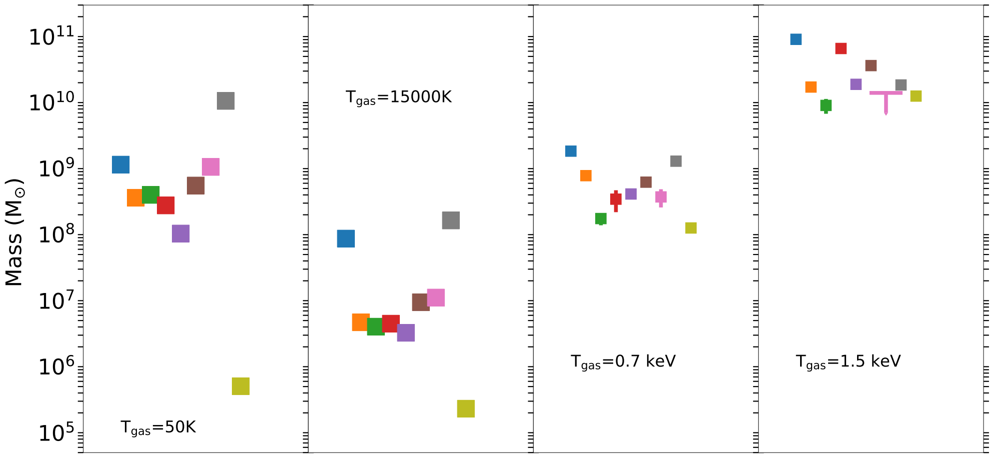

Fig. 4.1 Visualisation of mass-temperature profile presented in Table 4.2, with the coolest molecular gas from the left and the hot ambient ICM at 1.5 keV from the right. Within each panel, we shift the data points horizontally for clarity and the clusters are presented in the same order as the first column in Table 4.2, i.e. 2A0335+096 is on the left and Virgo is on the right.

4.3.2 Core cooling time

The radiative cooling time at 10 kpc is calculated using the definition

$$t_{\rm cool} = \frac{3(n_{\rm e}+n_{\rm i})k_{\rm B}T}{2n_{\rm e}n_{\rm i}\Lambda}, \tag{4.1}$$

where $n_{\rm e}$ and n_i are electron and ion densities in cm^{-3} and Λ is the cooling function. We assume the cooling process is isochoric at this radius, and hence 3/2 is required. For a fully ionised plasma, n_H is effectively 0.857 times the electron density if we assume the hydrogen mass fraction is 75 per cent. The cooling function is determined for the metallicity from the best fit model in SPEX. It is the ratio of the total luminosity (we calculate between 0.001 and 1000 keV) to the emission measure.

The cooling times are listed in Table 4.3 for gas at 0.7 and 1.5 keV. We can compare our results at 1.5 keV with the cooling time at 10 kpc in [26]. Our values are within 40 per cent lower in 5 clusters and more than a factor of 2 lower in the other half of the sample. The difference is mainly due to the ICM temperature being higher than 1.5 keV. The cooling time can be 2 times longer for a gas temperature of 2 keV. This temperature is commonly seen in the ICM of clusters at 10 kpc in [26]. The radial cooling time profile shows that it

Table 4.3 Pressure, cooling time and residual cooling rate of X-ray components

Name	$n_{\mathrm{e}}T$	$t_{\mathrm{cool,0.7\,keV}}$	$t_{\mathrm{cool,1.5\,keV}}$	$\dot{M}_{\mathrm{C,\,1cie+2cf}}$	τ_{x}
2A0335+096	0.12	42	230	12±4	150
A262	0.027	140	910	0.9±0.3	900
A496	0.097	34	230	<1.92	>90
A2052	0.050	99	550	<1.32	>230
A3526	0.050	57	420	0.6±0.1	700
A3581	0.032	120	770	2.1±0.9	290
AS1101	0.098	35	240	<5.09	>80
Perseus	0.18	25	148	31±2	40
Virgo	0.042	88	570	<0.07	>1800

The $n_{\mathrm{e}}T$ pressure at 10 kpc is in keVcm^{-3} and the cooling time is in Myr. $\dot{M}_{\mathrm{C,\,1cie+2cf}}$ is the residual cooling rate in $\mathrm{M}_{\odot}\,\mathrm{yr}^{-1}$ measured between 0.7 and 0.01 keV from Liu et al. [113]. τ_{x} is the lifetime in Myr of the X-ray component at 0.7 keV cooling at the rate of $\dot{M}_{\mathrm{C,\,1cie+2cf}}$.

can drop by a factor of a few at 2 kpc albeit at a slightly lower temperature. Hence, the true cooling time at the fixed temperatures might be lower if the gas is located further in than 10 kpc. Notice that the interpolation of the pressure is the major source of uncertainty in the cooling time in Perseus and A2052. It is difficult to estimate the density at 10 kpc due to the presence of X-ray cavities (e.g. the Perseus cluster [56]).

We can estimate the lifetime of the cool gas at 0.7 keV assuming it is cooling at the rate of the residual cooling flow $\dot{M}_{\mathrm{C,\,1cie+2cf}}$. We find that most of these components are long-lived (see Table 4.3). The lifetime are of course longer if AGN heating acts on these components. Note that in the Perseus cluster, we measured a higher cooling rate from a larger 99 per cent PSF core spectrum [113].

4.3.3 Mass of optical line-emitting ionised gas

The optical line-emitting gas is of interest because of the spatial coincidence with the soft X-ray emitting gas at around 0.7 keV [57]. The gas is partially ionised in this phase, which can be traced by Hα emission. Here, we estimate the approximate gas mass from the observed Hα luminosity $L_{\mathrm{H}\alpha}$. The mass of the Hα filaments is

$$M_{\mathrm{H}\alpha} = \frac{\mu_e m_p n_e L_{\mathrm{H}\alpha}}{j_{\mathrm{H}\alpha}}, \tag{4.2}$$

where $\mu_e m_p$ is the mean mass per electron, n_e is the electron number density. $j_{\mathrm{H}\alpha}$ is the emissivity of the Hα line, and is calculated from

$$j_{\mathrm{H}\alpha} = 1.3 \times 10^{-23} n_{\mathrm{e}} n_{\mathrm{H}} T^{-1/2} log(I_H/kT)\,\mathrm{erg\,s^{-1}\,cm^{-3}}, \tag{4.3}$$

where T is the temperature in K and I_H is the ionisation energy of hydrogen. The emissivity of the Hα line varies strongly with temperature. We assume the Hα filaments have a temperature of 15000 K estimated from its peak emissivity. We use the pressure at 10 kpc in general. In the Virgo and Centaurus clusters, the Hα nebula is smaller than 10 kpc in radius [34, 213, 78]. We hence use the pressure at 1 kpc for Virgo, and 5 kpc for Centaurus. Note that in A262, the Hα luminosity is taken from Crawford et al. [33] which used long slits. The true luminosity can therefore be higher if the filaments of the clusters are more extended than the slit.

We find that the optical line-emitting gas is two orders of magnitude less massive than the X-ray components in most clusters. This mass estimate is consistent with the literature e.g. Virgo [191]. Note that since the Perseus cluster has a highly extended Hα nebula [32, 54], the average density of the filaments might be lower than the value at 10 kpc. This suggests that the Hα nebula is likely more massive than our estimate in Perseus. O VI, which emits in the FUV, is generally not available for our sample. Our estimate of gas masses ignores photoelectric absorption by cooler gas and reddening by dust. This will be difficult to determine until we have much detailed spatial information.

4.3.4 Connection between soft X-ray and molecular gas

The most important finding of this work is the comparison between the mass of the soft X-ray gas and the molecular gas. The recent ALMA observations showed that cold ($\sim$ 50 K) molecular gas is located within the Hα nebula [145, 168]. It is therefore also within the soft X-ray emitting region albeit more compact. The molecular gas mass is calculated from the integrated CO intensity by adopting the Galactic value of CO-to-H_2 (X_{CO}) conversion factor and typical CO line ratios in Brightest Cluster Galaxies. Since CO is optically thick to radiation, there is an uncertainty in the conversion factor. From a ^{13}CO detection in RXJ0821+0752, Vantyghem et al. [202] suggested that using the Galactic value for X_{CO} likely overestimates the molecular mass by a factor of 2. Note that ALMA does not detect faint outer molecular filaments which only have a small fraction of the mass. A spread of molecular mass is seen in our sample. The molecular gas in the Perseus cluster is 4 orders of magnitude more massive than that of the Virgo cluster.

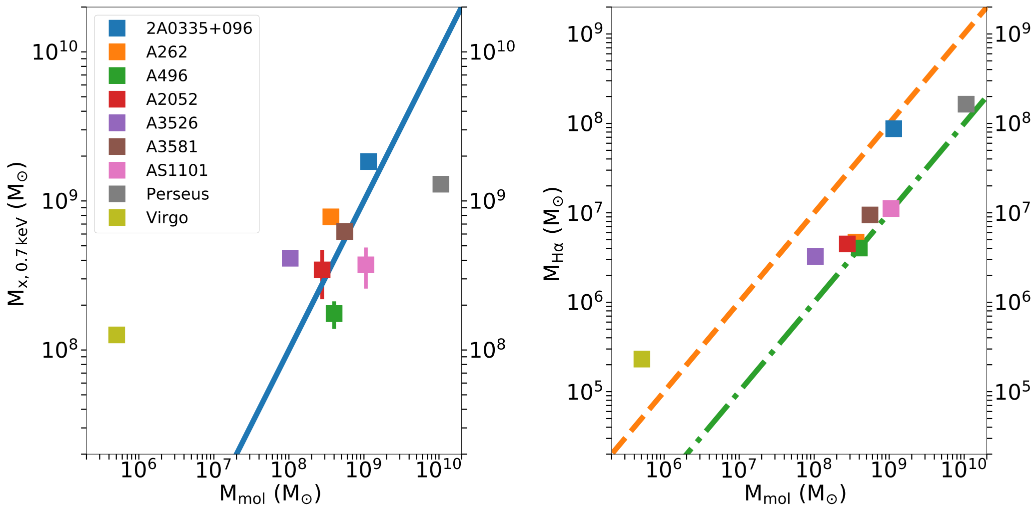

Fig. 4.2 Left: The X-ray emitting gas against molecular mass. The blue line indicates where the molecular mass would match the soft X-ray mass. Right: The mass of Hα component against molecular mass. The orange dash line has a constant $M_{\mathrm{H}\alpha}/M_{\mathrm{mol}}$ ratio of 0.1 and the green dash-dot line has a ratio of 0.01. The uncertainties in the mass of molecular and Hα emitting gas is smaller than the marker size.

The comparison between the 0.7 keV and molecular gas mass is seen in Fig. 4.2. We show that the soft X-ray and molecular gas have similar masses in most clusters. This suggests that these two gas phases are strongly linked. However, it is not clear to us why this should be the case. As we have seen, if mass exchange from the soft X-ray emitting gas is responsible, it takes more than $\sim 10^{8}$ yr by radiative cooling in most clusters. From spatially-resolved images, soft X-ray gas has a much larger extent than the molecular phase which is often only a few arcsec across (e.g. [168]). At the same time, assuming both phases are in pressure equilibrium, the volume of the gas would be proportional to its temperature. It requires that the soft X-ray component occupies 10^{5} times larger volume. Therefore the connection between these gas phases is not simple.

The Virgo and Perseus clusters are exceptions in our sample. For Virgo, the 0.7 keV gas mass is 250 times higher than the molecular mass. It has been suggested the molecular gas could have been destroyed or excited by X-ray shocks, or interacted with the radio lobe [189]. The deposition rate of the molecular gas can also be reduced by star formation, since the star formation rate is comparable to the X-ray cooling rate [113]. For the Perseus cluster, the molecular mass is 8 times more massive than 0.7 keV gas. Given the large systematic uncertainty in the molecular mass measurements, the difference in the mass of the two phases

Table 4.4 Scale of different gas phase in A3581.

Phase	Mass ($M_\odot$)	T (K)	n_e (cm^{-3})
Soft X-ray	6.2×10^8	8.2×10^6	0.046
Hα	9.46×10^6	1.5×10^4	25
Molecular	5.55×10^8	50	7500

is likely only a factor of 4. It can in part be explained by the fact that the molecular filaments are more extended than the 10 kpc core [173].

Since we assume gas of different phases are in pressure equilibrium, it is important to consider the physical scale of different phases if they have similar masses. We use the example of a typical cool core cluster A3581 with moderate X-ray emitting cool gas of $\sim 10^9 M_\odot$. Pressure equilibrium suggests that the volume ratio of the gas will be the same as the temperature ratio. It means that the molecular gas occupies about 5 orders of magnitude smaller volume than the 0.7 keV gas. If the mass is put in a spherical ball with a constant density, we can calculate the radius of that sphere. We list the details in Table 4.4. The size of the sphere of the molecular gas is less than 100 pc, even though it extends over 5 kpc [145]. The atomic and molecular gas is observed to be in many thin filaments at the highest resolution (e.g. HST image from [54, 62]). The spatial coincidence of different gas phases hence suggests they are intermingled. A magnetic field is required to give integrity to the filaments (e.g [62]), with pressure equilibrium implying $B \sim 50\mu G$. Note that the resolved HST filaments probably contain many much smaller threads [62].

4.4 Conclusion

In this chapter, we studied the mass-temperature profile of the gas in the inner regions of nearby cool core clusters of galaxies inspired by the similar morphology of the soft X-ray emitting gas, the optical nebula as well as the molecular gas. For the X-ray components, we used a three-temperature model to describe the XMM-*Newton* RGS spectra of the core of 9 nearby clusters. The gas mass is calculated from the emission measure by assuming pressure equilibrium at the selected radii. We showed that the X-ray mass-temperature profile is similar among these clusters particularly in the 1.5 and 0.7 keV components. The total X-ray mass below 1 keV is found to be comparable to that of the molecular gas in 7 out of 9 clusters. Although the Hα nebula is more closely aligned with the soft X-ray components, it only has 0.1-1 per cent of the mass of the other phases. Future models of cluster cores should consider using these relations. The molecular gas occupies by far the smallest volume in the form of thin magnetized filaments.

Chapter 5

Suppressed cooling and turbulent heating in the core of X-ray luminous clusters RXCJ1504.1-0248 and Abell 1664

Abstract

We present the analysis of *XMM*-Newton observations of two X-ray luminous cool core clusters, RXCJ1504.1-0248 and Abell 1664. The Reflection Grating Spectrometer reveals a radiative cooling rate of $180\pm40\,\mathrm{M_\odot\,yr^{-1}}$ and $34\pm6\,\mathrm{M_\odot\,yr^{-1}}$ in RXCJ1504.1-0248 and Abell 1664 for gas above 0.7 keV, respectively. These cooling rates are higher than the star formation rates observed in the clusters, and support simultaneous star formation and molecular gas mass growth on a timescale of 3×10^8 yr or longer. At these rates, the energy of the X-ray cooling gas is inadequate to power the observed UV/optical line-emitting nebulae, which suggests additional strong heating. No significant residual cooling is detected below 0.7 keV in RXCJ1504.1-0248. By simultaneously fitting the first and second order spectra, we place an upper limit on turbulent velocity of 300 $\mathrm{km\,s^{-1}}$ at 90 per cent confidence level for the soft X-ray emitting gas in both clusters. The turbulent energy density is considered to be less than 8.9 and 27 per cent of the thermal energy density in RXCJ1504.1-0248 and Abell 1664, respectively. This means it is insufficient for AGN heating to fully propagate throughout the cool core via turbulence. We find the cool X-ray component of Abell 1664 ($\sim$0.8 keV) is blueshifted from the systemic velocity by 750^{+800}_{-280} $\mathrm{km\,s^{-1}}$. This is consistent with one component of the molecular gas in the core and suggests a similar dynamical structure for the two phases. We find that an intrinsic absorption model allows the cooling rate to increase to $520\pm30\,\mathrm{M_\odot\,yr^{-1}}$ in RXCJ1504.1-0248.

5.1 Introduction

The inner core region of relaxed clusters of galaxies shows a complex structure of different gas phases. The short central cooling time indicates a massive cooling flow (e.g. [2, 117, 123]), while only less than 10 per cent of the predicted rate is observed [100, 151, 113]. This requires a heating process that needs an energy source and an efficient mechanism to transport the energy throughout the core. The central AGN can interact with its host environment. For cool core clusters at a low Eddington fraction, AGN feedback operates in the kinetic mode, where gas accretion generates powerful relativistic jets which inflate bubbles [51, 128]. Bubbles rise buoyantly with a mechanical power similar to the cooling rate in the absence of heating (e.g. [31, 12, 45, 162, 85]). The temperature map of clusters is roughly isotropic, which suggests heating occurs away from the jet axis. The mode of such energy transfer is still under debate. While the energy can be propagated azimuthally by gravity waves, it can not transport the energy radially. An alternative mode of powerful sound waves can provide the required velocity for radial energy transport [56, 63], but a suitable energy dissipation mechanism needs to be developed. Turbulent heating of the gas has also been of interest for this purpose. The Hitomi Soft X-ray Spectrometer (SXS) made an accurate measurement of the level of turbulence at 164 ± 10 km s^{-1} in the Perseus cluster [84]. The energy density of isotropic turbulence is only 4 per cent of the thermal energy density there which is too low to reach the full cooling core. Turbulence alone is insufficient to offset radiative cooling.

It is possible to measure an upper limit to the level of turbulence from line width in the RGS spectra (e.g. [184, 183, 180]). Since the RGS is a slitless spectrometer, the spectral lines are also broadened by the spatial extent of the source following the RGS dispersion law. It contributes significantly to the total line width in nearby sources [158]. This artificial broadening can be corrected for by using the surface brightness profile of the EPIC image (e.g. [7, 154]). A tight 90 per cent upper limit of 244 km s^{-1} is then found in A1835 and 246 km s^{-1} in A2204 [7]. These limits are similar to the level of turbulence in the Perseus cluster found by the Hitomi Collaboration et al. [84].

Another interesting feature is the possible connection between the Hα emission and soft X-ray gas. In Chapter 3, we have shown that the thermal energy of the radiative cooling gas is sufficient as the power source for the optical/UV nebula in clusters with a cooling rate below $\sim$10 M$_\odot$ yr^{-1}, but the most luminous clusters are likely powered by hotter gas or otherwise ([113]). Churazov et al. [30] argued that buoyant bubbles stretch fluid elements to form gaseous filaments with amplified magnetic field. The release of magnetic energy allows dissipation into filaments. Alternatively, Hα filaments can also powered by Cosmic Rays [170].

The origin and fate of the molecular gas is another mystery. A massive cold molecular gas reservoir is often present in the core and seen by CO lines from a component at $\sim$ 50K and/or NIR H$_2$ lines at $\sim$ 2000K [46, 47, 171, 221, 145, 168]. Star formation of up to hundreds of M$_\odot$ yr^{-1} in the most massive clusters is a major consumer of the molecular gas deposit. At the higher rates, the observed molecular gas reservoir will be depleted by star formation in 10^8-10^9 yr if not replenished (e.g. [160]). On the other hand, this timescale is comparable to the central radiative cooling time, which suggests the molecular gas cools from the hot X-ray atmosphere (e.g. [168]). The molecular gas filaments have a smaller spatial extent and are often embedded in the Hα nebula and hence the soft X-ray gas (e.g.

[145, 168]). Surprisingly, the RGS spectra have revealed that the molecular gas mass is comparable to the X-ray gas mass emitting below 1 keV in a sample of nearby luminous clusters, e.g. 2A0335+096, A2052, A3581 (see Chapter 4 [112]). These two gas phases are likely intermingled and the structural integrity is held by magnetic fields.

Both of our targets, RXCJ1504 and A1664, are remarkably luminous in both the X-ray and optical bands, and possess a massive molecular gas reservoir. RXCJ1504 is one of the most massive low redshift cool core clusters at $z = 0.2153$ with $M_{500} = 1.25 \times 10^{15} \mathrm{M}_{\odot}$ [153] and a high X-ray bolometric luminosity of 4.1×10^{45} $\mathrm{erg\,s^{-1}}$ and a classical cooling rate [1] of 1500-1900 $\mathrm{M}_{\odot}\,\mathrm{yr}^{-1}$ [16]. Giacintucci et al. [72] discovered a minihalo of 140 kpc in radius at the centre of the cluster confined to the cool core. This suggests a tight connection between the X-ray emitting cool core and the relativistic plasma. It also has an Hα luminosity of 3.2×10^{43} $\mathrm{erg\,s^{-1}}$ making it one of the most luminous optical nebulae. The observed UV flux indicates a strong star formation rate of 130 $\mathrm{M}_{\odot}\,\mathrm{yr}^{-1}$ [144]. The inner 5 kpc of the cool core contains most gas from the massive molecular gas reservoir of $1.9 \pm 0.1 \times 10^{10}$ $\mathrm{M}_{\odot}$ [203]. The kinematics of the molecular gas is complex as revealed by ALMA CO observations (e.g. [203]). Vantyghem et al. [203] infer a turbulent velocity of 335 ± 15 $\mathrm{km\,s^{-1}}$ for that gas and the central molecular filament shows a velocity range of $\sim$260 $\pm$11 $\mathrm{km\,s^{-1}}$ in RXCJ1504. A dynamically young gas structure also shows an offset velocity of $\sim$ -250 $\mathrm{km\,s^{-1}}$ from the rest of the gas in the BCG.

A1664 is one of the first cool core clusters in which CO emission was observed (e.g. [46]). It has a redshift of $z = 0.1283$ with $M_{500} = 4.06 \times 10^{14} \mathrm{M}_{\odot}$ [153]. It has a classical cooling rate of 100 ± 10 $\mathrm{M}_{\odot}\,\mathrm{yr}^{-1}$ [119], and hosts a bright Hα nebula of 1.5×10^{42} $\mathrm{erg\,s^{-1}}$ [220]. The star formation rate is estimated to be 14 $\mathrm{M}_{\odot}\,\mathrm{yr}^{-1}$ in IR or 4.3 $\mathrm{M}_{\odot}\,\mathrm{yr}^{-1}$ in FUV [142]. The BCG has a total molecular gas mass of $1.1 \pm 0.1 \times 10^{10}$ $\mathrm{M}_{\odot}$ [167]. The molecular gas is also seen disturbed within 10 kpc of the core [167]. The CO(1-0) and CO(3-2) lines are well resolved into two Gaussian components with a velocity difference of $\sim$590 $\mathrm{km\,s^{-1}}$. On a larger scale of $\sim$50 kpc, cold fronts are observed in the X-ray atmosphere produced by sloshing [20], and it is possible that core sloshing can affect lower temperature gas. If the X-ray and molecular gas are related, they are likely sharing a similar velocity structure (for theoretical modelling, see e.g. [70]).

At the present time, the *XMM*-Newton RGS can place the most accurate constraint on the velocity of the soft X-ray emitting gas. The dispersive nature of the RGS means the spectral resolution is improved with lower photon energies, and surpasses the Hitomi/XRISM

---

[1] In this work, we use the definition of the classical cooling rate as the ratio of gas mass enclosed in a radius with a radiative cooling time of 7.7 Gyr to the cooling time (see e.g. [119]).

resolution below 1 keV (12.4 Å) for point-like and extended sources below 1 arcmin of spatial extent.

In this chapter, we present recent deep *XMM*-Newton/RGS observations of these two X-ray luminous clusters: RXCJ1504.1-0248 (RXCJ1504) and Abell 1664 (A1664). We measure radiative cooling rates and place constraints on turbulent velocity at the 90 per cent confidence level, which is an important proxy for heat propagation. The structure of this chapter is as following. Section 5.2 provides observational details of the clusters and the data reduction procedures. Section 5.3 introduces the spectral models used to measure the cooling rate and place the upper limit on turbulent velocity. Section 5.4 discusses the implications of our results and we try to correct for intrinsic absorption of the clusters.

5.2 Observations and data reduction

The *XMM*-Newton observatory observed each of the clusters RXCJ1504 and A1664 for two orbits (PI Fabian). The observational details are listed in Table 5.1. RXCJ1504 was observed between 15-Aug-2019 and 17-Aug-2019 and between 09-Feb-2020 and 10-Fen-2020. The offset of the roll-angle of the pointings between observations is 171.65 degrees. A1664 was observed between 28-Jan-2020 and 29-Jan-2020 and between 30-Jan-2020 and 31-Jan-2020. The offset of the roll-angle of the pointings is 0.65 degrees.

Here we use data from the RGS and the EPIC onboard *XMM*-Newton. We follow the standard data reduction procedure described in section 2.1 with the *XMM-Newton* Science Analysis System v 17.0.0. We extract both the first and second order RGS spectra by the SAS task *rgsproc*. The second order spectra possess twice the spectral resolution and hence are used for turbulent velocity measurements. We set the *xpsfincl* mask to include 90 per cent of the point spread function, equivalent to a narrow 0.9 arcmin region. We use template background files based on count rates in CCD 9 to produce background-subtracted spectra. To achieve the highest S/N ratio, the RGS 1 and 2 spectra of both observations are stacked using the task *rgscombine* and then processed by the task *trafo* to be analysed by SPEX.

We check that the pointing of both observations is consistent to avoid spurious broadening of emission lines. The spatial broadening of the RGS spectra is corrected by the surface brightness profile of the MOS image. We only use MOS1 images from the earlier observation for each object (0840580101 for RXCJ1504 and 0840580301 for A1664). The images are produced by the SAS task *emproc*. We extract the surface brightness profiles in the 0.5-1.8 keV energy band using the task *rgsvprof*. We use SPEX version 3.05.00 for spectral analysis with its default proto-Solar abundances of Lodders and Palme [114] and ionisation balance [201].

Table 5.1 Observational details for RXCJ1504.1-0248 (Obsid:0840580101/201) and A1664 (Obsid:0840580301/401).

Name	Redshift	D_L (Mpc)	Scale (kpc/arcsec)	Clean time (ks)	N_{H} ($10^{20}\,\mathrm{cm}^{-2}$)
RXCJ1504.1-0248	0.21530	1030	3.36	220	8.34
A1664	0.12832	579	2.20	222	12.8

The redshifts are taken from the NED database (https://ned.ipac.caltech.edu/). The total Galactic column density N_{H} is taken from the UK Swift Science Data Centre (http://www.swift.ac.uk/analysis/nhtot/).

5.3 Results

The stacked RGS spectra are binned by a factor of 3 to be consistent with the spectral resolution and preserve most spectral information. We fit the first order spectra over the 7-28 Å (0.44-1.76 keV) band where the background is lower than the continuum. We include the 7-20 Å (0.62-1.76 keV) band for the second order spectra. We use the collisional ionisation equilibrium component (*cie*) and the cooling flow component (*cf*) available in SPEX to construct our cooling flow models as described in Chapter 3 [113]. We use the default value of n_{e} in the emission measure of the *cie* component in SPEX.

To reduce the number of free parameters, we fix the Ne/Fe and Mg/Fe ratios for both clusters. In the initial test fitting, we find that Ne/Fe=0.8 and Mg/Fe=0.75 in RXCJ1504 and Ne/Fe=Mg/Fe=0.6 in A1664. These ratios are measured from a 1*cie*+1*cf* model (Model 2) and do not change with additional *cf* components. The abundances of the other elements are coupled to Fe. The *cie* and *cf* components are modified by redshift, cold Galactic absorption with solar abundances and spatial broadening (*lpro*; [158]). The *lpro* component uses the surface brightness profile as the input. The scale factor s and the wavelength shift $\Delta\lambda$ are the free parameters. The scale factor fit for the amount of line broadening and the wavelength shift corrects for the centroid of emission.

5.3.1 Cooling flow analysis

To construct the cooling flow models, we first model the hot plasma ($>$ 2 keV) in the multi-phased intracluster medium (ICM) with a *cie* component (Model 1). Three cooling flow models are then considered combining *cie* and *cf* component: complete (one-stage), one-stage with a free minimum temperature and two-stage models. We define the 'complete' cooling rate as the rate measured from the *cie* temperature down to the minimum temperature of the *cf* component of 0.01 keV (Model 2). This minimum temperature of 0.01 keV is the lowest possible value allowed in SPEX. This one-stage cooling flow model is often sufficient for the spectra of clusters and groups with low statistics and a low *cie* temperature (e.g. [113]), but not necessarily for RXCJ1504.1-0248 and A1664. We then free the minimum temperature of the *cf* component to include the possibility that the ICM stops cooling radiatively in X-rays at a higher temperature (Model 3). This also leads to a 'two-stage' cooling flow model that has two *cf* components, where the cooling rates are measured between the *cie* temperature and 0.7 keV and between 0.7 keV and 0.01 keV, respectively. We refer to the cooling rate between 0.7 keV and 0.01 keV as the residual cooling rate in this work (Model 4). In Chapter 3, we discussed the effect of the transition temperature between two cooling flow components on the cooling rates in the two-stage model. For a high transition temperature up to 0.9 keV, the cooling rate above the transition temperature is likely increased by 20 per cent. For a low transition temperature, the cooling rate is likely decreased by 10 per cent, while the residual cooling rate is over-predicted due to a narrow temperature range. We found that the transition temperature of 0.7 keV is suitable for fitting the Fe XVII lines and its forbidden-to-resonance line ratio. It is also consistent with the one-stage cooling flow model with a free minimum temperature.

The cooling rates, *cie* temperatures and O and Fe abundances of three cooling flow models are detailed in Table 5.2 and 5.3. We show the stacked RGS spectra in Fig. 5.1 and 5.2 with the best fit cooling flow models.

In RXCJ1504, we find that both the one-stage cooling flow model with a free minimum temperature (Model 3) and the two-stage model (Model 4) yield the minimum C-stat for the same number of degrees of freedom (DoF). The transition temperature of the two-stage model is consistent with the free minimum temperature of the one-stage model. The other fit parameters are also consistent between these two models. We hence conclude a cooling rate to 0.7 keV of 180±40 $M_\odot\,yr^{-1}$ and a residual cooling rate of from 0.7 keV less than 53 $M_\odot\,yr^{-1}$ at 90 per cent confidence level. The Fe XVII resonance line is seen in the spectrum and mixed with a broad feature at 15 Å (0.82 keV) in rest wavelength (18.3 Å in observed wavelength or 0.67 keV). This indicates a cooling flow is present at around 0.7 keV. There are several possibilities for the nature of the broad feature. First, the Fe XVII resonance line is suppressed in the line of sight and re-emitted from the outer region. The spatial extent of the gas emitting the Fe XVII resonance line is broadened which results in a broader line at 15 Å (0.82 keV) due to the fact that the RGS detectors are slitless. Second, the gaseous neutral iron in the interstellar medium has 2 deep and broad absorption edges at 17.2 Å (0.72 keV) and 17.5 Å (0.70 keV). However, most iron is in dust, which has a different edge shape and position. A spectral modelling of the iron edge which does not account for dust might

Table 5.2 XMM/RGS fit parameters for RXCJ1504.

	Model 1	Model 2	Model 3	Model 4
Spectral components	1*cie*	1*cie*+1*cf*	1*cie*+1*cf*	1*cie*+2*cf*
C-stat/DoF	841/682	833/681	818/680	818/680
Fe/H	0.68±0.06	0.74±0.07	0.76±0.08	0.76±0.07
O/H	0.41±0.06	0.39±0.07	0.44±0.07	0.44±0.07
$T_{\rm H}$ (keV)	5.4±0.2	5.6±0.2	6.3±0.4	6.3±0.4, 0.7
$T_{\rm min}$ (keV)	n/a	0.01	0.7±0.1	0.7, 0.01
$\dot{M}_{\rm H}$ ($\rm M_\odot\,yr^{-1}$)	n/a	50±20	190±60	180±40
$\dot{M}_{\rm C}$ ($\rm M_\odot\,yr^{-1}$)	n/a	n/a	n/a	<53

Model 1 is the single-temperature (1*cie*) model, model 2 is the complete cooling (1*cie*+1*cf*) model, model 3 is the one-stage model with a free minimum temperature and model 4 is the two-stage (1*cie*+2*cf*) model. $T_{\rm H}$ and $T_{\rm min}$ are the *cie* temperature and the minimum temperature of the associated *cf* component, respectively. $\dot{M}_{\rm H}$ is the cooling rate between $T_{\rm H}$ and $T_{\rm min}$. $\dot{M}_{\rm C}$ is the residual cooling rate between 0.7 and 0.01 keV in the two-stage model.

introduce some systematic effects including a spurious bump around 18 Å (0.68 keV; see e.g. [98, 157]).

The O vii triplet is not observed. Due to the high continuum emission of the hot gas, the mass of cold gas at 0.2 keV is difficult to detect. The distinction between the complete and two-stage models is statistically significant. While some fit parameters are consistent such as the *cie* temperature and metallicity, the two-stage model gives 3.6 times higher cooling rate above 0.7 keV than the complete cooling rate. By comparison in Chapter 3 [113], we find such a ratio of 2.2, 1.7, 3.8 in A262, Centaurus and M87, respectively, all of which show a significant statistical improvement in the two-stage model. Given the 20-40 per cent uncertainty on the measurements, this ratio is broadly consistent with other nearby cool core clusters [113].

In A1664, we find that the cooling flow models are improved by using a second line broadening component for the *cf* components. The second *lpro* component uses the same surface brightness profile and we fit the scale factor and wavelength shift as the *lpro* component for the *cie*. The extra line broadening component improves the C-stat by 5 in comparison with using just one broadening component in the complete cooling model. We find that all the cooling flow models provide a similar fit to the spectrum with the same C-stat and consistent cooling rate. As a result, we only report a complete, one-stage, cooling rate of $34\pm6\rm M_\odot\,yr^{-1}$ from the current data (Model 1).

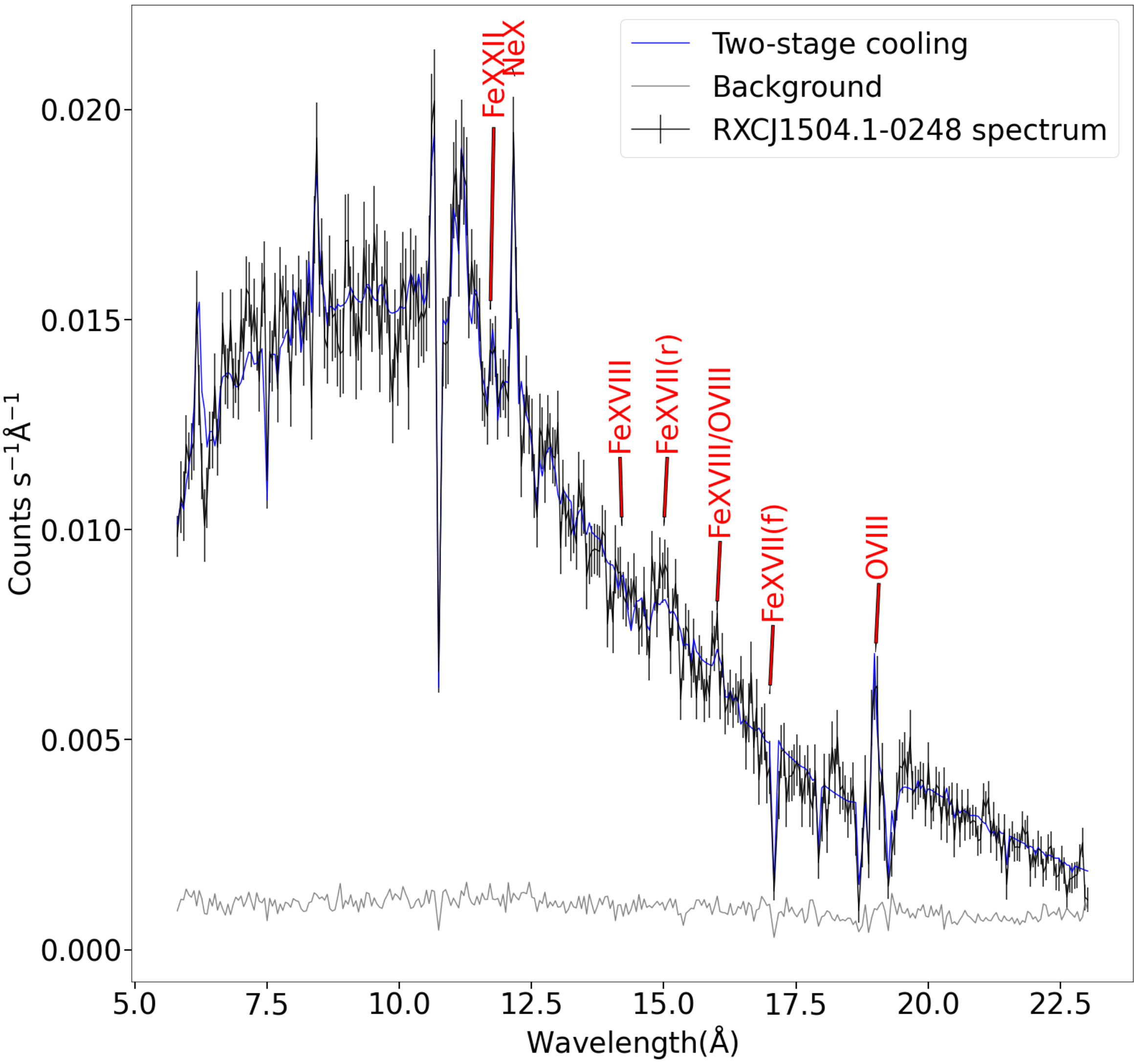

Fig. 5.1 Stacked first order RGS spectrum of RXCJ1504.1-0248 in rest wavelength. The RGS spectrum is shown in black and the best fit two-stage cooling models is seen in blue. The background is seen in grey. Strong emission lines are labelled in red. The spectrum is overbinned by a factor of 6 for plotting purposes.

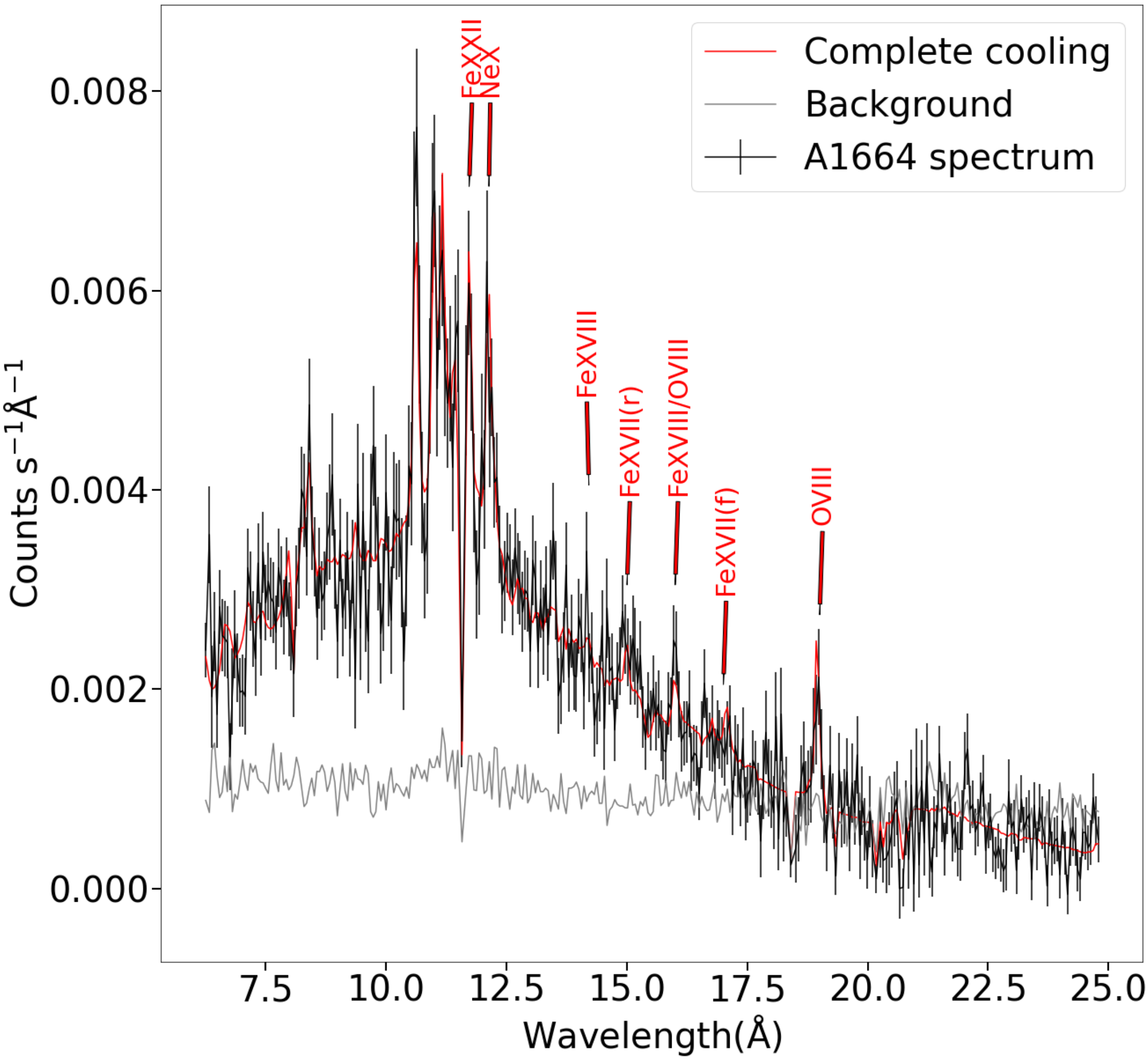

Fig. 5.2 As Fig. 5.1, the stacked RGS spectrum of A1664 with the best fit complete cooling flow model in red in rest wavelength.

Table 5.3 XMM/RGS fit parameters for A1664. Models, parameters and labels are the same as Table 5.2.

	Model 1	Model 2	Model 3	Model 4
Spectral components	1*cie*	1*cie*+1*cf*	1*cie*+1*cf*	1*cie*+2*cf*
C-stat/DoF	929/680	909/677	909/676	909/676
Fe/H	0.37±0.03	0.49±0.05	0.49±0.06	0.50±0.06
O/H	0.23±0.05	0.28±0.06	0.58±0.06	0.29±0.06
$T_{\rm H}$ (keV)	1.95±0.07	2.2±0.1	2.2±0.1	2.1±0.1, 0.7
$T_{\rm min}$ (keV)	n/a	0.01	<0.7	0.7, 0.01
$\dot{M}_{\rm H}$ ($\rm M_\odot\,yr^{-1}$)	n/a	34±6	34±6	40±20
$\dot{M}_{\rm C}$ ($\rm M_\odot\,yr^{-1}$)	n/a	n/a	n/a	30±10

5.3.2 Turbulence

Spatial broadening

The observed line broadening in RGS spectra is the sum of thermal broadening, turbulent motion and spatial broadening. Thermal broadening is already calculated in the thermal components such as *cie* or *cf*. To place constraints on the turbulent velocity, we need to estimate the level of spatial broadening. Since the scale of the hot ICM is much larger than that of the cool core, using the full spatial profile over-predicts the contribution to the spatial broadening and hence underestimate the turbulence. We follow the method used in Bambic et al. [7] and Pinto et al. [154] for a more accurate estimate of spatial broadening due to the cool gas.

The SPEX task *rgsvprof* gives a cumulative flux of the surface brightness profile of the MOS images as a function of wavelength. This can be inverted into a Gaussian shaped profile as expected from the image. Such a profile can be modelled by the sum of three Gaussians. The central narrowest Gaussian represents the coolest gas in the core. The bremsstrahlung continuum from the hot ICM is seen in the broadest outer Gaussian. The remaining intermediate Gaussian provides the transition between the ICM and the cool core. As we try to measure the turbulence in the cool core, the central and intermediate Gaussians are the relevant components in the estimation of spatial broadening.

The surface brightness profiles of RXCJ1504.1-0248 and A1664 are seen in Fig. 5.3. We find that the profile of A1664 is skewed and the asymmetry is seen in the DETY direction of the MOS 1 image. The separation between the centre of the central and intermediate Gaussian is 0.045±0.001 Å. From the RGS dispersion law, such a wavelength separation corresponds to a physical separation of 70 kpc. This means the intermediate Gaussian component is indeed at the rim of the cool core.

We reconstruct two profiles of cumulative flux that can be used in SPEX, which include either using the central Gaussian alone or using both the central and intermediate Gaussians.

Turbulent velocity measurements

We simultaneously fit the first and the second order spectra to measure the turbulent velocity. The observed spatial profile is replaced by the profiles reconstructed from the Gaussian approximations in the *lpro* component. To conserve the RGS dispersion law, we then set the scale factor of the lpro to $s = 1$ for the first order and $s = 0.5$ for the second order spectra. We also fit the wavelength shift parameter in the *lpro* component to adjust for redshift. We use the single-temperature (1*cie*) model and fit the micro-turbulent velocity (v_{turb}) of the *cie* components. The 1-dimensional turbulent velocity is then $v_{1\text{D}}$=$v_{\text{mic}}/\sqrt{2}$. The fit parameters between the two sectors (first and second order spectra) are then coupled.

We summarise the velocity limits in Table 5.4. The total line width due to turbulence and spatial broadening is calculated by using the full spatial profile and setting the scale factor to 0. The most accurate velocity limit is measured by simultaneously fitting the first and second order spectra. We find that correcting the spatial broadening both using the central Gaussian alone and using both the central and intermediate Gaussians give consistent velocity limits. We report that the best 90 per cent upper limit for RXCJ1504 and A1664 are both 300 $\text{km}\,\text{s}^{-1}$.

5.4 Discussion

5.4.1 Soft X-ray and cooler gas

It is possible to achieve a 3σ measurement of the cooling rate by the two-stage model (Model 4) or better for many nearby, $z < 0.01$, clusters [113], but only a few at the redshift similar to our targets or higher (e.g. [199, 154]). From the analysis of the deep observations of the luminous clusters RXCJ1504 and A1664, we can provide reliable measurements of the cooling rate at the 4-5σ confidence level. Both targets are already well-studied in other energy bands as well as spatially resolved analysis in Chandra (e.g. RXCJ1504: [16, 26, 144, 183, 203]; A1664: [46, 220, 105, 142, 167, 20]). It is then of great interest to understand the role of such X-ray cooling rate in cluster evolution at intermediate redshifts. To be more precise, in this section, we discuss the connection between the soft X-ray emitting gas and the cooler materials including the Hα nebula, molecular gas reservoir, gas consumed

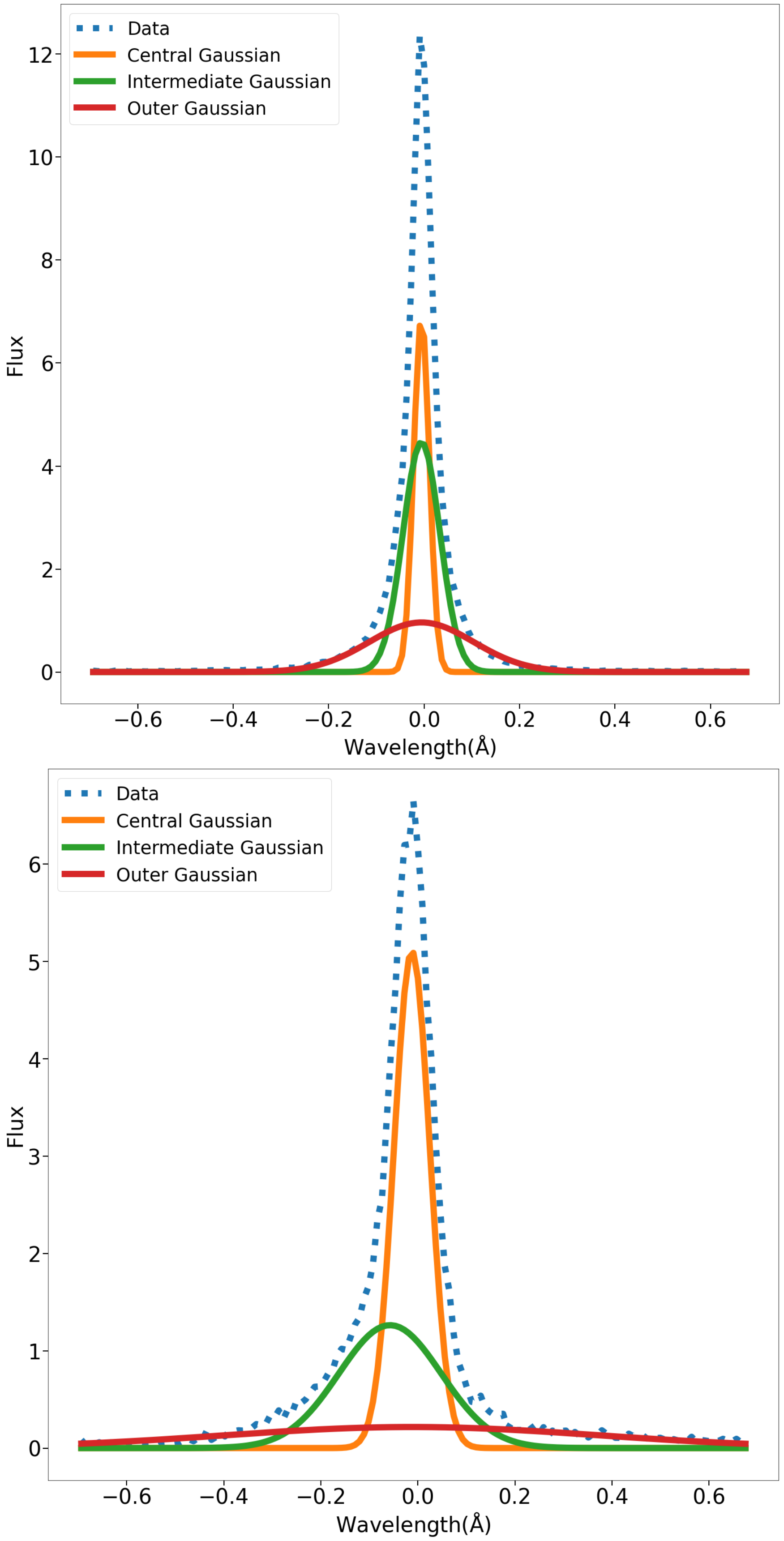

Fig. 5.3 Top panel: The surface brightness profile of RXCJ1504 (Data) and the components of three-Gaussian fit. Bottom panel: The surface brightness profile and Gaussian components of A1664.

Table 5.4 Turbulent velocity limits for RXCJ1504 and A1664.

		1st order spectrum Total width	Central	Central & intermediate
RXCJ1504	v_{1D} ($\mathrm{km\,s^{-1}}$)	600±100	500±100	<260
	C-stat/DoF	840/682	839/682	839/682
A1664	v_{1D} ($\mathrm{km\,s^{-1}}$)	800±200	<530	<420
	C-stat/DoF	941/680	931/680	938/680
		1st and 2nd order spectra Total width	Central	Central & intermediate
RXCJ1504	v_{1D} ($\mathrm{km\,s^{-1}}$)	550±90	300±100	<310
	C-stat/DoF	3111/2093	3082/2093	3087/2093
A1664	v_{1D} ($\mathrm{km\,s^{-1}}$)	700±100	<300	<320
	C-stat/DoF	2934/2089	2919/2089	2941/2089

Top half of the table includes the turbulence measurements using only the first order spectrum. The columns of total width represent the line width measurements without the correction of line broadening. The next column 'Central' is the turbulent velocity measured by correcting the spatial broadening using the central Gaussian only. The velocity limits in the last column 'Central & intermediate' are corrected by using both the central and intermediate Gaussians in the spatial profile. Turbulence is measured by simultaneously fitting the first and second order spectra in the bottom half.

by star formation activities and AGN accretion. We are currently analysing the archival spectra of luminous clusters at intermediate redshifts ($0.1 < z < 0.6$) with known optical nebula and will report in Chapter 6.

The Hα nebulae of RXCJ1504 and A1664 are exceedingly luminous for intermediate redshift clusters. To power these partially ionised nebulae, at least a factor of 15 times the observed Hα luminosity is required to include other UV/IR emission due to the same gas [57, 65]. O'Dea et al. [142] and Ogrean et al. [144] reported that the energy of stellar photoionisation is comparable to the Hα luminosity in our targets. This means that additional sources of energy are required to power the remaining emission. Fabian et al. [57] suggested that the soft X-ray gas can provide sufficient energy for the nebulae, as it can release a significant amount of energy if it continues to cool non-radiatively below 0.7 keV. Our analysis in Chapter 3 shows that the energy of the 0.7 keV gas is sufficient only for the less luminous nebulae, while the most luminous nebulae require a much warmer gas [113]. O'Dea et al. [141] found the same conclusion for the 1 keV gas to power 5 times the IR luminosity.

We use equation 3.2 to calculate the energy required by the nebulae in our clusters into a mass inflow rate ($\dot{M}_{\rm neb}$). For our targets, we find that $\dot{M}_{\rm neb}$ is $4.6\times10^3 \mathrm{M}_\odot\,\mathrm{yr}^{-1}$ for RXCJ1504 and $2.1\times10^2 \mathrm{M}_\odot\,\mathrm{yr}^{-1}$ for A1664. Both of these values are much larger than the observed cooling rate between the ICM temperature and 0.7 keV. They are also 2-3 times of the classical cooling rate predicted in the absence of heating. This means that the cooling flow at 0.7 keV is therefore insufficient to power the observed Hα nebulae. Alternatively, if the nebulae are powered by the warmer gas of the same rate as radiatively cooling, equation 3.2 suggests that the temperature of the gas is 25 keV and 6.3 keV for RXCJ1504 and A1664, respectively. The temperature is much hotter than the temperatures of the hot ICM in RXCJ1504 and is not expected in the cool core. Therefore, other sources of significant energy are required to power the Hα nebulae of at least RXCJ1504 in addition to stellar photoionisation and the soft X-ray cooling flow (see section 5.4 for additional energy in an alternative cooling flow model).

The gas properties of RXCJ1504 compare well to those of the Phoenix cluster at $z = 0.596$. It has a similar molecular gas mass of 2×10^{10} $\mathrm{M}_\odot$ [166] embedded in an optical line-emitting nebula with an Hα luminosity of $8.52\pm0.5 \times 10^{43}$ ergs^{-1} [123]. For the Phoenix cluster, Pinto et al. [154] reported a cooling rate of 350^{+150}_{-120} $M_\odot\,\mathrm{yr}^{-1}$ below 2 keV at 68 per cent confidence level. Both the Hα luminosity and the cooling rate are twice of those measured in RXCJ1504. We calculate $\dot{M}_{\rm neb}$ to be $4.3\times10^3 \mathrm{M}_\odot\,\mathrm{yr}^{-1}$ for the 2 keV gas. This means the soft X-ray gas and stellar photoionisation are also insufficient as the power source. However, the Phoenix cluster has a star burst of 500-800 $M_\odot\,\mathrm{yr}^{-1}$ that is comparable to the observed cooling rate at the 1σ confidence level [118, 123]. This suggests the molecular gas reservoir is likely growing slowly at the young age of the cluster.

The fate of the mass of the X-ray cooling gas still needs to be accounted for. The condensation of X-ray cooling gas is strongly linked to both the massive molecular gas reservoir and the star formation in the BCG, which are only present when the radiative cooling time falls below a Gyr [161, 160]. Russell et al. [168] and Liu et al. [112] found that the mass of the soft X-ray gas is consistent with the molecular gas mass in the inner 10 kpc. If the X-ray cooling flow is indeed a major source of gas for the molecular gas reservoir and then star formation, we can estimate the timescale for forming the reservoir. Without any star formation activity and AGN gas accretion, the molecular gas requires 10^8 yr to accumulate in RXCJ1504 and 3.2×10^8 yr in A1664.

However, both of our targets are extremely star forming clusters and may have a strong AGN activity. Our results show that RXCJ1504 is cooling at 10 per cent and A1664 is cooling at 34 per cent of the classical cooling rate predicted in the absence of heating. This means most radiative cooling is suppressed by AGN feedback. The amount of heating required can be deduced from the luminosity of the cooling flow component above 0.7 keV, which is available in SPEX. This indicates at least $2.25\times10^{45}\,\mathrm{erg s^{-1}}$ and $2.1\times10^{43}\,\mathrm{erg s^{-1}}$ for RXCJ1504 and A1664, respectively. Such energy is about a third of the mechanical power in A1664 and hence AGN feedback must supply the larger power of $6.8\times10^{43}\,\mathrm{erg s^{-1}}$ [160]. The required energy is 10 times larger than the mechanical power from the AGN in RXCJ1504, which suggests the AGN has been much more active than now observed. Ogrean et al. [144] found the same conclusion in RXCJ1504 using the 3σ upper limit of the cooling rate measured from archival EPIC/RGS spectra.

Assuming accretion efficiency of 0.1, the required energy is equivalent to a black hole growth rate of 0.39 $\mathrm{M_\odot\,yr^{-1}}$ and 0.012 $\mathrm{M_\odot\,yr^{-1}}$ for RXCJ1504 and A1664, respectively. If the AGN is powered by Bondi accretion from the X-ray emitting gas, it requires a cool component of about 0.5 keV in RXCJ1504 [17, 144]. Although our cooling flow models find most gas is above 0.7 keV, the detection of the Fe XVII resonance line shows that it is likely to have some cool gas at around 0.5 keV. In Chapter 4, we measured the mass of 0.7 keV in nearby cool core clusters of $10^8 - 10^9\mathrm{M_\odot}$ [112]. RXCJ1504 is likely to have a higher gas mass at this temperature, since the luminosity of the 0.7 keV gas in the two-temperature model is 9 times larger than that of 2A0335+096, which has the largest gas mass below 1 keV. Such a cool gas can fuel the AGN on the timescale of a few 10^9 yr. The ratio of the black hole growth rate to the star formation rate is 0.003 and 0.00086 for RXCJ1504 and A1664, respectively. The relation of black hole growth and star formation is in good agreement with other clusters [162]. Finally, the ratio of the radiative cooling rate to the star formation rate is between 1.5 and 2.5, which is smaller than most moderate star forming clusters but consistent with more luminous clusters such as A1835 [162, 141, 113]. We find a net mass deposition rate of 50 $M_{\odot}\,\mathrm{yr}^{-1}$ in RXCJ1504 and 20-30 $M_{\odot}\,\mathrm{yr}^{-1}$ in A1664. These increase the molecular gas formation timescale by 2-3 times. Nevertheless, these timescales are consistent with the typical radiative cooling time of cool core clusters (e.g. A1664 [105]), which suggests a strong link between the X-ray cooling gas and the molecular gas.

5.4.2 Turbulence versus heat propagation

The archival *XMM*-Newton observations of A1664 (ObsID: 0302030201/0302030201) did not point at the centre of the cluster and no turbulent velocity measurement was made by previous works. The previous spectroscopic analyses and Monte Carlo simulation of turbulence found a velocity of 670^{+600}_{-360} km s^{-1} and 1310^{+570}_{-670} km s^{-1} at 68 per cent confidence level, respectively [183, 180]. Our results using the new data show a much tighter limit (of 300 km s^{-1}). The turbulent velocity of our targets is comparable to the velocity measured in many bright clusters, e.g. <211 km s^{-1} in A1835 [180, 7], <400 km s^{-1} in 2A0335+096 [158], ∼164 km s^{-1} in Perseus [84] and <370 km s^{-1} in the Phoenix cluster [154].

It is worth noting that resonant scattering can place constraint on the level of turbulence in elliptical galaxies in galaxy groups [40, 143]. For elliptical galaxies with a temperature below 1 keV, strong Fe XVII lines are usually seen in the RGS spectra. Ogorzalek et al. [143] measured a mean turbulent velocity of 107±17 km s^{-1} in 13 elliptical galaxies. This is lower than the upper limit in our targets, but individual galaxies can have a higher turbulence (e.g. NGC 5044 [40]). The temperature of BCG in clusters is typically above 1.5-2 keV and Fe XVII lines are not detected in all clusters. It is also difficult to measure the Fe XVII resonance-to-forbidden ratio due to the high continuum. In the case of RXCJ1504, the Fe XVII forbidden line is redshifted to the RGS chip gap and therefore not detected by the RGS. It is ideal to place constraint on turbulence with resonant scattering in clusters with Fe L lines, which is beyond the scope of this work.

We can calculate the adiabatic sound speed $c_{\mathrm{s}} = \sqrt{\gamma kT/\mu \mathrm{m_p}}$, where γ is the adiabatic index, which is 5/3 for ideal monatomic gas, $\mu = 0.6$ is the mean atomic weight and $\mathrm{m_p}$ is the proton mass. This gives a sound speed of 1300 km s^{-1} and 750 km s^{-1} for RXCJ1504 and A1664, respectively. In this work, we calculate the 1-D Mach number for turbulence $M = V_{\mathrm{1D}}/c_{\mathrm{s}}$. The turbulent velocity then has a Mach number M of 0.23 in RXCJ1504 and 0.4 in A1664. To calculate the ratio of the energy density in turbulence to the thermal energy of the plasma, we follow equation 11 in Werner et al. [215] and obtain

$$\frac{\varepsilon_{\mathrm{turb}}}{\varepsilon_{\mathrm{therm}}} = \gamma M^2. \tag{5.1}$$

We find that the energy density ratio is less than 8.9 per cent in RXCJ1504, which is comparable to the ratio of 4 per cent in Perseus [84] and 13 per cent in A1835 [184]. In A1664, the turbulence energy is less than 27 per cent of thermal energy. Bambic et al. [7] and Pinto et al. [154] calculated the minimum propagation velocity required to balance radiative cooling as a function of radius in 4 cool core clusters. The gas properties of RXCJ1504 are similar to those of the Phoenix cluster and A1835, while the core of 1664 is similar to that of A2204. The upper limits of turbulent velocity of 300 $\mathrm{km\,s^{-1}}$ are lower than required in both clusters at more than 15 kpc from the core. It is clear that the energetics of the turbulent motion of hot gas can not fully balance radiative cooling throughout the cool core.

We now discuss the problem of energy transport and dissipation. Zhuravleva et al. [225] argued that the large ($\sim$ 10 per cent) surface brightness fluctuations in the X-ray images are isobaric and/or isothermal on spatial scales of 10-60 kpc and are likely associated with slow gas motions and bubbles of relativistic plasma (X-ray cavities). Bubbles tend to propagate along an axis but heating is also needed in directions away from that axis. This requires a faster propagation than turbulence alone. Internal waves or g-modes (buoyancy waves) are invoked on energetic grounds, but these waves do not propagate fast enough.

An alternative is to invoke time variability. Fujita et al. [69] presents a time-dependent 1D simulation of heating in cool core clusters with outbursts reaching 10^{46} $\mathrm{erg s^{-1}}$ from the AGN on Gyr timescale. The central density and temperature profiles make large excursions on this timescale with energy advected during the outbursts. However, Panagoulia et al. [147], Hogan et al. [89] and Babyk et al. [6] show a universal inner entropy shape which would not be seen if the central gas properties are cycling up and down. The issue of how the energy is replaced or flows remains open, with sound waves remaining a possibility.

5.4.3 Blueshifted component in A1664

The best fit cooling flow models of A1664 show that the spectrum is well fitted by two *lpro* components (see section 3.1). This is also seen in some other clusters, e.g. Centaurus, where the Fe XVII lines are narrower than emission lines from hot-gas [155, 113]. We find that although the scale factor is consistent in the *lpro* components in A1664, the wavelength shift is different. To understand the nature of this shift, we adopt a two-temperature model (2 *cie*) and each *cie* is associated with a separate *lpro* component. We find that the cooler component has a temperature of 0.80±0.08 keV and blueshifted by $0.046^{+0.049}_{-0.017}$ Å from the hot gas. Such a difference can be achieved by either a blueshifted gas component or the different centroids of the hot and cool gas phase. We extract the surface brightness profile of the MOS1 image in 0.5-1 keV and 1-3 keV energy bands. These bands cover most emission seen in the core RGS spectrum. The profiles are shown in Fig. 5.4. We find that the centroids of different gas phases are separated by 0.0017±0.0006 Å. This only accounts for 4 per cent of the observed wavelength shift. Therefore, the blueshift is due to the motion of the cool gas. Assuming the blueshift is driven by the Fe XVII resonance line, we estimate the blueshifted velocity of 750^{+800}_{-280} km s^{-1}. Independently, we also decouple the redshift of the two *cie* components and convolve both with the same *lpro* component. We find a consistent blueshifted velocity of 1000^{+500}_{-300} km s^{-1}. Note that the difference of the roll-angle of the pointings between the two observations is small. By simultaneously fitting the spectra of individual observations, we find that the fit parameters are consistent with the stacked spectrum of both observations.

A different line-of-sight velocity of different gas phases is seen in other clusters. By decoupling the redshift, Pinto et al. [154] found a velocity of 1000±400 km s^{-1} in the Phoenix cluster. A similar velocity of ∼1000 km s^{-1} is found in the non cool core Coma cluster, while gas in the Perseus cluster is more relaxed at 480±210 km s^{-1} (e.g. [174]). It is possible to drive cool gas by sloshing due to minor mergers (e.g. [5]). The shift in velocity is then seen in spatial coincidence with cold fronts [174].

In A1664, the molecular gas system in the centre is divided in 2 roughly equal clumps with a velocity separation of 600 km s^{-1} [167]. The blueshifted component is seen at a velocity of 571±7 km s^{-1} from CO(3-2) in our line-of-sight, with a FWHM of 190±20 km s^{-1}. Given the large uncertainty in the X-ray measurements, the velocities of the molecular and X-ray gas are consistent within 1σ. The observation of Hα emission by the integral field unit of the Very Large Telescope shows a similar complexity of the velocity structure [220]. Although it is unclear whether the blueshifted molecular gas lies in front or behind the BCG along the line of sight, the system is only a few kpc from the core in the transverse direction. This molecular gas is likely embedded in the soft X-ray gas cloud so these two gas phases may be related. The 0.8 keV gas has a sound speed of 460 km s^{-1}. The molecular gas will be shocked unless it comoves with the soft X-ray emitting gas.

5.4.4 Embedded multilayer cooling flow in RXCJ1504

There are larger amounts of cold obscuring material in the core of galaxy clusters, e.g. the Centaurus cluster (A3526) [34, 176]. This suggests intrinsic absorption of the target galaxy is likely important and can reduce the amount of observed emission from a radiative cooling flow. Sanders et al. [181] reported a factor of 3 larger cooling rate in the Centaurus cluster if there is a 4×10^{21}cm^{-2} column density intrinsic to the cluster. This represents a significant amount of extra intrinsic luminosity available for powering emission due to cold gas.

In this section, we reintroduce a simple multilayer, intrinsically absorbed, cooling flow model, which was first proposed by Allen and Fabian [1]. The schematic diagram of the model is shown in Fig. 5.5. For simplicity, we assume the cool core consists of several

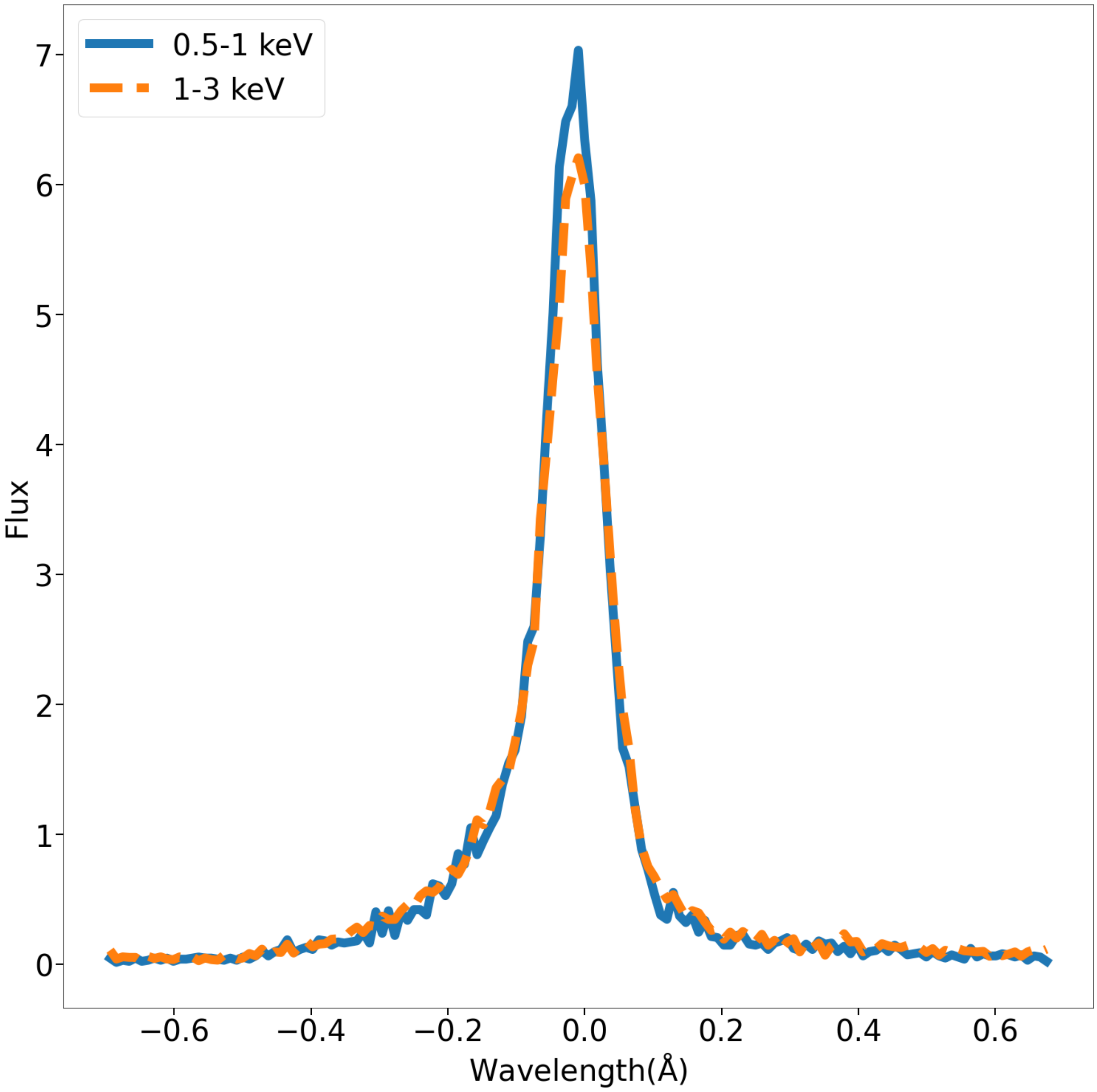

Fig. 5.4 The energy dependent surface brightness profile of A1664.

parallel sheets of material. Identical sheets of radiatively cooling gas in X-rays are placed in-between identical sheets of absorbing gas. The absorbing gas is assumed to be cold and neutral. An X-ray cooling sheet is absorbed by all absorbing sheets along the line-of-sight. This means the cooling sheet closest to the observer is absorbed once, and the furthest cooling sheet is absorbed three times in Fig. 5.5.

The physical depth of these sheets is irrelevant in this work.

We assume each cooling gas sheet is emitting a flux F_λ. The fraction of the emitted energy transmitted through one sheet of absorbing gas is f_λ. We can write this transmission fraction as

$$f_\lambda = e^{-\sigma(E)\Delta n_\mathrm{H}}, \tag{5.2}$$

where $-\sigma(E)$ is the absorption cross-section and Δn_H is the column density of one sheet of absorbing gas. The total observed flux is then

$$F_\mathrm{tot} = f_\lambda F_\lambda + f_\lambda^2 F_\lambda + ... + f_\lambda^{n_\mathrm{sheet}} F_\lambda = F_\lambda \sum_{m=1}^{n_\mathrm{sheet}} f_\lambda^m, \tag{5.3}$$

where n_sheet is the number of sheets of absorbing gas components. Since absorption is a multiplicative process, it is possible to use the geometric series and equation 5.3 becomes

$$F_\mathrm{tot} = F_\lambda \frac{1 - f_\lambda^{n_\mathrm{sheet}}}{1 - f_\lambda}. \tag{5.4}$$

This suggests only n_sheet and the total column density $n_\mathrm{H,tot}$ are the additional free parameters. Note that $n_\mathrm{H,tot} = n_\mathrm{sheet}\Delta n_\mathrm{H}$. In the large n_sheet limit, equation 5.2 can be expanded and Equation 5.4 rewritten as

$$F_\mathrm{tot} = F_\lambda n_\mathrm{sheet} \frac{1 - e^{-\sigma(E)\Delta n_\mathrm{H}}}{\sigma(E)\Delta n_\mathrm{H}}. \tag{5.5}$$

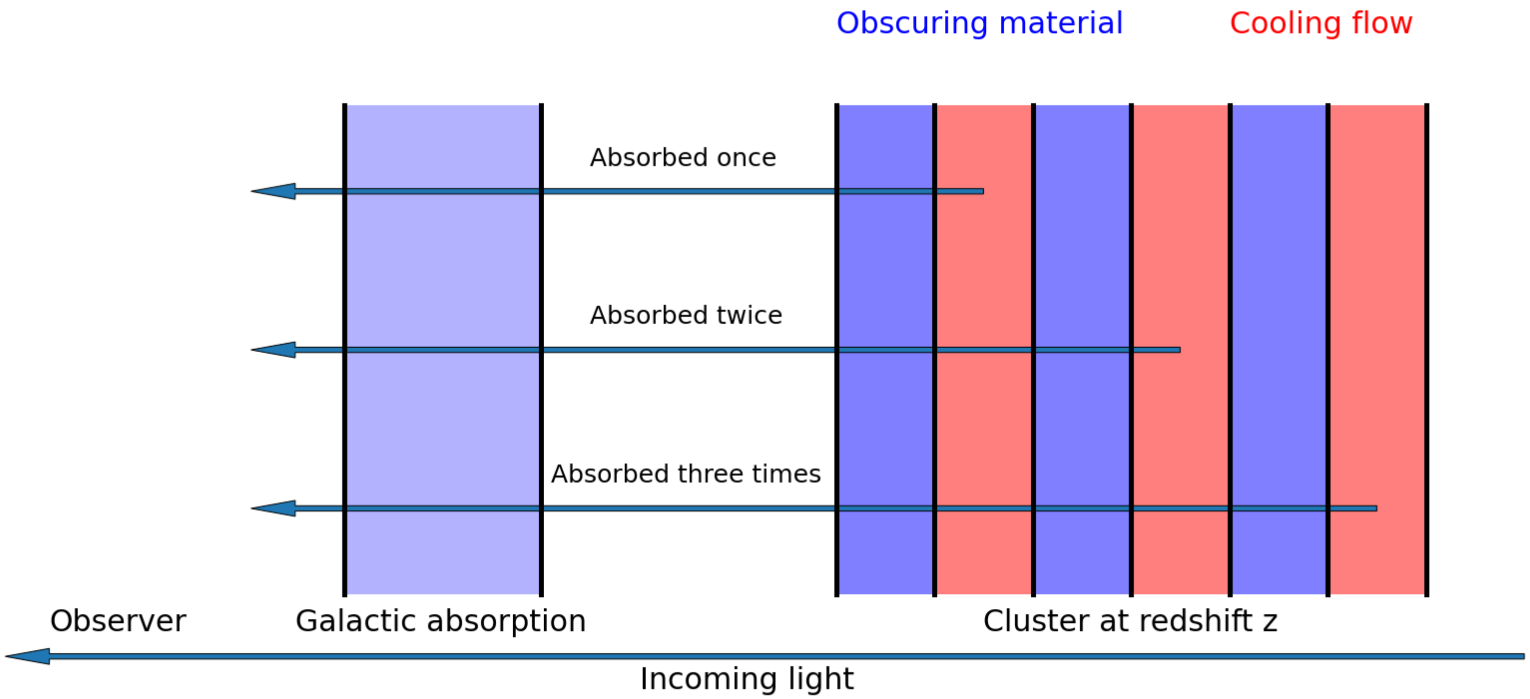

Fig. 5.5 The schematic diagram of embedded cooling flow with three absorbing sheets and three cooling flow sheets. In the cluster, the blue columns represent sheets of absorbing gas and red columns represent sheets of radiative cooling flow. The black lines are the boundary between the columns. Blue arrows originated from the cluster represent emission from the associated sheet of cooling flow.

Unfortunately, the geometric series implementation of absorption components is not yet available in SPEX. Nevertheless, it is possible to implement a brute-force model combining the existing spectral component of absorption and cooling flow. First, we select the number of absorbing sheets and choose a total column density. Each absorption component has the same column density of $n_{\mathrm{H,tot}}/n_{\mathrm{sheet}}$ and is fixed in the spectral fitting. We assume the temperature of the absorbing gas is 0.5 eV, and the abundances are coupled to the X-ray cooling gas. The X-ray cooling gas is modelled by n_{sheet} *cf* components. Each of these *cf* components will be modified by a different number of absorption components before Galactic absorption. We couple the fit parameters of all *cf* components to one *cf* component. Then we measure the cooling rate from the *cie* temperature down to 0.01 keV as the complete cooling flow model described in section 5.3.1. The intrinsic absorption corrected cooling rate is then the total cooling rate of all *cf* components. This reconstructs the multilayer cooling flow model, which is equivalent to the complete cooling flow model with intrinsic absorption.

We use a 15x15 grid in n_{sheet} and $n_{\mathrm{H,tot}}$ parameter space. We apply our model to RXCJ1504 and fit for minimal C-stat for each pair of n_{sheet} and $n_{\mathrm{H,tot}}$. The improvement of C-stat from the complete cooling model is seen in Fig. 5.6, where we have included the contour at 68 per cent, 90 per cent and 95 per cent confidence levels. We search for the total column density that gives the minimum C-stat at any given number of sheets of absorbing gas. We find a valley of minimal C-stats in the parameter space. The absolute minimum of C-stat occurs for 1 absorption component with a column density of $6 \times 10^{21}\mathrm{cm}^{-2}$. However, the difference between the C-stats is less than 0.3 on this valley. This means n_{sheet} and $n_{\mathrm{H,tot}}$ are highly degenerate. Allen and Fabian [1] found that the multilayer cooling flow model typically overpredicts the intrinsic column density by a factor of 1.5-3 in a sample of low redshift clusters. In conjunction with the valley of minimal C-stats in Fig. 5.6, this suggests that the true value of the intrinsic column density corresponds to a complex multilayer model with $n_{\mathrm{sheet}} \sim 10$.

We can compare the intrinsic absorption corrected cooling rate between the simplest 1 absorbing sheet model and the 10 sheets model. For the 1 sheet model, we measure a cooling rate of $430\pm90\ \mathrm{M_{\odot}\,yr^{-1}}$. This is 8 times higher than the complete cooling rate without intrinsic absorption (see Model 2 in Table 5.2). For the 10 sheet model with a total column density of $1.5 \times 10^{22}\mathrm{cm}^{-2}$, the cooling rate is $520\pm30\ \mathrm{M_{\odot}\,yr^{-1}}$. The intrinsic absorption corrected cooling rate is consistent between 1 sheet and 10 sheets model at the 1σ level. For an order of magnitude increase in the cooling rate above 0.7 keV in RXCJ1504, it can contribute ~40 per cent of the energy required to power the UV/optical line-emitting nebula, but not all. In other massive clusters with $\dot{M}_{\mathrm{neb}} > 100\,\mathrm{M_{\odot}\,yr^{-1}}$ (such as 2A0335+096, A1835

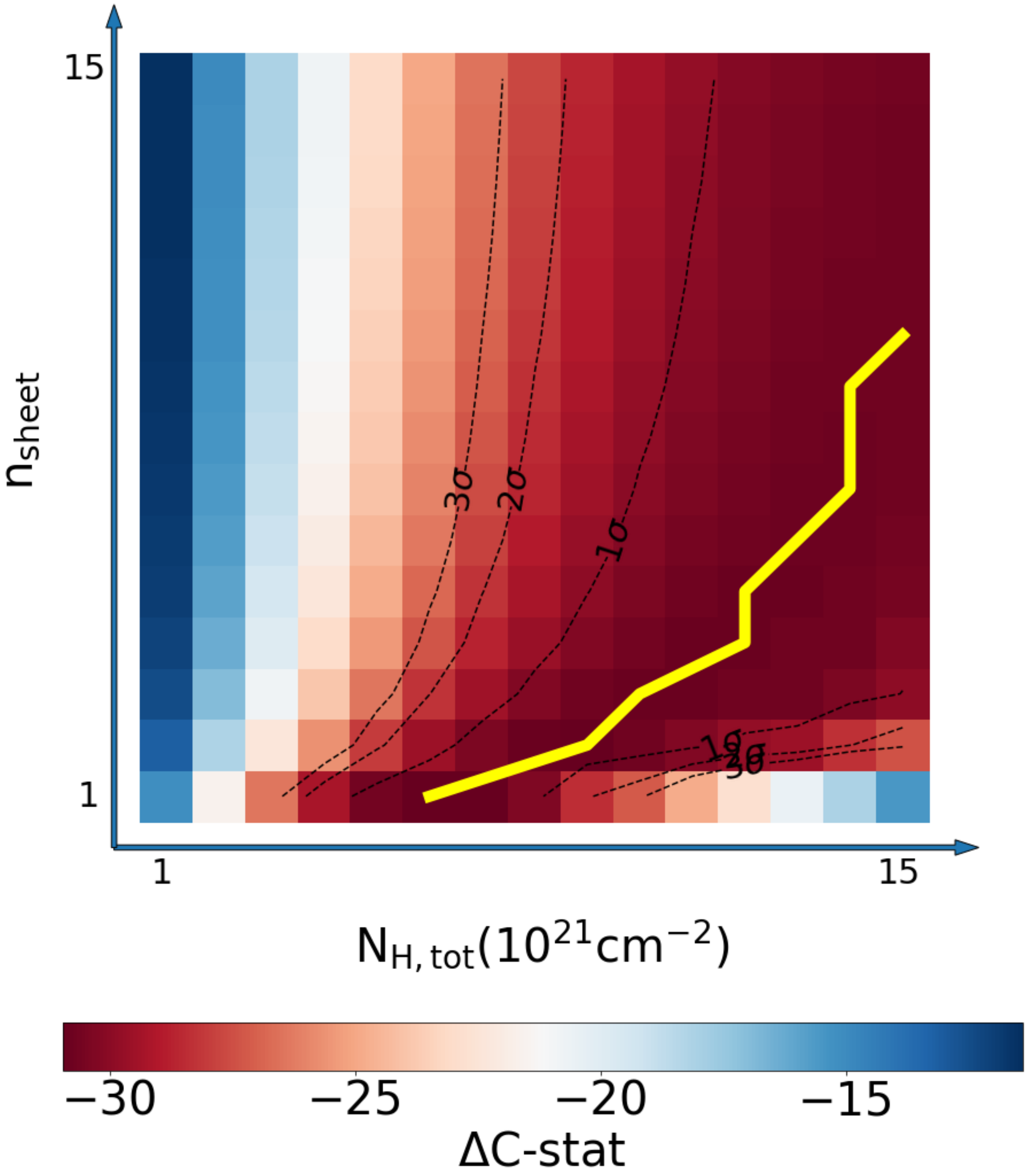

Fig. 5.6 The improvement of C-stat over the complete cooling model without intrinsic absorption. The yellow curve represents the maximum improvement of C-stat at each number of sheets of absorbing gas.

and A2597, see [113]), 10 times the cooling rate means the soft X-ray emitting gas can power the UV/optical nebula alone.

We also apply the embedded cooling flow model to A1664. For 10 sheets of absorbing gas with a total column density of 3×10^{21}cm^{-2}, we only measure a cooling rate of 31$\pm$7 $\mathrm{M}_{\odot}\,\mathrm{yr}^{-1}$. This is consistent with the cooling rate without intrinsic absorption. No significant change of the cooling rate is detected for other combinations of n_{sheet} and $n_{\mathrm{H,tot}}$. Note that the effect of embedded absorption on the optical line-emitting gas is explored by [159].

We also need to reexamine the role of absorption corrected cooling rate in the AGN feedback. It is 24 per cent of the predicted rate in the absence of heating. This only slightly reduces the amount of heating from the AGN and the black hole growth rate. On the other hand, the cooling rate is 3.3 times higher than the star formation rate. The difference between the cooling and star formation rates is 300 $\mathrm{M}_{\odot}\,\mathrm{yr}^{-1}$. This suggests the molecular gas reservoir is growing 6 times faster than the unabsorbed cooling model with a formation timescale less than 10^8 yr.

In future work, it will be interesting to reduce the degeneracy between intrinsic column density and the multilayer structure of embedded cooling flow model. Consideration will be needed for scattering of resonance lines (see studies of cool X-ray emitting gas in groups and elliptical galaxies by [155, 143]). Such lines can be absorbed by the cold gas as they scatter around in the plasma. The observational situation will be improved with the future high-spectral-resolution mission XRISM [224], with its non-dispersive calorimeter, and later by the X-IFU of Athena [9].

5.5 Conclusion

We have performed a multiphase cooling flow analysis on deep *XMM*-Newton RGS observations of two X-ray luminous cool core clusters RXCJ1504 at $z = 0.2153$ and A1664 at $z = 01283$. The cooling rate is measured to be 180$\pm$40$\mathrm{M}_{\odot}\,\mathrm{yr}^{-1}$ and 34$\pm$6$\mathrm{M}_{\odot}\,\mathrm{yr}^{-1}$ for RXCJ1504.1-0248 and A1664, respectively. It is higher than the observed star formation rate in both clusters. We detect an upper limit of residual cooling rate below 0.7 keV of 53$\mathrm{M}_{\odot}\,\mathrm{yr}^{-1}$ at 90 per cent confidence level in RXCJ1504.1-0248. The energy of the cooling gas is insufficient to power the UV/optical line-emitting nebula in both clusters and additional sources of energy are required. If the molecular gas reservoir is accumulating mass from the condensation of the radiatively cooling gas, the formation timescale is 1-3$\times10^8$ yr from the observed cooling rate but is likely longer due to the high star formation activities.

We also place a tight constraint on turbulence in the core. An upper limit of 300 km s^{-1} of 1-D turbulent velocity at 90 per cent confidence level is measured in both clusters. These velocities correspond to a Mach number of 0.23 and 0.4 for RXCJ1504.1-0248 and A1664, respectively. The energy density of turbulence is equivalent to 8.9 per cent and 27 per cent of the thermal energy density, which is inadequate to fully transfer AGN heating throughout the cooling core. We find the cool component of 0.80±0.08 keV is blueshifted from the systemic velocity of the cluster at 750^{+800}_{-280} $\mathrm{km\,s^{-1}}$ in A1664. This is consistent with the velocity of the blueshifted component in the molecular gas, but we cannot rule out an origin within a sloshing cold front for the blueshifted X-ray gas.

We reintroduce a multilayer, intrinsically-absorbed, cooling flow model. In RXCJ1504.1-0248, we find that the cooling rate increases to 520±30 $\mathrm{M_{\odot}\,yr^{-1}}$ using the 10 absorbing sheet model. This is an order of magnitude higher than the cooling rate measured without intrinsic absorption. The intrinsically absorbed cooling rate of A1664 is unaffected and consistent with the current measurement.

In the future, XRISM and Athena will help to unveil the connection between molecular and X-ray emitting gas phases and determine the influence of intrinsic absorption on cooling flows.

Chapter 6

Constraints on radiative cooling rate in galaxy clusters at intermediate redshift

Abstract

We analyse the RGS spectra of 40 cool-core clusters and search for evidence of radiative cooling flows, with particular focus onto high-redshift objects in order to extend the previous samples and search for any trend with redshift and, therefore, the age. The cooling rate is measured between the bulk ICM temperature and 0.01 keV. We obtain reliable measurements of cooling rates in 8 clusters. A combination of greater distance and shorter exposure times mean that we can only place upper limits for the rest. The soft X-ray cooling gas has sufficient energy to power optical/UV nebula with $L_{\mathrm{H}\alpha}$ up to $2 \times 10^{41}\,\mathrm{erg\,s^{-1}}$. Additional energy sources are required to power the most luminous optical line-emitting nebulae with $L_{\mathrm{H}\alpha} > 7 \times 10^{41}\,\mathrm{erg\,s^{-1}}$. In the strongest star-forming clusters, the star formation rate equals the observed cooling rate. This suggests that the molecular gas is growing slowly. Intrinsic absorption may underestimate the inferred cooling rate by a factor of 2-5 in distant luminous clusters. AGN heating balances radiative cooling in more than 80 per cent of clusters. We observe no redshift evolution of the heating to cooling ratio for z up to 0.6 from current observations.

6.1 Introduction

In Chapter 3, we analysed the RGS spectra of nearby galaxy clusters in the CHEERS sample [158, 39]. We find that the radiative cooling rate below 0.7 keV is very low in most clusters. If the gas continues to cool below that temperature, the missing X-ray luminosity should be observed in another form. Cool core clusters often have an optical line-emitting nebula which is spatially aligned with the soft X-ray gas. The missing luminosity of the soft X-ray gas likely contributes to the observed optical/UV emission. This is energetically possible for nebulae with a moderate Hα luminosity of 0.1-10$\times10^{40}\,\mathrm{ergs^{-1}}$ in the clusters of the CHEERS sample. However, more luminous Hα nebulae may require the cooling of warmer gas or have additional energy sources.

In this chapter, we expand our sample to include more luminous cool core clusters observed by the RGS onboard XMM-*Newton*. Most of these clusters have a high Hα

luminosity and are found at intermediate redshift $0.1 < z < 0.6$. The luminosity-temperature relation of clusters [4, 64, 73] shows that the bulk ICM has a temperature ranging from 5-10 keV. If radiative cooling occurs, the mean temperature of the cool core is about 2-3 keV, which means that the total line emissivity is dominated by O VIII and Fe XXII-XXIV emission [184]. Here we search for evidence of complete cooling down to < 0.01 keV and place constraints on the radiative cooling rates. This allows us to better understand the connection between the soft X-ray gas and cooler gas phases.

This chapter consists of 5 sections. The sample of clusters analysed is described in section 6.2. Section 6.3 shows the spectral analysis and results. We discuss the implication of our findings in section 6.4 and the conclusions are presented in section 6.5.

6.2 Sample and data reduction

We search the XMM-*Newton* Science Archive for observations of clusters which are reported to have optical line emission [33, 123, 79, 89, 160]. We require at least 1000 counts in the RGS spectrum after removal of particle background. Either O or Fe lines must be present so that the cooling rate can be constrained. The resulting sample contains 40 cool core clusters at redshift $0.01 < z < 0.6$ with a variety of ICM temperature, metallicity and Hα luminosity. 22 clusters have an Hα luminosity higher than $10^{41}\,\mathrm{ergs}^{-1}$. The observational details are listed in Table 6.1 and redshift and Galactic absorption information is listed in Table 6.2.

We follow the standard data reduction procedure described in 2.1. All XMM-*Newton* data were downloaded from the XSA archive and processed with the latest data reduction pipeline SAS v19.1.0. We extract the RGS spectra including 90 per cent of the cross dispersion PSF. The RGS light curve is grouped in 100s intervals and all bins with a count rate above 0.15 cts^{-1} are rejected. The RGS background is modelled by data from CCD number 9. It is also possible to use the observation background extracted beyond 98 per cent of the cross dispersion PSF. The observation background is comparable to the model background for clusters at higher redshift ($z > 0.3$, e.g. the Phoenix cluster [154]). Here we use the modelled background for all sources. The surface brightness profile is extracted from the MOS 1 image of the longest exposure in the 0.5-1.8 keV band.

All spectra are fitted with SPEX version 3.05.00 for spectral analysis with its default proto-Solar abundances and ionisation balance [114, 201]. We bin the spectra by a factor of 6 to achieve above 10 counts per bin unless otherwise stated. We use Cash-statistics and adopt uncertainties at the 68 per cent confidence level and the upper limits are defined at the 90 per cent confidence level.

Table 6.1 Observational details for extended cluster sample

Name	Obsid	Total RGS clean time (ks)
A1060	0206230101	39
AS805	0405550401/0694610101	54
A194	0136340101	21
AS555	0765010701	17
A2415	0720251201/0675472301	16
A2734	0675470801	13
RXCJ1539.5-8335	0720252501/0502670401/0502671101	12
A3806	0675472101	14
A3638	0765020101	13
A2566	0677180301/0720251301	28
A1663	0201901801	25
A478	0109880101	105
A3998	0677180401	13
RXCJ1558.3-1410	0720250201/0720253101/0675470201/0675472901	65
PKS 0745-19	0744340101/0105870101	135
A1348	0201901601	30
A1084	0201901501	29
A1068	0147630101/0827330401	53
A3378	0827330401	24
Z3179	0723161001	16
A2204	0112230301/0306490101/201/301/401	80
A2009	0693011001/0827350101	54
Hercules A	0401730101/0401730201/0401730301	120
RXCJ2014.8-2430	0201902201	26
RXJ1720.1+2638	0500670201/0500670301/0500670401	67
RXJ1750.2+3504	0673851501	31
A1914	0112230201	22
A383	0084230501	31
A291	0605000301	24
A115	0203220101	40
A3017	0692933401	93
A2390	0111270101/0111270301	11
A2667	0148990101	24
RXJ2129.6+0005	0093030201	40
Z348	0762870601	28
Z7160	0108670201	36
Z3146	0605540201/0605540301/0108670101/0108670401	233
MACS1532.9+3021	0039340101/0651240101	41
RXCJ1347.5-1144	0112960101	34
Phoenix	0693661801/0722700101/0722700201	236

Table 6.2 Redshift and Galactic absorption for extended cluster sample

Name	Redshift	D_L (Mpc)	Scale (kpc/arcsec)	$N_{\rm H}(10^{20}\,{\rm cm}^{-2})$
A1060	0.01260	52.3	0.247	6.00
AS805	0.01390	57.7	0.272	8.84
A194	0.01800	75.0	0.351	4.95
AS555	0.04400	186.9	0.832	3.92
A2415	0.05810	249.5	1.080	6.37
A2734	0.06250	269.2	1.156	1.46
RXCJ1539.5-8335	0.07280	315.9	1.331	10.5
A3806	0.07650	332.9	1.393	2.87
A3638	0.08060	351.7	1.460	7.70
A2566	0.08220	359.1	1.487	2.00
A1663	0.08430	368.8	1.521	1.72
A478	0.08810	386.5	1.583	34.0
A3998	0.08830	387.4	1.586	1.64
RXCJ1558.3-1410	0.09700	428.2	1.725	17.0
PKS 0745-19	0.10280	455.6	1.816	54.9
A1348	0.11880	532.3	2.062	3.06
A1084	0.13233	598.4	2.263	3.84
A1068	0.13750	623.9	2.338	1.83
A3378	0.14100	641.2	2.388	4.76
Z3179	0.14340	653.2	2.422	4.14
A2204	0.15216	697.0	2.546	7.17
A2009	0.15320	702.2	2.560	3.82
Hercules A	0.15500	711.3	2.585	8.78
RXCJ2014.8-2430	0.16120	742.7	2.670	11.5
RXJ1720.1+2638	0.16400	757.0	2.709	3.99
RXJ1750.2+3504	0.17057	790.6	2.797	3.18
A1914	0.17120	793.8	2.806	1.10
A383	0.18710	876.2	3.014	3.84
A291	0.19700	928.1	3.140	2.42
A115	0.19710	928.7	3.142	6.20
A3017	0.21950	1048.2	3.417	1.57
A2390	0.22800	1094.2	3.518	8.31
A2667	0.23000	1105.1	3.541	1.85
RXJ2129.6+0005	0.23500	1132.4	3.599	4.29
Z348	0.25450	1240.1	3.820	2.91
Z7160	0.25780	1258.5	3.857	3.60
Z3146	0.29060	1444.5	4.204	2.78
MACS1532.9+3021	0.36150	1764.2	4.728	2.52
RXCJ1347.5-1144	0.45100	2424.6	5.583	5.94
Phoenix	0.59600	3399.1	6.470	1.60

The redshifts are taken from the NED database (https://ned.ipac.caltech.edu/). Luminosity distance and scale are calculated by Wright [222]. The total Galactic column density $N_{\rm H}$ is taken from the UK Swift Science Data Centre (see http://www.swift.ac.uk/analysis/nhtot/; [104, 217]). The Galactic column density of A478 is taken from [38].

6.3 Spectral analysis

6.3.1 Cooling flow models

We fit the stacked spectra of RGS 1 and RGS 2 detectors. Since both detectors have a chip gap, the total effective area is halved between 10.6-13.8 Å (0.89-1.16 keV) and 20.0-24.1 Å (0.51-0.62 keV). No strong line emission except O VIII is present in these wavelength for nearby objects ($z < 0.1$). However, Fe XVII lines are shifted to the 20.0-24.1 Å (0.51-0.62 keV) band for clusters at intermediate redshift in this sample. The Fe XVII resonant line (15.0 Å at rest wavelength or 0.82 keV) falls in this band for $0.33 < z < 0.6$ (e.g. the Phoenix cluster). The Fe XVII forbidden line (17.1 Å at rest wavelength or 0.72 keV) is found in this band for $0.17 < z < 0.4$ (e.g. RXCJ1504.1-0248). Since clusters at intermediate redshift in this sample have short exposures and hence few counts, the weaker Fe XVII emission due to cooling gas below 0.7 keV may be undetectable from the ICM emission. This will lead to cooling rate limits for in these clusters.

In order to compare the results with our previous analyses, we construct the cooling flow models as in Chapter 3 and 5. We use the first order spectra between 7-28 Å (0.44-1.76 keV) in all clusters except the Phoenix cluster, where 7-33 Å (0.37-1.76 keV) is included. The Phoenix cluster has a redshift of 0.596 [15], which means that the O VIII line is shifted to 30.3 Å (0.41 keV) [154]. The O VIII line emission in Phoenix is so strong that it lies above the background emission in the only chip available at this wavelength. The RGS spectra are first modelled with an isothermal plasma (*cie* component) with a free temperature. The *cie* component is modified by the redshift, Galactic absorption and instrumental broadening. We assume that the Galactic absorption has a very cold temperature of $T = 0.5$ eV with Solar abundances [157]. The total hydrogen column density is taken from [104, 217]. For A478, the observed column density does not provide an acceptable fit. We use a higher column of $34.0 \times 10^{20}\,\mathrm{cm}^{-2}$ from the best fit value in [38]. The scale parameter is set free in the spatial broadening component (*lpro*). In a few low metallicity clusters, the wavelength shift parameter is fixed at 0 (see section 6.3.2 for details). Higher redshift clusters are much less affected by instrumental broadening. The Fe, O and Ne abundances are the free parameters and Mg is coupled to Ne. We observe the O VIII line in 30 out of 40 clusters. Since the emissivity of the O VIII line dominates over a broad energy band, it can only be used to place upper limits on the cooling rate if other strong lines (such as Fe XVII) are not present.

We measure the cooling rate by adding a *cf* component (complete/one-stage model), assuming that the *cf* component has the same metallicity as the *cie*. The cooling rate $\dot{M}_{\mathrm{1cie+1cf}}$ is determined by the differential emission measure (see equation 3.1) between the *cie* temperature and 0.01 keV. For completeness and following the approach previously discussed in previous chapters, we then add an additional *cf* component (two-stage model) so that the gas is cooling at a rate of $\dot{M}_{\rm H}$ between the *cie* temperature and 0.7 keV, and at a different rate $\dot{M}_{\rm C}$ between 0.7 and 0.01 keV. The spectra of A194 and A2734 are only fitted by the one-stage model due to lower statistics within the chosen wavelength band. The results are listed in Table 6.3.

We find that the *cie* temperature of both the one-stage and two-stage models is consistent within 1σ uncertainty. Using the one-stage model, the cooling rate is measured at better than 2σ in 8 clusters. Here, we discuss the analysis of these sources individually.

Hercules A has a similar spectrum to RXCJ1539.5-8335 but with a higher cooling rate. A strong O VIII line is observed. The one-stage model has a ΔC − stat improvement of 42, which is strong statistical evidence for a multi-temperature gas. The *cf* component has strong Fe XVII emission. The residual at the wavelength of Fe XVII lines is small due to large uncertainties. Further observation is required to improve the knowledge of the cool gas. The two-stage model improves ΔC − stat further by 4.

PKS 0745-19 has the highest Galactic absorption in this sample. The one-stage cooling flow model gives the highest cooling rate so far of 890 ± 120 $\rm M_{\odot}yr^{-1}$. This is about 5 times higher than the cooling rate determined from the EPIC data [27], where the atomic hydrogen column density of $40.5\times10^{20}\,\rm cm^{-2}$ is used. If we use the same atomic hydrogen column density on the RGS spectrum, the one-stage cooling flow model gives a cooling rate of 15 ± 4 $\rm M_{\odot}yr^{-1}$ with a core temperature of 8.4 ± 0.7 keV. This is a more reasonable cooling rate if AGN feedback occurs in this cluster. However, the C-stat is slightly worse than the best fit model with the total hydrogen column density (about 20 higher). The two-stage cooling model using atomic hydrogen column density gives $\dot{M}_{\rm H,1cie+2cf}$ of 31 ± 7 $\rm M_{\odot}yr^{-1}$ and $\dot{M}_{\rm C,1cie+2cf}$ of < 9.2 $\rm M_{\odot}yr^{-1}$.

Phoenix has a powerful obscured AGN where the contribution to the spectrum is negligible below 2 keV [199]. Both the one-stage and two-stage models fit the RGS spectrum well with the measurement of cooling rate better than 3 σ. The two-stage model improves ΔC − stat by 7 from the one-stage model. It shows a significant increase in the cooling rate $\dot{M}_{\rm H,1cie+2cf}$ in the 0.7-7 keV band, which is consistent with the cooling rate measured from MOS data [199]. Pinto et al. [154] reported the Fe XVII forbidden line is detected at 99.99 per cent confidence level indicating cool gas is present at around 0.5-0.8 keV. Our two-stage model finds that an upper limit of <194 $\dot{M}_{\rm H,1cie+2cf}$ is cooling below 0.7 keV and consistent with the results of [154]. The RGS spectrum of the Phoenix cluster is shown in Fig. 6.1. The model spectra of the *cf* components of one-stage and two-stage models show that the cooling rate is constrained by the Fe XVII and O VIII lines.

RXCJ1558.3-1410 We set the Fe abundance to 0.3 times Solar to fit the Fe-L complex. Fe XVII and O VIII lines are observed. The one-stage cooling model obtains a cooling rate of 70±15 $\mathrm{M_{\odot}yr^{-1}}$ with a $\Delta\mathrm{C-stat}$ of 22.5. The two-stage model further improves the spectral fit with a $\Delta\mathrm{C-stat}$ of 17.5, where $\dot{M}_{\mathrm{C,1cie+2cf}}$ is much higher than $\dot{M}_{\mathrm{H,1cie+2cf}}$. We find that the gas properties (e.g. temperature, metallicity and cooling rate) are similar to that of the Perseus cluster. This suggests that the high $\dot{M}_{\mathrm{C,1cie+2cf}}$ may be overestimated and due to resonance scattering of the Fe XVII lines.

A478 is affected by high absorption. The Fe XVII and O VIII lines are weaker than other strong cooling clusters. The O and Ne abundances are consistent with [38] at 0.9 arcmin. However, we find the Fe abundance of 0.8 times Solar. The one-stage model improves $\Delta\mathrm{C-stat}$ by 17 for 1 DoF. The two-stage model further reduces C-stat by 6.5 as substantial statistical evidence of multi-phase cooling. Most improvement is due to the continuum and the Fe-L complex below 13 Å (0.95 keV). Note that we use a higher column density than the Galactic column density. If the observed hydrogen (HI) density is used ($24.6 \times 10^{20}\,\mathrm{cm^{-2}}$), the one-stage model gives a cooling rate of $< 1.2\ \mathrm{M_{\odot}yr^{-1}}$ with a worse C-stat.

RXCJ1539.5-8335 has similar counts (2119) in the RGS spectrum. The uncertainty on the core temperature is much larger than most other clusters in this sample and the statistics is poor above 20 Å (0.62 keV). The one-stage model improves $\Delta\mathrm{C-stat}$ by 7.5 for 1 DoF. The improvements occurs at the Fe XVII lines and the continuum. The Mg XII line at 8.4 Å (1.47 keV) is very strong and broad. We determine a high Mg abundance of twice Solar. The Fe abundance is also twice Solar, but a strong Fe XVIII line feature at 14.2 Å (0.87 keV) is not fitted by the cooling flow models. This is likely due to poor constraints on the continuum. The two-stage cooling model measures a higher cooling rate than the one-stage model and improves $\Delta\mathrm{C-stat}$ further by 6 for 1 DoF.

AS805 is a nearby poor cluster. The spectrum has 2145 counts and shows strong Fe XVII and O VIII line emission. By setting the scale parameter of the *lpro* component to 0, the total line width is measured at $< 640\mathrm{kms^{-1}}$, which is dominated by spatial line broadening. The turbulence is expected to be low in this object. Full analysis of turbulence is not included in this work. The one-stage model improves $\Delta\mathrm{C-stat}$ (from the baseline 1*cie* model) by 4 for 1 DoF, and yields a moderate cooling rate of 1.3±0.2 $\mathrm{M_{\odot}yr^{-1}}$. The two-stage model provides a further small improvement of $\Delta\mathrm{C-stat} = 3$.

Z7160 has a strong O VIII line and Fe-L complex. Weak Fe XVII lines are also observed. The O and Fe abundances are similar to those of typical clusters (0.3-0.4 times Solar). The one-stage cooling model improves $\Delta\mathrm{C-stat}$ by 4 for 1 DoF, which indicates complete cooling of the gas. However, current data shows no evidence of multi-phase cooling, where only upper limits are obtained by the two-stage model.

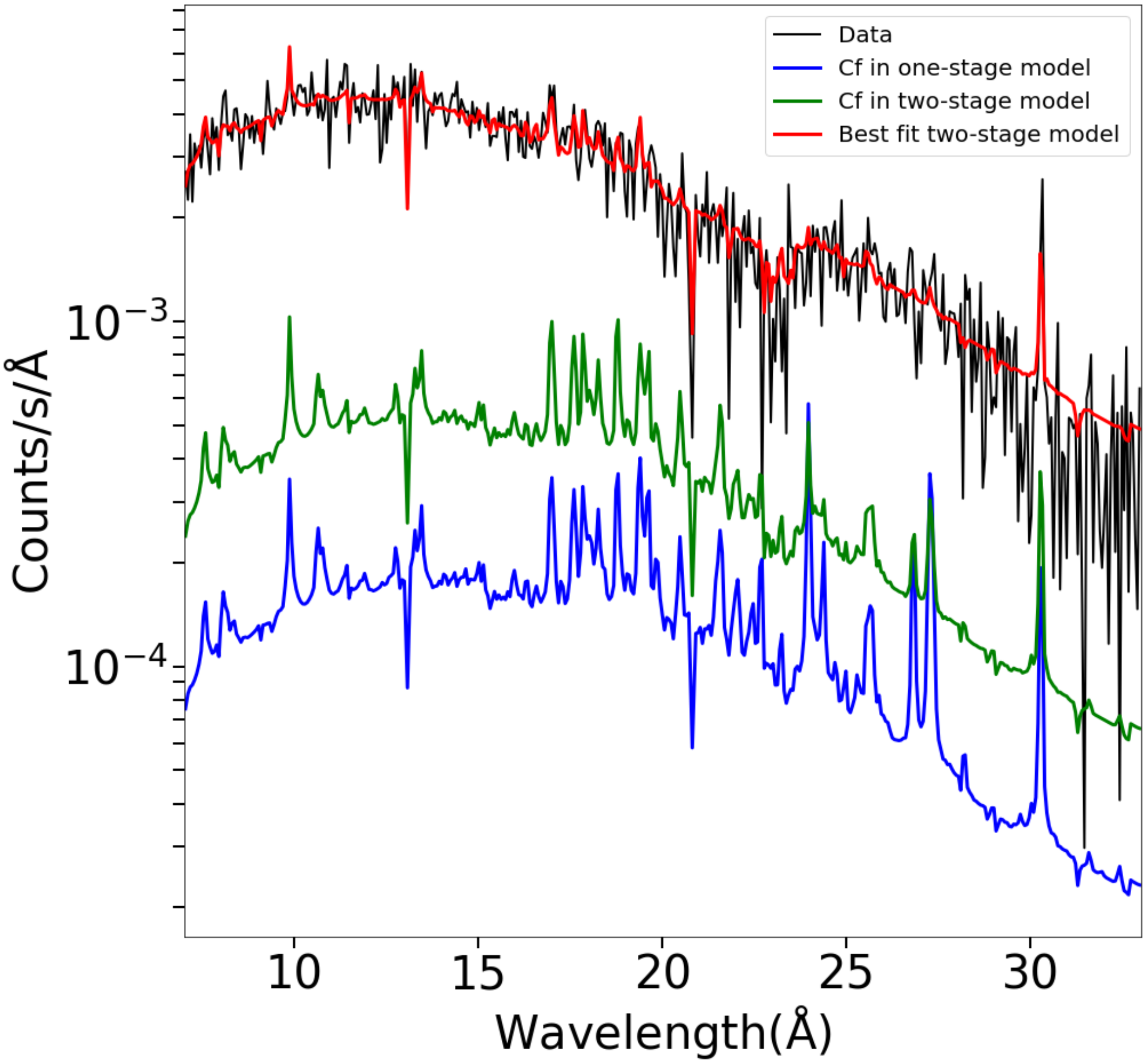

Fig. 6.1 The RGS spectrum (black) of the Phoenix cluster with the best fit two-stage model (red). The model spectrum of the *cf* components in the two-stage model is seen in green. The *cf* component of the one-stage model is seen in blue.

The improvement of C-stat of the cooling flow models is typically small ($\Delta\mathrm{C}-\mathrm{stat}<1$) for most other clusters. The current spectra only allow an upper limit on the cooling rate due to model sensitivity and relatively poor statistics of data compared to the CHEERS sample. The upper limit of $\dot{M}_{\mathrm{H,1cie+2cf}}$ is typically between 1.5-3 times higher than $\dot{M}_{\mathrm{1cie+1cf}}$. This is similar to the results of the CHEERS sample (see Chapter 3). In some clusters, the upper limit of $\dot{M}_{\mathrm{C,1cie+2cf}}$ is higher than $\dot{M}_{\mathrm{H,1cie+2cf}}$ due to the complexity of the two-stage model to the poor statistics of data. We primarily use the upper limit from the one-stage model for later analysis.

6.3.2 Low metallicity and high cooling rates

It is more challenging to apply the one-stage and two-stage models to these clusters than to the CHEERS sample due to lower counts. Here we discuss the problem of low metallicity. We find that most clusters in the CHEERS sample have an Fe abundance between 0.4 and 0.6 times Solar. In Table 6.3, we check if a cluster has a 'low metallicity' when the fitted Fe abundance is less than 0.1 times Solar within 1σ uncertainty. While some clusters are intrinsically metal poor (e.g. A194 [67]), the most likely reason for the deduced low metallicity is that the continuum is poorly constrained due to low statistics in this sample. The core temperature of clusters is determined from both the shape of the continuum and the relative line emissivities, and hence correlated to the abundances. If the uncertainty on the temperature is high due to a poorly constrained continuum, abundances tend to drop to fit the spectrum better across the whole wavelength band. In this case, local improvement of C-stat is ignored and certain line features are not fitted.

This causes trouble when fitting the cooling flow models to the data. First, the models do not always have a stable solution. Since the temperature is poorly constrained, C-stat is sometimes reduced by a small increase in temperature from the template model. If the metallicity is not determined accurately, the 'best fit' temperature will continue to rise above 10 keV as C-stat drops. This is found in distant luminous clusters, e.g. RXCJ1347.5-1144, A2390 and A3017. For these clusters, we fix the core temperature to the temperature of the 1*cie* model. The cooling rate is expected to be slightly overestimated by a fixed temperature. Second, in three clusters A1060, A194 and A3806, the wavelength shift parameter of the *lpro* component reaches the hard limit of 1 Å. Such a parameter can deviate from 0 if a gas component is blueshifted or has a different centroid, but is typically small (<0.1 Å). This is not expected in these clusters. Since these clusters are nearby ($z<0.1$), a large wavelength shift means that the models associated with wrong emission lines and hence the abundances and core temperature are inaccurate. We fix this parameter to be 0 in these clusters.

Table 6.3 Core temperature and upper limit on cooling rate

Name	$T_{\rm 1cie+1cf}$	$\dot{M}_{\rm 1cie+1cf}$	$\dot{M}_{\rm H,1cie+2cf}$	$\dot{M}_{\rm C,1cie+2cf}$	$Z/Z_{\odot} < 0.1$
A1060	1.9±0.1	<0.39	<1.0	<0.60	y
AS805	1.85 ± 0.2	1.3±0.2	1.8±0.2	0.8±0.2	y
A194	2.60	<0.59	N/A	N/A	y
AS555	1.6±0.1	<2.6	<7.1	<3.6	y
A2415	1.7±0.1	<11.7	<41.4	<9.1	y
A2734	4.31	<5.3	N/A	N/A	y
RXCJ1539.5-8335	4.8±1.1	6.4±3.1	16±7	<4.9	n
A3806	2.1±0.3	<10.1	<16.5	20.5	y
A3638	1.6±0.1	<7.8	<15.8	<13.9	y
A2566	1.8±0.1	<5.3	<9.2	<5.4	n
A1663	2.0±0.3	<9.85	<21.0	<12.8	y
A478	5.6±0.8	63±11	120±30	60±14	n
A3998	2.0±0.3	<8.4	<21.2	<13.6	n
RXCJ1558.3-1410	2.2±0.1	70±15	<17.3	140±20	n
PKS 0745-19	2.4±0.2	890±120	570±250	1200±300	n
PKS 0745-19[1]	8.4±0.7	15±4	31±7	<9.2	n
A1348	2.0±0.2	<16.4	<52.6	<21.4	n
A1084	2.5±0.2	<16.7	<47.5	<46.8	y
A1068	2.4±0.2	<9.5	<18.7	<17.5	n
A3378	2.8±0.4	<14.1	<27.8	<33.5	n
Z3179	3.9±0.9	<47.1	<17.5	<78.2	n
A2204	2.9±0.1	<65.9	<87.3	<93.6	n
A2009	4.1±0.7	<28.0	<71.5	<34	y
Hercules A	2.3±0.2	150±20	<79.4	220±40	n
RXCJ2014.8-2430	3.2±0.4	<78.7	<126	<118	n
RXJ1720.1+2638	4.1±0.4	<22.8	<46.1	<30.3	n
RXJ1750.2+3504	3.9±1.0	<36.2	<89.5	<55.3	n
A1914	5.58	<20.0	<34.3	<125	y
A383	2.8±0.4	<47.5	<101	<68.9	n
A291	2.6±0.2	<75.9	<69.6	<122	n
A115	4.3±1.4	<120	<243	<159	y
A3017	2.54	<75.8	<115	<272	y
A2390	2.54	<100	<112	<467	y
A2667	4.9±0.9	<122	<185	<236	n
RXJ2129.6+0005	3.4±0.5	<105	<46.2	<195	y
Z348	2.2±0.3	<138	<360	<245	n
Z7160	3.5±0.5	141±69	<283	<220	n
Z3146	4.5±0.3	<51.0	<98.2	<78.5	n
MACS1532.9+3021	3.3±0.3	<97	<258	<281	n
RXCJ1347.5-1144	3.86	<567	<1020	<1020	y
Phoenix	6.8±0.5	230±90	630±170	<194	n

The temperature is shown in keV and the cooling rates are measured in $\mathrm{M_{\odot}yr^{-1}}$. The core temperature is fixed in some clusters to obtain an stable spectral fit. [1] The second entry of PKS 0745-19 is modelled using the atomic hydrogen column density in the absorption component.

One consequence of 'low metallicity' is a high cooling rate (limit). The cooling rate is overestimate by at least a factor of 2 so that the emission of the strongest lines due to cool gas (e.g. Fe XVII) is similar to the emission of gas with a typical metallicity of $z/z_\odot = 0.3$ (e.g. RXCJ1347.5-1144 [74]). For all clusters which are classified as 'low metallicity', we fix $z/z_\odot = 0.3$ to obtain a lower upper limit of the cooling rates.

6.4 Discussion

6.4.1 Implications of cooling rate limits

In this section, we provide a brief discussion of the implications of cooling rate from all clusters studied in this thesis. Table 6.4 lists relevant gas properties deduced from literature.

Hα nebulae

One of the most important implications of our results in the previous chapters is the possible connection between the soft X-ray cooling gas and the optical line-emitting gas due to the spatial coincidence of the two gas phases. Optical line emission can be characterised by the Hα line and is often seen in cool core clusters, which are observed either in the form of nebula or filaments. In the two-stage cooling flow model, we find that the upper limit of the residual cooling below 0.7 keV is typically low in the spectra of clusters with high statistics. It is possible that the gas is cooling faster than the radiative process below 0.7 keV. The ions and electrons of the cooling gas at this temperature have a thermal energy of 0.7 keV each. This energy is not seen in the X-ray band which we call the 'missing luminosity' [57]. The missing luminosity likely contributes to the total optical/UV emission seen. We assume that the total optical/UV luminosity scales with $L_{\mathrm{H}\alpha}$ by a factor of 15. This can be converted into a mass cooling rate $\dot{M}_{\mathrm{neb}}$ using equation 3.2.

For most clusters in this sample, we calculate the Hα luminosity from [79]. We show that this sample has a broad range of $L_{\mathrm{H}\alpha}$ ($10^{38} - 10^{43}\mathrm{erg\,s^{-1}}$). This complements the CHEERS sample, which only has four clusters with $\dot{M}_{\mathrm{neb}} > 100$ $\mathrm{M_\odot yr^{-1}}$. We combine both samples and the two new observations of RXCJ1504.1-0248 and A1664 from Chapter 5. The result is seen is Fig. 6.2. For clusters in this sample, we use the more conservative cooling rate limit from the one-stage model if the two-stage does not statistically improve the spectral fit. The combined sample strongly supports the result from using CHEERS sample alone. We can separate $\dot{M}_{\mathrm{neb}}$ into three regimes. For the low $\dot{M}_{\mathrm{neb}}$ limit up to ~ 30 $\mathrm{M_\odot yr^{-1}}$ (~ 10 $\mathrm{M_\odot yr^{-1}}$ from the CHEERS sample alone), we find that the missing luminosity of the 0.7 keV gas in most clusters is at least 2-5 times more than required to power the nebulae. This

Table 6.4 Gas properties deduced from literature

Name	$L_{\mathrm{H}\alpha}(10^{40}\mathrm{erg\,s^{-1}})$	$\dot{M}_{\mathrm{neb}}$	$\dot{M}_{\mathrm{simple,7.7Gyr}}$	$\dot{M}_{\mathrm{SFR}}$	M_{mol}	Reference
A1060	0.055 ± 0.003	0.08 ± 0.005	5.93	$0.09\pm^{0.06}_{0.04}$	/	[a]
AS805	0.06 ± 0.03	0.09 ± 0.04	/	/	/	[a]
A194	0.38 ± 0.02	0.54 ± 0.04	/	/	/	[a]
AS555	4.4 ± 0.3	6.3 ± 0.5	/	/	/	[a]
A2415	3.7 ± 0.3	5.2 ± 0.4	/	/	/	[a]
A2734	0.9 ± 0.1	1.3 ± 0.2	/	/	/	[a]
RXCJ1539.5-8335	24 ± 1	33 ± 2	90.7	$1.9\pm^{0.3}_{0.2}$	11	[a,f]
A3806	2.0 ± 0.3	2.8 ± 0.4	/	/	/	[a]
A3638	5.5 ± 0.4	7.8 ± 0.5	/	/	/	[a]
A2566	7.9 ± 0.4	11.2 ± 0.6	/	/	/	[a]
A1663	1.4 ± 0.2	2.0 ± 0.3	/	/	/	[a]
A478	22 ± 1	31 ± 2	290	1.9 ± 0.2	2.6 ± 1.5	[a,c]
A3998	5.8 ± 0.3	8.2 ± 0.5	/	/	/	[a]
RXCJ1558.3-1410	18.5 ± 0.9	26 ± 1	126	$6\pm^{8}_{3}$	/	[a]
PKS 0745-19	130	184	473	$13\pm^{10}_{6}$	4.2 ± 0.2	[b,g]
A1348	27 ± 2	38 ± 3	/	/	/	[a]
A1084	15.2 ± 0.8	22 ± 1	/	/	/	[a]
A1068	157	222	171	$11\pm^{15}_{6}$	39 ± 2	[b,]
A3378	3.9 ± 0.4	5.5 ± 0.6	/	/	/	[a]
Z3179	3.3 ± 0.6	4.7 ± 0.8	/	/	/	[a]
A2204	106	150	221	$8\pm^{4}_{2}$	13 ± 3	[c]
A2009	5.81	8.22	/	/	/	[d]
Hercules A	23.2 ± 0.9	32 ± 1	56.4	$0.4\pm^{0.9}_{0.3}$	/	[a]
RXCJ2014.8-2430	116 ± 5	164 ± 7	/	/	/	[a]
RXJ1720.1+2638	7.15	10.1	426^{1}	$1.5\pm^{1.3}_{0.6}$	/	[a]
RXJ1750.2+350	8.03	11.4	/	/	/	[a]
A1914	/	/	75.4	/	/	
A383	35 ± 2	49 ± 3	166	$1.5\pm^{1.1}_{0.6}$	/	[a]
A291	175 ± 7	250 ± 10	/	/	<13	[a,c]
A115	10.1	14.3	/	/	/	[d]
A3017	92 ± 4	130 ± 5	/	/	/	[a]
A2390	69 ± 3	97 ± 5	174	$11\pm^{12}_{6}$	<28	[a,c]
A2667	/	/	200	/	/	
RXJ2129.6+0005	31 ± 2	44 ± 3	229^{1}	$3\pm^{3}_{2}$	/	[a]
Z348	290 ± 10	410 ± 20	/	/	/	[a]
Z7160	33.2	47.0	602^{1}	$11\pm^{11}_{5}$	35 ± 14	[c]
Z3146	466	659	427	$70\pm^{80}_{40}$	90 ± 20	[c]
MACS1532.9+3021	280	396	1070^{1}	$100\pm^{50}_{30}$	140 ± 20	[a,c]
RXCJ1347.5-1144	200	283	635	$12\pm^{8}_{5}$	<39	[a,c]
Phoenix	8500 ± 500	12100 ± 700	1700^{1}	740 ± 160	20	[e,h]

The references for $L_{\mathrm{H}\alpha}$ are [a] Hamer et al. [79], [b] Salomé and Combes [171], [c] Edge [46], [d] Crawford et al. [33], [e] McDonald et al. [123], We use the star formation rates from McDonald et al. [117, 119], ^{1} The classical cooling rate for these objects is taken from McDonald et al. [119]. All of the mass rates are expressed in $\mathrm{M}_{\odot}\mathrm{yr}^{-1}$. The molecular mass is expressed in $10^{9}M_{\odot}$ and the references are [b] Salomé and Combes [171], [c] Edge [46], [f] Olivares et al. [145], [g] Russell et al. [169], [h] Russell et al. [166].

allows correction of a different scaling factor between the total optical/UV emission and $L_{\mathrm{H}\alpha}$. We use a different scaling factor of 30 and find that the conclusion is not significantly affected. For the most luminous Hα nebulae, additional power is required either from the hotter X-ray atmosphere or other energy sources. The energy deficit in e.g. the Phoenix cluster is about 20 times the energy deduced from the cooling rate, which is comparable to the AGN heating estimated from the CHEERS sample. This suggests that AGN feedback is not only balancing cooling but also powering the extended nebular emission. The high $\dot{M}_{\mathrm{neb}}$ boundary likely occurs at around 100 $\mathrm{M}_{\odot}\mathrm{yr}^{-1}$. We obtain data from 12 additional sources above this threshold. This is 3 times the number of sources in the CHEERS sample which meet the criterion. Clusters with $\dot{M}_{\mathrm{neb}}$ between 30-100 $\mathrm{M}_{\odot}\mathrm{yr}^{-1}$ have not been observed by the RGS.

Star formation rates & molecular gas

Now we consider the by-product of the cooling flow. We first plot the cooling rate against the star formation rate. We find that for most clusters with moderate star formation $\dot{M}_{\mathrm{SFR}} < 10$ $\mathrm{M}_{\odot}\mathrm{yr}^{-1}$, the cooling rate is at least 5 times higher (see Fig. 6.3). This means that most gas is cooled directly into the molecular phase. The observed molecular filaments can then form rapidly. On the high $\dot{M}_{\mathrm{SFR}}$ limit, the star formation rate almost matches the cooling rate. This occurs almost exclusively in intermediate redshift cluster ($z \sim 0.2-0.6$) at the tail of the strong cosmic star formation activity [8] except Perseus. Radiative cooling likely sets an upper limit to the maximum star formation rate until AGN feedback operates in a different mode. The net result is of closely matched cooling rate and star formation rate is that the molecular gas is growing very slowly. Observations of massive molecular filaments in the Phoenix cluster [166] suggest that either the ICM was cooling at a much higher rate in the past or the filaments formed in a very long timescale. We show the cooling rate against the molecular gas mass in Fig. 6.4. We temporarily ignore the effect of star formation. The molecular gas clouds then form within 1 Gyr and some even less than 0.1 Gyr. This is comparable to the radiative cooling time in the core. If we consider the star formation rate in the most massive clusters, the formation timescale of molecular gas is then longer than 10 Gyr. This is unlikely as it traces back to the early universe ($z > 1$) when star formation was also much higher. One possible explanation is that AGN operates in a different mode at higher redshift and heating balances cooling poorly. We briefly discuss the redshift evolution in section 6.4.2. An alternative solution is the intrinsic absorption of the cluster (see section 6.4.3).

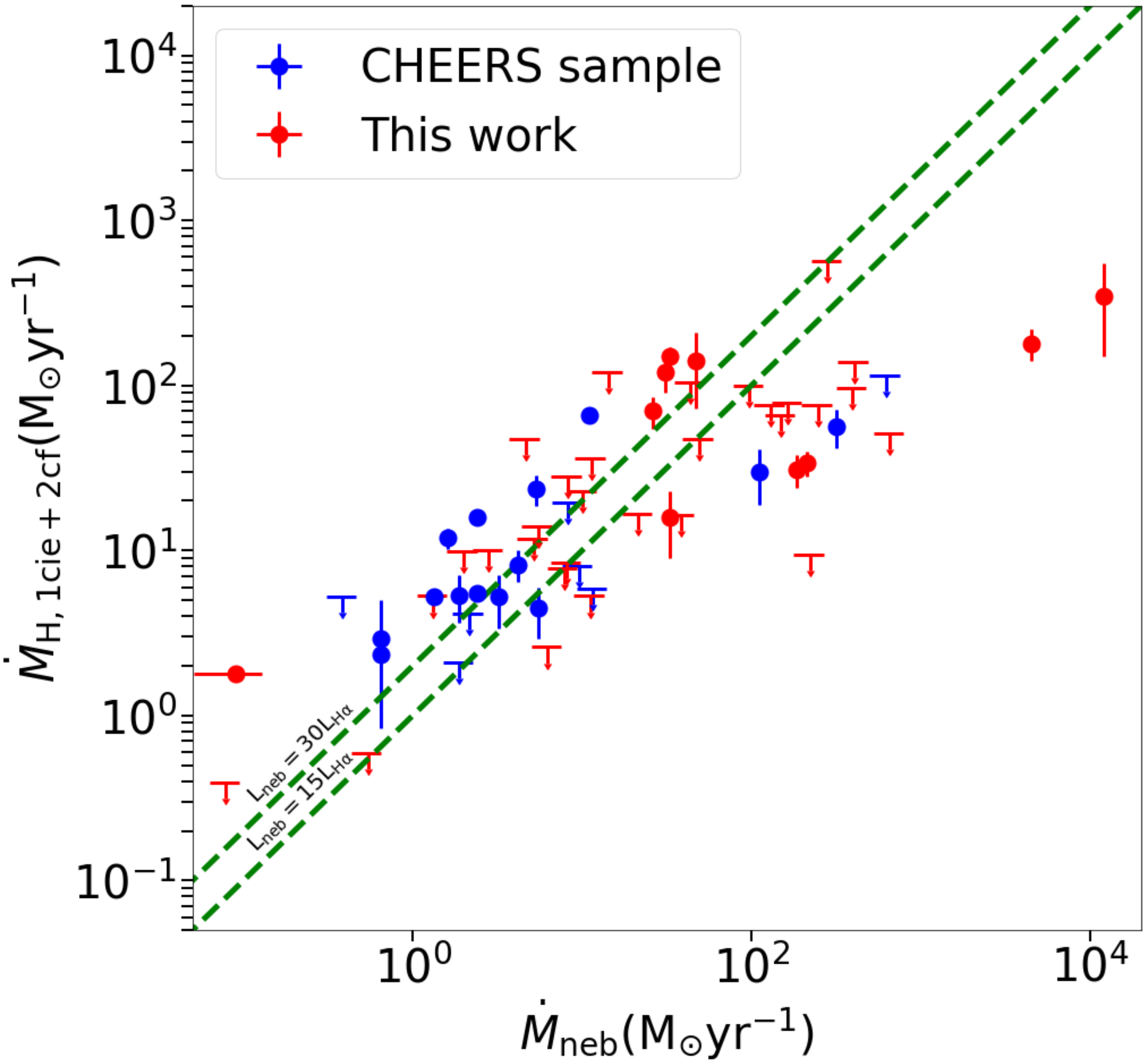

Fig. 6.2 The X-ray cooling rate versus the total optical/UV emission. Sources from the CHEERS sample are shown in blue. Clusters from this work are seen in red. Green dash lines represent the ratio of the total optical/UV emission to Hα luminosity.

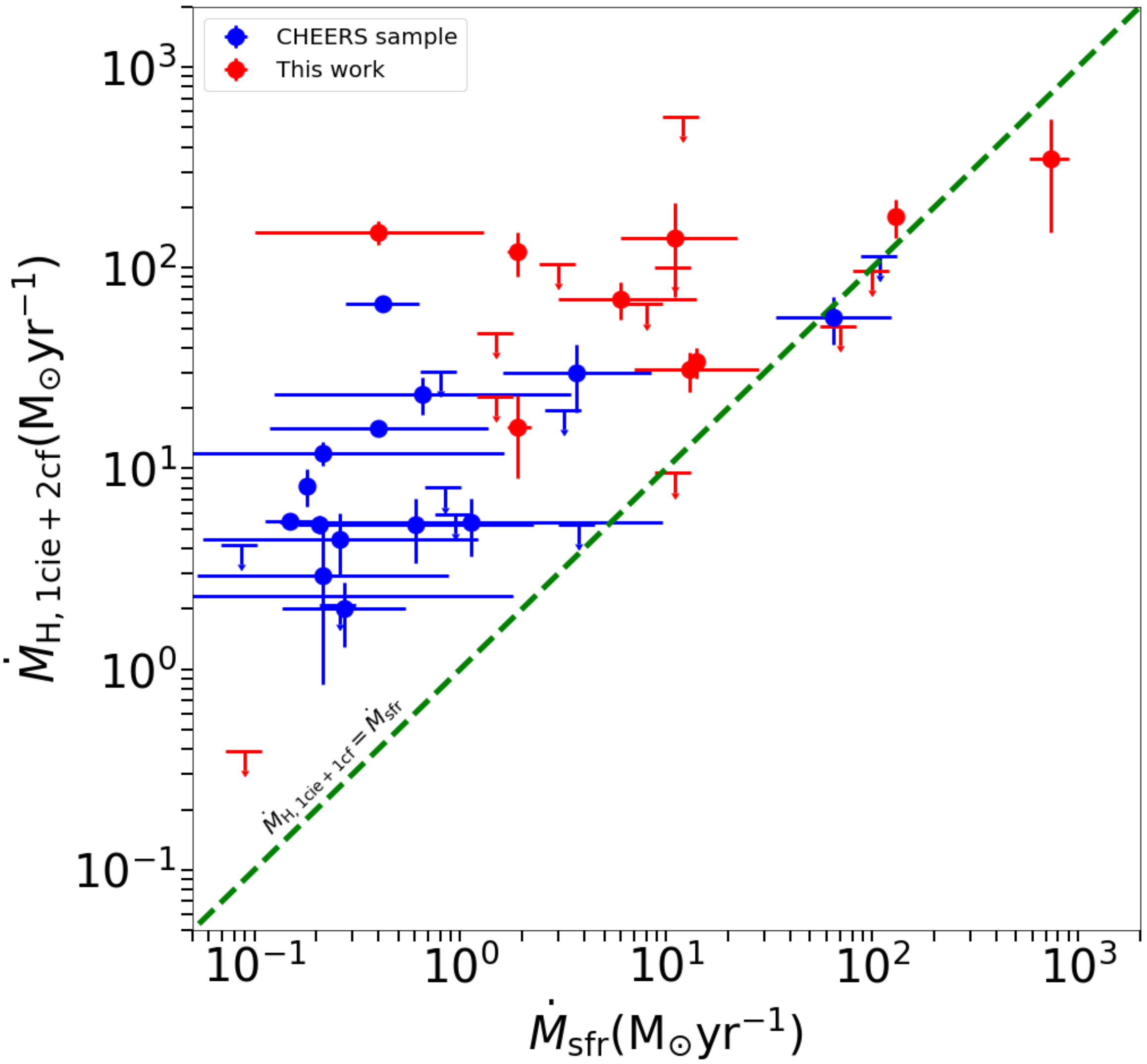

Fig. 6.3 Comparison between the X-ray cooling rate and star formation.

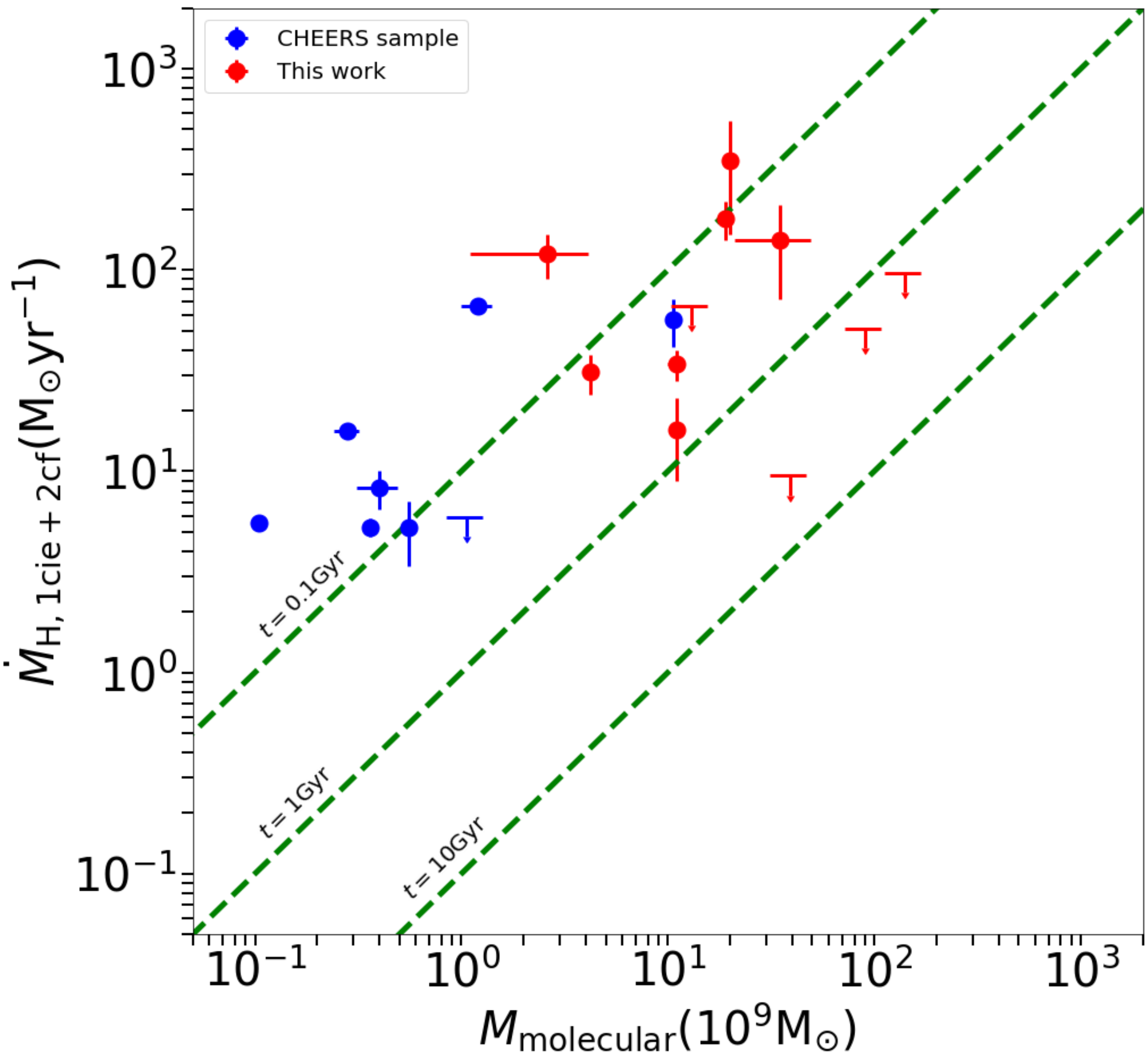

Fig. 6.4 Comparison between the X-ray cooling rate and molecular gas mass. Green dash lines represent the timescale required to form the observed molecular gas cloud directly from X-ray cooling.

6.4.2 Classical cooling rate & redshift evolution

The classical cooling rate commonly refers to the predicted maximum cooling rate in the absence of heating (see section 1.4.2). Here we calculate the classical cooling rate within the radius where the cooling time is 7.7 Gyr. We model the density profile from [26] with the function of form $n_e = Ar^b$ within the same radius. The results are seen in Table 6.4 ($\dot{M}_{\rm simple,7.7Gyr}$). By comparing our calculation with other studies (e.g. [119]), $\dot{M}_{\rm simple,7.7Gyr}$ is likely underestimated by a factor of 1.5-2. As the classical cooling rate is estimated globally, we compare $\dot{M}_{\rm simple,7.7Gyr}$ with the one-stage cooling rate $\dot{M}_{\rm 1cie+1cf}$ in Fig. 6.5. We combine the CHEERS sample and this sample and report 54 sources with a known classical cooling rate.

The ratio of $\dot{M}_{\rm 1cie+1cf}$ to $\dot{M}_{\rm simple,7.7Gyr}$ indicates the amount of extra heating required to exactly offset radiative cooling. In all clusters but one, the heating from AGN can quench at least 50 per cent of the predicted cooling rate. Depending on whether we increase $\dot{M}_{\rm simple,7.7Gyr}$ by a factor of 2 or not, AGN heating is above 80-90 per cent of the predicted cooling in at least 42 sources. These strongly suggest that AGN heating is efficient at reducing radiative cooling.

One anomaly is observed in Hercules A. Our result shows that the cooling rate is a factor of 3 higher than the classical cooling rate. Considering the high uncertainty of the Fe XVII lines and underestimation of $\dot{M}_{\rm simple,7.7Gyr}$, the cluster is likely cooling at the maximum rate possible if not above. Radio and Chandra observations [75, 137] shows that Hercules A has two bright radio jets which inflate X-ray cavities. It has a powerful FR2 radio source and the radio jets are almost symmetric and extending over 250 kpc. A strong shock front is detected at 160 kpc and heating the surrounding ICM. The mean power of the outburst is $1.6 \times 10^{46}{\rm erg\,s^{-1}}$ [137], which is more than sufficient to offset radiative cooling. The problem of energy dissipation needs to be considered. Most heating is transported by jets and gently dissipates away from the jet axis. The scale of the radio structure is much larger than the size of the cool core ($\sim$60 kpc in radius) and so the cooling gas is not heated directly by jets. If the energy dissipates through sound waves (the local sound speed is $\sim 800\,{\rm km\,s^{-1}}$), it travels $\sim 50-60$ kpc at the age of the outburst of 5.9×10^7 yr [137]. The heating just has enough time to reach the full core. However, the mystery of the high observed cooling rate is not explained. It will be interesting to measure the cooling rate more accurately with future observations.

Finally we need to consider the possibility of redshift evolution of AGN heating and cooling. Note that our combined sample is biased and selected based on the quality of spectral features. We regroup the 54 clusters into three redshift bins so that each bin has a similar number of sources. The redshift bins are $z < 0.036$, $0.036 < z < 0.1$ and $z > 0.1$. Clusters with $z > 0.1$ are at intermediate redshift.

We observe no apparent redshift evolution of the $\dot{M}_{\rm 1cie+1cf}$ to $\dot{M}_{\rm simple,7.7Gyr}$ ratio. 17 out of 19 nearest sources are consistent with $\dot{M}_{\rm 1cie+1cf}/\dot{M}_{\rm simple,7.7Gyr} < 0.1$. A similar fraction of 16 out of 17 is found for clusters $0.036 < z < 0.1$. For clusters at intermediate redshift, we report the upper limit of the cooling rate in most cases. The cooling rate is measured above 2σ in 7 clusters at intermediate redshift. Two of these clusters have $\dot{M}_{\rm 1cie+1cf}/\dot{M}_{\rm simple,7.7Gyr} > 0.1$. It is difficult to draw any firm conclusions from the current observations [1].

6.4.3 Intrinsic cold absorption

In section 5.4.4, we reintroduced a simple multilayer cooling flow (embedded *cf*) model considering the effect of intrinsic absorption due to the cold gas in clusters [1]. We assume a simple geometry of parallel and alternating gas sheets of X-ray cooling and cold molecular material (see Fig. 5.5). Each X-ray cooling gas sheet will be absorbed by all the foreground molecular gas sheets in the line-of-sight. Due to the limitation of the current SPEX fitting package, we implement a brute-force model using multiple absorption (*hot*) and *cf* components. We assume the absorption component has Solar metallicity and cold $T = 0.5$ eV. The additional free parameters are the number of gas sheets $n_{\rm sheet}$ and the total column density $n_{\rm H,tot}$. Applying the embedded *cf* model to RXCJ1504.1-0248, we find that the complete cooling rate increases by an order of magnitude.

Here we first apply the same model to 3 more clusters with a measurement of the complete cooling rate, Centaurus (A3526), A1835 and Phoenix. The spectra of these clusters have more than 25000 counts, which are higher than most other clusters at their redshift ($z = 0.0114$, 0.253 and 0.596, respectively). In the $n_{\rm sheet}$ and $n_{\rm H,tot}$ parameter space, we are interested in the 'absorption corrected' complete cooling rate and the C-stat for a chosen combination of the free parameters. The minimum C-stat for each $n_{\rm sheet}$ forms a valley along $n_{\rm H,tot}$ in RXCJ1504.1-0248 (see Fig. 5.6). We observed the same pattern in the Phoenix cluster. Along this valley, the difference in C-stat is very small (< 0.1) and the 'corrected' cooling rate is consistent within 1σ for $n_{\rm sheet} < 10$. Allen and Fabian [1] suggested that a large value of $n_{\rm sheet}$ is likely the general solution. For simplicity, we present results using the embedded *cf* model with $n_{\rm sheet} = 10$ in Table 6.5.

We find that the complete cooling rate is amplified by a factor of 5 in the Phoenix cluster if the intrinsic absorption has a column density of $1.1 \times 10^{22}\,{\rm cm}^{-2}$. The cooling rate of A3526 and A1835 is much less affected and consistent with the one-stage cooling model without

---

[1] We also observe no trend of redshift evolution of the measured-to-predicted ratio if $\dot{M}_{\rm H,1cie+2cf}$ is used.

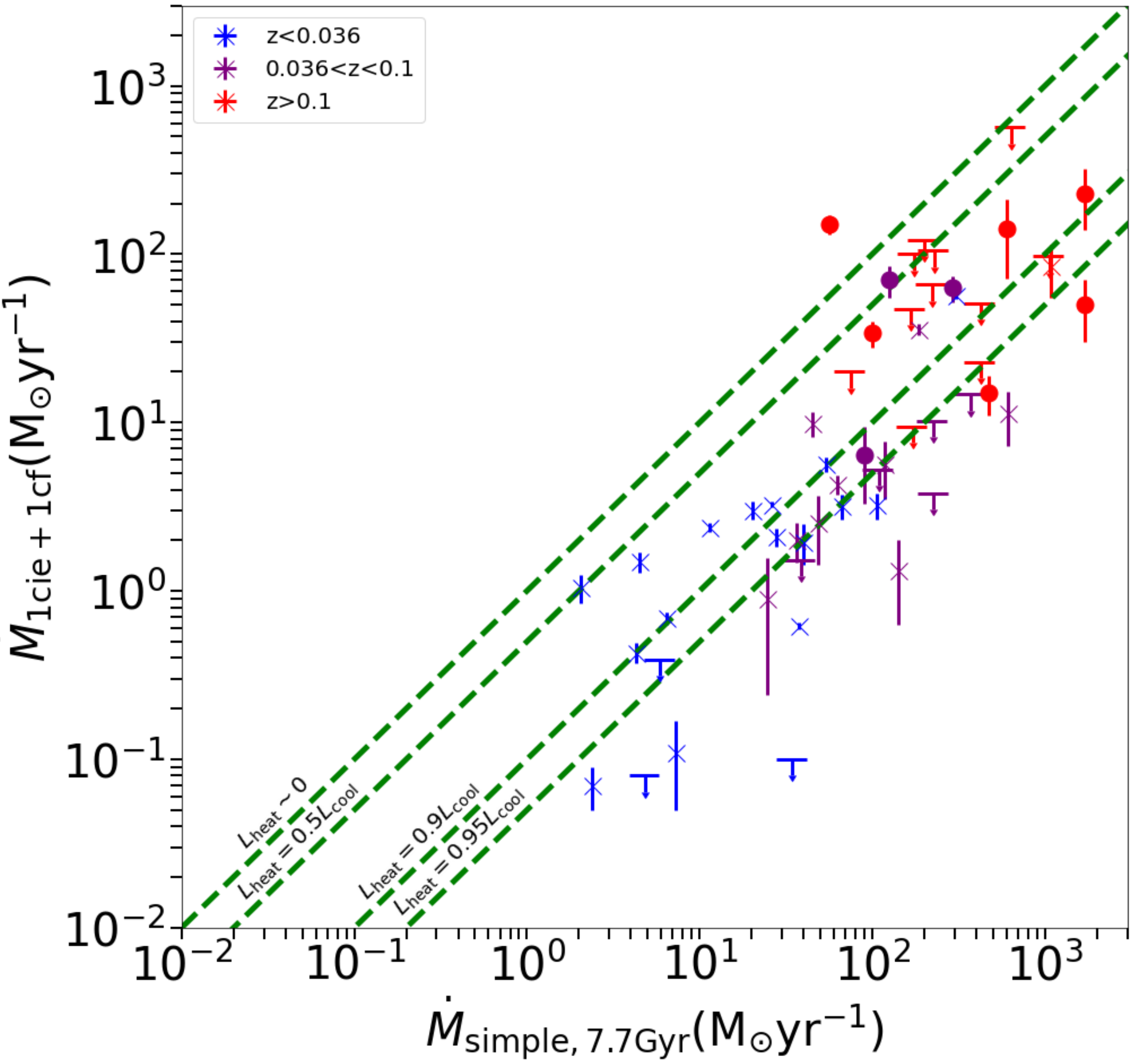

Fig. 6.5 The X-ray cooling rate versus the classical cooling rate predicted in the absence of heating. $L_{\rm cool}$ is the luminosity of the classical cooling rate. CHEERS sample with a detection of cooling rate is shown in cross and this sample is seen in circle. Green dash lines represent the ratio of heating to unheated cooling rate.

Table 6.5 Summary of results of embedded cooling flow model

Name	$n_{\rm H,tot}(10^{20}\,{\rm cm}^{-2})$	$\dot{M}_{\rm w/absorption}$ $({\rm M}_{\odot}{\rm yr}^{-1})$	$\Delta{\rm C}-{\rm stat}$
A3526	30	3.4±0.3	12
A1664	30	31 ±7	1
RXCJ1504.1-0248	150	520±30	31
A1835	30	110±40	1
Phoenix	110	1300±300	6.2

$\Delta{\rm C}-{\rm stat}$ is the improvement of C-stat from the one-stage model without intrinsic absorption.

intrinsic absorption [2]. The effect of different intrinsic column densities on the complete cooling rate in A1835 is seen in Fig. 6.6. The improvement of C-stat of the intrinsically absorbed model is small and the cooling rate is consistent within 1σ to the unabsorbed model.

The signature of the Fe XVII lines is very weak in the RGS spectrum. As a result, the *cf* component only contributes to ~ 1 per cent of the observed flux in the standard unabsorbed one-stage model. To preserve the total line emission of Fe XVII and O VIII, the continuum emission of the *cf* component drops when intrinsic absorption is introduced. The effect of absorption is stronger for longer wavelengths where the spectrum has lower counts per bin and the background dominates. Both the intrinsically absorbed and the standard cooling flow models fit the spectrum poorly at these wavelength and the continuum emission is dominated by the *cie* component (hot ICM). The difference of C-stat is hence very small.

The redshift is likely a key factor in A3526, where the effect is two-fold. A3526 is a nearby extended object. Since the RGS is a slitless detector, the emission lines are artificially broadened by the spatial extent. The spectrum of A3526 has high statistics such that any multi-component model can be well fitted by two line broadening components [181, 158, 113]. This is due to different gas temperatures that are spatially resolved in different scales. The geometry of the embedded cooling flow model is hence likely an oversimplification in A3526. A general solution for A3526 might include different intrinsic column densities and the number of gas sheets for different gas temperatures, which is beyond the scope of this work. RXCJ1504.1-0248 and Phoenix are more distant and so much less affected by spatial broadening. The O VIII line in the Phoenix cluster is indeed narrow [154]. The emission lines can be more easily modelled since the correction of spatial broadening is only an approximation.

Galactic absorption must also be considered. RXCJ1504.1-0248 and Phoenix have a low to moderate column density ($< 10^{21}\,\mathrm{cm}^{-2}$) and so the line emission is less absorbed than A3526. Furthermore, the observed wavelength of the strongest lines is much different from the rest wavelength in RXCJ1504.1-0248 and Phoenix due to higher redshift, which means is likely less affected by Galactic absorption. On the other hand, the spectrum of A3526 is observed almost at the rest wavelength. The question of whether the embedded cooling flow model works better on high redshift objects will be investigated in future research.

The gas properties of RXCJ1504.1-0248 and Phoenix are also fundamentally different from A3526. The continuum of these high redshift clusters is much stronger and so the Fe XVII lines are less prominent than in A3526. This can be interpreted as either a weak cooling flow

---

[2] Note that the effect of intrinsic absorption is more significant in A3526 using a more complicated 5-stage cooling model [181].

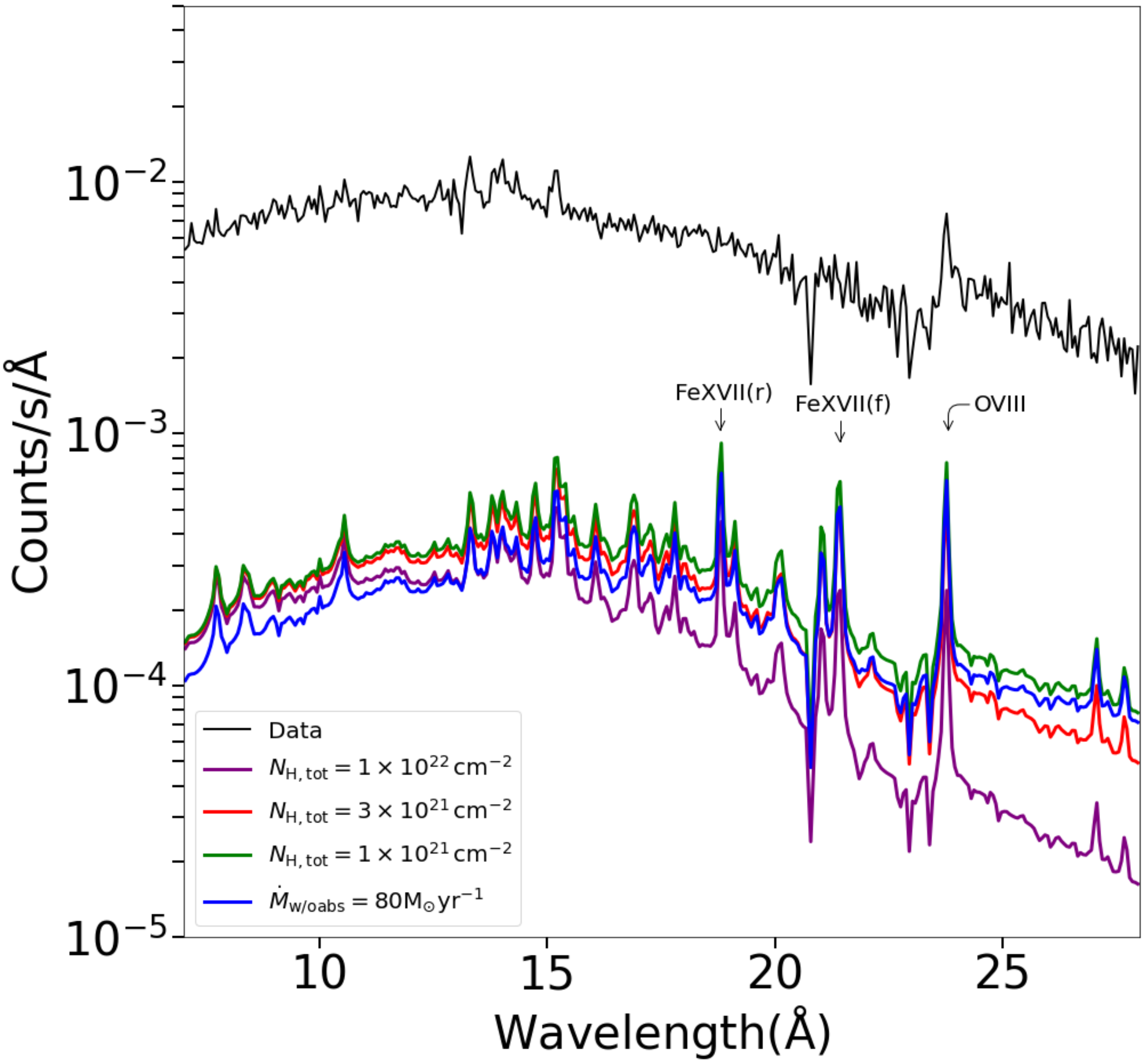

Fig. 6.6 The stacked RGS spectrum (black) of A1835 with model spectra of the intrinsically absorbed cooling flow components. For the intrinsically absorbed models, we use a cooling rate of 110 $\rm M_\odot yr^{-1}$. The cooling flow component of the best fit unabsorbed one-stage cooling model is seen in blue.

or a strong cooling flow affected by absorption. The cooling rate can be further constrained by all emission lines and the shape of the continuum. Both RXCJ1504.1-0248 and Phoenix have a highly luminous Hα nebula [144, 123] and star formation rates [144, 118, 123]. The embedded cooling flow provides a partial explanation for the observed optical emission and the formation of massive molecular gas filaments [166, 203].

Now we consider the problem of intrinsic column density. The $n_{\mathrm{H,tot}}$ listed in Table 6.5 is only the statistical best fit value of in the 10 sheet case instead of measured from observations. The embedded cooling flow model requires a large scale (similar to the size of the cool core) of molecular gas sheets. It is possible to make an order of magnitude estimate of the mass of these gas sheets. A 1 kpc^2 region of $10^{22}\,\mathrm{cm}^{-2}$ contains $10^8\mathrm{M}_\odot$. From the observed molecular gas mass, the gas sheets cover a $\sim 200\,\mathrm{kpc}^2$ region. It is similar to the coolest region of nearby clusters but much smaller than the 0.9 arcmin core of RXCJ1504.1-0248 and Phoenix. The molecular gas sheets can cover a much larger region if the column density is similar to that of the Galactic plane (see e.g. PKS 0745-19) or larger ($> 10^{23}\,\mathrm{cm}^{-2}$). This means further development of the embedded cooling flow model needs independent measurement of intrinsic column density.

We apply the embedded cooling flow model to 3 additional clusters (A2204, RXJ1720.1+2638 and Z3146) at intermediate redshift in this sample. The RGS spectra of these clusters have at least 10000 counts and we only obtain an upper limit of the unabsorbed complete cooling rate at 90 per cent confidence level. We use a set of intrinsic column densities until the absorption corrected cooling rate limit is similar to $\dot{M}_{\mathrm{neb}}$. The results are plotted in Fig. 6.7. We observe a general trend of increasing upper limits of the complete cooling rate with higher column densities. For the Phoenix cluster, we obtain reliable measurements for $n_{\mathrm{H,tot}} < 3\times 10^{22}\,\mathrm{cm}^{-2}$. It requires a very high intrinsic column density of $10^{24}\,\mathrm{cm}^{-2}$ so that the cooling rate limit is comparable to $\dot{M}_{\mathrm{neb}}$. However, such a high column density would prevent observations in other wavelengths, which is not the case. For most other clusters, the embedded cooling flow model can explain the observed optical nebular emission with a slightly lower column density between $4\times 10^{22}\,\mathrm{cm}^{-2}$ and $10^{23}\,\mathrm{cm}^{-2}$.

6.5 Conclusion

In this chapter, we studied the RGS spectra of 40 additional cool core clusters which have optical line emission. We obtain reliable measurement of the complete cooling rate above 2σ only in 8 clusters. For the other 32 clusters, we provide the upper limit of the complete cooling rate at 90 per cent confidence level. In A478, RXCJ1539.5-8335, PKS 0745-19 and Phoenix, we further apply the two-stage model and obtain a better spectral fit than the

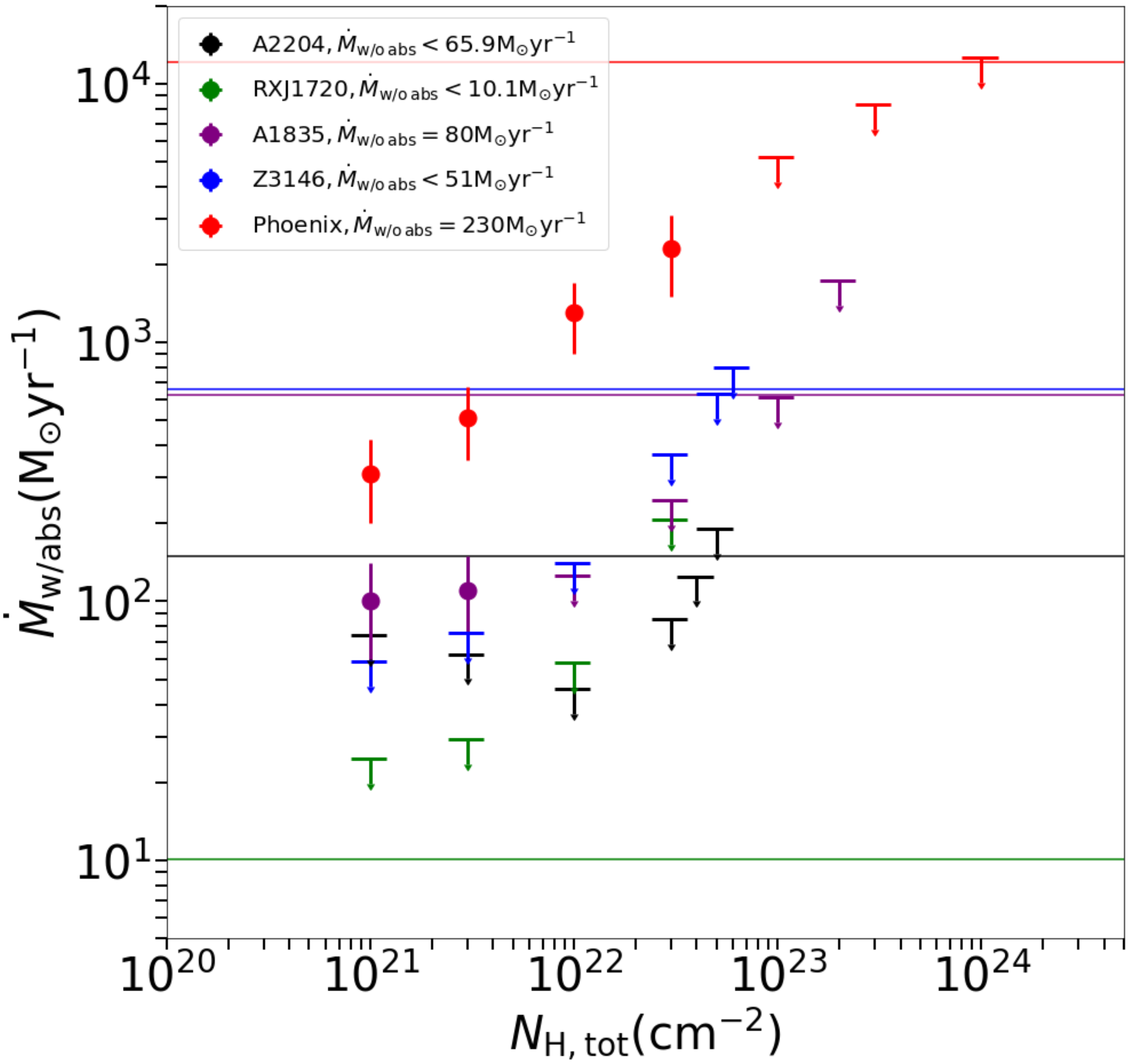

Fig. 6.7 The absorption corrected cooling rate limit against intrinsic column density. Horizontal lines represent the total optical/UV emission.

one-stage model (ΔC-stat$\geq$ 6 for 1 degree of freedom). We find that the cooling rate increases by at least a factor of 2 between the bulk temperature and 0.7 keV in these 4 clusters. We only measure upper limits for the rest due to the poor statistics of data and the complexity of the two-stage model. The residual cooling rate (limit) below 0.7 keV is significantly lower than the cooling rate above 0.7 keV. This is consistent with the results of the CHEERS sample. We combine the samples studied in this thesis and compare the radiative cooling rate with other gas properties. The results strongly support the conclusions obtained by using the CHEERS sample alone. We find that

- The maximum $L_{\mathrm{H}\alpha}$ limit is increased to $2 \times 10^{41}\,\mathrm{erg\,s^{-1}}$ for the observed optical/UV nebulae to be powered by the missing luminosity of soft X-ray gas below 0.7 keV.
- For clusters with $L_{\mathrm{H}\alpha}$ higher than $7 \times 10^{41}\,\mathrm{erg\,s^{-1}}$, additional energy sources are required to power the optical nebula such as AGN feedback.
- The observed cooling rate matches the star formation rate for the strongest star-forming clusters, which means the molecular gas is growing slowly in those clusters.
- The effect of intrinsic absorption on the observed cooling rate is studied in 6 clusters with good RGS spectra. The cooling rate can be underestimated by a factor of 5-10 in some clusters, which provides an alternative explanation for the matching of high star formation rate and radiative cooling.
- The measured-to-predicted ratio is less than 20 per cent in more than 44 out of 54 clusters. This means AGN heating strongly balances the radiative cooling.
- We observe no redshift evolution of the measured-to-predicted ratio for $z < 0.6$ from current observations.

Chapter 7

Conclusions

7.1 Summaries of chapters

In the first section of the concluding chapter, I provide a brief summary of the thesis. The main goals of this thesis include the investigation of the amount of radiative cooling in the core of galaxy clusters. The observed spectra of the cool cores provide information on the balance between cooling and heating from AGN. The by product of radiative cooling can also play an important role in secondary processes such as star formation and accretion on AGN. We also study whether intrinsic absorption of clusters contributes to the suppressed cooling rate seen. In the second section, I discuss the potential future projects of X-ray spectroscopy of clusters. Finally, I describe the upcoming X-ray observatories relevant to this field.

7.1.1 Chapter 3

The CHEERS sample includes 26 galaxy clusters and 18 groups and elliptical galaxies. We also include a distant cluster A1835. The RGS spectra of the sample exhibit the O VIII line in all sources allowing the O abundance to be detected above 5σ [158, 39]. The abundance of Fe is also well constrained. It is then possible to search for the cool gas below 1 keV through the presence of the Fe XVII lines. The bulk of the ICM is modelled by a simple isothermal plasma in collision ionisation equilibrium. We then include a cooling flow component to measure the radiative cooling rate between the ICM temperature and 0.01 keV (coolest temperature in the X-ray band). We call this the complete (one-stage) cooling rate and is measured above 2 σ level in 22 out of 27 clusters and in 11 out of 18 groups and galaxies. This means that AGN heating does not exactly offset radiative cooling. We further adopt a more complex two-stage cooling model with two cooling flow components, since it is possible that the gas stops cooling radiatively at a higher temperature. One suitable temperature for the transition between the two *cf* components is 0.7 keV. The two-stage model provides a better spectral fit than the one-stage model in 9 clusters. The cooling rate between the ICM temperature and 0.7 keV is also typically higher than the complete cooling rate. The residual cooling rate below 0.7 keV is very low. We compare the observed cooling rate with the maximum allowed (predicted) cooling rate. This is predicted from the gas mass within the cooling radius where the cooling time is less than 7.7 Gyr. We find that more than 90 per cent of the predicted rate is suppressed in these clusters.

Spatially-resolved Chandra images show that optical line emitting nebulae coincide with the soft X-ray gas below 1 keV in many cool core clusters. Since much less gas is observed below 1 keV, the luminosity of the missing gas is likely powering the observed nebular emission. This is possible for clusters with an Hα luminosity less than $10^{41}\,\mathrm{erg\,s^{-1}}$, which is seen in at least 11 sources in this sample. 4 clusters are observed with a high Hα luminosity. The observed nebular emission in these objects must be powered by the cooling of warmer gas or has a different energy source. A larger sample of bright clusters is required to determine which is the most likely process.

7.1.2 Chapter 4

This chapter focuses on the by-product of the radiative cooling flow. The molecular gas filaments are often found in the innermost region of the cool core and spatially embedded in the optical/UV nebula. If the thermal energy of the cooling gas is indeed powering the optical/UV nebula, the remaining gas mass is then contributing to the massive molecular gas seen. We study the mass-temperature profile of the gas within the 10 kpc radius in 9 clusters selected from the CHEERS sample. The RGS spectra are fitted by a three-temperature model. Under the assumption of pressure equilibrium, it is possible to calculate the gas mass from the emission measure.

We find that the X-ray mass-temperature profile is similar among these clusters particularly in the 1.5 and 0.7 keV components. The total X-ray mass below 1 keV is also comparable to that of the molecular gas in 7 out of 9 clusters. Surprisingly, the Hα nebula only contributes 0.1-1 per cent of total amount of gas.

7.1.3 Chapter 5

We obtain 240 ks new observations for each of the distant X-ray luminous clusters RXCJ1504.1-0248 and A1664. In this chapter, we not only study the cooling property of the cluster but also measure the level of turbulence. The radiative cooling rate is measured above 4 σ in both clusters. We find a cooling rate of 180$\pm$40 $\mathrm{M_{\odot}\,yr^{-1}}$ using the two-stage model, which is higher than all clusters in the CHEERS sample. Both clusters have a luminous optical nebula with $L_{\mathrm{H}\alpha} > 10^{42}\,\mathrm{erg\,s^{-1}}$. These nebulae require significantly higher energy than that available from the observed cooling rate. This suggests that the nebulae have additional power sources.

We consider the possibility that the true cooling rate is underestimated due to the intrinsic absorption of the cold gas in the clusters. We reintroduce a simplified intrinsic absorption model which we call the embedded cooling flow. Such a model consists of identical plane-parallel X-ray and cold absorption gas sheets perpendicular to our line-of-sight. Gas sheets of different types are placed alternatively such that each X-ray gas sheet is absorbed by all foreground cold gas sheets. We find that the number of gas sheets and the total intrinsic column density are degenerate. For a complex 10 sheet model with a high column denisty of $1.5 \times 10^{22}\,\mathrm{cm^{-2}}$, the complete cooling rate increases by an order of magnitude to 520±30 $\mathrm{M_{\odot}\,yr^{-1}}$ in RXCJ1504.1-0248. On the other hand, the cooling rate of A1664 is unaffected by intrinsic absorption. In A1664, we find that the cool component of 0.80±0.08 keV is blueshifted from the systemic velocity of the cluster at 750^{+800}_{-280} $\mathrm{km\,s^{-1}}$ in A1664. This is consistent with the velocity of the blueshifted component in the molecular gas. The two gas phases are likely highly connected.

Since the RGS detectors are slitless, the spectral lines are artificially broadened by the spatial extent of the source. The spatial broadening can be corrected by the surface brightness profile. Using the recently developed technique in [7, 154], we model the surface brightness profile with multiple gaussians and obtain a more accurate estimate of the spatial broadening due to the cool gas. The upper limit of turbulence is measured to be 300 $\mathrm{kms^{-1}}$ at 90 per cent confidence level in both clusters. This is similar to the level of turbulence in the Perseus cluster measured by Hitomi [84]. The turbulent energy density is calculated to be less than 8.9 and 27 per cent of the thermal energy density in RXCJ1504.1-0248 and Abell 1664, respectively. This supports the conclusion of the Hitomi observation that turbulence may be insufficient to propagate energy throughout the cool core.

7.1.4 Chapter 6

In this chapter, we expand the sample of clusters to include 40 additional sources with a broad range of $L_{\mathrm{H}\alpha}$. The statistics is typically poorer in these clusters due to short exposures and higher redshift than the CHEERS sample. We therefore only place upper limits on the cooling rates. Nevertheless, we obtain reliable measurement of the complete cooling rate in 8 clusters.

We combine this sample with the CHEERS sample to contain different variety of clusters. The combine sample improved the threshold of maximum $L_{\mathrm{H}\alpha}$ to $2 \times 10^{41}\,\mathrm{erg\,s^{-1}}$ where the optical/UV nebulae can be powered by the soft X-ray gas at 0.7 keV. For the most luminous nebulae where $L_{\mathrm{H}\alpha} \sim 7 \times 10^{41}\,\mathrm{erg\,s^{-1}}$, additional power sources is required such as AGN feedback. The radiative cooling rate is at least 5 times higher than the star formation rate in the weakest star-forming clusters. The molecular gas can then form within 1 Gyr. For the strongest star-forming clusters, the observed cooling rate matches the star formation rate. This implies a slowly growing molecular gas unless cooling was more rapid in the past or the cooling gas is affected by intrinsic absorption. We apply the embedded cooling flow model for 3 clusters and perform Monte Carlo simulations for 4. We find that the cooling rate is likely underestimated by a factor of 2-10. Finally, the redshift evolution of the measured-to-predicted ratio is weak up to $z < 0.6$ from the current data. It is interesting to verify these results with the future high resolution X-ray missions.

7.2 Future research

In this section, we brief discuss a few potential future research projects.

7.2.1 Intrinsic absorption

We can greatly improve the embedded cooling flow model used in Chapter 5 and 6. The current implementation of the model is limited by the architecture of the spectral fitting package. While the brute-force method is straight forward, the computational time is significantly longer than the standard cooling flow models without intrinsic absorption. Only a small number of gas sheets can be applied to the one-stage model. With the future release of SPEX, it will be possible to perform complex operations on spectral components. We can then study the effect of intrinsic absorption on more complicated cooling flow models and consider different geometry of the gas. We will also try to break down the degeneracy between the number of gas sheets and the total intrinsic column density.

7.2.2 Charge exchange

One important underlying assumption in this thesis is that the soft X-ray emitting gas is spatially aligned with the optical/UV nebula. The interaction between the warmer soft X-ray gas and the cooler nebula likely involves charge exchange. When charge exchange occurs, the outer electrons of neutral atoms are transferred to the excited levels of ions. The transitions of electrons into lower levels result in X-ray emission. The recombination of the ionised atoms with free electrons then contribute to the observed nebula. The spectral model of the charge exchange process is under development in SPEX (see SPEX reference manual, https://www.sron.nl/astrophysics-spex/manual [76, 155]).

To study the role of charge exchange in the narrow Hα filaments, we need to rely on high spatial resolution. Currently ACIS onboard Chandra X-ray observatory offers the best opportunity. Walker et al. [209] showed that the stacked spectrum of the filaments can be fitted by a charge exchange component and a thermal component in the Perseus. We will develop from here and investigate if the charge exchange process is a general solution to all filaments in different clusters.

7.2.3 Cluster outskirts

X-ray images with high spatial resolution can be used to study the cool core on a large scale and the outskirts of clusters. It is be interesting to study clusters with extreme features such as the strong jets in Hercules A. We will measure the cooling rate along the jet axis and its surrounding to investigate if there is spatial variation. The EPIC images are available from the new observations of RXCJ1504.1-0248 and A1664. Preliminary study shows that the cluster emission of RXCJ1504.1-0248 extends beyond 1.7 Mpc. Azimuthal variation of the surface brightness is observed in both clusters. We will analyse the radial profiles of these clusters and understand the nature of the observed asymmetry.

7.3 Looking ahead

7.3.1 eROSITA

eROSITA [131] was launched on 13th July 2019 and has collected data for two years. It is an all sky survey for galaxy clusters with the main goal to detect over 100 thousand clusters and provide X-ray image at moderate spectral resolution. The spatial resolution of eROSITA is $\sim$8 arcsec (FWHM), which is similar to that of the EPIC instruments. The effective area is also comparable in the soft 0.3-2 keV band but with a much wider field of view. This is ideal to image the cool core of clusters. The energy resolution is relatively poor of 60-80 eV at low energies and $\sim$150 eV above 8 keV. This results a resolving power $R \sim 10-50$. The future data release will provide a more complete sample of cool core clusters to be studied by the upcoming high resolution X-ray observatories.

7.3.2 X-ray Imaging and Spectroscopy Mission (XRISM)

XRISM [224] is scheduled to launch in 2023 as the replacement for the Hitomi satellite lost in 2016. The main science instrument is the X-ray micro-calorimeter detecting the variation of temperature due to incident photons. It has a very high energy resolution of 5-7 eV across a broad energy band. This results in a resolving power of over 1000 in the Fe K band (around 7 keV). The resolving power drops below 200 at the soft band ($<$1 keV), which is slightly worse than the RGS. This suggests that XRISM can be used together with the RGS to study clusters from the coolest core to the hotter ICM.

7.3.3 Advanced Telescope for High Energy Astrophysics (Athena)

Athena [135] is the next generation X-ray observatory of high resolution spectroscopy. It has both an imaging instrument, the Wide Field Imager [163], and a micro-calorimeter similar to that of XRISM (the X-ray Integral Field Unit [9]). Both instruments have a large collecting area of 1.4 m^2. This allows observations of clusters 100 times fainter than with XRISM (see Fig 7.1). We simulate the Athena and XRISM spectra of RXCJ1504.1-0248 using the best fit two-stage cooling model. ATHENA can obtain a very high quality spectrum with a much shorter exposure. The XIFU has a spectral resolution of 2.5 eV over a broad energy band up to 7 keV. This is twice the resolution of XRISM and also significantly better than the RGS. The Fe XVII lines are clearly revealed in the 25 ks simulated spectrum of RXCJ1504.1-0248 with ATHENA. It therefore possible to search for the coolest X-ray emitting gas at much higher redshift.

As a final remark, future X-ray missions will greatly expand the catalogue of galaxy clusters and provide much more detailed spectral information to study the mystery of their evolution.

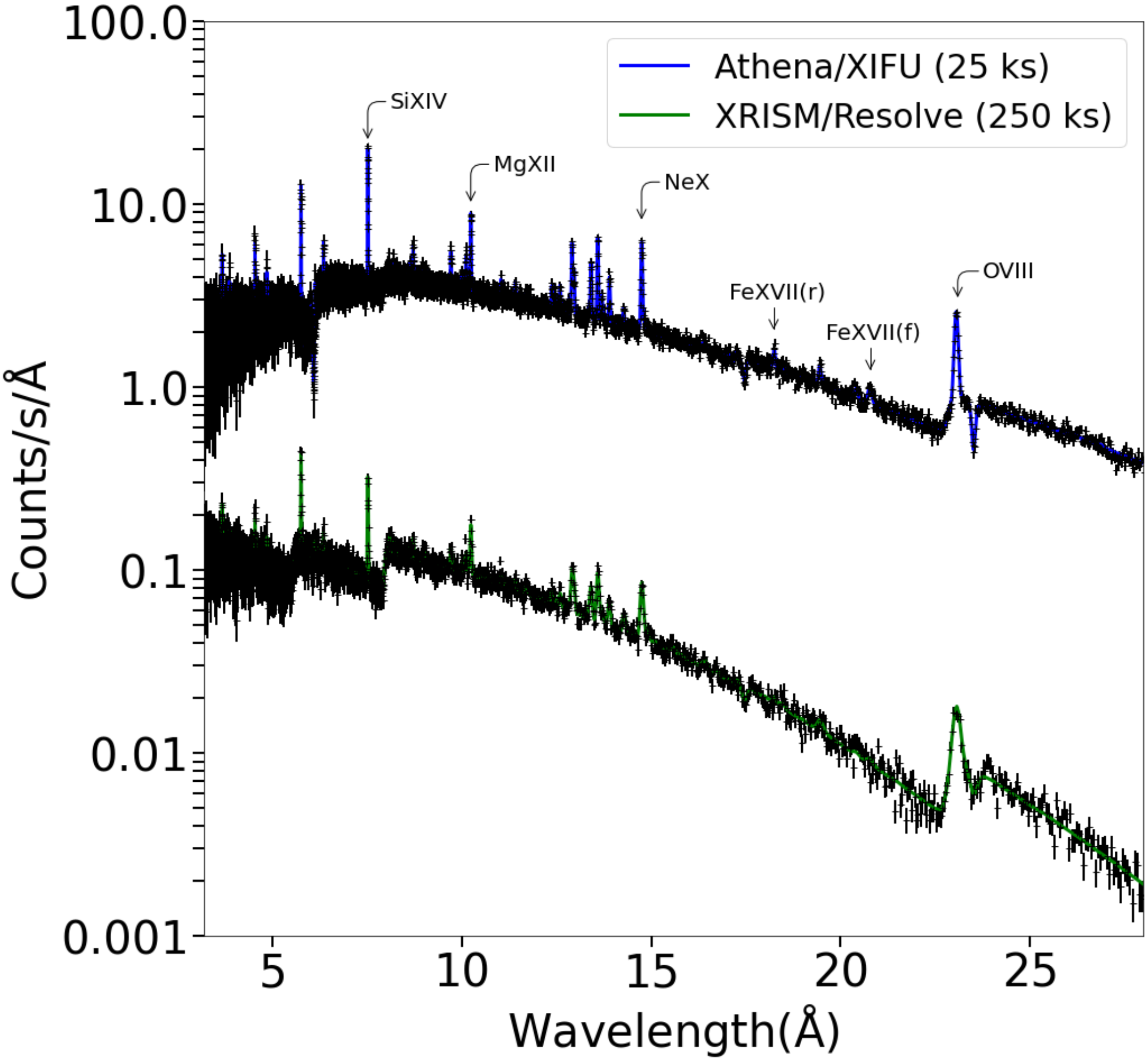

Fig. 7.1 A 25 ks simulated spectrum of RXCJ1504.1-0248 with Athena and 250 ks simulated spectrum with XRISM.

References

[1] Allen, S. W. and Fabian, A. C. (1997). The spatial distributions of cooling gas and intrinsic X-ray-absorbing material in cooling flows. , 286(3):583–603.

[2] Allen, S. W., Fabian, A. C., Edge, A. C., Bautz, M. W., Furuzawa, A., and Tawara, Y. (1996). ASCA and ROSAT observations of distant, massive cooling flows. , 283(1):263–281.

[3] Allen, S. W., Fabian, A. C., Johnstone, R. M., Arnaud, K. A., and Nulsen, P. E. J. (2001). ASCA and ROSAT observations of nearby cluster cooling flows. , 322:589–613.

[4] Arnaud, M. and Evrard, A. E. (1999). The L_X-T relation and intracluster gas fractions of X-ray clusters. , 305(3):631–640.

[5] Ascasibar, Y. and Markevitch, M. (2006). The Origin of Cold Fronts in the Cores of Relaxed Galaxy Clusters. , 650(1):102–127.

[6] Babyk, I. V., McNamara, B. R., Nulsen, P. E. J., Russell, H. R., Vantyghem, A. N., Hogan, M. T., and Pulido, F. A. (2018). A Universal Entropy Profile for the Hot Atmospheres of Galaxies and Clusters within R $_{2500}$. , 862(1):39.

[7] Bambic, C. J., Pinto, C., Fabian, A. C., Sanders, J., and Reynolds, C. S. (2018). Limits on turbulent propagation of energy in cool-core clusters of galaxies. , 478:L44–L48.

[8] Barger, A. J., Cowie, L. L., Chen, C. C., Owen, F. N., Wang, W. H., Casey, C. M., Lee, N., Sanders, D. B., and Williams, J. P. (2014). Is There a Maximum Star Formation Rate in High-redshift Galaxies? , 784(1):9.

[9] Barret, D., Lam Trong, T., den Herder, J.-W., Piro, L., Cappi, M., Houvelin, J., Kelley, R., Mas-Hesse, J. M., Mitsuda, K., Paltani, S., Rauw, G., Rozanska, A., Wilms, J., Bandler, S., Barbera, M., Barcons, X., Bozzo, E., Ceballos, M. T., Charles, I., Costantini, E., Decourchelle, A., den Hartog, R., Duband, L., Duval, J.-M., Fiore, F., Gatti, F., Goldwurm, A., Jackson, B., Jonker, P., Kilbourne, C., Macculi, C., Mendez, M., Molendi, S., Orleanski, P., Pajot, F., Pointecouteau, E., Porter, F., Pratt, G. W., Prêle, D., Ravera, L., Sato, K., Schaye, J., Shinozaki, K., Thibert, T., Valenziano, L., Valette, V., Vink, J., Webb, N., Wise, M., Yamasaki, N., Douchin, F., Mesnager, J.-M., Pontet, B., Pradines, A., Branduardi-Raymont, G., Bulbul, E., Dadina, M., Ettori, S., Finoguenov, A., Fukazawa, Y., Janiuk, A., Kaastra, J., Mazzotta, P., Miller, J., Miniutti, G., Naze, Y., Nicastro, F., Scioritino, S., Simonescu, A., Torrejon, J. M., Frezouls, B., Geoffray, H., Peille, P., Aicardi, C., André, J., Daniel, C., Clénet, A., Etcheverry, C., Gloaguen, E., Hervet, G., Jolly, A., Ledot, A., Paillet, I., Schmisser, R., Vella, B., Damery, J.-C., Boyce, K., Dipirro,

M., Lotti, S., Schwander, D., Smith, S., Van Leeuwen, B.-J., van Weers, H., Clerc, N., Cobo, B., Dauser, T., Kirsch, C., Cucchetti, E., Eckart, M., Ferrando, P., and Natalucci, L. (2018). The ATHENA X-ray Integral Field Unit (X-IFU). In den Herder, J.-W. A., Nikzad, S., and Nakazawa, K., editors, *Space Telescopes and Instrumentation 2018: Ultraviolet to Gamma Ray*, volume 10699 of *Society of Photo-Optical Instrumentation Engineers (SPIE) Conference Series*, page 106991G.

[10] Bauer, F. E., Fabian, A. C., Sanders, J. S., Allen, S. W., and Johnstone, R. M. (2005). The prevalence of cooling cores in clusters of galaxies at z˜ 0.15-0.4. , 359:1481–1490.

[11] Bernal, T., Robles, V. H., and Matos, T. (2017). Scalar field dark matter in clusters of galaxies. , 468(3):3135–3149.

[12] Bîrzan, L., Rafferty, D. A., McNamara, B. R., Wise, M. W., and Nulsen, P. E. J. (2004). A Systematic Study of Radio-induced X-Ray Cavities in Clusters, Groups, and Galaxies. , 607(2):800–809.

[13] Blanton, E. L., Randall, S. W., Clarke, T. E., Sarazin, C. L., McNamara, B. R., Douglass, E. M., and McDonald, M. (2011). A Very Deep Chandra Observation of A2052: Bubbles, Shocks, and Sloshing. , 737(2):99.

[14] Blanton, E. L., Sarazin, C. L., McNamara, B. R., and Clarke, T. E. (2004). Chandra Observation of the Central Region of the Cooling Flow Cluster A262: A Radio Source That Is a Shadow of Its Former Self? , 612:817–824.

[15] Bleem, L. E., Stalder, B., de Haan, T., Aird, K. A., Allen, S. W., Applegate, D. E., Ashby, M. L. N., Bautz, M., Bayliss, M., Benson, B. A., Bocquet, S., Brodwin, M., Carlstrom, J. E., Chang, C. L., Chiu, I., Cho, H. M., Clocchiatti, A., Crawford, T. M., Crites, A. T., Desai, S., Dietrich, J. P., Dobbs, M. A., Foley, R. J., Forman, W. R., George, E. M., Gladders, M. D., Gonzalez, A. H., Halverson, N. W., Hennig, C., Hoekstra, H., Holder, G. P., Holzapfel, W. L., Hrubes, J. D., Jones, C., Keisler, R., Knox, L., Lee, A. T., Leitch, E. M., Liu, J., Lueker, M., Luong-Van, D., Mantz, A., Marrone, D. P., McDonald, M., McMahon, J. J., Meyer, S. S., Mocanu, L., Mohr, J. J., Murray, S. S., Padin, S., Pryke, C., Reichardt, C. L., Rest, A., Ruel, J., Ruhl, J. E., Saliwanchik, B. R., Saro, A., Sayre, J. T., Schaffer, K. K., Schrabback, T., Shirokoff, E., Song, J., Spieler, H. G., Stanford, S. A., Staniszewski, Z., Stark, A. A., Story, K. T., Stubbs, C. W., Vanderlinde, K., Vieira, J. D., Vikhlinin, A., Williamson, R., Zahn, O., and Zenteno, A. (2015). Galaxy Clusters Discovered via the Sunyaev-Zel'dovich Effect in the 2500-Square-Degree SPT-SZ Survey. , 216(2):27.

[16] Böhringer, H., Burwitz, V., Zhang, Y. Y., Schuecker, P., and Nowak, N. (2005). Chandra Reveals Galaxy Cluster with the Most Massive Nearby Cooling Core: RXC J1504.1-0248. , 633(1):148–153.

[17] Bondi, H. (1952). On spherically symmetrical accretion. , 112:195.

[18] Bregman, J. N., Miller, E. D., Athey, A. E., and Irwin, J. A. (2005). On VI in Elliptical Galaxies: Indicators of Cooling Flows. , 635:1031–1043.

[19] Brinkman, A., Aarts, H., den Boggende, A., Bootsma, T., Dubbeldam, L., den Herder, J., Kaastra, J., de Korte, P., van Leeuwen, B., Mewe, R., Paerels, F., and de Vries, C. (1998). In *The Reflection Grating Spectrometer on board XMM*.

[20] Calzadilla, M. S., Russell, H. R., McDonald, M. A., Fabian, A. C., Baum, S. A., Combes, F., Donahue, M., Edge, A. C., McNamara, B. R., Nulsen, P. E. J., O'Dea, C. P., Oonk, J. B. R., Tremblay, G. R., and Vantyghem, A. N. (2019). Revealing a Highly Dynamic Cluster Core in Abell 1664 with Chandra. , 875(1):65.

[21] Canning, R. E. A., Fabian, A. C., Johnstone, R. M., Sanders, J. S., Conselice, C. J., Crawford, C. S., Gallagher, J. S., and Zweibel, E. (2010). Star formation in the outer filaments of NGC 1275. , 405:115–128.

[22] Canning, R. E. A., Ryon, J. E., Gallagher, J. S., Kotulla, R., O'Connell, R. W., Fabian, A. C., Johnstone, R. M., Conselice, C. J., Hicks, A., Rosario, D., and Wyse, R. F. G. (2014). Filamentary star formation in NGC 1275. , 444:336–349.

[23] Canning, R. E. A., Sun, M., Sanders, J. S., Clarke, T. E., Fabian, A. C., Giacintucci, S., Lal, D. V., Werner, N., Allen, S. W., Donahue, M., Edge, A. C., Johnstone, R. M., Nulsen, P. E. J., Salomé, P., and Sarazin, C. L. (2013). A multiwavelength view of cooling versus AGN heating in the X-ray luminous cool-core of Abell 3581. , 435(2):1108–1125.

[24] Cash, W. (1979). Parameter estimation in astronomy through application of the likelihood ratio. , 228:939–947.

[25] Cavagnolo, K. W., Donahue, M., Voit, G. M., and Sun, M. (2008). An Entropy Threshold for Strong Hα and Radio Emission in the Cores of Galaxy Clusters. , 683:L107.

[26] Cavagnolo, K. W., Donahue, M., Voit, G. M., and Sun, M. (2009). Intracluster Medium Entropy Profiles for a Chandra Archival Sample of Galaxy Clusters. , 182:12–32.

[27] Chen, Y., Ikebe, Y., and Böhringer, H. (2003). X-ray spectroscopy of the cluster of galaxies <ASTROBJ>PKS 0745-191</ASTROBJ>with XMM-Newton. , 407:41–50.

[28] Chen, Y., Reiprich, T. H., Böhringer, H., Ikebe, Y., and Zhang, Y.-Y. (2007). Statistics of X-ray observables for the cooling-core and non-cooling core galaxy clusters. , 466:805–812.

[29] Churazov, E., Forman, W., Jones, C., and Böhringer, H. (2003). XMM-Newton Observations of the Perseus Cluster. I. The Temperature and Surface Brightness Structure. *ApJ*, 590:225–237.

[30] Churazov, E., Ruszkowski, M., and Schekochihin, A. (2013). Powering of cool filaments in cluster cores by buoyant bubbles - I. Qualitative model. , 436(1):526–530.

[31] Churazov, E., Sunyaev, R., Forman, W., and Böhringer, H. (2002). Cooling flows as a calorimeter of active galactic nucleus mechanical power. , 332(3):729–734.

[32] Conselice, C. J., Gallagher, III, J. S., and Wyse, R. F. G. (2001). On the Nature of the NGC 1275 System. , 122:2281–2300.

[33] Crawford, C. S., Allen, S. W., Ebeling, H., Edge, A. C., and Fabian, A. C. (1999). The ROSAT Brightest Cluster Sample - III. Optical spectra of the central cluster galaxies. , 306:857–896.

[34] Crawford, C. S., Hatch, N. A., Fabian, A. C., and Sanders, J. S. (2005a). The extended Hα-emitting filaments surrounding NGC 4696, the central galaxy of the Centaurus cluster. , 363:216–222.

[35] Crawford, C. S., Sanders, J. S., and Fabian, A. C. (2005b). The giant Hα/X-ray filament in the cluster of galaxies A1795. , 361:17–33.

[36] Croston, J. H., Pratt, G. W., Böhringer, H., Arnaud, M., Pointecouteau, E., Ponman, T. J., Sanderson, A. J. R., Temple, R. F., Bower, R. G., and Donahue, M. (2008). Galaxy-cluster gas-density distributions of the representative XMM-Newton cluster structure survey (REXCESS). , 487(2):431–443.

[37] David, L. P., Nulsen, P. E. J., McNamara, B. R., Forman, W., Jones, C., Ponman, T., Robertson, B., and Wise, M. (2001). A High-Resolution Study of the Hydra A Cluster with Chandra: Comparison of the Core Mass Distribution with Theoretical Predictions and Evidence for Feedback in the Cooling Flow. , 557:546–559.

[38] de Plaa, J., Kaastra, J. S., Tamura, T., Pointecouteau, E., Mendez, M., and Peterson, J. R. (2004). X-ray spectroscopy on Abell 478 with XMM-Newton. , 423:49–56.

[39] de Plaa, J., Kaastra, J. S., Werner, N., Pinto, C., and Kosec, P. e. a. (2017). CHEERS: The chemical evolution RGS sample. *A&A*, 607:A98.

[40] de Plaa, J., Zhuravleva, I., Werner, N., Kaastra, J. S., Churazov, E., Smith, R. K., Raassen, A. J. J., and Grange, Y. G. (2012). Estimating turbulent velocities in the elliptical galaxies NGC 5044 and NGC 5813. , 539:A34.

[41] den Herder, J. W., Brinkman, A. C., Kahn, S. M., Branduardi-Raymont, G., Thomsen, K., Aarts, H., Audard, M., Bixler, J. V., den Boggende, A. J., Cottam, J., Decker, T., Dubbeldam, L., Erd, C., Goulooze, H., Güdel, M., Guttridge, P., Hailey, C. J., Janabi, K. A., Kaastra, J. S., de Korte, P. A. J., van Leeuwen, B. J., Mauche, C., McCalden, A. J., Mewe, R., Naber, A., Paerels, F. B., Peterson, J. R., Rasmussen, A. P., Rees, K., Sakelliou, I., Sako, M., Spodek, J., Stern, M., Tamura, T., Tandy, J., de Vries, C. P., Welch, S., and Zehnder, A. (2001). The Reflection Grating Spectrometer on board XMM-Newton. , 365:L7–L17.

[42] Donahue, M., Mack, J., Voit, G. M., Sparks, W., Elston, R., and Maloney, P. R. (2000). Hubble Space Telescope Observations of Vibrationally Excited Molecular Hydrogen in Cluster Cooling Flow Nebulae. , 545(2):670–694.

[43] Donahue, M., Sun, M., O'Dea, C. P., Voit, G. M., and Cavagnolo, K. W. (2007). Star Formation, Radio Sources, Cooling X-Ray Gas, and Galaxy Interactions in the Brightest Cluster Galaxy in 2A0335+096. , 134:14–25.

[44] Donato, D., Sambruna, R. M., and Gliozzi, M. (2004). Obscuration and Origin of Nuclear X-Ray Emission in FR I Radio Galaxies. *ApJ*, 617:915–929.

[45] Dunn, R. J. H. and Fabian, A. C. (2006). Investigating AGN heating in a sample of nearby clusters. , 373(3):959–971.

[46] Edge, A. C. (2001). The detection of molecular gas in the central galaxies of cooling flow clusters. , 328:762–782.

[47] Edge, A. C., Wilman, R. J., Johnstone, R. M., Crawford, C. S., Fabian, A. C., and Allen, S. W. (2002). A survey of molecular hydrogen in the central galaxies of cooling flows. , 337(1):49–62.

[48] Elwert, G. (1952). Über die Ionisations- und Rekombinationsprozesse in einem Plasma und die Ionisationsformel der Sonnenkorona. *Zeitschrift Naturforschung Teil A*, 7(6):432–439.

[49] Evrard, A. E. (1990). Formation and Evolution of X-Ray Clusters: A Hydrodynamic Simulation of the Intracluster Medium. , 363:349.

[50] Fabian, A. C. (1994). Cooling Flows in Clusters of Galaxies. , 32:277–318.

[51] Fabian, A. C. (2012). Observational Evidence of Active Galactic Nuclei Feedback. , 50:455–489.

[52] Fabian, A. C., Allen, S. W., Crawford, C. S., Johnstone, R. M., Morris, R. G., Sanders, J. S., and Schmidt, R. W. (2002). The missing soft X-ray luminosity in cluster cooling flows. , 332:L50–L54.

[53] Fabian, A. C., Arnaud, K. A., Nulsen, P. E. J., Watson, M. G., Stewart, G. C., McHardy, I., Smith, A., Cooke, B., Elvis, M., and Mushotzky, R. F. (1985). An X-ray, optical and radio study of PKS 0745-191 - A massive cooling flow. , 216:923–932.

[54] Fabian, A. C., Johnstone, R. M., Sanders, J. S., Conselice, C. J., Crawford, C. S., Gallagher, III, J. S., and Zweibel, E. (2008). Magnetic support of the optical emission line filaments in NGC 1275. *Nature*, 454:968–970.

[55] Fabian, A. C., Reynolds, C. S., Taylor, G. B., and Dunn, R. J. H. (2005). On viscosity, conduction and sound waves in the intracluster medium. , 363:891–896.

[56] Fabian, A. C., Sanders, J. S., Allen, S. W., Crawford, C. S., Iwasawa, K., Johnstone, R. M., Schmidt, R. W., and Taylor, G. B. (2003a). A deep Chandra observation of the Perseus cluster: shocks and ripples. , 344(3):L43–L47.

[57] Fabian, A. C., Sanders, J. S., Crawford, C. S., Conselice, C. J., Gallagher, J. S., and Wyse, R. F. G. (2003b). The relationship between the optical Hα filaments and the X-ray emission in the core of the Perseus cluster. , 344:L48–L52.

[58] Fabian, A. C., Sanders, J. S., Ettori, S., Taylor, G. B., Allen, S. W., Crawford, C. S., Iwasawa, K., and Johnstone, R. M. (2001). Chandra imaging of the X-ray core of Abell 1795. , 321:L33–L36.

[59] Fabian, A. C., Sanders, J. S., Taylor, G. B., Allen, S. W., Crawford, C. S., Johnstone, R. M., and Iwasawa, K. (2006). A very deep Chandra observation of the Perseus cluster: shocks, ripples and conduction. , 366:417–428.

[60] Fabian, A. C., Sanders, J. S., Williams, R. J. R., Lazarian, A., Ferland, G. J., and Johnstone, R. M. (2011). The energy source of the filaments around the giant galaxy NGC 1275. , 417:172–177.

[61] Fabian, A. C., Vasudevan, R. V., Mushotzky, R. F., Winter, L. M., and Reynolds, C. S. (2009). Radiation pressure and absorption in AGN: results from a complete unbiased sample from Swift. , 394(1):L89–L92.

[62] Fabian, A. C., Walker, S. A., Russell, H. R., Pinto, C., Canning, R. E. A., Salome, P., Sanders, J. S., Taylor, G. B., Zweibel, E. G., Conselice, C. J., Combes, F., Crawford, C. S., Ferland, G. J., Gallagher, III, J. S., Hatch, N. A., Johnstone, R. M., and Reynolds, C. S. (2016). HST imaging of the dusty filaments and nucleus swirl in NGC4696 at the centre of the Centaurus Cluster. , 461:922–928.

[63] Fabian, A. C., Walker, S. A., Russell, H. R., Pinto, C., Sanders, J. S., and Reynolds, C. S. (2017). Do sound waves transport the AGN energy in the Perseus cluster? , 464:L1–L5.

[64] Fairley, B. W., Jones, L. R., Scharf, C., Ebeling, H., Perlman, E., Horner, D., Wegner, G., and Malkan, M. (2000). The WARPS survey - IV. The X-ray luminosity-temperature relation of high-redshift galaxy clusters. , 315(4):669–678.

[65] Ferland, G. J., Fabian, A. C., Hatch, N. A., Johnstone, R. M., Porter, R. L., van Hoof, P. A. M., and Williams, R. J. R. (2009). Collisional heating as the origin of filament emission in galaxy clusters. , 392:1475–1502.

[66] Field, G. B. (1965). Thermal Instability. , 142:531.

[67] Finoguenov, A., Arnaud, M., and David, L. P. (2001). Temperature and Heavy-Element Abundance Profiles of Cool Clusters of Galaxies from ASCA. , 555(1):191–204.

[68] Forman, W., Nulsen, P., Heinz, S., Owen, F., Eilek, J., Vikhlinin, A., Markevitch, M., Kraft, R., Churazov, E., and Jones, C. (2005). Reflections of Active Galactic Nucleus Outbursts in the Gaseous Atmosphere of M87. , 635(2):894–906.

[69] Fujita, Y., Cen, R., and Zhuravleva, I. (2020). Non-steady heating of cool cores of galaxy clusters by ubiquitous turbulence and AGN. , 494(4):5507–5519.

[70] Gaspari, M., Temi, P., and Brighenti, F. (2017). Raining on black holes and massive galaxies: the top-down multiphase condensation model. , 466(1):677–704.

[71] Gendron-Marsolais, M., Hlavacek-Larrondo, J., Martin, T. B., Drissen, L., McDonald, M., Fabian, A. C., Edge, A. C., Hamer, S. L., McNamara, B., and Morrison, G. (2018). Revealing the velocity structure of the filamentary nebula in NGC 1275 in its entirety. , 479(1):L28–L33.

[72] Giacintucci, S., Markevitch, M., Brunetti, G., Cassano, R., and Venturi, T. (2011). A radio minihalo in the extreme cool-core galaxy cluster RXC J1504.1-0248. , 525:L10.

[73] Giles, P. A., Maughan, B. J., Pacaud, F., Lieu, M., Clerc, N., Pierre, M., Adami, C., Chiappetti, L., Démoclés, J., Ettori, S., Le Févre, J. P., Ponman, T., Sadibekova, T., Smith, G. P., Willis, J. P., and Ziparo, F. (2016). The XXL Survey. III. Luminosity-temperature relation of the bright cluster sample. , 592:A3.

[74] Gitti, M. and Schindler, S. (2004). XMM-Newton observation of the most X-ray-luminous galaxy cluster RX J1347.5-1145. , 427:L9–L12.

[75] Gizani, N. A. B. and Leahy, J. P. (2003). A multiband study of Hercules A - II. Multifrequency Very Large Array imaging. , 342(2):399–421.

[76] Gu, L., Kaastra, J., Raassen, A. J. J., Mullen, P. D., Cumbee, R. S., Lyons, D., and Stancil, P. C. (2015). A novel scenario for the possible X-ray line feature at ~3.5 keV. Charge exchange with bare sulfur ions. , 584:L11.

[77] Gunn, J. E. and Gott, J. Richard, I. (1972). On the Infall of Matter Into Clusters of Galaxies and Some Effects on Their Evolution. , 176:1.

[78] Hamer, S. L., Edge, A. C., Swinbank, A. M., Oonk, J. B. R., Mittal, R., McNamara, B. R., Russell, H. R., Bremer, M. N., Combes, F., Fabian, A. C., Nesvadba, N. P. H., O'Dea, C. P., Baum, S. A., Salomé, P., Tremblay, G., Donahue, M., Ferland, G. J., and Sarazin, C. L. (2014). Cold gas dynamics in Hydra-A: evidence for a rotating disc. , 437(1):862–878.

[79] Hamer, S. L., Edge, A. C., Swinbank, A. M., Wilman, R. J., Combes, F., Salomé, P., Fabian, A. C., Crawford, C. S., Russell, H. R., Hlavacek-Larrondo, J., McNamara, B. R., and Bremer, M. N. (2016). Optical emission line nebulae in galaxy cluster cores 1: the morphological, kinematic and spectral properties of the sample. , 460:1758–1789.

[80] Hamer, S. L., Fabian, A. C., Russell, H. R., Salomé, P., Combes, F., Olivares, V., Polles, F. L., Edge, A. C., and Beckmann, R. S. (2018). Discovery of a diffuse optical line emitting halo in the core of the Centaurus cluster of galaxies: Line emission outside the protection of the filaments. *arXiv e-prints*.

[81] Harrison, C. M., Alexander, D. M., Mullaney, J. R., and Swinbank, A. M. (2014). Kiloparsec-scale outflows are prevalent among luminous AGN: outflows and feedback in the context of the overall AGN population. , 441(4):3306–3347.

[82] Hatch, N. A., Crawford, C. S., Fabian, A. C., and Johnstone, R. M. (2005). Detections of molecular hydrogen in the outer filaments of NGC1275. , 358(3):765–773.

[83] Heckman, T. M., Baum, S. A., van Breugel, W. J. M., and McCarthy, P. (1989). Dynamical, physical, and chemical properties of emission-line nebulae in cooling flows. , 338:48–77.

[84] Hitomi Collaboration, Aharonian, F., Akamatsu, H., Akimoto, F., Allen, S. W., Anabuki, N., Angelini, L., Arnaud, K., Audard, M., Awaki, H., Axelsson, M., Bamba, A., Bautz, M., Blandford, R., Brenneman, L., Brown, G. V., Bulbul, E., Cackett, E., Chernyakova, M., Chiao, M., Coppi, P., Costantini, E., de Plaa, J., den Herder, J.-W., Done, C., Dotani, T., Ebisawa, K., Eckart, M., Enoto, T., Ezoe, Y., Fabian, A. C., Ferrigno, C., Foster, A., Fujimoto, R., Fukazawa, Y., Furuzawa, A., Galeazzi, M., Gallo, L., Gandhi, P., Giustini, M., Goldwurm, A., Gu, L., Guainazzi, M., Haba, Y., Hagino, K., Hamaguchi, K., Harrus, I., Hatsukade, I., Hayashi, K., Hayashi, T., Hayashida, K., Hiraga, J., Hornschemeier, A., Hoshino, A., Hughes, J., Iizuka, R., Inoue, H., Inoue, Y., Ishibashi, K., Ishida, M., Ishikawa, K., Ishisaki, Y., Itoh, M., Iyomoto, N., Kaastra, J., Kallman, T., Kamae, T., Kara, E., Kataoka, J., Katsuda, S., Katsuta, J., Kawaharada, M., Kawai, N., Kelley, R., Khangulyan, D., Kilbourne, C., King, A., Kitaguchi, T., Kitamoto, S., Kitayama, T., Kohmura, T., Kokubun, M., Koyama, S., Koyama, K., Kretschmar, P., Krimm, H., Kubota, A., Kunieda, H., Laurent, P., Lebrun, F., Lee, S.-H., Leutenegger, M., Limousin, O.,

Loewenstein, M., Long, K. S., Lumb, D., Madejski, G., Maeda, Y., Maier, D., Makishima, K., Markevitch, M., Matsumoto, H., Matsushita, K., McCammon, D., McNamara, B., Mehdipour, M., Miller, E., Miller, J., Mineshige, S., Mitsuda, K., Mitsuishi, I., Miyazawa, T., Mizuno, T., Mori, H., Mori, K., Moseley, H., Mukai, K., Murakami, H., Murakami, T., Mushotzky, R., Nagino, R., Nakagawa, T., Nakajima, H., Nakamori, T., Nakano, T., Nakashima, S., Nakazawa, K., Nobukawa, M., Noda, H., Nomachi, M., O'Dell, S., Odaka, H., Ohashi, T., Ohno, M., Okajima, T., Ota, N., Ozaki, M., Paerels, F., Paltani, S., Parmar, A., Petre, R., Pinto, C., Pohl, M., Porter, F. S., Pottschmidt, K., Ramsey, B., Reynolds, C., Russell, H., Safi-Harb, S., Saito, S., Sakai, K., Sameshima, H., Sato, G., Sato, K., Sato, R., Sawada, M., Schartel, N., Serlemitsos, P., Seta, H., Shidatsu, M., Simionescu, A., Smith, R., Soong, Y., Stawarz, L., Sugawara, Y., Sugita, S., Szymkowiak, A., Tajima, H., Takahashi, H., Takahashi, T., Takeda, S., Takei, Y., Tamagawa, T., Tamura, K., Tamura, T., Tanaka, T., Tanaka, Y., Tanaka, Y., Tashiro, M., Tawara, Y., Terada, Y., Terashima, Y., Tombesi, F., Tomida, H., Tsuboi, Y., Tsujimoto, M., Tsunemi, H., Tsuru, T., Uchida, H., Uchiyama, H., Uchiyama, Y., Ueda, S., Ueda, Y., Ueno, S., Uno, S., Urry, M., Ursino, E., de Vries, C., Watanabe, S., Werner, N., Wik, D., Wilkins, D., Williams, B., Yamada, S., Yamaguchi, H., Yamaoka, K., Yamasaki, N. Y., Yamauchi, M., Yamauchi, S., Yaqoob, T., Yatsu, Y., Yonetoku, D., Yoshida, A., Yuasa, T., Zhuravleva, I., and Zoghbi, A. (2016). The quiescent intracluster medium in the core of the Perseus cluster. , 535(7610):117–121.

[85] Hlavacek-Larrondo, J., Fabian, A. C., Edge, A. C., Ebeling, H., Sanders, J. S., Hogan, M. T., and Taylor, G. B. (2012). Extreme AGN feedback in the MAssive Cluster Survey: a detailed study of X-ray cavities at z>0.3. , 421(2):1360–1384.

[86] Hlavacek-Larrondo, J., McDonald, M., Benson, B. A., Forman, W. R., Allen, S. W., Bleem, L. E., Ashby, M. L. N., Bocquet, S., Brodwin, M., Dietrich, J. P., Jones, C., Liu, J., Reichardt, C. L., Saliwanchik, B. R., Saro, A., Schrabback, T., Song, J., Stalder, B., Vikhlinin, A., and Zenteno, A. (2015). X-Ray Cavities in a Sample of 83 SPT-selected Clusters of Galaxies: Tracing the Evolution of AGN Feedback in Clusters of Galaxies out to z=1.2. , 805(1):35.

[87] Hogan, M. T., Edge, A. C., Hlavacek-Larrondo, J., Grainge, K. J. B., Hamer, S. L., Mahony, E. K., Russell, H. R., Fabian, A. C., McNamara, B. R., and Wilman, R. J. (2015). A comprehensive study of the radio properties of brightest cluster galaxies. , 453(2):1201–1222.

[88] Hogan, M. T., McNamara, B. R., Pulido, F., Nulsen, P. E. J., Russell, H. R., Vantyghem, A. N., Edge, A. C., and Main, R. A. (2017a). Mass Distribution in Galaxy Cluster Cores. , 837(1):51.

[89] Hogan, M. T., McNamara, B. R., Pulido, F. A., Nulsen, P. E. J., Vantyghem, A. N., Russell, H. R., Edge, A. C., Babyk, I., Main, R. A., and McDonald, M. (2017b). The Onset of Thermally Unstable Cooling from the Hot Atmospheres of Giant Galaxies in Clusters: Constraints on Feedback Models. , 851(1):66.

[90] Hudson, D. S., Mittal, R., Reiprich, T. H., Nulsen, P. E. J., Andernach, H., and Sarazin, C. L. (2010). What is a cool-core cluster? a detailed analysis of the cores of the X-ray flux-limited HIFLUGCS cluster sample. , 513:A37.

[91] Humphrey, P. J., Liu, W., and Buote, D. A. (2009). χ^2 and Poissonian Data: Biases Even in the High-Count Regime and How to Avoid Them. , 693(1):822–829.

[92] Imazawa, R., Fukazawa, Y., and Takahashi, H. (2021). The Study of X-Ray Flux Variability of M87. , 919(2):110.

[93] Jaffe, W., Bremer, M. N., and Baker, K. (2005). HII and H_2 in the envelopes of cooling flow central galaxies. , 360:748–762.

[94] Jansen, F., Lumb, D., Altieri, B., Clavel, J., Ehle, M., Erd, C., Gabriel, C., Guainazzi, M., Gondoin, P., Much, R., Munoz, R., Santos, M., Schartel, N., Texier, D., and Vacanti, G. (2001). XMM-Newton observatory. I. The spacecraft and operations. , 365:L1–L6.

[95] Johnstone, R. M., Fabian, A. C., Morris, R. G., and Taylor, G. B. (2005). The galaxy cluster Abell 3581 as seen by Chandra. , 356(1):237–246.

[96] Johnstone, R. M., Fabian, A. C., and Nulsen, P. E. J. (1987). The optical spectra of central galaxies in southern clusters Evidence for star formation. , 224:75–91.

[97] Johnstone, R. M., Hatch, N. A., Ferland, G. J., Fabian, A. C., Crawford, C. S., and Wilman, R. J. (2007). Discovery of atomic and molecular mid-infrared emission lines in off-nuclear regions of NGC 1275 and NGC4696 with the Spitzer Space Telescope. , 382(3):1246–1260.

[98] Juett, A. M., Schulz, N. S., Chakrabarty, D., and Gorczyca, T. W. (2006). High-Resolution X-Ray Spectroscopy of the Interstellar Medium. II. Neon and Iron Absorption Edges. , 648(2):1066–1078.

[99] Kaastra, J. S. (2017). On the use of C-stat in testing models for X-ray spectra. , 605:A51.

[100] Kaastra, J. S., Ferrigno, C., Tamura, T., Paerels, F. B. S., Peterson, J. R., and Mittaz, J. P. D. (2001). XMM-Newton observations of the cluster of galaxies Sérsic 159-03. , 365:L99–L103.

[101] Kaastra, J. S., Mewe, R., and Nieuwenhuijzen, H. (1996). SPEX: a new code for spectral analysis of X & UV spectra. In *UV and X-ray Spectroscopy of Astrophysical and Laboratory Plasmas*, pages 411–414.

[102] Kaastra, J. S., Paerels, F. B. S., Durret, F., Schindler, S., and Richter, P. (2008). Thermal Radiation Processes. , 134(1-4):155–190.

[103] Kaiser, N. (1991). Evolution of clusters of galaxies. , 383:104–111.

[104] Kalberla, P. M. W., Burton, W. B., Hartmann, D., Arnal, E. M., Bajaja, E., Morras, R., and Pöppel, W. G. L. (2005). The Leiden/Argentine/Bonn (LAB) Survey of Galactic HI. Final data release of the combined LDS and IAR surveys with improved stray-radiation corrections. , 440:775–782.

[105] Kirkpatrick, C. C., McNamara, B. R., Rafferty, D. A., Nulsen, P. E. J., Bîrzan, L., Kazemzadeh, F., Wise, M. W., Gitti, M., and Cavagnolo, K. W. (2009). A Chandra X-Ray Analysis of Abell 1664: Cooling, Feedback, and Star Formation in the Central Cluster Galaxy. , 697(1):867–879.

[106] Lakhchaura, K., Saini, T. D., and Sharma, P. (2016). Decoding X-ray observations from centres of galaxy clusters using MCMC. , 460(3):2625–2647.

[107] Lakhchaura, K., Werner, N., Sun, M., Canning, R. E. A., Gaspari, M., Allen, S. W., Connor, T., Donahue, M., and Sarazin, C. (2018). Thermodynamic properties, multiphase gas, and AGN feedback in a large sample of giant ellipticals. , 481:4472–4504.

[108] Larson, R. B. and Dinerstein, H. L. (1975). Gas loss in groups of galaxies. , 87:911–915.

[109] Lazarian, A. and Desiati, P. (2010). Magnetic Reconnection as the Cause of Cosmic Ray Excess from the Heliospheric Tail. , 722(1):188–196.

[110] Leccardi, A. and Molendi, S. (2008). Radial metallicity profiles for a large sample of galaxy clusters observed with XMM-Newton. , 487(2):461–466.

[111] Li, Y., Gendron-Marsolais, M.-L., Zhuravleva, I., Xu, S., Simionescu, A., Tremblay, G. R., Lochhaas, C., Bryan, G. L., Quataert, E., Murray, N. W., Boselli, A., Hlavacek-Larrondo, J., Zheng, Y., Fossati, M., Li, M., Emsellem, E., Sarzi, M., Arzamasskiy, L., and Vishniac, E. T. (2020). Direct Detection of Black Hole-driven Turbulence in the Centers of Galaxy Clusters. , 889(1):L1.

[112] Liu, H., Fabian, A. C., and Pinto, C. (2020). The inner gas mass-temperature profile in the core of nearby galaxy clusters. , 497(1):1256–1262.

[113] Liu, H., Pinto, C., Fabian, A. C., Russell, H. R., and Sanders, J. S. (2019). Searching for cool and cooling X-ray emitting gas in 45 galaxy clusters and groups. , 485(2):1757–1774.

[114] Lodders, K. and Palme, H. (2009). Solar System Elemental Abundances in 2009. *Meteoritics and Planetary Science Supplement*, 72:5154.

[115] Lotz, W. (1968). Electron-impact ionization cross-sections and ionization rate coefficients for atoms and ions from hydrogen to calcium. *Zeitschrift fur Physik*, 216(3):241–247.

[116] Matteucci, F. and Vettolani, G. (1988). Chemical abundances in galaxy clusters : a theoretical approach. , 202:21–26.

[117] McDonald, M., Bayliss, M., Benson, B. A., Foley, R. J., Ruel, J., Sullivan, P., Veilleux, S., Aird, K. A., Ashby, M. L. N., Bautz, M., Bazin, G., Bleem, L. E., Brodwin, M., Carlstrom, J. E., Chang, C. L., Cho, H. M., Clocchiatti, A., Crawford, T. M., Crites, A. T., de Haan, T., Desai, S., Dobbs, M. A., Dudley, J. P., Egami, E., Forman, W. R., Garmire, G. P., George, E. M., Gladders, M. D., Gonzalez, A. H., Halverson, N. W., Harrington, N. L., High, F. W., Holder, G. P., Holzapfel, W. L., Hoover, S., Hrubes, J. D., Jones, C., Joy, M., Keisler, R., Knox, L., Lee, A. T., Leitch, E. M., Liu, J., Lueker, M., Luong-van, D., Mantz, A., Marrone, D. P., McMahon, J. J., Mehl, J., Meyer, S. S., Miller, E. D., Mocanu, L., Mohr, J. J., Montroy, T. E., Murray, S. S., Natoli, T., Padin, S., Plagge, T., Pryke, C., Rawle, T. D., Reichardt, C. L., Rest, A., Rex, M., Ruhl, J. E., Saliwanchik, B. R., Saro, A., Sayre, J. T., Schaffer, K. K., Shaw, L., Shirokoff, E., Simcoe, R., Song, J., Spieler, H. G., Stalder, B., Staniszewski, Z., Stark, A. A., Story, K., Stubbs, C. W.,

Šuhada, R., van Engelen, A., Vanderlinde, K., Vieira, J. D., Vikhlinin, A., Williamson, R., Zahn, O., and Zenteno, A. (2012). A massive, cooling-flow-induced starburst in the core of a luminous cluster of galaxies. , 488(7411):349–352.

[118] McDonald, M., Benson, B., Veilleux, S., Bautz, M. W., and Reichardt, C. L. (2013). An HST/WFC3-UVIS View of the Starburst in the Cool Core of the Phoenix Cluster. , 765(2):L37.

[119] McDonald, M., Gaspari, M., McNamara, B. R., and Tremblay, G. R. (2018). Revisiting the Cooling Flow Problem in Galaxies, Groups, and Clusters of Galaxies. , 858:45.

[120] McDonald, M., McNamara, B. R., van Weeren, R. J., Applegate, D. E., Bayliss, M., Bautz, M. W., Benson, B. A., Carlstrom, J. E., Bleem, L. E., Chatzikos, M., Edge, A. C., Fabian, A. C., Garmire, G. P., Hlavacek-Larrondo, J., Jones-Forman, C., Mantz, A. B., Miller, E. D., Stalder, B., Veilleux, S., and ZuHone, J. A. (2015a). Deep Chandra, HST-COS, and Megacam Observations of the Phoenix Cluster: Extreme Star Formation and AGN Feedback on Hundred Kiloparsec Scales. , 811(2):111.

[121] McDonald, M., McNamara, B. R., Voit, G. M., Bayliss, M., Benson, B. A., Brodwin, M., Canning, R. E. A., Florian, M. K., Garmire, G. P., Gaspari, M., Gladders, M. D., Hlavacek-Larrondo, J., Kara, E., Reichardt, C. L., Russell, H. R., Saro, A., Sharon, K., Somboonpanyakul, T., Tremblay, G. R., and van Weeren, R. J. (2019). Anatomy of a Cooling Flow: The Feedback Response to Pure Cooling in the Core of the Phoenix Cluster. , 885(1):63.

[122] McDonald, M., Roediger, J., Veilleux, S., and Ehlert, S. (2014a). HST-COS Spectroscopy of the Cooling Flow in A1795—Evidence for Inefficient Star Formation in Condensing Intracluster Gas. , 791(2):L30.

[123] McDonald, M., Swinbank, M., Edge, A. C., Wilner, D. J., Veilleux, S., Benson, B. A., Hogan, M. T., Marrone, D. P., McNamara, B. R., Wei, L. H., Bayliss, M. B., and Bautz, M. W. (2014b). The State of the Warm and Cold Gas in the Extreme Starburst at the Core of the Phoenix Galaxy Cluster (SPT-CLJ2344-4243). , 784(1):18.

[124] McDonald, M., Veilleux, S., Rupke, D. S. N., and Mushotzky, R. (2010). On the Origin of the Extended Hα Filaments in Cooling Flow Clusters. , 721(2):1262–1283.

[125] McDonald, M., Veilleux, S., Rupke, D. S. N., Mushotzky, R., and Reynolds, C. (2011). Star Formation Efficiency in the Cool Cores of Galaxy Clusters. , 734(2):95.

[126] McDonald, M., Werner, N., Oonk, J. B. R., and Veilleux, S. (2015b). Extended, Dusty Star Formation Fueled by a Residual Cooling Flow in the Cluster of Galaxies Sérsic 159-03. , 804(1):16.

[127] McNamara, B. R. and Nulsen, P. E. J. (2007). Heating Hot Atmospheres with Active Galactic Nuclei. , 45:117–175.

[128] McNamara, B. R. and Nulsen, P. E. J. (2012). Mechanical feedback from active galactic nuclei in galaxies, groups and clusters. *New Journal of Physics*, 14(5):055023.

[129] McNamara, B. R., Rafferty, D. A., Bîrzan, L., Steiner, J., Wise, M. W., Nulsen, P. E. J., Carilli, C. L., Ryan, R., and Sharma, M. (2006). The Starburst in the Abell 1835 Cluster Central Galaxy: A Case Study of Galaxy Formation Regulated by an Outburst from a Supermassive Black Hole. , 648(1):164–175.

[130] McNamara, B. R., Russell, H. R., Nulsen, P. E. J., Edge, A. C., Murray, N. W., Main, R. A., Vantyghem, A. N., Combes, F., Fabian, A. C., Salome, P., Kirkpatrick, C. C., Baum, S. A., Bregman, J. N., Donahue, M., Egami, E., Hamer, S., O'Dea, C. P., Oonk, J. B. R., Tremblay, G., and Voit, G. M. (2014). A 10^{10} Solar Mass Flow of Molecular Gas in the A1835 Brightest Cluster Galaxy. , 785(1):44.

[131] Merloni, A., Predehl, P., Becker, W., Böhringer, H., Boller, T., Brunner, H., Brusa, M., Dennerl, K., Freyberg, M., Friedrich, P., Georgakakis, A., Haberl, F., Hasinger, G., Meidinger, N., Mohr, J., Nandra, K., Rau, A., Reiprich, T. H., Robrade, J., Salvato, M., Santangelo, A., Sasaki, M., Schwope, A., Wilms, J., and German eROSITA Consortium, t. (2012). eROSITA Science Book: Mapping the Structure of the Energetic Universe. *arXiv e-prints*, page arXiv:1209.3114.

[132] Mighell, K. J. (1999). Parameter Estimation in Astronomy with Poisson-distributed Data. I.The χ^2 $_\gamma$ Statistic. , 518(1):380–393.

[133] Million, E. T. and Allen, S. W. (2009). Chandra measurements of non-thermal-like X-ray emission from massive, merging, radio halo clusters. , 399(3):1307–1327.

[134] Mushotzky, R. F. and Szymkowiak, A. E. (1988). *Cooling Flows in Clusters and Galaxies (Nato ASI Series C:).* Kluwer Academic Publishers.

[135] Nandra, K., Barret, D., Barcons, X., Fabian, A., den Herder, J.-W., Piro, L., Watson, M., Adami, C., Aird, J., Afonso, J. M., Alexander, D., Argiroffi, C., Amati, L., Arnaud, M., Atteia, J.-L., Audard, M., Badenes, C., Ballet, J., Ballo, L., Bamba, A., Bhardwaj, A., Stefano Battistelli, E., Becker, W., De Becker, M., Behar, E., Bianchi, S., Biffi, V., Bîrzan, L., Bocchino, F., Bogdanov, S., Boirin, L., Boller, T., Borgani, S., Borm, K., Bouché, N., Bourdin, H., Bower, R., Braito, V., Branchini, E., Branduardi-Raymont, G., Bregman, J., Brenneman, L., Brightman, M., Brüggen, M., Buchner, J., Bulbul, E., Brusa, M., Bursa, M., Caccianiga, A., Cackett, E., Campana, S., Cappelluti, N., Cappi, M., Carrera, F., Ceballos, M., Christensen, F., Chu, Y.-H., Churazov, E., Clerc, N., Corbel, S., Corral, A., Comastri, A., Costantini, E., Croston, J., Dadina, M., D'Ai, A., Decourchelle, A., Della Ceca, R., Dennerl, K., Dolag, K., Done, C., Dovciak, M., Drake, J., Eckert, D., Edge, A., Ettori, S., Ezoe, Y., Feigelson, E., Fender, R., Feruglio, C., Finoguenov, A., Fiore, F., Galeazzi, M., Gallagher, S., Gandhi, P., Gaspari, M., Gastaldello, F., Georgakakis, A., Georgantopoulos, I., Gilfanov, M., Gitti, M., Gladstone, R., Goosmann, R., Gosset, E., Grosso, N., Guedel, M., Guerrero, M., Haberl, F., Hardcastle, M., Heinz, S., Alonso Herrero, A., Hervé, A., Holmstrom, M., Iwasawa, K., Jonker, P., Kaastra, J., Kara, E., Karas, V., Kastner, J., King, A., Kosenko, D., Koutroumpa, D., Kraft, R., Kreykenbohm, I., Lallement, R., Lanzuisi, G., Lee, J., Lemoine-Goumard, M., Lobban, A., Lodato, G., Lovisari, L., Lotti, S., McCharthy, I., McNamara, B., Maggio, A., Maiolino, R., De Marco, B., de Martino, D., Mateos, S., Matt, G., Maughan, B., Mazzotta, P., Mendez, M., Merloni, A., Micela, G., Miceli, M., Mignani, R., Miller, J., Miniutti, G., Molendi, S., Montez, R., Moretti, A., Motch, C., Nazé, Y., Nevalainen, J., Nicastro, F., Nulsen, P., Ohashi, T., O'Brien, P., Osborne, J., Oskinova, L., Pacaud, F., Paerels, F., Page, M., Papadakis, I.,

Pareschi, G., Petre, R., Petrucci, P.-O., Piconcelli, E., Pillitteri, I., Pinto, C., de Plaa, J., Pointecouteau, E., Ponman, T., Ponti, G., Porquet, D., Pounds, K., Pratt, G., Predehl, P., Proga, D., Psaltis, D., Rafferty, D., Ramos-Ceja, M., Ranalli, P., Rasia, E., Rau, A., Rauw, G., Rea, N., Read, A., Reeves, J., Reiprich, T., Renaud, M., Reynolds, C., Risaliti, G., Rodriguez, J., Rodriguez Hidalgo, P., Roncarelli, M., Rosario, D., Rossetti, M., Rozanska, A., Rovilos, E., Salvaterra, R., Salvato, M., Di Salvo, T., Sanders, J., Sanz-Forcada, J., Schawinski, K., Schaye, J., Schwope, A., Sciortino, S., Severgnini, P., Shankar, F., Sijacki, D., Sim, S., Schmid, C., Smith, R., Steiner, A., Stelzer, B., Stewart, G., Strohmayer, T., Strüder, L., Sun, M., Takei, Y., Tatischeff, V., Tiengo, A., Tombesi, F., Trinchieri, G., Tsuru, T. G., Ud-Doula, A., Ursino, E., Valencic, L., Vanzella, E., Vaughan, S., Vignali, C., Vink, J., Vito, F., Volonteri, M., Wang, D., Webb, N., Willingale, R., Wilms, J., Wise, M., Worrall, D., Young, A., Zampieri, L., In't Zand, J., Zane, S., Zezas, A., Zhang, Y., and Zhuravleva, I. (2013). The Hot and Energetic Universe: A White Paper presenting the science theme motivating the Athena+ mission. *arXiv e-prints*, page arXiv:1306.2307.

[136] Nousek, J. A. and Shue, D. R. (1989). Psi 2 and C Statistic Minimization for Low Count per Bin Data. , 342:1207.

[137] Nulsen, P. E. J., Hambrick, D. C., McNamara, B. R., Rafferty, D., Birzan, L., Wise, M. W., and David, L. P. (2005a). The Powerful Outburst in Hercules A. , 625(1):L9–L12.

[138] Nulsen, P. E. J., Johnstone, R. M., and Fabian, A. C. (1987). Star formation in cooling flows. *Proceedings of the Astronomical Society of Australia*, 7:132–135.

[139] Nulsen, P. E. J., Jones, C., Forman, W. R., David, L. P., McNamara, B. R., Rafferty, D. A., Bîrzan, L., and Wise, M. W. (2007). AGN Heating Through Cavities and Shocks. In Böhringer, H., Pratt, G. W., Finoguenov, A., and Schuecker, P., editors, *Heating versus Cooling in Galaxies and Clusters of Galaxies*, page 210.

[140] Nulsen, P. E. J., McNamara, B. R., Wise, M. W., and David, L. P. (2005b). The Cluster-Scale AGN Outburst in Hydra A. , 628(2):629–636.

[141] O'Dea, C. P., Baum, S. A., Privon, G., Noel-Storr, J., Quillen, A. C., Zufelt, N., Park, J., Edge, A., Russell, H., Fabian, A. C., Donahue, M., Sarazin, C. L., McNamara, B., Bregman, J. N., and Egami, E. (2008). An Infrared Survey of Brightest Cluster Galaxies. II. Why are Some Brightest Cluster Galaxies Forming Stars? , 681:1035–1045.

[142] O'Dea, K. P., Quillen, A. C., O'Dea, C. P., Tremblay, G. R., Snios, B. T., Baum, S. A., Christiansen, K., Noel-Storr, J., Edge, A. C., Donahue, M., and Voit, G. M. (2010). Hubble Space Telescope Far-ultraviolet Observations of Brightest Cluster Galaxies: The Role of Star Formation in Cooling Flows and BCG Evolution. , 719(2):1619–1632.

[143] Ogorzalek, A., Zhuravleva, I., Allen, S. W., Pinto, C., Werner, N., Mantz, A. B., Canning, R. E. A., Fabian, A. C., Kaastra, J. S., and de Plaa, J. (2017). Improved measurements of turbulence in the hot gaseous atmospheres of nearby giant elliptical galaxies. , 472(2):1659–1676.

[144] Ogrean, G. A., Hatch, N. A., Simionescu, A., Böhringer, H., Brüggen, M., Fabian, A. C., and Werner, N. (2010). Central galaxy growth and feedback in the most massive nearby cool core cluster. , 406(1):354–367.

[145] Olivares, V., Salome, P., Combes, F., Hamer, S., Guillard, P., Lehnert, M. D., Polles, F. L., Beckmann, R. S., Dubois, Y., Donahue, M., Edge, A., Fabian, A. C., McNamara, B., Rose, T., Russell, H. R., Tremblay, G., Vantyghem, A., Canning, R. E. A., Ferland , G., Godard, B., Peirani, S., and Pineau des Forets, G. (2019). Ubiquitous cold and massive filaments in cool core clusters. , 631:A22.

[146] Panagoulia, E. K., Fabian, A. C., and Sanders, J. S. (2013). Searching for the missing iron mass in the core of the Centaurus cluster. , 433:3290–3296.

[147] Panagoulia, E. K., Fabian, A. C., and Sanders, J. S. (2014). A volume-limited sample of X-ray galaxy groups and clusters - I. Radial entropy and cooling time profiles. , 438:2341–2354.

[148] Panagoulia, E. K., Sanders, J. S., and Fabian, A. C. (2015). A volume-limited sample of X-ray galaxy groups and clusters - III. Central abundance drops. , 447:417–436.

[149] Peres, C. B., Fabian, A. C., Edge, A. C., Allen, S. W., Johnstone, R. M., and White, D. A. (1998). A ROSAT study of the cores of clusters of galaxies - I. Cooling flows in an X-ray flux-limited sample. , 298:416–432.

[150] Peterson, J. R. and Fabian, A. C. (2006). X-ray spectroscopy of cooling clusters. *Physics Reports*, 427:1–39.

[151] Peterson, J. R., Kahn, S. M., Paerels, F. B. S., Kaastra, J. S., Tamura, T., Bleeker, J. A. M., Ferrigno, C., and Jernigan, J. G. (2003). High-Resolution X-Ray Spectroscopic Constraints on Cooling-Flow Models for Clusters of Galaxies. , 590:207–224.

[152] Peterson, J. R., Paerels, F. B. S., Kaastra, J. S., Arnaud, M., Reiprich, T. H., Fabian, A. C., Mushotzky, R. F., Jernigan, J. G., and Sakelliou, I. (2001). X-ray imaging-spectroscopy of Abell 1835. , 365:L104–L109.

[153] Piffaretti, R., Arnaud, M., Pratt, G. W., Pointecouteau, E., and Melin, J. B. (2011). The MCXC: a meta-catalogue of x-ray detected clusters of galaxies. , 534:A109.

[154] Pinto, C., Bambic, C. J., Sanders, J. S., Fabian, A. C., McDonald, M., Russell, H. R., Liu, H., and Reynolds, C. S. (2018). AGN feedback in the Phoenix cluster. , 480:4113–4123.

[155] Pinto, C., Fabian, A. C., Ogorzalek, A., Zhuravleva, I., Werner, N., Sanders, J., Zhang, Y.-Y., Gu, L., de Plaa, J., Ahoranta, J., Finoguenov, A., Johnstone, R., and Canning, R. E. A. (2016). Insights into the location and dynamics of the coolest X-ray emitting gas in clusters of galaxies. , 461:2077–2084.

[156] Pinto, C., Fabian, A. C., Werner, N., Kosec, P., Ahoranta, J., de Plaa, J., Kaastra, J. S., Sanders, J. S., Zhang, Y.-Y., and Finoguenov, A. (2014). Discovery of O VII line emitting gas in elliptical galaxies. , 572:L8.

[157] Pinto, C., Kaastra, J. S., Costantini, E., and de Vries, C. (2013). Interstellar medium composition through X-ray spectroscopy of low-mass X-ray binaries. , 551:A25.

[158] Pinto, C., Sanders, J. S., Werner, N., de Plaa, J., Fabian, A. C., Zhang, Y.-Y., Kaastra, J. S., Finoguenov, A., and Ahoranta, J. (2015). Chemical Enrichment RGS cluster Sample (CHEERS): Constraints on turbulence. , 575:A38.

[159] Polles, F. L., Salomé, P., Guillard, P., Godard, B., Pineau des Forêts, G., Olivares, V., Beckmann, R. S., Canning, R. E. A., Combes, F., Dubois, Y., Edge, A. C., Fabian, A. C., Ferland, G. J., Hamer, S. L., and Lehnert, M. D. (2021). Excitation mechanisms in the intracluster filaments surrounding Brightest Cluster Galaxies. *arXiv e-prints*, page arXiv:2103.09842.

[160] Pulido, F. A., McNamara, B. R., Edge, A. C., Hogan, M. T., Vantyghem, A. N., Russell, H. R., Nulsen, P. E. J., Babyk, I., and Salomé, P. (2018). The Origin of Molecular Clouds in Central Galaxies. , 853(2):177.

[161] Rafferty, D. A., McNamara, B. R., and Nulsen, P. E. J. (2008). The Regulation of Cooling and Star Formation in Luminous Galaxies by Active Galactic Nucleus Feedback and the Cooling-Time/Entropy Threshold for the Onset of Star Formation. , 687:899–918.

[162] Rafferty, D. A., McNamara, B. R., Nulsen, P. E. J., and Wise, M. W. (2006). The Feedback-regulated Growth of Black Holes and Bulges through Gas Accretion and Starbursts in Cluster Central Dominant Galaxies. , 652(1):216–231.

[163] Rau, A., Meidinger, N., Nandra, K., Porro, M., Barret, D., Santangelo, A., Schmid, C., Struder, L., Tenzer, C., Wilms, J., Amoros, C., Andritschke, R., Aschauer, F., Bahr, A., Gunther, B., Furmetz, M., Ott, B., Perinati, E., Rambaud, D., Reiffers, J., Treis, J., von Kienlin, A., and Weidenspointner, G. (2013). The Hot and Energetic Universe: The Wide Field Imager (WFI) for Athena+. *arXiv e-prints*, page arXiv:1308.6785.

[164] Reynolds, C. S., Balbus, S. A., and Schekochihin, A. A. (2015). Inefficient Driving of Bulk Turbulence By Active Galactic Nuclei in a Hydrodynamic Model of the Intracluster Medium. , 815(1):41.

[165] Russell, H. R., Fabian, A. C., Sanders, J. S., Johnstone, R. M., Blundell, K. M., Brandt, W. N., and Crawford, C. S. (2010). The X-ray luminous cluster underlying the bright radio-quiet quasar H1821+643. , 402(3):1561–1579.

[166] Russell, H. R., McDonald, M., McNamara, B. R., Fabian, A. C., Nulsen, P. E. J., Bayliss, M. B., Benson, B. A., Brodwin, M., Carlstrom, J. E., Edge, A. C., Hlavacek-Larrondo, J., Marrone, D. P., Reichardt, C. L., and Vieira, J. D. (2017). Alma Observations of Massive Molecular Gas Filaments Encasing Radio Bubbles in the Phoenix Cluster. , 836(1):130.

[167] Russell, H. R., McNamara, B. R., Edge, A. C., Nulsen, P. E. J., Main, R. A., Vantyghem, A. N., Combes, F., Fabian, A. C., Murray, N., Salomé, P., Wilman, R. J., Baum, S. A., Donahue, M., O'Dea, C. P., Oonk, J. B. R., Tremblay, G. R., and Voit, G. M. (2014). Massive Molecular Gas Flows in the A1664 Brightest Cluster Galaxy. , 784(1):78.

[168] Russell, H. R., McNamara, B. R., Fabian, A. C., Nulsen, P. E. J., Combes, F., Edge, A. C., Madar, M., Olivares, V., Salomé, P., and Vantyghem, A. N. (2019). Driving massive molecular gas flows in central cluster galaxies with AGN feedback. , 490(3):3025–3045.

[169] Russell, H. R., McNamara, B. R., Fabian, A. C., Nulsen, P. E. J., Edge, A. C., Combes, F., Murray, N. W., Parrish, I. J., Salomé, P., Sanders, J. S., Baum, S. A., Donahue, M., Main, R. A., O'Connell, R. W., O'Dea, C. P., Oonk, J. B. R., Tremblay, G., Vantyghem, A. N., and Voit, G. M. (2016). ALMA observations of cold molecular gas filaments trailing rising radio bubbles in PKS 0745-191. , 458(3):3134–3149.

[170] Ruszkowski, M., Yang, H. Y. K., and Reynolds, C. S. (2018). Powering of Hα Filaments by Cosmic Rays. , 858(1):64.

[171] Salomé, P. and Combes, F. (2003). Cold molecular gas in cooling flow clusters of galaxies. , 412:657–667.

[172] Salomé, P., Combes, F., Edge, A. C., Crawford, C., Erlund, M., Fabian, A. C., Hatch, N. A., Johnstone, R. M., Sanders, J. S., and Wilman, R. J. (2006). Cold molecular gas in the Perseus cluster core. Association with X-ray cavity, Hα filaments and cooling flow. , 454:437–445.

[173] Salomé, P., Combes, F., Revaz, Y., Downes, D., Edge, A. C., and Fabian, A. C. (2011). A very extended molecular web around NGC 1275. , 531:A85.

[174] Sanders, J. S., Dennerl, K., Russell, H. R., Eckert, D., Pinto, C., Fabian, A. C., Walker, S. A., Tamura, T., ZuHone, J., and Hofmann, F. (2020). Measuring bulk flows of the intracluster medium in the Perseus and Coma galaxy clusters using XMM-Newton. , 633:A42.

[175] Sanders, J. S. and Fabian, A. C. (2006a). Isothermal shocks in Abell 2199 and 2A 0335+096? , 371(1):L65–L69.

[176] Sanders, J. S. and Fabian, A. C. (2006b). Resonance scattering, absorption and off-centre abundance peaks in clusters of galaxies. , 370(1):63–73.

[177] Sanders, J. S. and Fabian, A. C. (2007). A deeper X-ray study of the core of the Perseus galaxy cluster: the power of sound waves and the distribution of metals and cosmic rays. , 381(4):1381–1399.

[178] Sanders, J. S. and Fabian, A. C. (2011). Revealing O VII from stacked X-ray grating spectra of clusters, groups and elliptical galaxies. , 412:L35–L39.

[179] Sanders, J. S. and Fabian, A. C. (2012). Deep Chandra and XMM-Newton X-ray observations of AWM 7 - I. Investigating X-ray surface brightness fluctuations. , 421:726–742.

[180] Sanders, J. S. and Fabian, A. C. (2013). Velocity width measurements of the coolest X-ray emitting material in the cores of clusters, groups and elliptical galaxies. , 429:2727–2738.

[181] Sanders, J. S., Fabian, A. C., Allen, S. W., Morris, R. G., Graham, J., and Johnstone, R. M. (2008). Cool X-ray emitting gas in the core of the Centaurus cluster of galaxies. , 385:1186–1200.

[182] Sanders, J. S., Fabian, A. C., Frank, K. A., Peterson, J. R., and Russell, H. R. (2010a). Deep high-resolution X-ray spectra from cool-core clusters. , 402:127–144.

[183] Sanders, J. S., Fabian, A. C., and Smith, R. K. (2011). Constraints on turbulent velocity broadening for a sample of clusters, groups and elliptical galaxies using XMM-Newton. , 410:1797–1812.

[184] Sanders, J. S., Fabian, A. C., Smith, R. K., and Peterson, J. R. (2010b). A direct limit on the turbulent velocity of the intracluster medium in the core of Abell 1835 from XMM-Newton. , 402:L11–L15.

[185] Sanders, J. S., Fabian, A. C., and Taylor, G. B. (2009). Feedback through multiple outbursts in the cluster 2A 0335+096. , 396(3):1449–1459.

[186] Sanders, J. S., Fabian, A. C., Taylor, G. B., Russell, H. R., Blundell, K. M., Canning, R. E. A., Hlavacek-Larrondo, J., Walker, S. A., and Grimes, C. K. (2016). A very deep Chandra view of metals, sloshing and feedback in the Centaurus cluster of galaxies. , 457:82–109.

[187] Santos, J. S., Rosati, P., Tozzi, P., Böhringer, H., Ettori, S., and Bignamini, A. (2008). Searching for cool core clusters at high redshift. , 483(1):35–47.

[188] Semler, D. R., Šuhada, R., Aird, K. A., Ashby, M. L. N., Bautz, M., Bayliss, M., Bazin, G., Bocquet, S., Benson, B. A., Bleem, L. E., Brodwin, M., Carlstrom, J. E., Chang, C. L., Cho, H. M., Clocchiatti, A., Crawford, T. M., Crites, A. T., de Haan, T., Desai, S., Dobbs, M. A., Dudley, J. P., Foley, R. J., George, E. M., Gladders, M. D., Gonzalez, A. H., Halverson, N. W., Harrington, N. L., High, F. W., Holder, G. P., Holzapfel, W. L., Hoover, S., Hrubes, J. D., Jones, C., Joy, M., Keisler, R., Knox, L., Lee, A. T., Leitch, E. M., Liu, J., Lueker, M., Luong-Van, D., Mantz, A., Marrone, D. P., McDonald, M., McMahon, J. J., Mehl, J., Meyer, S. S., Mocanu, L., Mohr, J. J., Montroy, T. E., Murray, S. S., Natoli, T., Padin, S., Plagge, T., Pryke, C., Reichardt, C. L., Rest, A., Ruel, J., Ruhl, J. E., Saliwanchik, B. R., Saro, A., Sayre, J. T., Schaffer, K. K., Shaw, L., Shirokoff, E., Song, J., Spieler, H. G., Stalder, B., Staniszewski, Z., Stark, A. A., Story, K., Stubbs, C. W., van Engelen, A., Vanderlinde, K., Vieira, J. D., Vikhlinin, A., Williamson, R., Zahn, O., and Zenteno, A. (2012). High-redshift Cool-core Galaxy Clusters Detected via the Sunyaev-Zel'dovich Effect in the South Pole Telescope Survey. , 761(2):183.

[189] Simionescu, A., Tremblay, G., Werner, N., Canning, R. E. A., Allen, S. W., and Oonk, J. B. R. (2018). ALMA observation of the disruption of molecular gas in M87. , 475(3):3004–3009.

[190] Snowden, S. L., Mushotzky, R. F., Kuntz, K. D., and Davis, D. S. (2008). A catalog of galaxy clusters observed by XMM-Newton. , 478:615–658.

[191] Sparks, W. B., Ford, H. C., and Kinney, A. L. (1993). The Dusty Emission Filaments of M87. , 413:531.

[192] Sparks, W. B., Macchetto, F., and Golombek, D. (1989). Imaging Observations of Gas and Dust in NGC 4696 and Implications for Cooling Flow Models. , 345:153.

[193] Stewart, G. C., Fabian, A. C., Jones, C., and Forman, W. (1984). The prevalence of cooling flows in clusters of galaxies. , 285:1–6.

[194] Strüder, L., Briel, U., Dennerl, K., Hartmann, R., Kendziorra, E., Meidinger, N., Pfeffermann, E., Reppin, C., Aschenbach, B., Bornemann, W., Bräuninger, H., Burkert, W., Elender, M., Freyberg, M., Haberl, F., Hartner, G., Heuschmann, F., Hippmann, H., Kastelic, E., Kemmer, S., Kettenring, G., Kink, W., Krause, N., Müller, S., Oppitz, A., Pietsch, W., Popp, M., Predehl, P., Read, A., Stephan, K. H., Stötter, D., Trümper, J., Holl, P., Kemmer, J., Soltau, H., Stötter, R., Weber, U., Weichert, U., von Zanthier, C., Carathanassis, D., Lutz, G., Richter, R. H., Solc, P., Böttcher, H., Kuster, M., Staubert, R., Abbey, A., Holland, A., Turner, M., Balasini, M., Bignami, G. F., La Palombara, N., Villa, G., Buttler, W., Gianini, F., Lainé, R., Lumb, D., and Dhez, P. (2001). The European Photon Imaging Camera on XMM-Newton: The pn-CCD camera. , 365:L18–L26.

[195] Sunyaev, R. A. and Zeldovich, Y. B. (1972). The Observations of Relic Radiation as a Test of the Nature of X-Ray Radiation from the Clusters of Galaxies. *Comments on Astrophysics and Space Physics*, 4:173.

[196] Takahashi, T., Mitsuda, K., Kelley, R., Aarts, H., Aharonian, F., Akamatsu, H., Akimoto, F., Allen, S., Anabuki, N., Angelini, L., Arnaud, K., Asai, M., Audard, M., Awaki, H., Azzarello, P., Baluta, C., Bamba, A., Bando, N., Bautz, M., Blandford, R., Boyce, K., Brown, G., Cackett, E., Chernyakova, M., Coppi, P., Costantini, E., de Plaa, J., den Herder, J.-W., DiPirro, M., Done, C., Dotani, T., Doty, J., Ebisawa, K., Eckart, M., Enoto, T., Ezoe, Y., Fabian, A., Ferrigno, C., Foster, A., Fujimoto, R., Fukazawa, Y., Funk, S., Furuzawa, A., Galeazzi, M., Gallo, L., Gandhi, P., Gendreau, K., Gilmore, K., Haas, D., Haba, Y., Hamaguchi, K., Hatsukade, I., Hayashi, T., Hayashida, K., Hiraga, J., Hirose, K., Hornschemeier, A., Hoshino, A., Hughes, J., Hwang, U., Iizuka, R., Inoue, Y., Ishibashi, K., Ishida, M., Ishimura, K., Ishisaki, Y., Ito, M., Iwata, N., Iyomoto, N., Kaastra, J., Kallman, T., Kamae, T., Kataoka, J., Katsuda, S., Kawahara, H., Kawaharada, M., Kawai, N., Kawasaki, S., Khangaluyan, D., Kilbourne, C., Kimura, M., Kinugasa, K., Kitamoto, S., Kitayama, T., Kohmura, T., Kokubun, M., Kosaka, T., Koujelev, A., Koyama, K., Krimm, H., Kubota, A., Kunieda, H., LaMassa, S., Laurent, P., Lebrun, F., Leutenegger, M., Limousin, O., Loewenstein, M., Long, K., Lumb, D., Madejski, G., Maeda, Y., Makishima, K., Marchand, G., Markevitch, M., Matsumoto, H., Matsushita, K., McCammon, D., McNamara, B., Miller, J., Miller, E., Mineshige, S., Minesugi, K., Mitsuishi, I., Miyazawa, T., Mizuno, T., Mori, H., Mori, K., Mukai, K., Murakami, T., Murakami, H., Mushotzky, R., Nagano, H., Nagino, R., Nakagawa, T., Nakajima, H., Nakamori, T., Nakazawa, K., Namba, Y., Natsukari, C., Nishioka, Y., Nobukawa, M., Nomachi, M., O'Dell, S., Odaka, H., Ogawa, H., Ogawa, M., Ogi, K., Ohashi, T., Ohno, M., Ohta, M., Okajima, T., Okamoto, A., Okazaki, T., Ota, N., Ozaki, M., Paerels, F., Paltani, S., Parmar, A., Petre, R., Pohl, M., Porter, F. S., Ramsey, B., Reis, R., Reynolds, C., Russell, H., Safi-Harb, S., Sakai, S.-i., Sameshima, H., Sanders, J., Sato, G., Sato, R., Sato, Y., Sato, K., Sawada, M., Serlemitsos, P., Seta, H., Shibano, Y., Shida, M., Shimada, T., Shinozaki, K., Shirron, P., Simionescu, A., Simmons, C., Smith, R., Sneiderman, G., Soong, Y., Stawarz, L., Sugawara, Y., Sugita, H., Sugita, S., Szymkowiak, A., Tajima, H., Takahashi, H., Takeda, S.-i., Takei, Y., Tamagawa, T., Tamura, T., Tamura, K., Tanaka, T., Tanaka, Y., Tashiro, M., Tawara, Y., Terada, Y., Terashima, Y., Tombesi, F., Tomida, H., Tsuboi, Y., Tsujimoto, M., Tsunemi, H., Tsuru, T., Uchida, H., Uchiyama, Y., Uchiyama, H., Ueda, Y., Ueno, S., Uno, S., Urry, M., Ursino, E., de Vries, C., Wada, A., Watanabe, S., Werner, N., White, N., Yamada, T., Yamada, S., Yamaguchi, H., Yamasaki, N., Yamauchi, S., Yamauchi, M., Yatsu, Y., Yonetoku, D., Yoshida, A., and Yuasa, T. (2012). The ASTRO-H X-ray Observatory. In Takahashi, T., Murray, S. S., and den Herder, J.-W. A.,

editors, *Space Telescopes and Instrumentation 2012: Ultraviolet to Gamma Ray*, volume 8443 of *Society of Photo-Optical Instrumentation Engineers (SPIE) Conference Series*, page 84431Z.

[197] Tamura, T., Kaastra, J. S., Peterson, J. R., Paerels, F. B. S., Mittaz, J. P. D., Trudolyubov, S. P., Stewart, G., Fabian, A. C., Mushotzky, R. F., Lumb, D. H., and Ikebe, Y. (2001). X-ray spectroscopy of the cluster of galaxies Abell 1795 with XMM-Newton. , 365:L87–L92.

[198] Taylor, G. B., Fabian, A. C., Gentile, G., Allen, S. W., Crawford, C., and Sanders, J. S. (2007). Fields and filaments in the core of the Centaurus cluster. , 382(1):67–72.

[199] Tozzi, P., Gastaldello, F., Molendi, S., Ettori, S., Santos, J. S., De Grandi, S., Balestra, I., Rosati, P., Altieri, B., Cresci, G., Menanteau, F., and Valtchanov, I. (2015). New XMM-Newton observation of the Phoenix cluster: properties of the cool core. , 580:A6.

[200] Turner, M. J. L., Abbey, A., Arnaud, M., Balasini, M., Barbera, M., Belsole, E., Bennie, P. J., Bernard, J. P., Bignami, G. F., Boer, M., Briel, U., Butler, I., Cara, C., Chabaud, C., Cole, R., Collura, A., Conte, M., Cros, A., Denby, M., Dhez, P., Di Coco, G., Dowson, J., Ferrando, P., Ghizzardi, S., Gianotti, F., Goodall, C. V., Gretton, L., Griffiths, R. G., Hainaut, O., Hochedez, J. F., Holland, A. D., Jourdain, E., Kendziorra, E., Lagostina, A., Laine, R., La Palombara, N., Lortholary, M., Lumb, D., Marty, P., Molendi, S., Pigot, C., Poindron, E., Pounds, K. A., Reeves, J. N., Reppin, C., Rothenflug, R., Salvetat, P., Sauvageot, J. L., Schmitt, D., Sembay, S., Short, A. D. T., Spragg, J., Stephen, J., Strüder, L., Tiengo, A., Trifoglio, M., Trümper, J., Vercellone, S., Vigroux, L., Villa, G., Ward, M. J., Whitehead, S., and Zonca, E. (2001). The European Photon Imaging Camera on XMM-Newton: The MOS cameras. , 365:L27–L35.

[201] Urdampilleta, I., Kaastra, J. S., and Mehdipour, M. (2017). X-ray emission from thin plasmas. Collisional ionization for atoms and ions of H to Zn. , 601:A85.

[202] Vantyghem, A. N., McNamara, B. R., Edge, A. C., Combes, F., Russell, H. R., Fabian, A. C., Hogan, M. T., McDonald, M., Nulsen, P. E. J., and Salomé, P. (2017). A ^{13}CO Detection in a Brightest Cluster Galaxy. , 848(2):101.

[203] Vantyghem, A. N., McNamara, B. R., Russell, H. R., Edge, A. C., Nulsen, P. E. J., Combes, F., Fabian, A. C., McDonald, M., and Salomé, P. (2018). Molecular Gas Filaments and Star-forming Knots Beneath an X-Ray Cavity in RXC J1504-0248. , 863(2):193.

[204] Vantyghem, A. N., McNamara, B. R., Russell, H. R., Hogan, M. T., Edge, A. C., Nulsen, P. E. J., Fabian, A. C., Combes, F., Salomé, P., Baum, S. A., Donahue, M., Main, R. A., Murray, N. W., O'Connell, R. W., O'Dea, C. P., Oonk, J. B. R., Parrish, I. J., Sanders, J. S., Tremblay, G., and Voit, G. M. (2016). Molecular Gas Along a Bright Hα Filament in 2A 0335+096 Revealed by ALMA. , 832(2):148.

[205] Voigt, L. M. and Fabian, A. C. (2004). Thermal conduction and reduced cooling flows in galaxy clusters. , 347:1130–1149.

[206] Voit, G. M., Bryan, G. L., Balogh, M. L., and Bower, R. G. (2002). Modified Entropy Models for the Intracluster Medium. , 576:601–624.

[207] Walker, S. A., Fabian, A. C., Russell, H. R., and Sanders, J. S. (2014). The effect of the quasar H1821+643 on the surrounding intracluster medium: revealing the underlying cooling flow. , 442(3):2809–2816.

[208] Walker, S. A., Hlavacek-Larrondo, J., Gendron-Marsolais, M., Fabian, A. C., Intema, H., Sanders, J. S., Bamford, J. T., and van Weeren, R. (2017). Is there a giant Kelvin-Helmholtz instability in the sloshing cold front of the Perseus cluster? , 468(2):2506–2516.

[209] Walker, S. A., Kosec, P., Fabian, A. C., and Sanders, J. S. (2015). X-ray analysis of filaments in galaxy clusters. , 453:2480–2489.

[210] Walker, S. A., Sanders, J. S., and Fabian, A. C. (2018). What fraction of the density fluctuations in the Perseus cluster core is due to gas sloshing rather than AGN feedback? , 481(2):1718–1725.

[211] Weisskopf, M. C., Tananbaum, H. D., Van Speybroeck, L. P., and O'Dell, S. L. (2000). Chandra X-ray Observatory (CXO): overview. In Truemper, J. E. and Aschenbach, B., editors, *X-Ray Optics, Instruments, and Missions III*, volume 4012 of *Society of Photo-Optical Instrumentation Engineers (SPIE) Conference Series*, pages 2–16.

[212] Werner, N., Oonk, J. B. R., Canning, R. E. A., Allen, S. W., Simionescu, A., Kos, J., van Weeren, R. J., Edge, A. C., Fabian, A. C., von der Linden, A., Nulsen, P. E. J., Reynolds, C. S., and Ruszkowski, M. (2013). The Nature of Filamentary Cold Gas in the Core of the Virgo Cluster. , 767(2):153.

[213] Werner, N., Simionescu, A., Million, E. T., Allen, S. W., Nulsen, P. E. J., von der Linden, A., Hansen, S. M., Böhringer, H., Churazov, E., Fabian, A. C., Forman, W. R., Jones, C., Sanders, J. S., and Taylor, G. B. (2010). Feedback under the microscope-II. Heating, gas uplift and mixing in the nearest cluster core. , 407:2063–2074.

[214] Werner, N., Sun, M., Bagchi, J., Allen, S. W., Taylor, G. B., Sirothia, S. K., Simionescu, A., Million, E. T., Jacob, J., and Donahue, M. (2011). Violent interaction between the active galactic nucleus and the hot gas in the core of the galaxy cluster Sérsic 159-03. , 415(4):3369–3379.

[215] Werner, N., Zhuravleva, I., Churazov, E., Simionescu, A., Allen, S. W., Forman, W., Jones, C., and Kaastra, J. S. (2009). Constraints on turbulent pressure in the X-ray haloes of giant elliptical galaxies from resonant scattering. , 398(1):23–32.

[216] White, D. A., Jones, C., and Forman, W. (1997). An investigation of cooling flows and general cluster properties from an X-ray image deprojection analysis of 207 clusters of galaxies. , 292:419.

[217] Willingale, R., Starling, R. L. C., Beardmore, A. P., Tanvir, N. R., and O'Brien, P. T. (2013). Calibration of X-ray absorption in our Galaxy. , 431:394–404.

[218] Wilman, R. J., Edge, A. C., and Johnstone, R. M. (2005). The nature of the molecular gas system in the core of NGC 1275. , 359(2):755–764.

[219] Wilman, R. J., Edge, A. C., Johnstone, R. M., Fabian, A. C., Allen, S. W., and Crawford, C. S. (2002). Exciting molecular hydrogen in the central galaxies of cooling flows. , 337(1):63–70.

[220] Wilman, R. J., Edge, A. C., and Swinbank, A. M. (2006). Integral field spectroscopy of Hα emission in cooling flow cluster cores: disturbing the molecular gas reservoir. , 371:93–107.

[221] Wilman, R. J., Edge, A. C., and Swinbank, A. M. (2009). Integral field spectroscopy of ionized and molecular gas in cool cluster cores: evidence for cold feedback? , 395(3):1355–1370.

[222] Wright, E. L. (2006). A Cosmology Calculator for the World Wide Web. , 118:1711–1715.

[223] Wu, K. K. S., Fabian, A. C., and Nulsen, P. E. J. (2000). Non-gravitational heating in the hierarchical formation of X-ray clusters. , 318:889–912.

[224] XRISM Science Team (2020). Science with the X-ray Imaging and Spectroscopy Mission (XRISM). *arXiv e-prints*, page arXiv:2003.04962.

[225] Zhuravleva, I., Allen, S. W., Mantz, A., and Werner, N. (2018). Gas Perturbations in the Cool Cores of Galaxy Clusters: Effective Equation of State, Velocity Power Spectra, and Turbulent Heating. , 865(1):53.

[226] ZuHone, J. A., Markevitch, M., and Lee, D. (2011). Sloshing of the Magnetized Cool Gas in the Cores of Galaxy Clusters. , 743(1):16.

[227] ZuHone, J. A., Markevitch, M., Ruszkowski, M., and Lee, D. (2013). Cold Fronts and Gas Sloshing in Galaxy Clusters with Anisotropic Thermal Conduction. , 762(2):69.